Study of the High Energy Gamma-ray Emission from the Crab Pulsar with the MAGIC telescope and *Fermi*-LAT

Takayuki Saito

SIGILL:UNIVERSITAT:LUDOVIC:MAXIM:

München 2010

Study of the High Energy Gamma-ray Emission from the Crab Pulsar with the MAGIC telescope and *Fermi*-LAT

Takayuki Saito

Dissertation
an der Fakultät für Physik
der Ludwig–Maximilians–Universiät
München

vorgelegt von
Takayuki Saito
aus Saitama, Japan

München, den 30.09.2010

Erstgutachter: Prof. Dr. Christian Kiesling
Zweitgutachter: Prof. Dr. Masahiro Teshima
Tag der mündlichen Prüfung: 06.12.2010

Abstract

My thesis deals with a fundamental question of high energy gamma-ray astronomy. Namely, I studied the cut-off shape of the Crab pulsar spectrum to distinguish between the leading scenarios for the pulsar models.

Pulsars are celestial objects, which emit periodic pulsed electromagnetic radiation (pulsation) from radio to high energy gamma-rays. Two major scenarios evolved in past 40 years to explain the pulsation mechanism: the inner magnetosphere scenario and the outer magnetosphere scenario. Both scenarios predict a high energy cut-off in the gamma-ray energy spectrum, but with different cut-off sharpness. An exponential cut-off is expected for the outer magnetosphere scenario while a super-exponential cut-off is predicted for the inner magnetosphere scenario. Therefore, one of the best ways to confirm or refute these scenarios is to measure the energy spectrum of a pulsar at around the cut-off energy, i.e., at energies between a few GeV and a few tens of GeV. All past attempts to measure pulsar spectra with ground-based instruments have failed while satellite-borne detectors had a too small area to study detailed spectra in the GeV domain.

In this thesis, the gamma-ray emission at around the cut-off energy from the Crab pulsar is studied with the MAGIC telescope. The public data of the satellite-borne gamma-ray detector, *Fermi*-LAT, are also analyzed in order to discuss the MAGIC observation results in comparison with the adjacent energy band.

In late 2007, a new trigger system (SUM trigger system) allowed to reduce the threshold energy of the MAGIC telescope from 50 GeV to 25 GeV and the Crab pulsar was successfully detected during observations from October 2007 and January 2009. My analysis reveals that the energy spectrum is consistent with a simple power law between 25 GeV to 100 GeV. The extension of the energy spectrum up to 100 GeV rules out the inner magnetosphere scenario.

Fermi-LAT started operation in August 2008. The *Fermi*-LAT data reveal that a power law with an exponential cut-off at a few GeV can well describe the energy spectrum of the Crab pulsar between 100 MeV and 30 GeV. This is consistent with the outer magnetosphere scenario and again, inconsistent with the inner magnetosphere scenario.

The measurements of both experiments strongly disfavor the inner magnetosphere scenario. However, by combining the results of the two experiments, it turns out that even the standard outer magnetosphere scenario cannot explain the measurements. Various assumptions have been made to explain this discrepancy. By modifying the energy spectrum of the electrons which emit high energy gamma-rays via the curvature radiation, the combined measurements can be reproduced but further studies with higher statistics and a better energy resolution are needed to support this assumption.

The energy-dependent pulse profile from 100 MeV to 100 GeV has also been studied in detail. Many interesting features have been found, among which the variabilities of both the pulse edges and the pulse peak phases are the most remarkable. More data would allow a more thorough investigation of the fine structure of the pulsar magnetosphere based on these features.

Aiming for better observations of pulsars and other sources below 100 GeV, a new photosensor, HPD R9792U-40, has been investigated. Many beneficial properties, such as a very high photodetection efficiency, an extremely low ion-feedback probability and an excellent charge resolution have been found.

Zusammenfassung

Diese Dissertation behandelt eine grundlegende Fragestellung der Hochenergie-Astrophysik. Um herauszufinden, welches der führenden Modelle die Emission von Pulsaren korrekt beschreibt, untersuche ich das Abknickverhalten des Energiespektrums des Pulsars im Krebsnebel bei hohen Energien.

Pulsare sind astronomische Objekte, die durch periodische Abstrahlung (Pulsation) elektromagnetischer Wellen vom Radiobereich bis hin zur Gammastrahlung gekennzeichnet sind. Zwei Modellklassen bildeten sich in den vergangenen 40 Jahren heraus, welche den Pulsationsmechanismus mit Teilchenbeschleunigung in der inneren beziehungsweise äußeren Magnetosphäre erklären. Beide sagen ein Abknicken des Gamma-Energiespektrums voraus, allerdings mit unterschiedlicher Stärke. Bei Erzeugung der Strahlung in der äußeren Magnetosphäre erwartet man einen exponentiellen Abfall, während für die Erzeugung in der inneren Magnetosphäre ein noch stärkerer Abfall vorhergesagt wird. Daher ist die Bestimmung eines Pulsar-Energiespektrums in der Nähe des erwarteten Abknickens, also bei Energien zwischen einigen GeV und einigen zehn GeV eine gute Methode, einem dieser Szenerien Glaubwürdigkeit zu verleihen oder es andererseits auszuschließen. Alle bisherigen Versuche, Pulsarspektren mit bodengebundenen Instrumenten zu vermessen, schlugen fehl; gleichzeitig hatten satellitengestützte Detektoren eine zu kleine Sammelfläche, als dass die genaue Vermessung von Spektren möglich gewesen wäre.

Diese Arbeit untersucht die Gammastrahlungsemission des Krebsnebels in der Umgebung der Abknick-Energie mit Hilfe des MAGIC-Teleskops. Ebenfalls ausgewertet werden öffentlich zugängliche Daten des satellitengestützten Gammastrahlungsdetektors *Fermi*-LAT, so dass die MAGIC-Ergebnisse mit dem bei niedrigeren Energien anschließenden Energiebereich von *Fermi*-LAT verglichen werden können.

Ende 2007 wurde ein neues Triggersystem (ein analoger Summentrigger) in Betrieb genommen, welches die Energieschwelle des MAGIC-Teleskops von 50 GeV auf 25 GeV heruntersetzt; damit wurde während Beobachtungen von Oktober 2007 bis Januar 2009 der Pulsar im Krebsnebel erstmalig nachgewiesen. Meine Untersuchungen zeigen, dass das Energiespektum im Bereich von 25 GeV bis 100 GeV mit einem einfachen Potenzgesetz verträglich ist. Allein schon die Tatsache, dass sich das Spektrum bis 100 GeV erstreckt, schließt eine Erzeugung in der inneren Magnetosphäre aus.

Die *Fermi*-LAT Beobachtungen begannen im August 2008. Sie zeigen, dass ein Potenzgesetz mit exponentiellem Abfall bei einigen GeV das Energiespektrum des Krebspulsars zwischen 100 MeV und 30 GeV gut beschreibt. Das ist verträglich mit einer Erzeugung in der äußeren, aber nicht in der inneren Magnetosphäre. Die Messungen beider Instrumente deuten somit stark darauf hin, dass eine Erzeugung in der inneren Magnetosphäre die Daten nicht korrekt beschreibt. Wenn man nun die Resultate beider Messungen kombiniert, zeigt sich, dass selbst ein einfaches Modell zur Gammastrahlungs-Erzeugung in der äußeren Magnetosphäre die Daten nicht korrekt beschreibt. Verschiedene Annahmen sind notwendig, um die Abweichungen zu erklären. Das Spektrum der Elektronen, die die Gammastrahlung als Krümmungsstrahlung erzeugen, kann so angepasst werden, dass es die Messungen erklärt. Um diese Erklärung zu untermauern, sind eine bessere Statistik sowie Energieauflösung notwendig.

Weiterhin wurde die Energieabhängigkeit des Pulsprofils zwischen 100 MeV und 100 GeV genau untersucht. Diverse interessante Eigenschaften wurden gefunden, von denen die Veränderungen in den Pulsflanken und die Entwicklung der Phasen der Pulsationsmaxima die erwähnenswertesten sind. Von diesen ausgehend, würde eine größere Menge von Beobachtungsdaten erlauben, den Aufbau der Pulsarmagnetosphäre genau zu untersuchen.

Um Beobachachtungen von weiteren Pulsare und mehr Quellklassen unter 100 GeV zu verbessern, wurde eine neuer Photondetektor, der HPD R9792U-40, charakterisiert. Viele positive Eigenschaften konnten gefunden werden, wie beispielsweise eine sehr hohe Photon-Nachweiseffizienz, eine außerordentlich niedrige Ionenrückkopplungswahrscheinlichkeit, sowie eine ausgezeichnete Ladungsauflösung.

Contents

Introduction 1

1 Very High Energy Gamma Ray Astronomy 3

1.1 Cosmic Rays . . . 4
  1.1.1 Discovery of Cosmic Rays . . . 4
  1.1.2 Energy Spectrum of Cosmic Rays . . . 4
  1.1.3 Energy Density of Cosmic Rays in Our Galaxy . . . 6
1.2 Acceleration and Propagation of Charged Particles . . . 6
  1.2.1 Second Order Fermi Acceleration . . . 6
  1.2.2 First Order Fermi Acceleration . . . 8
  1.2.3 Electric Field Acceleration . . . 10
  1.2.4 Magnetic Dipole Radiation Acceleration . . . 10
  1.2.5 Other Acceleration Mechanism . . . 12
  1.2.6 Propagation of CRs inside Our Galaxy . . . 12
  1.2.7 Propagation of CRs outside Our Galaxy . . . 12
1.3 Gamma-ray Emission Mechanisms . . . 13
  1.3.1 Decay of a Neutral Pion . . . 13
  1.3.2 Inverse Compton Scattering Process . . . 14
  1.3.3 Synchrotron Radiation . . . 16
  1.3.4 Curvature Radiation . . . 18
  1.3.5 Bremsstrahlung . . . 19
1.4 Possible Acceleration Sites and Known VHE Gamma-ray Sources . . . 20
  1.4.1 Galactic Sources . . . 20
  1.4.2 Extragalactic Sources . . . 23
  1.4.3 List of Known VHE Gamma-ray Sources . . . 24
1.5 VHE Gamma-rays as Probes for Fundamental Physics and Cosmology . . . 26
  1.5.1 Extragalactic Background Light . . . 26
  1.5.2 Quantum Gravity Effect . . . 27
  1.5.3 Search for Dark Matter . . . 28
1.6 Concluding Remarks and the Topic of this Thesis . . . 28

2 Pulsars 31
2.1 Discovery of the First Pulsar and Currently Known Pulsars 32
  2.1.1 Discovery 32
  2.1.2 Number of Known Pulsars 32
  2.1.3 Periods of Pulsars 33
  2.1.4 Light Curves of Pulsars 33
2.2 Neutron Stars 34
  2.2.1 Neutron Stars as Identity of Pulsars 34
  2.2.2 General Properties of a Neutron Star 35
2.3 Magnetic Dipole Radiation 36
  2.3.1 Spin Down Luminosity 37
  2.3.2 Radiation Caused by a Rotating Magnetic Dipole 38
  2.3.3 Estimation of the Magnetic Field Strength at the Pole 38
  2.3.4 Estimation of the Pulsar Age 38
  2.3.5 Application to the Crab Pulsar 39
2.4 Glitches of pulsars 39
2.5 Plasma around a Pulsar 40
  2.5.1 Can a Pulsar Exist without being Surrounded by a Plasma? 40
  2.5.2 Light Cylinder 41
  2.5.3 Plasma Distribution around a Pulsar 41
  2.5.4 Current Outflow from the Pulsar Magnetosphere 42
2.6 Particle Acceleration within the Light Cylinder 44
  2.6.1 The Polar Cap Model 45
  2.6.2 The Slot Gap Model 47
  2.6.3 The Outer Gap Model 48
2.7 Non-thermal Radiations in the Pulsar Magnetosphere 49
  2.7.1 The Overall Energy Spectrum 50
  2.7.2 The Energy Cut-off 50
  2.7.3 The Light Curve 53
2.8 How to Determine the Emission Region? 57
  2.8.1 By the Highest Energy of the Observed Photons 57
  2.8.2 By the Steepness of the Cut-off 57
  2.8.3 Why was the Emission Region not Determined before 2007? 59
2.9 The Crab Pulsar 60
  2.9.1 Discovery of the Crab Pulsar and its Nebula 60
  2.9.2 Basic Properties of the Crab Pulsar 60
  2.9.3 Geometry of the Crab Pulsar, the Crab Nebula and the Supernova Remnant 61
  2.9.4 Light Curve of the Crab Pulsar 63
  2.9.5 Naming of the Pulse Phases 65
  2.9.6 The Energy Spectrum around the Cut-off Energy Measured before 2007 . 65
  2.9.7 Energy Spectrum of the Crab Nebula 68
2.10 Concluding Remarks 69

3 Imaging Atmospheric Cherenkov Telescope Technique and The MAGIC Telescope 71
- 3.1 Air Showers . . . 72
  - 3.1.1 Overview . . . 72
  - 3.1.2 Electron-Positron Pair Creation . . . 74
  - 3.1.3 Bremsstrahlung . . . 74
  - 3.1.4 Ionization and Critical Energy . . . 74
  - 3.1.5 Multiple Coulomb Scattering . . . 75
  - 3.1.6 Other Interactions . . . 75
  - 3.1.7 Hadronic Cascade . . . 76
  - 3.1.8 Differences between Hadron-induced and Gamma-ray-induced Showers . 77
  - 3.1.9 Density Profile of the Atmosphere . . . 78
  - 3.1.10 Characteristics of the Electromagnetic Cascade Development as a Function of Depth . . . 80
- 3.2 Atmospheric Cherenkov Radiation . . . 80
  - 3.2.1 Principle of Cherenkov Radiation . . . 80
  - 3.2.2 Absorption of the Cherenkov Photons by Air . . . 83
  - 3.2.3 Distribution of the Cherenkov Photons on the Ground . . . 83
  - 3.2.4 Arrival Time Spread of the Cherenkov Photon on the Ground . . . 84
- 3.3 Imaging Atmospheric Cherenkov Telescope . . . 85
  - 3.3.1 General Concept . . . 85
  - 3.3.2 Background . . . 85
  - 3.3.3 Stereo Observations . . . 86
  - 3.3.4 IACTs in the World . . . 86
- 3.4 The MAGIC Telescope . . . 87
  - 3.4.1 Frame and Drive System . . . 87
  - 3.4.2 Reflector . . . 88
  - 3.4.3 Camera . . . 89
  - 3.4.4 Signal Transmission . . . 90
  - 3.4.5 Data Acquisition . . . 91
  - 3.4.6 Standard Trigger . . . 92
  - 3.4.7 Analogue Sum Trigger . . . 94
  - 3.4.8 Pyrometer . . . 99
  - 3.4.9 Central Pixel . . . 99
  - 3.4.10 Rubidium and GPS Clock . . . 100
  - 3.4.11 Calibration Box for Calibrating the PMTs . . . 101
  - 3.4.12 Observation Mode . . . 101
- 3.5 Concluding Remarks . . . 103

4 Analysis Method of MAGIC Data 105
- 4.1 Signal Calibration . . . 106
  - 4.1.1 Pedestal and Calibration Pulse Events . . . 107
  - 4.1.2 Conversion Factor . . . 107

4.1.3 Relative Timing Offset . . . 108
4.2 Image Cleaning . . . 109
4.2.1 Shower Core Search . . . 109
4.2.2 Boundary Search . . . 109
4.2.3 Rejection of Pixels and Charge Recalculations . . . 109
4.2.4 Examples of Image Cleaning . . . 109
4.3 Parameterization of Images . . . 111
4.3.1 Example of Different Types of Images . . . 111
4.3.2 Parameterization of the Images . . . 112
4.4 Hadron/Gamma-ray Separation . . . 113
4.4.1 Differences in Image Parameters between Gamma-rays and Hadrons+Muons 113
4.4.2 Random Forest Method . . . 116
4.5 Energy Reconstruction . . . 119
4.6 Arrival Direction Reconstruction . . . 120
4.7 Pulse Phase Calculation . . . 121
4.8 Signal Extraction . . . 122
4.8.1 By Using the $ALPHA$ Distribution . . . 123
4.8.2 By Using the θ^2 Distribution . . . 124
4.8.3 By Using the Pulsar Light Curve . . . 124
4.8.4 Evaluation of Statistical Significance for an Extracted Signal . . . 125
4.9 Energy Spectrum Calculation . . . 125
4.9.1 Effective Area Calculation . . . 125
4.9.2 Observation Time Calculation . . . 126
4.9.3 The Number of Excess Events for Each Energy Bin . . . 126
4.10 Sky Map . . . 128
4.11 Reflector Performance Calibration with Muon events . . . 129
4.12 Systematic Uncertainties . . . 131
4.13 Concluding Remarks . . . 133

5 MAGIC Observations of the Crab Pulsar and Data Analysis 135
5.1 Observations . . . 135
5.2 Sum Trigger Sub-patch Malfunction . . . 135
5.3 Data Selection . . . 138
5.3.1 Reflector Performance Selection . . . 138
5.3.2 Zenith Angle Selection . . . 139
5.3.3 Cloudiness Selection . . . 139
5.3.4 Event Rate Selection . . . 141
5.3.5 Nebula Measurement Selection . . . 141
5.3.6 Summary of the Data Selection . . . 142
5.4 $ALPHA$ Cut Optimization for Pulsar Analysis . . . 144
5.5 Analysis of the Energy Spectrum of the Crab Nebula . . . 146
5.5.1 Data Sample for the Crab Nebula Analysis . . . 146
5.5.2 Energy Range of the Crab Nebula Analysis . . . 146

5.6 Analysis of Optical Pulsation . . . 149
5.7 Detection of the Very High Energy Gamma-ray Pulsation from the Crab Pulsar . 150
5.7.1 The Pulsed Gamma-ray Signal . . . 150
5.7.2 Further Investigation of the Signal . . . 151
5.8 SIZE Dependence of the Pulsation . . . 152
5.9 Time Variation of the Pulsation from the Crab Pulsar . . . 155
5.9.1 Variability in Light Curve . . . 155
5.9.2 Variability in Flux . . . 155
5.10 Energy Spectra of the Pulsation from the Crab Pulsar . . . 155
5.10.1 Excess Distribution in the Reconstructed Energy and Size . . . 156
5.10.2 Spectrum Calculation by Forward Unfolding Assuming a Power Law . . 156
5.10.3 Spectrum Calculation by Unfolding with Different Regularization Methods . . . 157
5.10.4 Discussion of the Results . . . 158
5.11 Concluding Remarks . . . 158

6 Analysis of *Fermi*-LAT public Data 161
6.1 Detector Design of *Fermi*-LAT . . . 161
6.2 Detector Performance of *Fermi*-LAT . . . 163
6.3 Data Sample . . . 164
6.4 The Light Curve . . . 165
6.5 The Crab Nebula Analysis . . . 167
6.6 The Crab Pulsar Spectrum . . . 169
6.6.1 Power Law + Cut-off Assumption for the Crab Pulsar Spectrum . . . 169
6.6.2 Power Law Extension Assumption for the Crab Pulsar Spectrum above the Cut-Off . . . 174
6.7 Concluding Remarks . . . 174

7 Analysis of the Energy Spectrum and the Light Curve Combining MAGIC and *Fermi*-LAT results 177
7.1 Energy Spectra of P1 + P2, P1 and P2 . . . 177
7.1.1 How Much Do the MAGIC Measurements Deviate from an Exponential Cut-off Spectrum? . . . 179
7.1.2 How Much Do the MAGIC Measurements Deviate from an Sub-Exponential Cut-off Spectrum? . . . 184
7.1.3 Power Law Fit above 4 GeV . . . 189
7.2 P2/P1 Ratio and Bridge/P1 Ratio . . . 191
7.3 Rising and Falling Edges . . . 195
7.4 Peak Phases . . . 200
7.4.1 Kernel Density Method . . . 200
7.4.2 Example of the Kernel Density for Different Energies . . . 205
7.4.3 Results . . . 207
7.5 Possible Existence of the Third Peak . . . 208

7.5.1 Definition of the ON and OFF Phases for the Third Peak P3 208
7.5.2 MAGIC and *Fermi*-LAT above 10 GeV 208
7.6 Concluding Remarks 209

8 Discussion 211
8.1 Constraints on the Emission Region 211
8.1.1 By the Steepness of the Cut-off 212
8.1.2 By the Highest Energy of the Observed Photons 212
8.2 Estimates of the Electron Spectrum and Constraints on the Acceleration Electric Field 212
8.2.1 Basic Equations for the Electron Energy and the Curvature Radiation Photon Energy 213
8.2.2 Estimates of the Electron Spectrum Based on the Measured Gamma-ray Spectrum 214
8.2.3 Constraints on the Acceleration Electric Field in an Ideal Dipole Magnetic Field 220
8.2.4 Possible Explanations for the High Energy Tail of the Gamma-ray Spectrum in an Imperfect Dipole Magnetic Field 221
8.3 Inverse Compton Scattering as a Second Radiation Component 222
8.4 Radiation Efficiency 222
8.5 Remarks on the High Energy Tail of the Crab Pulsar Energy Spectrum 224
8.6 Energy Dependence of the Rising and Falling Edges in the Light Curve 224
8.7 Energy Dependence of the Peak Phase 226

9 Development of High Quantum Efficiency Hybrid Photodetector HPD R9792U-40 229
9.1 Structure and Operation Principle of the HPD R9792U-40 230
9.1.1 Overall Structure 230
9.1.2 Operation Principle 230
9.2 Photodetection Efficiency 232
9.2.1 Quantum Efficiency 232
9.2.2 Collection Efficiency 232
9.2.3 Improvement in PDE Compared to PMTs 233
9.2.4 Uniformity of the photocathode 233
9.3 Gain 234
9.3.1 Bombardment Gain 234
9.3.2 Avalanche Gain and Leakage Current 235
9.4 Pulse Shape 236
9.4.1 Standard Readout 236
9.4.2 Inverted Polarity 236
9.5 Charge Resolution 238
9.5.1 Photoelectron Resolution 238
9.5.2 Backscattering of Electrons 238
9.6 Dynamic Range 240

9.7 Afterpulsing 240
9.7.1 Afterpulsing Probability 240
9.7.2 Timing Properties of Afterpulses 243
9.7.3 Fast-and-huge afterpulses 245
9.8 Lifetime 247
9.9 Temperature Compensation 249
9.10 Safety Circuit 251
9.10.1 Limitation of the Photocathode Current 251
9.10.2 Limitation of the APD Current 252
9.11 Installation to MAGIC 252
9.12 Concluding Remarks 254

10 Conclusions and Outlook 257
10.1 Conclusions 257
10.2 Future Prospect: Observations of Other Gamma-ray Pulsars 260
10.3 Future Prospect: Improvement of the Telescope Performance 260
10.3.1 Installation of the HPD R9792U-40 261
10.3.2 Stereoscopic Observation with the MAGIC Stereoscopic System 261
10.3.3 Pulsar Observation with CTA 262

Acknowledgement 277

List of Acronyms and Abbreviations

AGASA	Akeno Giant Air Shower Array
AGN	Active Galactic Nuclei
a.s.l.	above sea level
BeppoSAX	Satellite per Astronomia X (”Beppo” in honor of Giuseppe Occhialini)
CANGAROO	Collaboration of Australia and Nippon (Japan) for a GAmma Ray Observatory in the Outback
CCD	Charge-Coupled Device
CE	Collection Efficiency
CGRO	Compton Gamma-Ray Observatory
CIB	Cosmic Infrared Background
CMB	Cosmic Microwave Background
COB	Cosmic Optical Background
COG	Center Of Gravity
COMPTEL	imaging COMPton TELescope (on CGRO)
CR	Cosmic Ray
CTA	Cherenkov Telescope Array
DAQ	Data AcQuisition
dof	degree of freedom
EBL	Extragalactic Background Light
EGRET	Energetic Gamma-Ray Experiment Telescope (on CGRO)
FADC	Flash Analogue-to-Digital Converter
FoV	Field of View
FWHM	Full Width Half Maximum
GRB	Gamma-Ray Burst
GBM	Gamma-ray Burst Monitor (on *Fermi* gamma-ray space telescope)
GPS	Global Positioning System
GZK	Greisen-Zatsepin-Kuzmin
HESS	High Energy Stereoscopic System
HiRes	High Resolution fly’s eye
HRI	High Resolution Imager
HV	High Voltage

IR	InfraRed
IACT	Imaging Atmospheric Cherenkov Telescope
LAT	Large Area Telescope (on *Fermi* gamma-ray space telescope)
LED	Light Emitting Diode
MAGIC	Major Atmospheric Gamma-ray Imaging Cherenkov telescope
MECS	Medium Energy Concentrator Spectrometer
MC	Monte Carlo simulation
MJD	Modified Julian Day
MSSM	Minimal Supersymmetric Standard Model
NN	Next Neighboring
NSB	Night Sky Background
OG	Outer Gap
PC	Polar Cap
PDE	Photodetection Efficiency
PFF	Pair Formation Front
ph.e.	PhotoElectron
PCB	Print Circuit Board
PDS	Phoswich Detector System
PMT	PhotoMulitiplier Tube
PSF	Point Spread Function
PSR	Pulsar
PWN	Pulsar Wind Nebula
QCD	Quantum ChromoDynamics
QE	Quantum Efficiency
QG	Quantum Gravity
RMS	Root Mean Square
ROSAT	RÖntgenSATellit
SCLF	Space Charge Limited Flow
SED	Spectral Energy Distribution
SG	Slot Gap
SMBH	SuperMassive Black Hole
SNR	SuperNova Remnant
SUSY	SUperSYmmetry
UV	UltraViolet
VCSEL	Vertical-Cavity Surface-Emitting Laser
VERITAS	Very Energetic Radiation Imaging Telescope Array System
VHE	Very High Energy (>10 GeV)
WIMP	Weakly Interacting Massive Particle
WLS	WaveLength Shifter
WMAP	Wilkinson Microwave Anisotropy Probe
WR	Wolf-Rayet
ZA	Zenith Angle

List of Useful Units

In addition to the standard units in the cgs system, following units are useful in astrophysics and will be used in this thesis.

eV	1.602×10^{-12} erg
keV	10^3 eV
MeV	10^6 eV
GeV	10^9 eV
TeV	10^{12} eV
PeV	10^{15} eV
pc	3.086×10^{18} cm
kpc	10^3 pc
Mpc	10^6 pc
b	10^{-24} cm^{-2}
mb	10^{-3} b

List of Useful Physics Constants and Parameters

c	speed of light	2.998×10^{10} cm/s
h	Planck constant	6.602×10^{-27} erg s
$\hbar$	= $h/2\pi$, reduced Planck constant	1.054×10^{-27} erg s
G	Newtonian gravitational constant	6.6742×10^{-8} $\mathrm{cm}^3\ \mathrm{g}^{-1}\ \mathrm{s}^{-2}$
e	electric charge of an electron	4.803×10^{-10} esu, 1.602×10^{-19} C
m_e	mass of an electron	9.109×10^{-28} g, 511 $\mathrm{keV/c}^2$
m_μ	mass of muon	105.7 $\mathrm{MeV/c}^2$
m_{π_0}	mass of a neutral pion	135.0 $\mathrm{MeV/c}^2$
α	$= e^2/\hbar c$, fine structure constant	7.297×10^{-3} = 1/137.035
r_e	$= e^2/m_e c^2$, classical electron radius	2.818×10^{-13} cm
σ_T	$= 8\pi r_e^2/3$, Thomson cross section	6.652×10^{-25} cm^2
ƛ	$= \hbar/m_e c = r_e/\alpha$, electron Compton wavelength	3.862×10^{-11} cm
B_c	$= m_e^2 c^3/\hbar e$, critical magnetic field strength	4.414×10^{13} G
$M_\odot$	solar mass	1.988×10^{33} g

Introduction

The first detection of the TeV gamma-rays from a celestial object, i.e. the discovery of the Crab Nebula by the Whipple telescope in 1989, opened a new field in astronomy, which is called very high energy (VHE) gamma-ray astronomy. In this thesis, VHE gamma-ray stands for photons with energies above 10 GeV. As of now approximately 100 VHE gamma-ray sources are known, which are categorized into several classes such as active galactic nuclei, supernova remnants, pulsar wind nebulae and gamma-ray binaries. Observations in VHE gamma-rays have given first insight into the nature of these extremely dynamical objects emitting non-thermal radiation.

Pulsars are a class of celestial objects, which emit periodic pulsed radiation (pulsation) extending from radio up to gamma-rays. VHE gamma-rays can serve as an important probe for the radiation mechanism of pulsars, too. Pulsars are explained as rapidly rotating neutron stars which possess extremely strong magnetic fields. Electrons are accelerated within their magnetosphere by strong electric field and emit beamed electromagnetic radiation, which will be observed as pulsation due to the rotation of the neutrons star. On top of this general picture of the pulsation mechanism, there are two competing major scenarios which specify the acceleration/emission region within the magnetosphere. One is the inner magnetosphere scenario, in which the pulsation originates from near the magnetic pole on the neutron star surface. The other is the outer magnetosphere scenario, in which the pulsation comes from a region along the last closed magnetic field lines in the outer magnetosphere. Both scenarios could reasonably explain all the features of pulsars observed before 2007. One of the best ways to verify or refute these scenarios is measuring the energy spectrum at around cut-off energy, i.e. at energies between a few GeV and a few tens of GeV. The reason is as follows: Both scenarios predict a high energy cut-off in the gamma-ray energy spectrum, but with different cut-off sharpness. An exponential cut-off is expected for the outer magnetosphere scenario while a super-exponential cut-off is predicted for the inner magnetosphere scenario. The sharpness of the cut-off and the highest energy of the observed photons allow one to constrain the emission region.

Before 2007, a satellite-borne detector, EGRET, detected 7 gamma-ray pulsars and the energy spectra could well be measured only up to ~ 5 GeV. On the other hand, ground-based imaging atmospheric Cherenkov telescopes (IACTs) could set flux upper limits only above 100 GeV. There existed no sufficient measurement in the important energy range, i.e., at energies between a few GeV and a few tens of GeV. It was evident that filling this energy gap would lead to a clarification between the competing scenarios and a better understanding of the pulsation mechanism.

The MAGIC telescope is the IACT that has a largest single dish reflector with a 17 m diameter. Accordingly, it has the lowest energy threshold among IACTs (50 GeV in the case of the standard trigger). MAGIC has been the best instrument to fill the energy gap from the higher side. Moreover, in October 2007, the new trigger system (SUM trigger system) was implemented, which reduced the energy threshold even further, from 50 GeV to 25 GeV. Nearly at the same time, a new satellite-borne gamma-ray detector, *Fermi*-LAT, became operational in August 2008, which has a ~ 10 times better sensitivity than EGRET and could measure the pulsar energy spectrum well beyond 10 GeV. It began filling the gap from the lower side.

In this thesis, the observational results on the Crab pulsar by MAGIC at energies above 25 GeV are presented. The public data of the *Fermi*-LAT on the Crab pulsar are also analyzed from 100 MeV to ~ 30 GeV. The combined analysis of the results from two experiments is also carried out, carefully taking into account the systematic uncertainties of both experiments. Then, several constraints in the pulsar model based on the combined energy spectrum are discussed. In addition to the spectral study, energy-dependent pulse profiles between 100 MeV to 100 GeV are intensely studied. The possibility to infer the fine structure of the emission region based on the pulse profile is also discussed.

Aiming for better observations of some selected pulsars and other sources below 100 GeV with MAGIC, a new photodetector, HPD R9792U-40, is investigated. HPD R9792U-40 is a hybrid photodetector. Since a hybrid photodetector has never been used in any IACTs, its properties and performance are thoroughly studied.

The thesis is structured as follows. An introduction to VHE gamma-ray astronomy is given in Chapter 1. Pulsars and theoretical models of the pulsation mechanism are introduced in Chapter 2. Chapter 3 describes the IACT technique and the MAGIC telescope. The analysis methods of the MAGIC data and its performance are explained in detail in Chapter 4. The analysis results of the MAGIC data and the public *Fermi*-LAT data on the Crab pulsar are presented in Chapter 5 and Chapter 6, respectively. In Chapter 7, a combined analysis of the results of the two experiments is performed. Physics discussions on the results are presented in Chapter 8. The properties and performance of HPD R9792U-40 and the development of associated operation circuits are presented in Chapter 9. Conclusions and outlook are added in Chapter 10.

Chapter 1

Very High Energy Gamma Ray Astronomy

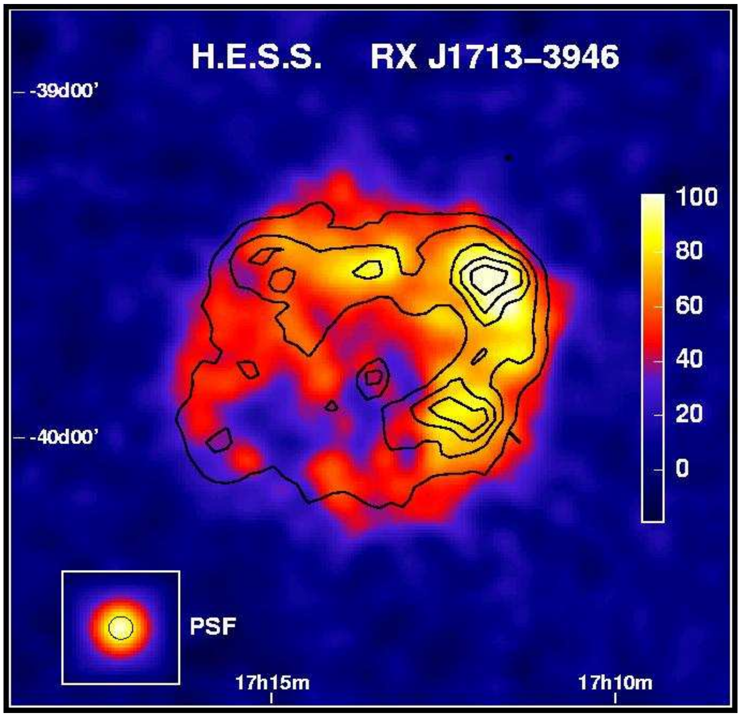

Figure 1.1: A VHE gamma-ray skymap of a supernova remnant, RX J1713.7-3946, observed by HESS (High Energy Stereoscopic System). The superimposed contours show the X-ray surface brightness. Figure adopted from [13].

In order to explore the Universe, one needs to catch its "messengers" such as cosmic-ray nuclei, electrons, neutrinos, photons and gravitational waves. Among them, photons are the most useful ones because they retain directional information of their origin unlike charged particles which suffer magnetic field scattering, while efficiently interacting with detectors via electromagnetic force. Neutrinos and gravitational waves are also free from magnetic fields but detection of them relies on weak or gravitational interactions, which are much less efficient than the electromagnetic one. Nowadays the Universe is being observed by photons with energies ranging from 10^{-7} eV to 10^{14} eV. Photons are called by different names depending on the energies: radio (below 10^{-2} eV), infrared (10^{-2} to 2 eV), optical (2 to 3 eV), ultraviolet (3 to 100 eV), X-ray (100 to 5×10^5 eV) and gamma-rays (above 5×10^5 eV). The energy range between 10^{10} and 10^{14} eV is named "very high energy" (VHE) and is the main energy domain of observations analyzed in this thesis. Photons in different energy bands deliver different kinds of information and the major role of the VHE gamma-rays is to transmit information from locations in the Universe where very high energy particle processes take place. Efficient particle acceleration can occur mostly when there are extreme astronomical objects or phenomena such as neutron stars, black holes, supernova explosions and gamma-ray bursts. Consequently, VHE gamma-ray astronomy is connected to the extreme aspect of the Universe. In addition, VHE gamma-rays can provide valuable information about some aspects of fundamental astrophysics and cosmology such as deducing the energy spectra of the extra-galactic background light (EBL), probing for the quantum gravity effect and searching for the dark matter.

In this chapter, VHE astronomy is introduced, starting in Sect. 1.1 with cosmic rays, through which human beings first realized the presence of strong particle acceleration in the Universe. The mechanisms of charged particle acceleration and propagation will be described in Sect. 1.2, while Sect. 1.3 explains various mechanisms for gamma-ray production. The possible sites for charged particle acceleration and known VHE sources will be depicted in Sect. 1.4. In Sect. 1.5, I will introduce several topics of fundamental physics and cosmology for which VHE gamma-ray astronomy can be a useful probe. Finally, concluding remarks of this chapter and the reason for the choice of a pulsar as a topic of this thesis will be given in Sect. 1.6.

1.1 Cosmic Rays

Cosmic Rays (CRs) are high energy atomic nuclei and electrons generated at various locations in the Universe. The earth is constantly bombarded by CRs. Most of them are absorbed by the atmosphere, or else life would not have developed on Earth.

1.1.1 Discovery of Cosmic Rays

In 1912, an Austrian physicist, Viktor Hess, found through balloon experiments that ionization in the atmosphere increased with increasing altitude, indicating the presence of radiation coming from the Universe (see [98]). This was the discovery of CR and the start of a new research field still very active today. In 1939, Pierre Auger discovered the phenomenon of cosmic ray air showers (see [32] and Sect. 3.1). Measurements of air showers led to the determination of the energy spectrum of CRs and proof that CRs up to 10^{20} eV were generated in the Universe.

1.1.2 Energy Spectrum of Cosmic Rays

The energy spectrum of the CRs has been measured by various experiments. Surprisingly, it shows a power law over 10 decades, from 10^{10} to 10^{20}eV as displayed in Fig. 1.2. The existence

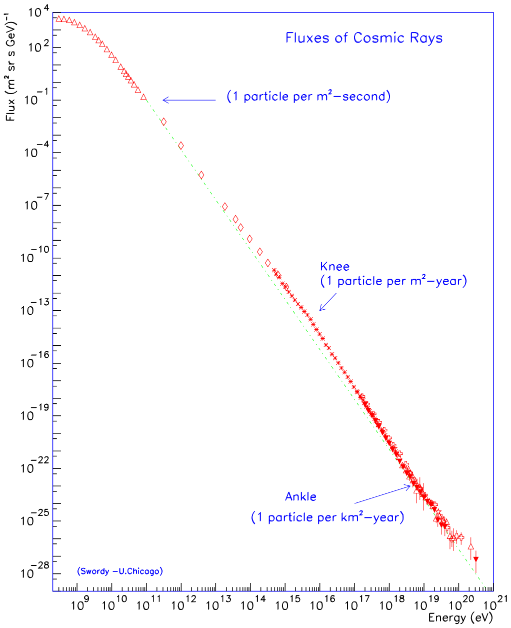

Figure 1.2: CR spectrum from $\sim 10^8$ *to* $\sim 10^{20}$ *eV. It shows a power low above* 10^{10} *eV but the index changes at* 3×10^{15} *eV and* 3×10^{18} *eV, respectively called "knee" and "ankle". Figure adopted from [58].*

of such high energies and the power law spectrum clearly show that CRs are produced by non-thermal processes. Below 10^{10} eV, the spectrum of the CR does not follow the power law but is curved in log-log plot. This is mainly due to the observational effect around the Earth because the geomagnetic field and solar wind magnetic field prevent low energy charged particles from entering the Earth's atmosphere. From 10^{10} to $3{\times}10^{15}$ eV and from $3\ {\times}10^{15}$ eV to 3×10^{18} eV, the spectrum follows a power law with an index of -2.7 and -3.0, respectively. The break of the spectrum at $3{\times}10^{15}$ eV (3 PeV) is called the "knee" of the CR spectrum. At 3×10^{18} eV, which is called the "ankle", the index again changes to -2.5. The two breaks of the spectrum, "knee" and "ankle", are thought to be connected with the origin of CRs i.e. the knee indicates the acceleration limit of protons and the successive limits of heavier ions inside the Galaxy while extragalactic CR dominates above the ankle. However, these matters are still under debate (see. e.g.[101]). Due to the interaction with Cosmic Microwave Background (CMB) photons (2.7 K black body radiation spectrum with a density of 400 photons/cm^3), the mean free path of charged particles with energy higher than $\sim 6 \times 10^{19}$ eV is very short ($\sim$ 30 Mpc for 10^{20} eV protons) and, therefore, a cut-off (the Greisen-Zatsepin-Kuzmin or GZK cut-off, see [199] and [198]) is expected at around this energy in the spectrum, unless there are some nearby powerful accelerators. The AGASA experiment claimed an absence of the GZK cut-off (see [176]) while HiRes experiment results suggested its existence (see [1]). Now, the Auger experiment is accumulating ultra high energy CR data to clarify the controversial results.

1.1.3 Energy Density of Cosmic Rays in Our Galaxy

The energy density of CRs near the solar system is ~1 eV/cm^3 and is comparable to that of the galactic magnetic field, the starlight in the Galaxy and CMB photons. Approximating the Galaxy volume as a flat cylinder with a radius R = 15 kpc and a height h = 200 pc and assuming that the local CR energy density $\rho = 1$ eV/cm^2 is constant over the Galaxy, the total CR energy in the Galaxy is calculated to be

$$E_{G,CR} = \pi R^2 h \rho \simeq 4 \times 10^{66}\mathrm{eV} \simeq 5 \times 10^{54}\mathrm{erg} \tag{1.1}$$

CRs generated in the Galaxy are trapped for some time within the Galaxy due to the magnetic field (3μG). The average time spent by CR particles in the Galaxy is $\sim 10^{14}$ sec (see e.g. [82]). Therefore, only a few galactic astronomical objects, which have acceleration power of $\sim 10^{40}$ erg/s, can naturally explain the observed energy density. Supernovae are the best candidates for accelerating galactic CRs, as will be discussed in Sect. 1.2.2.

1.2 Acceleration and Propagation of Charged Particles

How can CR particles be accelerated in the Universe? Here, several acceleration mechanisms will be described. The following sub-sections are basically a synthesis taken from a number of text books and papers, referenced in the Bibliography, dealing with the acceleration and propagation of CRs.

1.2.1 Second Order Fermi Acceleration

Our galaxy is filled with highly variable magnetic "clouds". In the rest frame of a cloud, charged particles will be elastically scattered. If clouds are moving, the particles will gain energy. Here, I describe this acceleration mechanism which is called the second order Fermi acceleration named after its original proposer E. Fermi (see [75]).

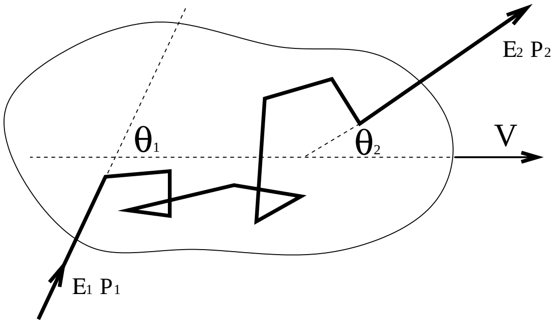

Figure 1.3: Schematic view of scattering of a particle by a large moving magnetic cloud. In the rest frame of the cloud, the magnetic fields change the direction of the particle keeping the energy constant. In the lab frame, the particle gains energy. The gain comes from the motion of the cloud, i.e. its kinetic energy.

Let us consider the collision of a particle with a magnetic cloud moving with a velocity of V. The energy (momentum) of the particles before and after scattering are E_1 (P_1) and E_2 (P_2), respectively. In the rest frame of the cloud, the energy of the particle before scattering E'_1 would be

$$E'_1 = \gamma(E_1 - \beta P_1 \mathrm{cos}\theta_1) \simeq \gamma E_1(1 - \beta\mathrm{cos}\theta_1) \tag{1.2}$$

where $\gamma = 1/\sqrt{1-\beta^2}$, $\beta = V/c$, θ_1 is the angle of the incoming direction of the particle with respect to the direction of the movement of the cloud (see Fig. 1.3). Similarly, the energy of the particle after scattering E'_2 would be

$$E_2 \simeq \gamma E'_2(1 + \beta\mathrm{cos}\theta'_2) \tag{1.3}$$

where θ'^2 is the angle of outgoing direction of the particle in the cloud rest frame, with respect to the direction of the movement of the cloud. In the cloud rest frame, the scattering is elastic and thus $E'_1 = E'_2$. Therefore, the energy gain of the particle by a single collision is

$$\frac{\Delta E}{E} = \frac{E_2 - E_1}{E_1} = \frac{1 - \beta\mathrm{cos}\theta_1 + \beta\mathrm{cos}\theta'_2 - \beta^2\mathrm{cos}\theta_1\mathrm{cos}\theta'_2}{1-\beta^2} - 1 \tag{1.4}$$

Now, the mean value of cosθ_1 and cosθ'_2 should be calculated. Since scattering is isotropic in the cloud rest frame, $< \mathrm{cos}\theta'_2 >$ = 0. The probability of the collision with an angle θ_1 is proportional to $v - V\mathrm{cos}\theta_1$. When $v \simeq c$,

$$\frac{dP}{d\Omega_1} \propto 1 - \beta\mathrm{cos}\theta_1 \tag{1.5}$$

where $\Omega_1 = 2\pi(1 - \mathrm{cos}\theta_1)$. Therefore,

$$\begin{aligned} < \mathrm{cos}\theta_1 > &= \int_{\theta_1=0}^{\theta_1=\pi} \mathrm{cos}\theta_1 \frac{dP}{d\Omega_1} d\Omega_1 \Big/ \int_{\theta_1=0}^{\theta_1=\pi} \frac{dP}{d\Omega_1} d\Omega_1 = -\frac{\beta}{3} && (1.6) \\ \frac{\Delta E}{E} &= \frac{1+\beta^2/3}{1-\beta^2} - 1 \simeq \frac{4}{3}\beta^2 \equiv \alpha && (1.7) \end{aligned}$$

Since the energy gain is proportional to β^2, it is called the "second order" Fermi acceleration. After n collisions, the energy of the particle will be

$$E(n) = E_0(1+\alpha)^n \tag{1.8}$$

where E_0 is the initial energy. When particles stay in a galaxy for τ on average and they collide with clouds every τ_{col}, the probability that a CR particle can collide n times without escaping from Galaxy should be

$$P(> n) = (1 - \tau_{col}/\tau)^n \tag{1.9}$$

where $\tau_{col} << \tau$ is assumed. Therefore, from Eqs. 1.8 and 1.9, CR flux $F(>E)$ above energy E would be

$$\log F(>E) \propto \log P(>n) = \log(E/E_0)/\log(1+\alpha) \times \log(1-\tau_{col}/\tau) \tag{1.10}$$

$$F(>E) \propto (E/E_0)^{\frac{\log(1-\tau_{col}/\tau)}{\log(1+\alpha)}} \simeq (E/E_0)^{\frac{-\tau_{col}}{\tau\alpha}} \tag{1.11}$$

Typically, the velocity of clouds is 30 km/sec corresponding to $\alpha \sim 10^{-8}$ and τ_{col}/τ is 10^{-6}, leading to the spectral index of -100, which is by far steeper than the CR spectrum (the index of -1.7 between 10 GeV and 3 PeV). Therefore, this mechanism is unable to explain CR acceleration.

1.2.2 First Order Fermi Acceleration

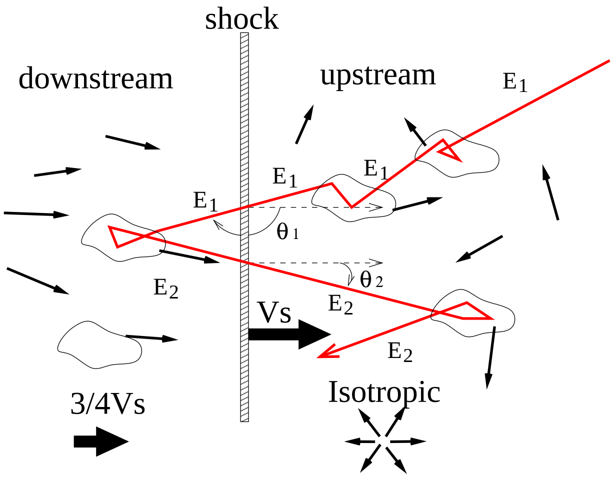

Figure 1.4: Scattering of a particle near a shock wave in the rest frame of upstream interstellar medium. A particle crosses the shock from upstream to downstream and is scattered back by a magnetic field. As with the 2nd order Fermi acceleration (Sect. 1.2.1), the particle gains energy each time it crosses the shock front.

In order to obtain the observed hard spectrum, a more efficient acceleration mechanism is required. A shock wave of plasma can provide a more efficient mechanism, as also advocated by E. Fermi (see [75], [76] and [116]). During the propagation of the shock wave, particles can cross the shock front back and forth many times because the magnetic fields scatter them. Each time particles cross the shock, they gain energy. As a result, they can be accelerated up to very high energies.

Let us consider the shock wave with the velocity V_s. According to the Rankine-Hugoniot relations (see [151]) assuming fully ionized gas and non-relativistic shocks, the mean velocity of the downstream particles (the shock passed) is $3V_s/4$ (see Fig. 1.4). If a particle passes the shock front from upstream to downstream with an angle θ_1 and comes back with an angle θ_2' (in the rest frame of downstream matters), the energy of the particle increases and the gain is exactly the same as Eq.1.4, where $\beta = (3V_s)/(4c)$ in this case. The difference compared to the second order Fermi acceleration arises in the mean value of $\cos\theta_1$ and $\cos\theta_2'$ because of the shock front. Hereafter, I assume that the velocity of particles v is much larger than the shock speed V_s, $V_s << v$. The probabilities that a particle crosses the shock from upstream to downstream with an angle θ_1 and that from downstream to upstream with an angle θ_2' are

$$\frac{dP}{d\Omega_1} \propto -\cos\theta_1, \quad \frac{dP}{d\Omega_2'} \propto \cos\theta_2' \tag{1.12}$$

$< \cos\theta_1 >$ and $< \cos\theta_2' >$ can be calculated by Eq. 1.6 but with a different integration range of $\pi/2$ to π and 0 to $\pi/2$, respectively.

$$< \cos\theta_1 > = - < \cos\theta_2' >= -\frac{2}{3} \tag{1.13}$$

Substituting these in Eq. 1.4, one obtains

$$\frac{\Delta E}{E} \simeq \frac{4}{3}\beta = V_s/c \equiv \alpha \tag{1.14}$$

In this mechanism, the energy gain per crossing (back and forth) is proportional to first order in β, and that is why this process is called First order Fermi acceleration. It should be remembered that β is the velocity of the magnetic cloud for the second order Fermi acceleration while it is 3/4 of the velocity of the shock wave for the first order Fermi acceleration. The energy spectrum of the accelerated particles can be calculated as follows: As one can see from the relative velocity between the shock front downstream particles (see Fig.1.4), the number of particles which escape from the acceleration region per unit of time is

$$r_{loss} = n_{CR}V_s/4 \tag{1.15}$$

where n_{CR} is the number density of CRs. The number of particles which cross the shock front is

$$r_{cross} \simeq n_{CR}\frac{1}{4\pi}\int_0^1 (v\cos\theta)2\pi d(\cos\theta) \simeq n_{CR}v/4 \tag{1.16}$$

The probability that a particle escapes from the acceleration region without another crossing is $P_{esc} = r_{loss}/r_{cross} = V_s/v << 1$. The probability $P(> n)$ that a particle can cross the shock more than n times and the energy $E(n)$ after n times crossing are,

$$P(> n) = (1 - V_s/v)^n \tag{1.17}$$

$$E(n) = E_0(1 + \alpha)^n \tag{1.18}$$

As with the argument for Eqs. 1.8 to 1.11, the energy spectrum of the accelerated particle would be

$$F(> E) \propto (E/E_0)^{\frac{-V_s}{\alpha v}} \simeq (E/E_0)^{-1} \tag{1.19}$$

The integral spectrum shows a power law behavior with an index of -1, which is comparable to the observed one of -1.7. Residual difference can be explained by the propagation effect of CRs (see Sect. 1.2.6).

Shock waves can be produced by, for example, supernovae explosions. The average total energy of a supernova explosion is $E_{SN} = 10^{51}$ erg. If one percent of the total energy is transferred to the CR particles by the first order Fermi acceleration and if there is one supernova every 30 years in our galaxy, then the acceleration power would be

$$P = 0.01 E_{SN}/30\text{years} = 10^{40}\text{erg/s} \tag{1.20}$$

which is consistent with the power needed to sustain the observed CR (see Sect. 1.1.3). Because of this good agreement to the measurements in both spectral shape and energy density, and also because of absence of competitive mechanisms, the first order Fermi acceleration is believed to be the major mechanism for CR acceleration.

1.2.3 Electric Field Acceleration

The most efficient acceleration of charged particles is electric field acceleration as used in the man-made accelerators for high energy particle physics. However, it is not easy to establish strong and persistent electrical fields in the Universe. One possible site is near a magnetized neutron star. This is directly connected to the pulsar emission mechanism and will be discussed in Sect. 2.6.

1.2.4 Magnetic Dipole Radiation Acceleration

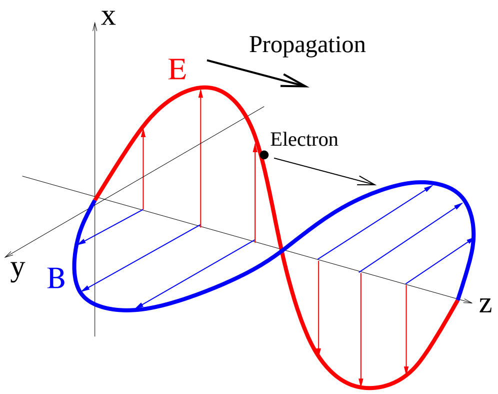

Figure 1.5: Schematic view of magnetic dipole acceleration. Charged particles are efficiently accelerated along the direction of radiation propagation because of the very strong fields and very low frequency of the radiation.

As will be described in Sect. 2.3, a pulsar has magnetic dipole radiation. It propagates spherically in the wind zone out of the light cylinder (see Fig. 1.10 and Sect. 2.5.2,). The frequency of the radiation is equal to the rotation frequency of the pulsar Ω, which is mostly between 1 and 10^4 s^{-1}. This very low frequency radiation can accelerate particles very efficiently, This was first advocated by Gunn and Ostriker (see [89]).

The magnetic fields and electric fields of the radiation in a rotating pulsar are perpendicular to each other. The strength of the electric field $|E|$ and magnetic field $|B|$ at a distance r (from the pulsar) and time t are expressed as

$$|E| = |B| = \frac{r_L}{r} B_L \mathrm{sin}\Omega(t - r/c) \tag{1.21}$$

where r_L and B_L are the radius of the light cylinder and the magnetic field strength at r_L. Defining the x, y, and z axes as electric field, magnetic field and wave propagation direction respectively (see Fig. 1.5), the acceleration mechanism can be explained as follows: The electric field tries to accelerate charged particles in direction x while the magnetic field bends the direction in the z direction. As a result, charged particles will be accelerated in the z direction. Thanks to the very strong fields and low frequency of the radiation, the velocity of the particles can reach $\sim c$ in a very short time and consequently they stay in the same phase of the radiation long enough to be accelerated to a very high energy. Following the original argument by Gunn and Ostriker (see [89]), a more quantitative estimation can be done as follows: The equations of motion of a charged particle, taking into account relativistic effects, are

$$\begin{aligned}
\frac{dv_0}{d\tau} &= \frac{ev_xE}{mc} = \frac{\omega_L r_L}{r} v_x \mathrm{sin}[\Omega(t - r/c)] && (1.22)\\
\frac{dv_x}{d\tau} &= \frac{ev_0E}{mc} - \frac{ev_zB}{mc} = \frac{\omega_L r_L}{r}(v_0 - v_z)\mathrm{sin}[\Omega(t - r/c)] && (1.23)\\
\frac{dv_y}{d\tau} &= 0 && (1.24)\\
\frac{dv_z}{d\tau} &= \frac{ev_xB}{mc} = \frac{\omega_L r_L}{r} v_x \mathrm{sin}[\Omega(t - r/c)] && (1.25)
\end{aligned}$$

where $\omega_L = eB_L/(mc)$ is the gyro-frequency and m is the mass of the particle. τ is the proper time and v_μs are the four-velocity. Solutions for these equations under the condition that a particle is at rest at $t = 0$ are

$$\begin{aligned}
v_z = v_x^2/(2c), \qquad v_0 = c + v_z && (1.26)\\
\frac{\sqrt{2}}{3}\frac{d(v_3/c)^{3/2}}{d(\mathrm{ln}r)} = \frac{\omega_L}{\Omega}\mathrm{sin}\Omega(t - r/c) && (1.27)
\end{aligned}$$

Let us assume that particles are accelerated from $r = r_0$ to $r = r_c$ while staying the same phase ϕ_0. From Eq. 1.27, the maximum attainable energy of the particle can be calculated to be

$$E^{max} = mv_0^{max}c \simeq mv_3^{max}c = mc^2\left[\frac{\omega_L}{\Omega}\frac{3}{\sqrt{2}}\mathrm{ln}\left(\frac{r_c}{r_L}\right)\mathrm{sin}\phi_0\right]^{2/3} \tag{1.28}$$

Typically ln$(r_c/r_L) \simeq 10$. In the case of the Crab pulsar, $\Omega \simeq 200$ s^{-1} and $\omega_L \simeq 10^{13}$ (10^{10}) s^{-1} for the electron (proton). Electrons and protons can reach 10^{14} eV and 10^{15} eV, respectively. This very powerful acceleration mechanism creates strong pulsar winds.

It should be noted that this mechanism works only when a condition $\Gamma_0 \omega_L \Omega > \omega_p^2$ is met, where Γ_0 is the Lorentz factor of the particle at injection point and ω_p is the plasma frequency in the wind zone (see [89]). Even if the condition is not fulfilled, for example, due to high plasma density, Poynting energy flux $\mathbf{E} \times \mathbf{B}$ should be transferred into plasma energy in one way or another, resulting in strong pulsar winds. Therefore, in general, the rotation energy of a pulsar is carried away mostly in the form of relativistic pulsar winds (see Sect. 2.3).

1.2.5 Other Acceleration Mechanism

The first order Fermi acceleration (see Sect. 1.2.2) was explained assuming non-relativistic shock speed. However, shock speed can be relativistic when, for example, pulsar winds are involved. Particles are also accelerated in a relativistic wind collision in a similar manner but the spectral index would be different (see e.g. [148]). The reconnection of magnetic fields is another mechanism for efficient acceleration, which is thought to take place in a variety of astrophysical objects from the Earth's magneto-tail (see e.g. [197]) to solar flares (see e.g. [108]) or active galactic nucleus jets (see e.g. [45]).

1.2.6 Propagation of CRs inside Our Galaxy

The CR particles produced in the Galaxy are trapped by the galactic magnetic field. The time τ_{esc} which the CR particles spend in the galaxy is rigidity-dependent, and hence, energy-dependent. The dependency can be measured by, for example, the boron to carbon nuclei ratio in the CRs. Since almost all boron nuclei are produced by spallation of carbon nuclei, the ratio of the two components reflects τ_{esc}. The measurements (see e.g. [83] and [172]) show $\tau_{esc} \propto E^{-0.6}$, where E is the energy of the particle. This energy dependence of τ_{esc} affects the energy spectrum of CRs, i.e.

$$\frac{dN}{dE}_{obs} \propto \frac{dN}{dE}_{src} \times E^{-0.6} \tag{1.29}$$

where $\frac{dN}{dE}_{obs}$ and $\frac{dN}{dE}_{src}$ are the energy spectra of the CRs at the origin and near the earth. Assuming the first order Fermi acceleration, the CR energy spectrum near the earth should be $\frac{dN}{dE}_{obs} \propto E^{-2.6}$, which is in good agreement with the observational results $\frac{dN}{dE}_{obs} \propto E^{-2.7}$ below 3 PeV.

1.2.7 Propagation of CRs outside Our Galaxy

Observed CRs above the ankle energy are thought to originate from extragalactic sources because the galactic magnetic fields cannot confine such ultra high energy particles and known galactic sources are insufficient to accelerate particles well above 10^{18} eV. Outside the Galaxy, CRs propagate in an extragalactic magnetic field. The strength and structure of extragalactic magnetic fields are poorly known. Assuming the turbulent structure with ~ 1 nG for a coherent length of ~ 1 Mpc (outside the galaxy clusters) one can explain well the measurement of CRs above 10^{18} eV (see e.g. [173] and [85]). As mentioned in Sect. 1.1.2 CRs with energy higher than $\sim 6 \times 10^{19}$ eV interact with CMB photons to produce pions via the Δ resonance, leading to a small mean free path (~ 30 Mpc for 10^{20} eV protons), which causes suppression of the flux of CRs from far outside of the Universe (GZK cut-off, see [199] and [198]).

1.3 Gamma-ray Emission Mechanisms

Once charged particles are accelerated to a very high energy, there exist several mechanisms to produce non-thermal gamma-rays. Here, I briefly describe these emission mechanisms. If the accelerated particles have a power law energy spectrum with an index of $-p$, the resulting gamma-rays often have a power law spectrum with an index of $-q$. The relation between p and q is different for different emission mechanisms and it is a powerful tool for VHE astronomy to study the source objects. The relation p and q will also be discussed for each mechanisms.

1.3.1 Decay of a Neutral Pion

When accelerated hadrons collide with other hadrons, mainly pions are produced with about one third of them being neutral pions, π_0. The π_0 has mass of 135 MeV/c^2 and decays nearly instantaneously into 2 photons with the lifetime of 8$\times 10^{-17}$ second.

$$p + p \to \pi_0 + X \to \gamma + \gamma + X \tag{1.30}$$

where X denotes associated products such as protons, neutrons pions and other mesons. The energy of gamma-rays from π_0 with the energy $E_{\pi_0} = \Gamma m_{\pi_0} c^2$ can be calculated as follows: In the rest frame of the π_0, the energy of the two gamma-rays is $E'_\gamma = m_{\pi_0} c^2/2$. In the lab frame, the energy of the gamma-ray is boosted to be $E_\gamma = \Gamma E'_\gamma (1+\beta \cos\theta)$,where θ is an angle between the gamma-ray momentum in the rest frame with respect to the boost direction (see Fig. 1.6). The emission angle θ should be isotropic, i.e. the mean of cosθ should be $<$cos$\theta >$ = 0. Therefore, the average gamma-ray energy will be $E_\gamma = E'_\gamma \Gamma = E_{\pi_0}/2$. If a pion has a power law energy spectra $dN_{\pi_0}/dE_{\pi_0} = K E_{\pi_0}^{-p}$, the resulting gamma-ray spectra dN_γ/dE_γ can be calculated as follows:

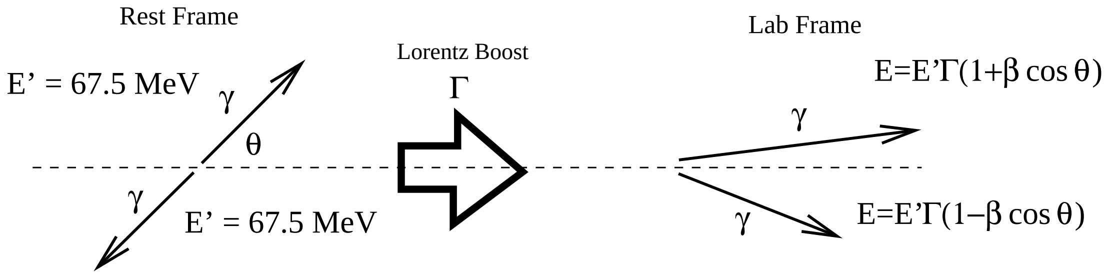

Figure 1.6: Decay of a neutral pion in the rest frame of the pion and in the lab frame

$$\begin{aligned} E_\gamma &= 1/2 E_{\pi_0}, \quad N_\gamma = 2N_{\pi_0} & (1.31)\\ \frac{dN_\gamma}{dE_\gamma} &= \frac{4dN_{\pi_0}}{dE_{\pi_0}} \propto E^{-p} & (1.32)\end{aligned}$$

The gamma-ray spectra is also a power law and its index $-q$ is equal to $-p$.

The similar argument applies to the relation between the π_0 spectrum and their parent hadron spectrum, i.e., the energy spectrum of π_0s follows that of parent hadrons. If CRs are accelerated by the first order Fermi acceleration and they produce gamma-rays via hadronic interactions, observed gamma-rays would show a power law spectrum with an index of $-q \simeq -2.0$ (see Sect. 1.2.2).

1.3.2 Inverse Compton Scattering Process

High energy electrons scatter ambient photons and transfer energy to them via the inverse Compton scattering process.

$$e + \gamma_{low} \rightarrow e + \gamma_{high} \tag{1.33}$$

In the rest frame of the electron, it is Compton scattering. The cross section of this interaction can be written as (see [107])

$$d\sigma = \frac{r_0^2}{2}\left(\frac{\epsilon''}{\epsilon'}\right)^2\left(\frac{\epsilon''}{\epsilon'} + \frac{\epsilon'}{\epsilon''} - \sin^2\theta\right) d\Omega \tag{1.34}$$

$$\frac{\epsilon''}{\epsilon'} = \frac{1}{1 + \frac{\epsilon'}{m_e c^2}(1 - \cos\theta)} \tag{1.35}$$

where ϵ', ϵ'' and θ are the energy of photon before scattering, after scattering and the scattering angle in the electron rest frame.

Thomson Regime

For the so-called Thomson regime ($\epsilon' << m_e c^2$), ϵ' should be approximately equal to ϵ'' (see Eq. 1.35) and, hence, the total cross section is simplified as (see Eq. 1.34)

$$\sigma \simeq \frac{8}{3}\pi r_0^2 = \sigma_T \tag{1.36}$$

It is independent of the photon energy and equal to the Thomson cross section σ_T. When the energies of the electron and the target photon in the lab frame are $E_e = \Gamma m_e c^2$ and ϵ, and if $\epsilon << E_e$, the mean energies of scattered photons E_γ in the lab frame can be estimated as follows (See Fig. 1.7):

In the electron rest frame, target photons come from the boost direction and the mean energy of them is $\Gamma\epsilon$ (see the middle panel of Fig. 1.7). The photons are scattered by Thomson scattering and change the direction holding the same energy. In the lab frame, the scattered photons gain energy by Lorentz boost by a factor of $\sim \Gamma$ on average. Consequently, the energy of the photon after scattering E_γ is (see the right panel of Fig. 1.7)

$$E_\gamma \simeq \epsilon\Gamma^2 \tag{1.37}$$

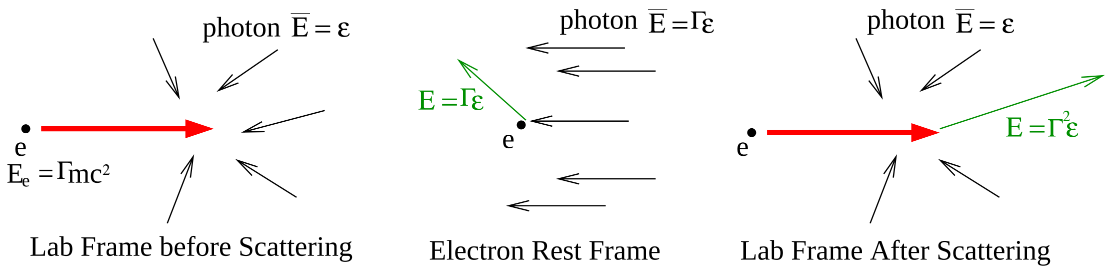

Figure 1.7: Schematic view of the inverse Compton scattering in the Thomson regime. Left: A high energy electron and ambient photons before scattering in the lab frame. The energy of the electron is $\Gamma m_e c^2$. The photons are isotropic and the mean energy is ϵ. Middle: Scattering of the photon in the electron rest frame. The ambient photons come from the boost direction and their mean energy before scattering is $\Gamma\epsilon$. The scattering changes the direction of the photon but its energy remains the same. Right: the electron and photons after the scattering. The energy of the scattered photon is $\Gamma^2\epsilon$ on average.

When energy density of the ambient photon field is U_{rad}, the number of photons scattered in a unit time is

$$n \simeq \sigma_T c U_{rad}/\epsilon = const. \tag{1.38}$$

It is independent of the electron energy; If there are electrons with a power law energy spectrum $dN_e/dE_e = KE_e^{-p}$, the energy spectrum of scattered photons would be

$$E_e \propto E_\gamma^{1/2}, \quad dE_e \propto E_\gamma^{-1/2} dE_\gamma \tag{1.39}$$

$$\frac{d^2 N_\gamma}{dE_\gamma dt} \propto \frac{n dN_e}{E_\gamma^{1/2} dE_e} = nKE_e^{-p} E_\gamma^{-1/2} \tag{1.40}$$

$$\propto E_\gamma^{-(p+1)/2} \tag{1.41}$$

The scattered photons show a power law with an index of $-q = -(p+1)/2$.

Klein-Nishina Regime

For the so-called Klein-Nishina regime ($\epsilon' >> m_e c^2$), the cross-section can be approximated as (see [10])

$$\sigma_{K-N} \simeq 3/8 \sigma_T \kappa_0^{-1} \ln(4\kappa_0) \tag{1.42}$$

$$\kappa_0 = E_e \epsilon/(m_e c^2)^2 \tag{1.43}$$

It decreases approximately proportionally to the energy of the electron or the target photon. In the electron rest frame, scattering is not the Thomson process but the photon loses energy by transferring a fraction to the electron. In the Klein-Nishina regime, by definition, $\epsilon' >> m_e c^2$. Therefore, from Eq. 1.35, the energy of the photon after scattering ϵ'' is

$$\epsilon'' \simeq m_e c^2/(1 - \cos\theta) \tag{1.44}$$

Consequently, the energy of the photon after scattering E_γ in the lab frame is

$$E_\gamma \simeq \Gamma m_e c^2 = E_e \tag{1.45}$$

When energy density of the ambient photon field is U_{rad}, the number of photons scattered per unit time is

$$n \simeq \sigma_{K-N} c U_{rad}/\epsilon \propto E_e^{-1} \tag{1.46}$$

If there are electrons with a power law energy spectrum $dN_e/dE_e = KE_e^{-p}$, the energy spectrum of scattered photons would be

$$\frac{dN_\gamma}{dE_\gamma dt} \propto \frac{ndN_e}{dE_e} \propto E_e^{-p} E_e^{-1} \tag{1.47}$$

$$\propto E_\gamma^{-(p+1)} \tag{1.48}$$

The scattered photons follow a power law spectrum with an index of $-q = -(p+1)$.

1.3.3 Synchrotron Radiation

When a charged particle moves in a magnetic field, the trajectory is bent perpendicularly to the magnetic field by the Lorentz force and emits electromagnetic radiation.

$$e + B \rightarrow e + B + \gamma \tag{1.49}$$

When the particle is relativistic, the emission is beamed in the direction of the motion and is called synchrotron radiation (see e.g. [106]). The energy spectrum of the synchrotron radiation from a single electron with the energy of $E_e = \Gamma m_e c^2$ in a unit time can be written as (see e.g. [116])

$$\frac{d^2 N_\gamma}{dE_\gamma dt}_{mono} = \frac{\sqrt{3} e^3 B \sin\alpha}{h m_e c^2 E_\gamma} F(E_\gamma/E_c) \tag{1.50}$$

$$F(x) = x \int_x^\infty K_{5/3}(z) dz \tag{1.51}$$

$$E_c = \frac{3}{2}\Gamma^2 h\nu_g \sin\alpha \tag{1.52}$$

where, B, α, and ν_g are the magnetic field strength, the pitch angle of the electron with respect to the magnetic field and the gyro-frequency $\nu_g = eB/(2\pi m_e c)$. $K_{5/3}(z)$ is the modified Bessel function of the second kind with an order of 5/3. It is not easy to express $F(x)$ in a mathematically simple form. A function $ax^b \exp(-x^c)$, however, can represent it very accurately as shown in Fig. 1.8. Fitting gives as best parameters $a = 1.787$, $b = 0.299$, and $c = 0.992$. Therefore $F(x)$ can be well approximated as

$$F(x) \simeq 1.79 x^{0.3} \exp(-x) \tag{1.53}$$

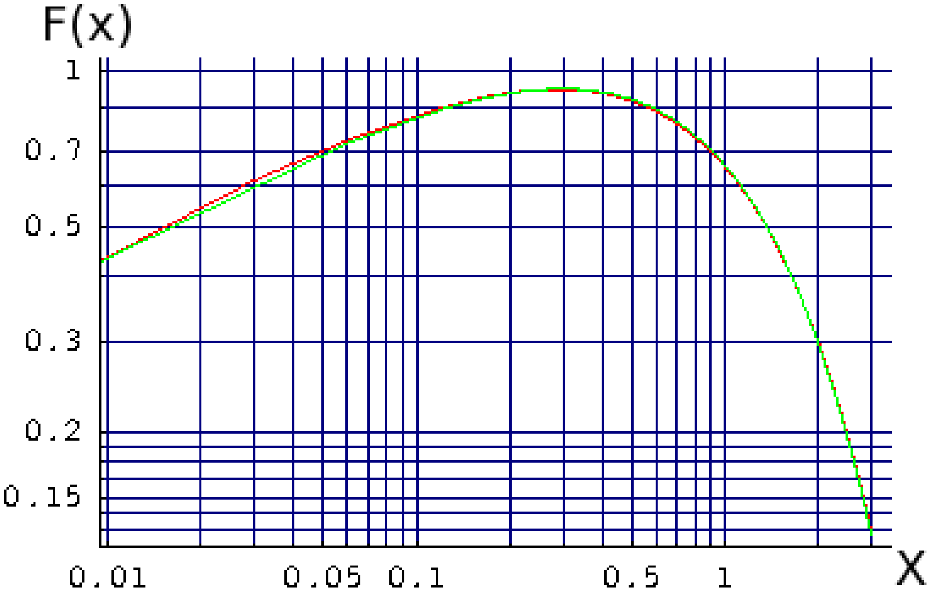

Figure 1.8: The synchrotron radiation spectrum function F(x) in log-log plot. The red line and the green line indicate the true function (Eq. 1.52) and the approximated function (Eq. 1.53). The approximation is very precise. Figure and fitting provided by J. Sitarek.

Therefore, from Eq. 1.50

$$\frac{d^2N_\gamma}{dE_\gamma dt}_{mono} \simeq \frac{1.79\sqrt{3}e^3 B\sin\alpha}{hm_e c^2 E_\gamma}(E_\gamma/E_c)^{0.3}\exp(-E_\gamma/Ec) \tag{1.54}$$

The mean energy of the emitted photon is

$$\bar{E}_\gamma = \int_0^\infty E_\gamma \frac{dN_\gamma}{dE_\gamma}_{mono} dE_\gamma / \int_0^\infty \frac{dN_\gamma}{dE_\gamma}_{mono} dE_\gamma \simeq E_c \tag{1.55}$$

$$\tag{1.56}$$

The number of photons emitted in a unit time is

$$n = \int_0^\infty \frac{d^2N_\gamma}{dE_\gamma dt}_{mono} dE_\gamma \sim \frac{e^3 B\sin\alpha}{hm_e c^2} \tag{1.57}$$

If electrons are not monoenergetic but have a power law energy spectrum KE^{-p}, the resulting synchrotron radiation spectrum will be

$$E_e \propto E_\gamma^{1/2}, \quad dE_e \propto E_\gamma^{-1/2} dE_\gamma \tag{1.58}$$

$$\frac{dN_\gamma}{dE_\gamma dt} \propto \frac{ndN_e}{E_\gamma^{1/2} dE_e} = nKE_e^{-p} E_\gamma^{-1/2} \tag{1.59}$$

$$\propto E_\gamma^{-(p+1)/2} \tag{1.60}$$

The spectral index is exactly the same as that of the inverse Compton scattering in the Thompson regime ($-q = -(p+1)/2$). It is interesting to compare the energies of emitted photons by the same electron with energy $E_e = \Gamma m_e c^2$. The typical photon energy from the inverse Compton scattering is $E_\gamma^{IC} \sim \Gamma^2 h\nu_{amb}$ while that from synchrotron radiation is $E_\gamma^{IC} \sim \Gamma^2 h\nu_g$, where ν_{amb} and ν_g are the frequency of the ambient photon and the gyrofrequency. The mean frequency of the CMB photons, which are normally the most abundant in number in the Universe, is $\nu_{amb} = 10^{11}$Hz. The magnetic field in a SuperNova Remnant (SNR) can reach 300 μ G which corresponds to 1×10^3 Hz in gyrofrequency. The emitted photon energies differ by an order of 8. For example, 5.1 TeV electrons can emit ~ 40 GeV photons by inverse Compton scattering of CMB photons while synchrotron radiation in the SNR would be ~ 400 eV.

1.3.4 Curvature Radiation

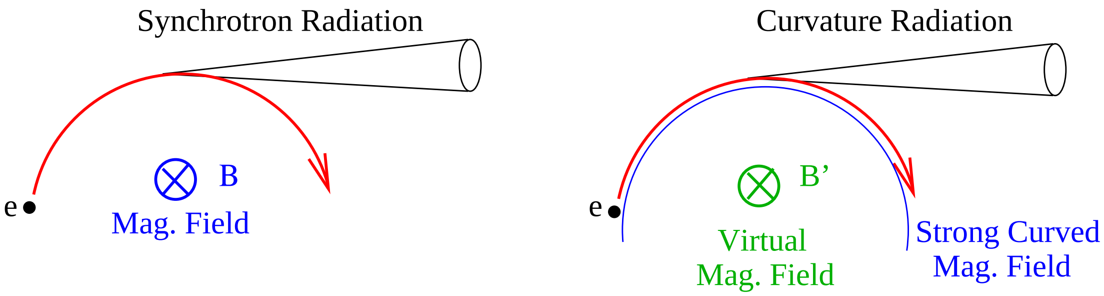

Figure 1.9: Comparison between synchrotron radiation (left) and curvature radiation (right). Both are radiation generated by the magnetic field braking. For synchrotron radiation, Lorentz force causes the brake, while for curvature radiation, the curvature of the strong magnetic field is the origin of the brake. All the properties of curvature radiation can be obtained by the analogy with synchrotron radiation by presuming that the curvature of the electron motion is caused by Lorentz force from the virtual magnetic field B'.

If there is a curved magnetic field and the gyroradius of an electron is much smaller than the curvature, the electron moves along the curved magnetic field. Since the trajectory of the electron is bent by the curvature of the magnetic field, in addition to synchrotron radiation, the electron emits another component of radiation called curvature radiation.

By assuming that curved motion is not due to the curved magnetic field but due to an imaginary magnetic field B_{curv} perpendicular to the curved field plane (see Fig. 1.14), properties of the curvature radiation could easily be obtained by an analogy with synchrotron radiation (see [144]). In the case of synchrotron radiation, the curvature of the electron motion is $R_{sync} = (m_e c^2 \Gamma)/(eB)$, thus, $B = (m_e c^2 \Gamma)/(eR_{sync})$. Therefore when the curvature of the field is R_{curv}, the imaginary magnetic field is defined as $B_{curv} = (m_e c^2 \Gamma)/(eR_{curv})$, which is dependent on the energy of a particle and curvature of the field. By replacing B in the Eqs. 1.56 - 1.60 with B_{curv} and substituting $\alpha = \pi/2$,

$$\frac{dN_\gamma}{dE_\gamma dt}_{mono} \simeq \frac{1.79\sqrt{3}e^3 B_{curv}}{hm_e c^2 E_\gamma}(E_\gamma/E_c)^{0.3}\exp(-E_\gamma/Ec) \tag{1.61}$$

$$\bar{E}_\gamma \simeq E_c = \frac{3}{2}\Gamma^2 h\frac{eB_{curv}}{2\pi m_e c} = \frac{3}{2}\Gamma^3 h\nu_{curv} \tag{1.62}$$

$$\nu_{curv} = \frac{c}{2\pi R_{curv}} \tag{1.63}$$

$$n \simeq \frac{e^3 B_{curv}}{hm_e c^2} \propto E_e \tag{1.64}$$

If electrons are not monoenergetic but have a power law energy spectrum KE^{-p}, the resulting curvature radiation spectrum will be

$$E_e \propto E_\gamma^{1/3}, \quad dE_e \propto E_\gamma^{-2/3} dE_\gamma \tag{1.65}$$

$$\frac{d^2 N_\gamma}{dE_\gamma dt} \propto \frac{ndN_e}{E_\gamma^{2/3} dE_e} \propto E_e^{-p+1} E_\gamma^{-2/3} \tag{1.66}$$

$$\propto E_\gamma^{-(p+1)/3} \tag{1.67}$$

The resulting gamma-ray spectrum will be a power law with an index of $-q = -(p+1)/3$.

1.3.5 Bremsstrahlung

When a charged particle hits the nuclei, it is braked by the electric field of the nuclei. As a result, it emits radiation called bremsstrahlung (braking radiation).

$$e + Z \to e + Z + \gamma \tag{1.68}$$

The mean energy of the emitted photon E_γ is proportional to the energy of the charged particle (see e.g. [10]). If electrons have a power law energy spectrum KE_e^{-p}, the resulting bremsstrahlung spectrum will be

$$E_e \propto E_\gamma, \quad dE_e \propto dE_\gamma \tag{1.69}$$

$$\frac{dN_\gamma^2}{dE_\gamma dt} \propto \frac{dN_e}{dE_e} \propto E_\gamma^{-p} \tag{1.70}$$

The gamma-ray spectrum would also have the power with the index $-q = -p$.

However, in most of the astrophysical sources, electrons lose energy by synchrotron radiation or inverse Compton radiation rather than bremsstrahlung. Only in very dense environments such as γ Cygni SNR in which nuclei density is in the order of 300 cm^{-3} in number, can bremsstrahlung dominate (see [187]).

1.4 Possible Acceleration Sites and Known VHE Gamma-ray Sources

As described in Sect. 1.2, there exist quite a few particle acceleration mechanisms. Here, I will list several possible acceleration sites where those mechanisms may be working. In addition, as described in Sect. 1.3, VHE gamma-ray emission is expected in such places. I will also show the known VHE gamma-ray sources.

1.4.1 Galactic Sources

Supernova Remnants

A supernova explosion ejects dense energetic plasma and this sweeps up the nearby interstellar medium. A shock wave is generated in the place where supernova ejecta and the interstellar medium collide. There, the first order Fermi acceleration (see Sect. 1.2.2) works and thus charged particles can be accelerated. Considering the shock speed, scale of the system, magnetic field and explosion rate, SNR can explain basically all the features of CRs at least below the knee energy. Fig. 1.1 shows the emission areas of VHE gamma-rays of the supernova remnant RX J1713-3946.

Pulsars, Pulsar Winds and Pulsar Wind Nebulae

Inside a pulsar magnetosphere, a persistent and strong electric field can exist. Also a high density of electrons and positrons exist there and these can be accelerated by the strong electric field. The details will be explained in the next chapter.

As described in Sect. 1.2.4, pulsars can accelerate particles by low frequency magnetic dipole radiation. This relativistic plasma wind is called a pulsar wind and the energy of electrons there can be as high as 10^{14}eV (see [10]).

At a certain distance from the pulsar, the pulsar wind will be terminated due to the interaction with interstellar plasma. At the termination point, a standing reverse shock is created. The shock accelerates electrons up to 10^{15} eV and randomizes their pitch angles. This results in the formation of an extended synchrotron source (see [10]) which is called a pulsar wind nebula (PWN).

In summary, one expects in a pulsar system both pulsed gamma-ray emission within the light cylinder and steady gamma-ray emission from the unshocked region and the termination shock region (PWN). Many of PWN and one pulsar have been detected in VHE gamma-rays.

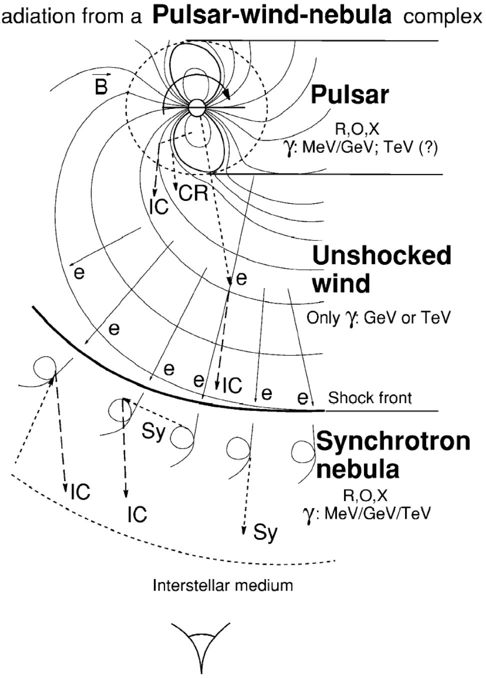

Figure 1.10: Acceleration region around the pulsar. Inside the light cylinder (see Sect. 2.5.2) , the electric field accelerates particles. Outside the light cylinder, magnetic dipole radiation accelerates particles and produces strong pulsar winds. In addition, shock acceleration happens in the place where the pulsar winds produce termination shock, resulting in pulsar wind nebula. Figure adopted from [10].

Binary Systems

Binary systems may accelerate particles either in the stellar wind shock or in the microquasar jets (see the right panel of Fig. 1.11). Three VHE gamma-ray binaries have been discovered so far.

If both stars have strong plasma wind as do pulsars, Wolf-Rayet stars or OB stars, their winds collide and produce a strong shock (see the right panel of Fig. 1.11). Then particles can be accelerated by shock acceleration. In this case, since the binary orbit is usually eccentric, the modulations of gamma-ray flux is expected according to the orbital phase (see [12] and [16]).

If one star is a compact object like a neutron star or a black hole and the other star has a huge mass loss, accretion of the matter to the strong gravitational star may create an accretion disc and relativistic plasma jets. Such a system is called a microquasar (see the left panel of Fig. 1.11). Inside the microquasar jets, shock waves may exist and particles can be accelerated. Magnetic reconnection which accelerates the particles can also happen (see [64]).

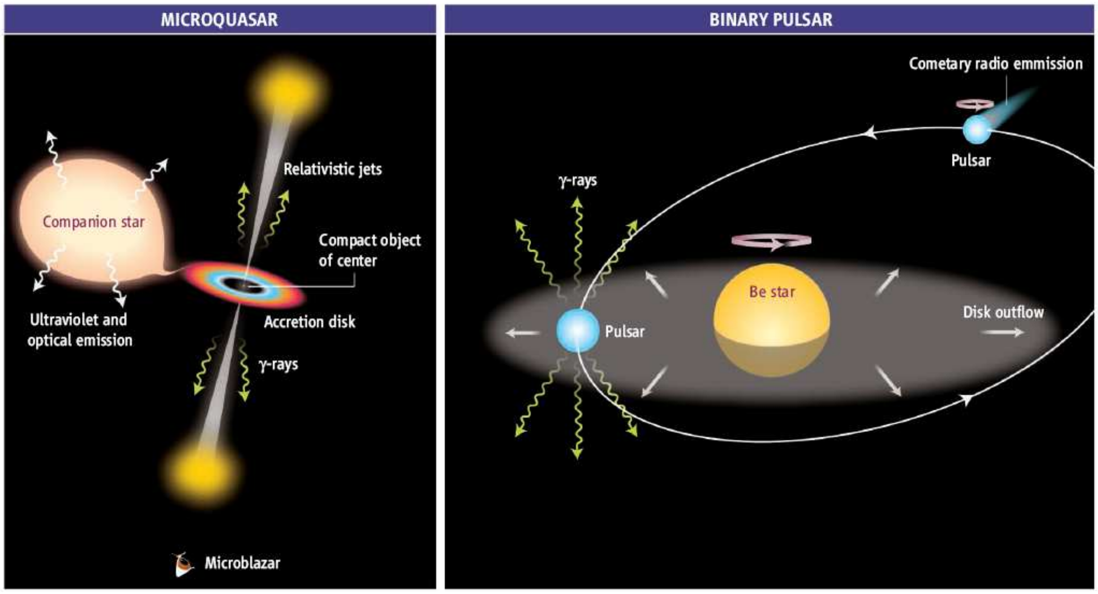

Figure 1.11: Schematic view of the binary system. Binary systems can accelerate particles either in the microquasar jet or in the wind collision shock. If one star is a compact object like a pulsar or a black hole and the other star has a large mass loss rate, the accretion of matter may generate relativistic jets where particles are accelerated (left, microquasar scenario). If both stars have strong stellar winds and they collide with each other, shocks will occur and particles will be accelerated there (right, wind collision scenario). Figure adopted from [133].

.

Open Clusters and Globular Clusters

In a young open cluster, there are numerous young massive stars which have a strong plasma wind. Because of the smaller distance between stars, the winds collide with each other or collective winds collide with surrounding matters. Then, shock will be created which leads to particle acceleration (see e.g. [38]). Similarly, in a globular cluster, plasma winds from many pulsars can accelerate particles (see e.g. [39]). Currently no open/globular clusters have been detected in VHE gamma-rays.

Other Sources

Wolf-Rayet stars and OB stars have strong plasma winds and it is possible that termination shocks or turbulence can accelerate particles to high energy. Up till now only one VHE source has been found by HESS which may be associated with a Wolf-Rayet star (see [51]).

Our galaxy has in its center a supermassive black hole with 10^6 solar masses. The compact radio source Sgr A* is associated with it. A VHE gamma-ray source is also found in there (see e.g. [17]) and hence, it is possible that particle acceleration takes place there. However, it should be noted that there are also quite a few different objects near the galactic center such as supernova remnant Sgr A East and pulsar wind nebula G359.95, which are within the error circle of the VHE gamma-ray source position.

1.4.2 Extragalactic Sources

Figure 1.12: Left: An artist's conception of an active galactic nucleus (AGN). The particle acceleration and VHE gamma-ray emission take place in the relativistic jets from the core. Figure adopted from [205]. Right: The image of the starburst galaxy M82 recorded by the Hubble space telescope. Starburst galaxies have exceptionally high star formation and supernova explosion rates and thus CR densities are high in such a galaxy leading to a high VHE gamma-ray flux. Figure adopted from [212].

Active Galactic Nuclei

Active galactic nuclei (AGNs) are galaxies with an active core, i.e. being brighter and more energetic than the ones of standard galaxies. AGNs are believed to be the most powerful sources of non-thermal energy in the Universe. They host a very compact (order of big planets) supermassive black hole (SMBH) in the central region with a mass around 10^6 to 10^{10} solar masses. The SMBH is surrounded by a disc of accreted material and has two jets perpendicularly to the disc (see Fig. 1.12). Inside the jets, particles are accelerated by the Fermi acceleration (see e.g. [44]) or magnetic reconnection (see e.g. [122]). Most of the currently known extragalactic sources emitting VHE gamma-rays are AGNs.

Starburst Galaxies

Starburst galaxies (see Fig. 1.12) are galaxies with an exceptionally high star formation rate and high supernova rate. Such galaxies are often created after a collision or close encounter between two galaxies. A high supernova rate makes the CR density also high, thus resulting in detectable VHE gamma-ray emission (see e.g. [188]). Recently, VHE gamma-ray emission was detected from two starburst galaxies, M82 (see [202]) and NGC 253 (see [7]).

Gamma Ray Bursts

Gamma ray bursts (GRBs) are short (seconds to minutes) but very violent phenomena in the Universe. GRBs are frequently observed at a rate of 1-2 per day. The most distant GRB ever observed is GRB050904 at the redshift $z = 6.29$ (see [59]). GRBs are uniformly distributed in the Universe. The emission energy ranges from optical to gamma-rays (~ 30 GeV). The emission mechanism is not yet well known but one of the most successful models is the hypernova model, which assumes an asymmetric supernova explosion (see e.g. [143]). In this model, radiation is beamed pointing towards the earth and the opening angle is below 20 degree (see e.g. [73]). Total radiation energy is $\sim 10^{51}$ erg, which is comparable to the total kinetic energy of the normal supernova explosion. The strong radiation up to gamma-ray energies suggests the particle acceleration there. Many of theoretical models such as relativistic shock acceleration (see e.g. [125]) are under discussion. So far, no GRB has been detected in VHE gamma-rays. This can be the consequence either that the acceleration mechanism is not sufficient to produce VHE gamma-rays or that EBL photons absorb VHE gamma-rays (see Sect. 1.5.1).

1.4.3 List of Known VHE Gamma-ray Sources

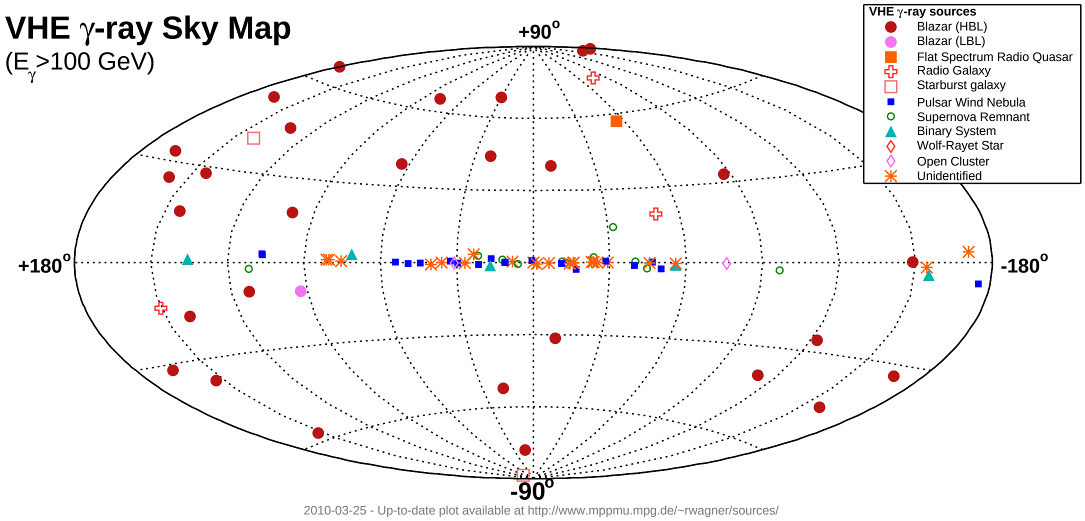

2010-03-25 - Up-to-date plot available at http://www.mppmu.mpg.de/~rwagner/sources/

Figure 1.13: Distribution of the VHE gamma-ray sources above 100 GeV. 97 sources are known. Figure adopted from [190].

As of 1st April 2010, 97 VHE sources have been discovered. The sources are categorized as shown in Table 1.1. 59 are galactic and 38 are extragalactic sources. Among galactic sources, while many of them are associated with extreme astronomical objects described above, 24 are unidentified sources. Such sources are normally found during the galactic plane survey, without being associated with any sources in other wavelengths. This implies that VHE gamma-ray astronomy is still primitive and an actively progressing field. Among extragalactic sources, all but two sources are active AGNs although AGNs can be divided into more sub-categories. The two starburst galaxies were discovered only recently (see [7] and [202]). New classes of objects may be discovered when VHE gamma-ray astronomy is more developed.

Type	# sources	Examples
Supernova Remnants	9	Cassiopeia A, RX J1713.7-3946 SN 1006 etc.
Pulsars	1	Crab Pulsar
Pulsar Wind Nebulae	19	Crab Nebula, Vela X, MSH 15-52 etc
Binary system	3	LS I +61 303, LS 5039, PSR B1259-63
Open Cluster	1	Westerlund 2
Wolf Rayet star	1	HESS J1848-018
Galactic Center	1	Sgr A*
Unidentified sources	24	TeV 2032-42,HESS J1632-478 etc.
Active Galactic Nuclei	36	Mrk 421, Mrk 501, 3C279 etc.
Starburst Galaxies	2	M82, NGC253

Table 1.1: List of known VHE gamma-ray sources (see [190]).

1.5 VHE Gamma-rays as Probes for Fundamental Physics and Cosmology

In addition to the study of astronomical sources which accelerate particles, VHE gamma-rays can also be a good probe for fundamental physics and cosmology. Here, I will describe several topics.

1.5.1 Extragalactic Background Light

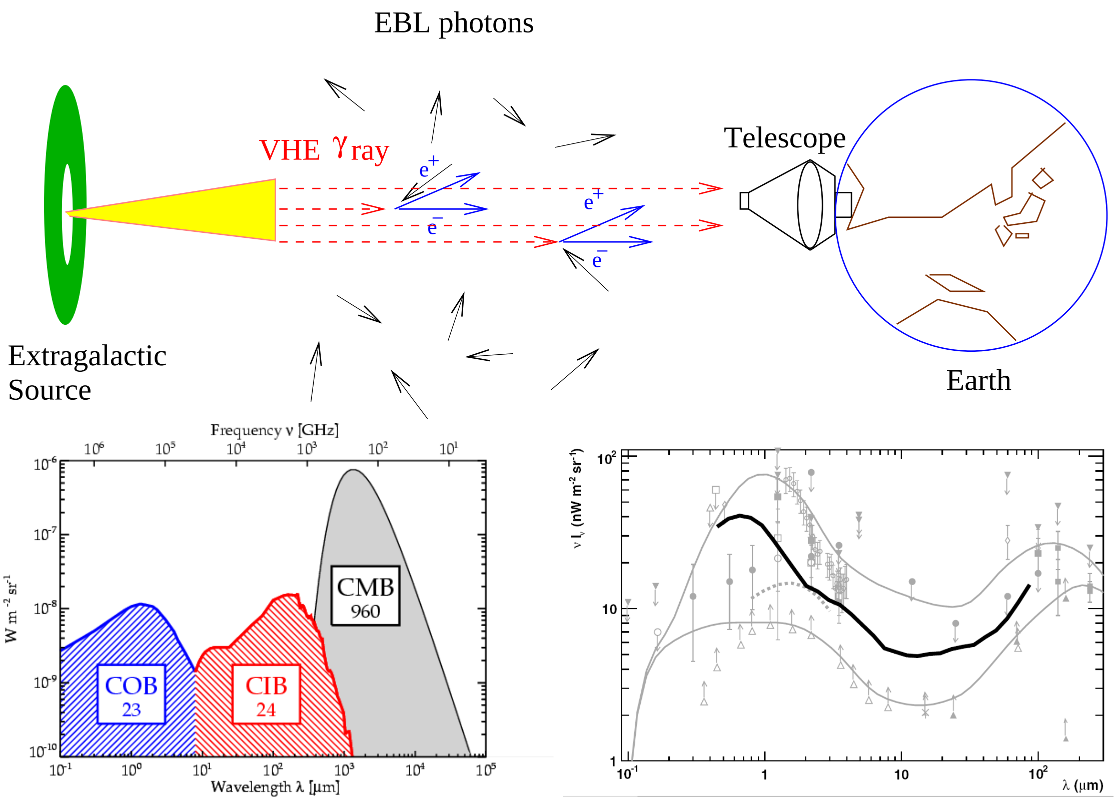

Figure 1.14: Top; Schematic view of the extragalactic background light (EBL) absorption. Some of VHE photons emitted by extragalactic sources are absorbed by EBL via pair creation on their way to the earth. Bottom left: Spectral energy distribution of EBL. Below 10 μm in wavelength, the cosmic optical background (COB) – mainly a collection of starlight – dominates. Above 300 μm, the cosmic microwave background (CMB) dominates. Between them, dominates the cosmic infrared background (CIB) which is mostly radiation from dust heated by starlight. Figure adopted from [66]. Bottom right: An example of an estimation of EBL spectrum deduced from observed spectra of extragalactic VHE sources. Figure adopted from [129].

The extragalactic space is filled with optical photons (cosmic optical background, COB), infrared photons (cosmic infrared background, CIB) and cosmic microwave background (CMB). These low energy electromagnetic waves are called extragalactic background light (EBL). COB originates mainly from starlight while infrared photons are from dust which are heated by the starlight and re-emits lower energy photons. The energy spectrum of COB and CIB are connected to the recent evolution of the Universe and thus the measurement of this radiation has a significant impact on the study of the evolution of the Universe. However, it is not easy to directly measure them because the Galaxy itself has strong emission in the optical and infrared bands.

VHE gamma-rays interact with the EBL photons via the pair creation process. The cross-section of pair creation has a peak at $s \simeq E_{\gamma 1} E_{\gamma 2} \simeq (m_e c^2)^2$, where $E_{\gamma 1}$ and $E_{\gamma 2}$ are the energies of the two interacting photons. The energy of COB and CIB ranges from 0.01 eV to 10 eV and, hence, VHE gamma-rays between 25 GeV and 25 TeV would interact with them most efficiently. Consequently, the spectrum of observed VHE gamma-rays from distant sources would be affected by these EBL photons. Therefore, the observed VHE gamma-ray spectrum can be a good probe for the COB and CIB spectra (see e.g. [129], [201] and [14]).

1.5.2 Quantum Gravity Effect

It is widely speculated that space-time is a dynamical medium, subject to quantum-gravitational (QG) effects that cause space-time to fluctuate on the Planck time and distance scales, for reviews see [160], [150] and [128]. It has also been suggested that this “foaming” of space-time might be reflected in modifications of the propagation of energetic particles, namely dispersive effects due to a non-trivial refractive index induced by the QG fluctuations in the space-time foam. In some models (e.g. [71]), the propagation of light is suppressed either linearly or quadratically by some QG mass scale:

$$\frac{\Delta c}{c} = -\frac{E_\gamma}{M_{QG1} c^2}, \quad \text{or} \quad \frac{\Delta c}{c} = -\frac{E_\gamma^2}{(M_{QG2} c^2)^2} \tag{1.71}$$

where E_γ is the energy of a photon and c is the speed of light. One might deduce that the scale M_{QG1} or M_{QG2} would be related to M_P, where $M_P = 2.4 \times 10^{18}$ GeV/c^2 is the reduced Planck mass, but smaller values might be possible in some string theories (see [24]), or models with large extra dimensions (see [86]). Expected arrival time difference of two gamma-rays of different energies being emitted at the same time at a distant source can be estimated to be

$$\begin{aligned} \Delta t &= \frac{d}{c} - \frac{d}{c + \Delta c} \simeq \frac{\Delta c d}{c^2} = \frac{\Delta E_\gamma d}{M_{QG1} c^2} && (1.72) \\ &= 30 \ \frac{\Delta E}{10^3 \mathrm{GeV}} \frac{d}{400 \mathrm{Mpc}} \frac{10^{18} \mathrm{GeV}/c^2}{M_{QG1}} \ [\mathrm{sec}] && (1.73) \end{aligned}$$

where ΔE and d are the difference in energy between the two photons and the distance to the source, respectively. By assuming that the flux variability is the same in different energies at the source, one can explore the quantum gravity effect from the observed variability in different energies, if the flux is high enough to see minute scale variabilities (see [18] and [43]).

1.5.3 Search for Dark Matter

After the precise measurement of the anisotropy of CMB by the Wilkinson Microwave Anisotropy Probe (WMAP, see [170]), a standard model of cosmology holds that the Universe consists of 4% ordinary baryonic matter, ~ 23% dark matter, and ~ 73% dark energy, with a tiny abundance of relic neutrinos. The identity of dark matter is not yet known but some of the most likely candidates are Weakly Interacting Massive Particles (WIMPs). The best WIMP candidate is motivated by Supersymmetry (SUSY), the lightest neutralino in the Minimal Supersymmetric Standard Model (MSSM, see e.g. [79]). Accelerator experiments showed the possible range of the lightest neutralino mass to be from ~ 50 GeV to ~ 2 TeV (see e.g. [112]). Two-neutralino annihilation can produce VHE gamma-rays via various channels (see e.g. [27]). Therefore, VHE gamma-rays can be used to search for dark matter.

WIMP distribution should follow the gravitational field and, thus, the galactic center (see e.g. [40]) and galaxy clusters with a high mass/luminosity ratio (see e.g. [21]) are some of the best targets for searching for the VHE gamma-ray emission from dark matter.

1.6 Concluding Remarks and the Topic of this Thesis

In the Universe, there are plenty and a variety of extreme astronomical objects where particles can be accelerated to very high energies. These high energy particles have several channels to produce gamma-rays and one can distinguish them by, for example, the energy spectrum. Therefore, VHE gamma-rays are useful probes for investigating the nature of these extreme objects. VHE gamma-rays are also useful tools for some questions of fundamental physics and cosmology.

Among the particle accelerator objects, pulsars are unique in a sense that they accelerate particles in several different manners, i.e. by electric fields within their magnetosphere, by converting their rotation energy into ultrarelativistic plasma winds and by shock acceleration at the termination of the winds. The name “pulsar” comes from its extremely precise periodic radiation (pulsation) from its magnetosphere. It was first discovered 43 years ago, but the precise emission mechanism is not yet clearly revealed. One of the essential keys for further understanding of pulsation mechanism is the feature of the energy spectra around the cut-off energies between a few GeV and a few tens of GeV, whereas no sufficient measurement in this energy region was possible before 2007.

In October 2007, the trigger system of the MAGIC was upgraded and the energy threshold was lowered from ~ 50 GeV to ~ 25 GeV. In August 2008, the new gamma-ray detector, LAT on the Fermi satellite became operational which can measure gamma-rays from 100 MeV to well above 10 GeV with reasonable sensitivity. I was sure that the study of pulsars with *Fermi*-LAT and upgraded MAGIC observations would shed new light on the nature of the pulsars. MAGIC is a ground-based telescope and, thus, the observable region in the sky is limited. The Crab pulsar is the brightest pulsar in gamma-rays that can be observed by MAGIC. In fact, the Crab pulsar was successfully detected by MAGIC during observations between October 2007 and February 2008 through the collective efforts of my colleagues, T. Schweizer, M. L. Lepez, A. N. Otte, M.

Rissi and M. Shayduk (see [22]). However, detailed studies of the energy spectrum, the pulse profile and the interpretation of the results require more statistics and careful and novel analysis methods. Discussion in comparison with *Fermi*-LAT measurements also remains to be done. For these reasons, I have chosen to study the emission mechanism of the Crab pulsar as the topic of this thesis.

Chapter 2

Pulsars

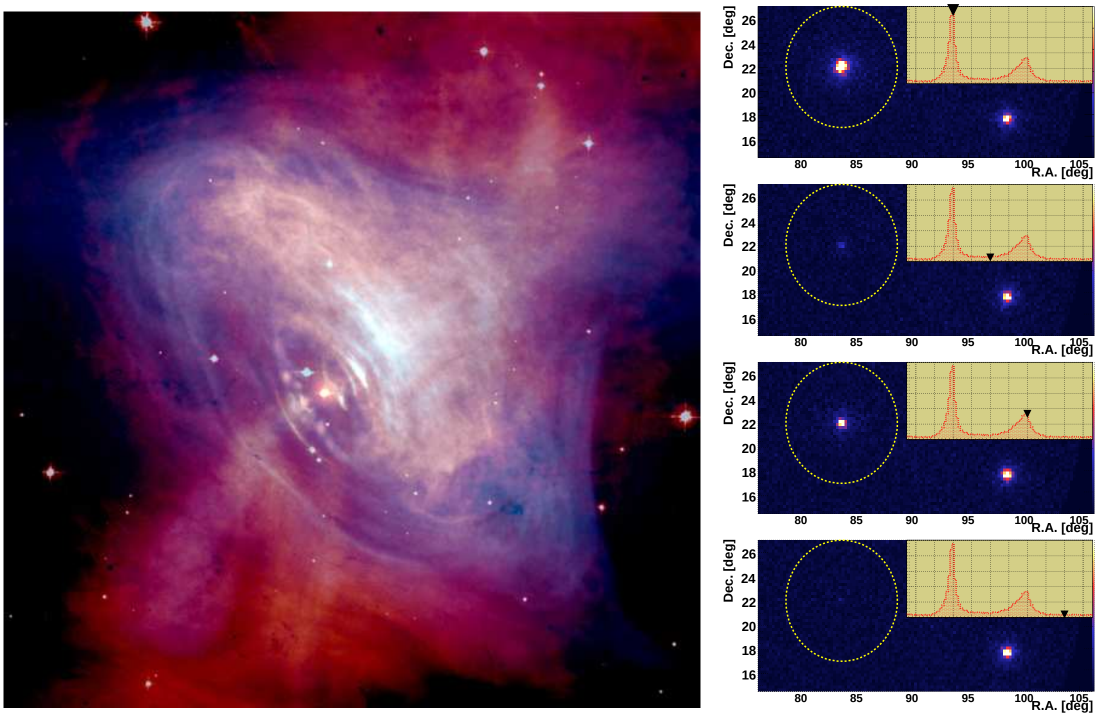

Figure 2.1: Left: X-ray image (blue) of the Crab Pulsar and the Crab Nebula taken by Chandra, overlaid with the optical image (red) taken by Hubble Space Telescope. Figure adopted from [206]. Right: Rotation-phase-folded skymaps around the Crab pulsar produced with Fermi-LAT data above 100 MeV. The phases for each maps are indicated by the pulse profile diagram at the upper right corner.

Pulsars are astronomical objects, which emit periodic radiation of very high accuracy. In spite of the long observational history and numerous remarkable radiation features, the emission mechanism has not yet been completely understood.

In this chapter, the current understanding of pulsars will be described. In Sect. 2.1 general observational facts in the energy range between 10^{-7} eV to 10^{10} eV will be briefly summarized. There is little doubt that pulsars are neutron stars with a high rotation speed. Therefore, in Sect.

2.2 properties of neutron stars will be discussed. From the pulsation period and its time derivative, one can derive many pulsar properties, which will be explained in Sect. 2.3. An irregular behavior of pulsar periods, a glitch, is briefly introduced in Sect. 2.4. In order to investigate the pulsar emission mechanism, it is essential to understand the plasma distribution around the pulsar and possible particle acceleration places, which will be shown in Sect. 2.5 and 2.6. Then, Sect. 2.7 provides explanations for the observed spectra and light curves of pulsars. In these sections, it will be shown that both the inner and the outer magnetosphere sphere hypotheses reasonably explain all the observational results before 2007. Sect. 2.8 explains how to test the two hypotheses with the more recent observations. The properties and observational status of the Crab pulsar, with which pulsation mechanism is studied in this thesis, will be introduced in Sect. 2.9. Concluding remarks are added in 2.10.

2.1 Discovery of the First Pulsar and Currently Known Pulsars

2.1.1 Discovery

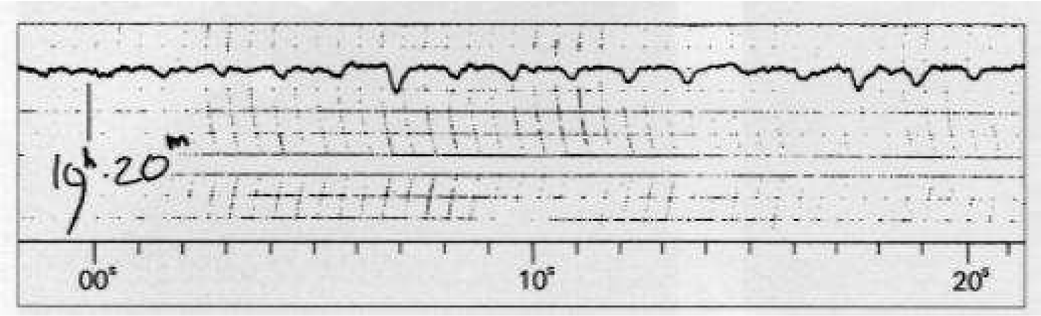

Figure 2.2: Discovery of the first pulsar, PSR B1919+21, at 81.5 MHz in the radio band (see [99]). Periodic signals can be seen. Figure adopted from [116]

In 1967, Jocelyn Bell Burnell discovered a pulsating radio emission in 81.5 MHz band with a period of 1.337 second (see [99]), as shown in Fig. 2.2. Since the source direction showed annual parallax as for other stars, it was clear that the periodic signal was not an artifact of the measurement but came from some astronomical object. This source is the first pulsar detected and is now called PSR B1919+21. One year later, the Crab pulsar, which is the topic of this thesis, was discovered by Comella et al. (see [56]).

2.1.2 Number of Known Pulsars

In most cases, the radio band is the best energy band to detect a pulsar because the instrumental sensitivity compared to flux level is more favorable than in any other wavelength. In the radio band, ~ 1800 pulsars have been discovered. On the other hand, in the optical band less than

10 are known, one of which is the Crab pulsar. In the X-ray band, tens of pulsars have been discovered. However, most of them are in a binary system and, therefore, the emission mechanism is quite different. They are often called **accretion-powered** pulsars and are distinguished from the other **rotation-powered** pulsars. Hereafter, I will not discuss these accretion-powered pulsars. In the gamma-ray band, after six months of operation with *Fermi*-LAT (see Chapter 6), 46 pulsars have been identified (see [5]).

2.1.3 Periods of Pulsars

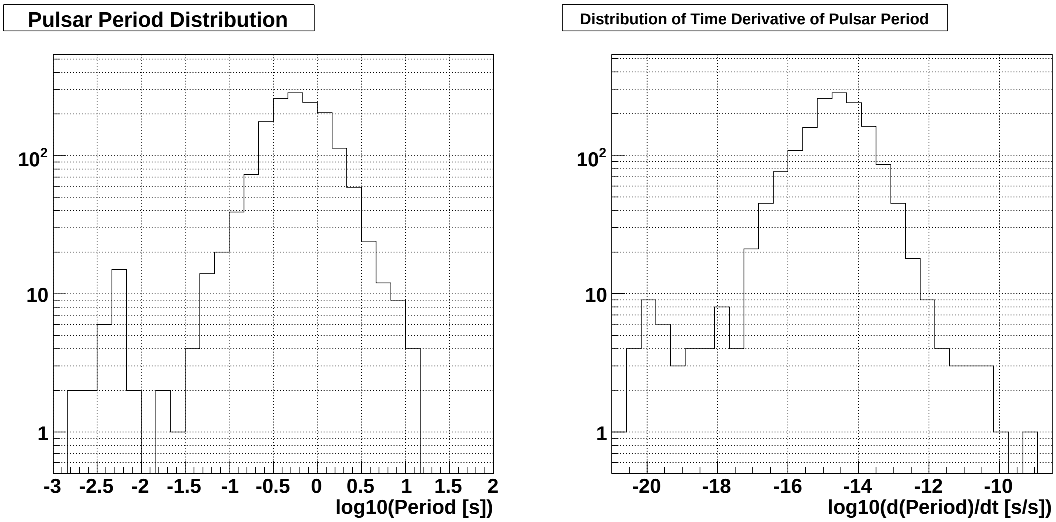

Figure 2.3: Distribution of pulsar periods P (left) and time derivatives $\dot{P}$ (right) for all rotation-powered pulsars. Two populations can be seen in both plots. Data are obtained from [203]. The correlation between P and $\dot{P}$ is shown in Fig. 2.6

The period of rotation-powered pulsars ranges from 1 millisecond to 10 seconds as shown in the left panel of Fig 2.3. The distribution shows two populations, one below and one above 10 milliseconds. The pulsars with a period less than 10 milliseconds are called **millisecond pulsars** and they are thought to be very old pulsars. The periods increase with time. The time derivatives of the periods are also shown in the right panel of Fig. 2.3. It should be noted that in the case of accretion-powered pulsars, the period decreases with time. The precision of a period can be as high as 10^{-15}.

2.1.4 Light Curves of Pulsars

Figure 2.4 shows the light curves of 7 gamma-ray pulsars detected by EGRET in different energies. Some pulsars have two peaks and some have only one. Pulse widths are different for different pulsars. In addition, except for the Crab pulsar, peak phases and shapes change with the energies.

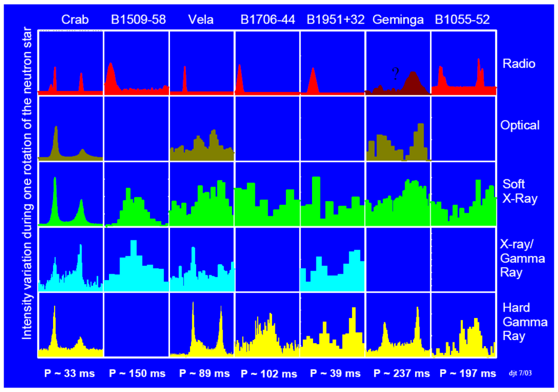

Figure 2.4: Light curves of 7 gamma-ray pulsars in different wavelengths. Some have two peaks and some have one. The peak phases and pulse shapes change with energy except for the Crab pulsar. Figure adopted from [179]

2.2 Neutron Stars

2.2.1 Neutron Stars as Identity of Pulsars

The shortest known period of a pulsar is about 1 millisecond. Since nothing can travel more than 300 km in such a short time ($c \times 1\ \mathrm{ms} = 300$ km), the size of the emission system should be less than that. It is still possible that the emission region is part of a bigger system but, in such a case, it is hard to expect such a precise periodicity as is normally observed. Therefore, only compact astronomical objects could be pulsars, namely white dwarfs, neutron stars or black holes. Periodic behavior would be expected from either vibration or rotation of stars. However, in the case of vibration, the period should decrease in time, which is in contradiction to the observational facts. Only rotating compact objects can explain pulsars.

The shortest period for a rotating star occurs when it is rotating at break-up angular velocity Ω, i.e. when the centrifugal force is equal to the gravitational force at the surface.

$$\Omega^2 R \sim \frac{GM}{R^2} \tag{2.1}$$

where R, G, and M are the radius of the star, the gravitational constant, and the mass of the star. So, the maximum angular velocity is set by the density ρ of the object,

$$\Omega^2 \sim G\rho \tag{2.2}$$

The maximum mean density of a white dwarf is 10^8g/cm^3 leading to the shortest period of ~ 1 second, which rules out a white dwarf as the origin of a pulsar. On the other hand, the density of a neutron star 10^{14}g/cm^3 can naturally explain the observed pulsar periods. An isolated rotating black hole is axisymmetric and can not produce periodic radiation. Accretion may make it asymmetric but then periodicity would not be so precise.

Because of these arguments, only a rotating neutron star can explain the observed pulsar periods. It should be noted that, in addition, there must be a beamed radiation mechanism to produce the (apparent) periodic radiation, which will be discussed in the following sections.

2.2.2 General Properties of a Neutron Star

The evolutions of stars with different mass are well described in, for example, [116]. A star with the initial mass of 8 to 20 $M_\odot$ forms a neutron star at the end of its evolution. The mass of the neutron star must be higher than the Chandrasekhar Limit $\sim 1.4M_\odot$, but should be lower than $\sim 2M_\odot$ in order to sustain its self-gravity by neutron degenerate pressure [1]. This leads to the common properties of all neutron stars, which will be described in this section.

Radius, Mass and Density

Neutron stars have an extremely high density, typically in the order of 10^{14}g/cm^3, which is as high as or higher than atomic nucleus density. The mass of a typical neutron star is about 1.5$M_\odot$ and, thus, the radius is about 10 km.

Angular Momentum and Magnetic Field

From the moment of their birth, stars are spinning and possess a dipole magnetic field. The angular momentum and magnetic flux will be conserved even in case of a supernova explosion. The explosion decreases the star radius dramatically by about 5 orders of magnitude, increasing the angular velocity and the surface magnetic field strength by about 10 orders of magnitude. The magnetic field of pulsars ranges from 10^8 to 10^{14} G and, as already noted, the rotation period ranges from 1 millisecond to 10 seconds, which can reasonably be explained by the conservation of the angular momentum and magnetic flux of the precursor stars after the supernova explosion.

Inner Structure

The neutron star body is not uniform but has some structure, as shown in Fig. 2.5. Although details are still unclear, especially for the inner core, the structures are roughly as follows (see, e.g., [49], [35] and [139]):

- The atmosphere is only a few cm thick and consists of light and heavy nuclei. They are pinned to the neutron star by the strong surface magnetic fields.

- The outer crust is about 200 m thick and its density is $\rho = \sim 10^{9-11}$ g cm^{-3}. It consists of a lattice of atomic nuclei and Fermi liquid of relativistic degenerate electrons

- The inner crust is about 1-2 km thick and its density is $\rho = \sim 10^{11-14}$ g cm^{-3}. It consists of electrons, neutrons and nucleons. The free neutrons may pair in a $^1S_0$ state to form a superfluid.

- The outer core is about 9 km thick and its density is $\rho = \sim 10^{14}$ g cm^{-3}. It consists of neutron - proton Fermi liquid and a few % of Electron Fermi gas.

---

[1] The upper limit of the mass of a neutron star has a relatively large uncertainty because the equation of states for extremely high density matter is not well known

- The inner core is about 0-3 km thick and its density is $\rho = \sim 10^{15}$ g cm^{-3}. It consists of hyperons, quarks and meson liquids.

The strong magnetic field is maintained by electric currents inside the neutron star.

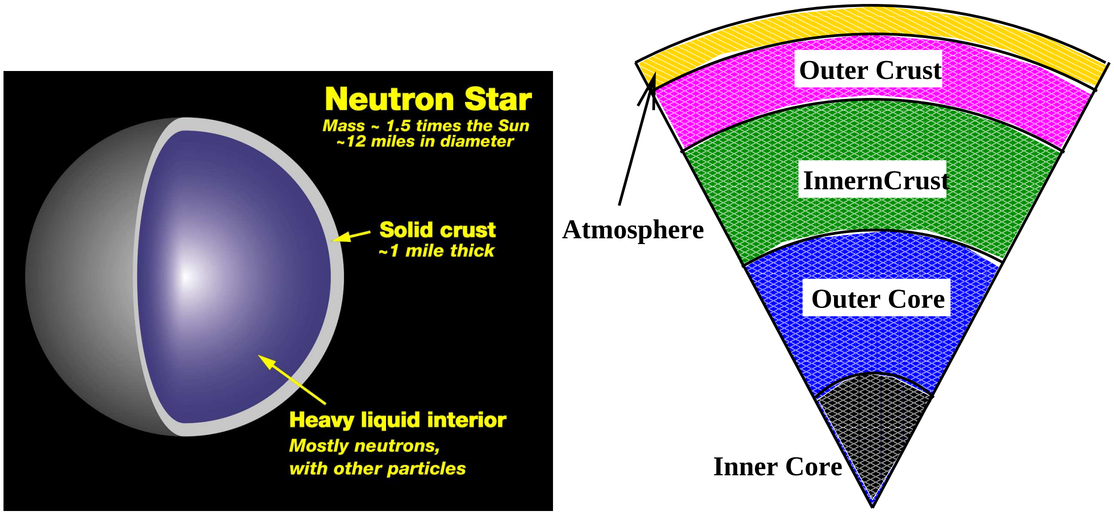

Figure 2.5: Structure of a neutron star. It consists of inner core, outer core, inner crust, outer crust and atmosphere. The density is different in different parts and on average, $\sim 10^{14}$ g/cm^3. Figure adopted from [215].

Surface Temperature

It is generally believed that neutron stars have a very high interior temperature (10^{11}K) in their initial state of formation (see, e.g. [166]). Neutron stars are cooled down by neutrino emission via the following catalytic reactions:

$$\begin{aligned} n &\rightarrow p + e^- + \bar{\nu}_e \rightarrow n + \bar{\nu}_e + \nu_e && (2.3) \\ n + n &\rightarrow n + p + e^- + \bar{\nu}_e \rightarrow n + n + \bar{\nu}_e + \nu_e && (2.4) \\ &\ldots \end{aligned}$$

until the internal temperature falls to 10^8K (10^6 K on the surface) (see [54]). After that, photon emission cooling becomes dominant (see [78]). Typically, the surface temperature falls to several times 10^6 K after approximately 300 years since birth and remain in the vicinity of (0.5-2.0) $\times 10^6$ K for at least 10^4 years. Therefore, neutron stars should emit thermal X-rays.

2.3 Magnetic Dipole Radiation

Figure 2.6 shows the distribution of (P, $\dot{P}$) of all detected radio pulsars (see [203]), where P is the pulsar period and $\dot{P}$ is its time derivative. From these two quantities, one can deduce quite a few properties of a pulsar in relation to the misaligned magnetic dipole hypothesis.

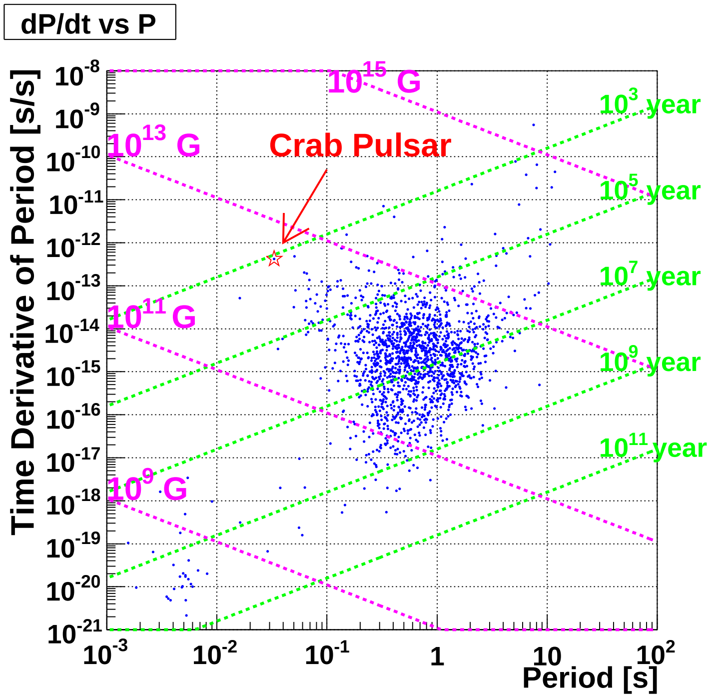

Figure 2.6: The correlation between the pulsar period P and its time derivative $\dot{P}$ (blue dots). Data are obtained from [203]. The dot for the Crab pulsar is highlighted with a red star and an arrow. Millisecond pulsars are clearly separated from other pulsars and shown at the lower left corner. From P and $\dot{P}$, one can estimate the age of pulsars and surface magnetic field strength, as indicated by green and pink dotted lines, respectively (see Sect. 2.3.3 and 2.3.4).

2.3.1 Spin Down Luminosity

As mentioned in Sect. 2.1.3, periods of pulsars P increase with time, i.e. $\dot{P} > 0$. The rotation energy of a pulsar can be expressed as

$$E = \frac{1}{2} I \Omega^2 \tag{2.5}$$

where I is the moment of inertia and $\Omega = 2\pi/P$ is the angular frequency of rotation. Therefore, $\dot{P} > 0$ implies continuous loss of rotation energy.

$$-\dot{E} = -I\Omega\dot{\Omega} = 4\pi^2 I \dot{P}/P^3 > 0 \tag{2.6}$$

This energy loss rate is called **spin down luminosity**. Assuming that the neutron star has a radius of R = 10 km and a mass of M =1.5 $M_\odot$ with a uniform density, the moment of inertia I of a pulsar can be estimated to be $I = 2/5MR^2 = 1.2 \times 10^{45}$g cm^2. By substituting this in Eq. 2.6, it can be simplified as

$$-\dot{E} = 4 \times 10^{46} \dot{P}/P^3 \quad \mathrm{erg/s} \tag{2.7}$$

The mechanism of energy loss can be explained by radiation caused by misaligned rotation of the magnetic dipole, as will be discussed in the next subsection.

2.3.2 Radiation Caused by a Rotating Magnetic Dipole

The magnetic dipole moment of a pulsar is expressed as;

$$\mathbf{m} = \frac{1}{2} B_0 R_0^3 (\mathbf{e_z} \mathrm{cos}\alpha + \mathbf{e_x} \mathrm{sin}\alpha \mathrm{cos}\Omega t + \mathbf{e_y} \mathrm{sin}\alpha \mathrm{sin}\Omega t) \tag{2.8}$$

where B_0 is the magnetic field strength at the pole, R_0 is the radius of the neutron star and α is the angle between rotation axis and dipole axis. The z axis is parallel to the rotation axis and $\mathbf{e_x}$,$\mathbf{e_y}$ and $\mathbf{e_z}$, are unit vectors parallel to the x, y and z axes respectively.

If $\alpha \neq 0$, the direction of the dipole moment changes in time and thus emits electromagnetic radiation. The luminosity of the radiation $\dot{E}$ is (see e.g. [106])

$$\dot{E} = -\frac{2}{3c^3} |\ddot{\mathbf{m}}|^2. \tag{2.9}$$

Substituting Eq. 2.8 to Eq. 2.9, one obtains

$$\dot{E} = -\frac{B_0^2 R^6 \Omega^4 \mathrm{sin}^2 \alpha}{6c^3} \tag{2.10}$$

The frequency of this radiation is Ω and such a low frequency radiation can accelerate particles efficiently, as discussed in Sect. 1.2.4. Therefore, this radiation energy will be converted into the pulsar wind energy.

2.3.3 Estimation of the Magnetic Field Strength at the Pole

Using Eq. 2.6, Eq. 2.10 and $\Omega = 2\pi/P$, magnetic field strength is easily estimated as

$$B_0^2 \;\; = \;\; -\frac{6Ic^3 \dot{P} P}{4\pi^2 R^6 \mathrm{sin}^2 \alpha} \tag{2.11}$$

Substituting nominal values used in Sect. 2.3.1 and assuming sinα =1,

$$B_0 \;\; \simeq \;\; 7 \times 10^{19} \sqrt{P\dot{P}} \qquad \mathrm{G} \tag{2.12}$$

is obtained. The mean value of the surface magnetic field is about half of this value. In Fig. 2.6 the surface magnetic field strength is indicated by pink dotted lines.

2.3.4 Estimation of the Pulsar Age

Eq. 2.6 and Eq. 2.10 lead to

$$\Omega(t) \;\; = \;\; \Omega_0 \left(1 + \frac{2\Omega_0^2}{\Omega_{now}^2} \frac{t}{T} \right)^{-\frac{1}{2}} \tag{2.13}$$

$$T \;\; \equiv \;\; -\frac{\Omega_{now}}{\dot{\Omega}_{now}} = \frac{6Ic^3}{B_0^2 R^6 \mathrm{sin}^2 \alpha \Omega_{now}^2} \tag{2.14}$$

where Ω_0 and Ω_{now} are the angular velocity at $t = 0$ and the current angular velocity. From Eq. 2.13, one can estimate the age of the pulsar as

$$t = \frac{T}{2}\left(1 - \frac{\Omega_{now}^2}{\Omega_0^2}\right) \simeq \frac{T}{2} = -\frac{\Omega}{2\dot{\Omega}} = \frac{P}{2\dot{P}} \tag{2.15}$$

In Fig. 2.6 the age t is indicated by green dotted lines.

2.3.5 Application to the Crab Pulsar

In the case of the Crab pulsar, currently $P = 3.36 \times 10^{-2}$ sec, and $\dot{P} = 4.2 \times 10^{-13}$. According to Eq. 2.10, they correspond to the spin down luminosity of 4.6×10^{38} erg/s. This radiative energy should be transferred to the pulsar wind and the nebula. Observational results estimate their kinetic and radiation power to be 5×10^{38} erg/s (see [123]), i.e., nearly the same as the spin down luminosity. This remarkable agreement verifies the misaligned dipole rotation hypothesis. Moreover, Eq. 2.15 predicts 1270 years as its age. The supernova was observed in year 1054, which is 956 years ago. This agreement supports the hypothesis as well. Eq. 2.11 leads to $B_0 = 8 \times 10^{12}$G (the average over surface would be half of this value).

2.4 Glitches of pulsars

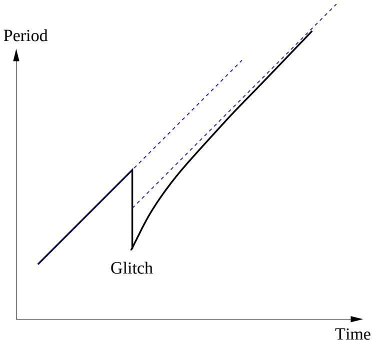

Figure 2.7: The pulsar period as a function of time around a glitch.

For young pulsars such as the Crab pulsar ($\sim 10^3$ years) and the Vela pulsar ($\sim 10^4$ years), sudden decreases of the pulsation period P occur randomly once in a few years. The decrease of the period, ΔP, amounts to $\Delta P/P \sim 10^{-6}$ for the Vela pulsar and $\Delta P/P \sim 10^{-8}$ for the Crab pulsar. The decrease in P is accompanied by an increase in $\dot{P}$, which typically decreases to the ‘before-glitch-value’ in about $10 - 100$ days (see Fig. 2.7). This sudden decrease in the pulsar period is called **glitch**. Glitches are explained as follows:

A sudden decrease in P means a sudden spin-up. Numerous models have been proposed to explain the origin of sudden spin-ups such as starquakes, vortex pinning, magnetospheric instabilities and instabilities in the motion of the superfluid neutrons. Here I introduce the starquake scenario, which is one of the most widely accepted scenarios. As described in Sect. 2.2.2, the nuclei in the outer crust of a neutron star are thought to form a solid lattice structure through Coulomb forces. This crust is oblate in shape because of the star's rotation. As the star slows down, centrifugal forces on the crust decrease and a stress arises to drive the crust to a less oblate shape. However, the rigidity of the solid crust resists this stress and the shape remains more oblate than the equilibrium one. Finally, when the crust stress reach a critical value, the crust cracks. Some stress is relieved and the oblateness decreases. As a result, the moment of inertia of the crust suddenly decreases and, hence, the rotation speed of the crust suddenly increases to conserve the angular momentum. Charged particles in the neutron star body are strongly coupled with the Coulomb lattice via the strong magnetic field. Therefore, the charged particles immediately follow the crust spin-up. On the other hand, a significant part of a neutron star body is made of superfluid neutrons, which are only weakly coupled to the Coulomb lattice. When the starquake occurs, the rotation speed of the charged component (the outer crust and the charged particles) suddenly increases, while that of the neutral component (superfluid neutrons) does not change. Subsequently, weak friction between the charged particles and the superfluid neutrons slow down the charged component and accelerate the neutral component, resulting in the observed behavior of the period around a glitch (see Fig. 2.7). For a more detailed explanation, see [166] and references therein.

2.5 Plasma around a Pulsar

2.5.1 Can a Pulsar Exist without being Surrounded by a Plasma?

A neutron star possesses a extremely strong dipole magnetic field and is spinning fast. The neutron star can be considered as a conductive material, as described in Sect. 2.2.2. Therefore, inside the neutron star, charges will be distributed such that the electric field $\mathbf{E}^{\mathrm{in}}$ and magnetic field $\mathbf{B}^{\mathrm{in}}$ fulfill the following equation:

$$\mathbf{E}^{\mathrm{in}} + \frac{\boldsymbol{\Omega} \times \mathbf{r}}{c} \times \mathbf{B}^{\mathrm{in}} = 0 \tag{2.16}$$

where Ω is the rotation vector of the pulsar and $\mathbf{r}$ is the position vector measured from the pulsar center. Outside the pulsar, the magnetic field follows a dipole shape

$$\mathbf{B}^{\mathrm{out}} = B_0 R_0^3 \left(\frac{\cos\theta}{r^3} \mathbf{e_r} + \frac{\sin\theta}{2r^3} \mathbf{e}_\theta \right) \tag{2.17}$$

where B_0, R_0, θ and r are the magnetic field strength at the magnetic pole, the pulsar radius, the inclination angle between the rotation axis and the dipole axis, and the distance from the pulsar center, respectively.

Now let us assume that pulsars are surrounded by vacuum, i.e. $\nabla \cdot \mathbf{E}^{\mathrm{out}} = -\Delta\phi^{\mathrm{out}} = 0$, where ϕ is the electric potential. The boundary condition that the θ component of the fields should be continuous across the pulsar surface determines the electric field outside the pulsar $\mathbf{E}^{\mathrm{out}}$ to be

$$\begin{aligned}
\phi^{\mathrm{out}} &= -\frac{B_0 \Omega R_0^5}{3cr^2} P_2(cos\theta) = -\frac{B_0 \Omega R_0^5}{3cr^3} \frac{3\cos^2\theta - 1}{2} && (2.18)\\
\mathbf{E}^{\mathrm{out}} &= -\frac{B_0 \Omega R_0^5}{c} \left(\frac{3\cos^2\theta - 1}{2r^4} \mathbf{e_r} + \frac{\sin\theta\cos\theta}{r^4} \mathbf{e}_\theta \right) && (2.19)\\
\mathbf{E}^{\mathrm{out}} \cdot \mathbf{B}^{\mathrm{out}} &= -\frac{R_0 \Omega}{c} \left(\frac{R_0}{r} \right)^7 B_0^2 \cos^3\theta && (2.20)
\end{aligned}$$

At the surface, the electric field parallel to $\mathbf{B}$ is quite strong (see [166]),

$$\begin{aligned}
E_{||} &\simeq \frac{R_0 \Omega}{c} B_0 \simeq 2 \times 10^8 P^{-1} B_{12} \quad \mathrm{statV\ cm}^{-1} && (2.21)\\
&\simeq 6 \times 10^{10} P^{-1} B_{12} \quad \mathrm{V\ cm}^{-1} && (2.22)
\end{aligned}$$

where P is the period in seconds and B_{12} is the magnetic field strength in units of 10^{12}G.

It is strong enough to rip electrons or positrons from the surface of the neutron star. Those electrons or positrons are further accelerated and induce a electromagnetic cascade in the strong magnetic field, thus creating huge numbers of electron positron pairs. Therefore, the vacuum around the neutron star will not be stable and the pulsar should be surrounded by a dense plasma.

2.5.2 Light Cylinder

Magnetic fields are frozen in a plasma. The plasma is dragged by the magnetic field and co-rotates with the neutron star. With increasing distance from the pulsar, the co-rotation speed becomes larger ($v = \Omega \times r$). However, particles cannot move faster than light. The distance $R_L = c/\Omega = Pc/(2\pi)$ is called the **co-rotation radius** and an imaginary cylinder along the rotation axis with the radius of R_L is called the **light cylinder**. Outside the light cylinder, the plasma does not co-rotate with the neutron star and, thus, magnetic fields are also distorted by the plasma, making a spiral structure (see Fig. 1.10). Dipole approximation for magnetic fields is not valid here and field lines which cross the light cylinder do not close. The highest latitude field lines that close within the light cylinder are called **last closed field lines**, as shown in Fig. 2.8.

2.5.3 Plasma Distribution around a Pulsar

Plasma inside the light cylinder distributes such that the forces working on a charged particle is 0.

$$\mathbf{E} + \frac{\mathbf{\Omega} \times \mathbf{r}}{c} \times \mathbf{B} = 0 \tag{2.23}$$

resulting in $\mathbf{E}\cdot\mathbf{B}=0$. The Poisson law $\rho=\nabla\cdot\mathbf{E}/4\pi$ requires

$$\rho_{GJ}=-\frac{1}{4\pi c}\frac{\mathbf{\Omega}\cdot\mathbf{B}}{1-\frac{|\mathbf{\Omega}\times\mathbf{r}|^2}{c}} \tag{2.24}$$

This space charge density was first pointed out by P. Goldreich and W. H. Julian in 1969 (see [87]) and it is called the **Goldreich-Julian density**.

A sketch of the magnetic field and charge distribution about a rotating neutron star, assuming the magnetic dipole axis is parallel to the rotation axis, is shown in Fig 2.8. It should be noted that magnetic field lines are at the same time equi-potential contours because $\mathbf{E}\cdot\mathbf{B}=0$. As is easily derived from Eq. 2.24, at the points where $\mathbf{B}$ is perpendicular to $\mathbf{\Omega}$, the charge density ρ_{GJ} is zero, i.e. the number densities of electrons and positrons are the same. In the three-dimensional view, these points form a surface which is called the **null surface**, indicated by a red dashed line in Fig. 2.8. .

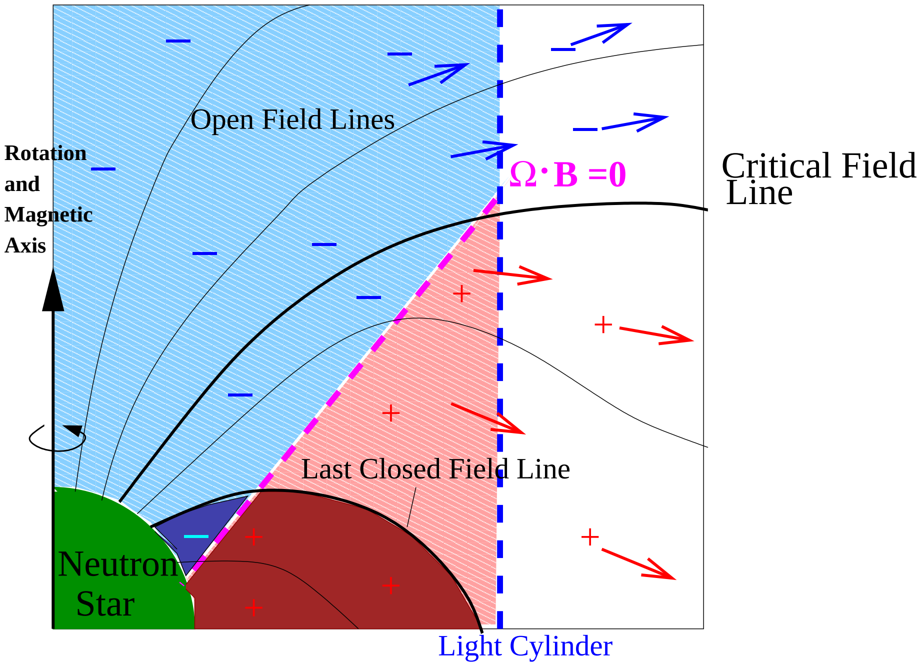

Figure 2.8: Typical plasma distribution around the pulsar assuming that the rotation axis and the magnetic dipole axis are parallel. Within the light cylinder, plasma charge density follows the Goldreich-Julian density. It is 0 on the null surface where the magnetic field direction is perpendicular to the rotation axis (pink dotted line). There is also a current outflow along the magnetic field lines. The sign of the current changes at the critical field line (thick black line). Figure adopted from [166].

2.5.4 Current Outflow from the Pulsar Magnetosphere

As mentioned above, magnetic field lines shown in Fig. 2.8 are at the same time equi-potential contours, which means that there exists a potential gradient over the pulsar surface. Let us estimate the potential difference between the last closed field line and the pole, following the original argument made by by P. Goldreich and W. H. Julian (see [87]). Let θ_0 be the co-latitude of the point on the stellar surface where the last field line starts. The curvature of the last field line at the surface can be well approximated to be $\sqrt{R_0 R_L}$, leading to sin$\theta_0 \simeq \sqrt{R_0/R_L}$. From Eq. 2.18 the potential difference would be,

$$\Delta\phi = \phi(\theta_0) - \phi(0) = -\frac{B_0 \Omega R_0^2}{2c}(cos^2\theta_0 - 1) \simeq \frac{B_0 \Omega R_0^2}{2c}\frac{R_0}{R_L} \tag{2.25}$$

This $\Delta\phi$ is called **open field line voltage** (see e.g. [180]). Using R_0 = 10 km, $R_L = c/\Omega$, $\Omega = 2\pi/\Omega$, and Eq. 2.12

$$\Delta\phi \sim 1 \times 10^{18} P^{-3/2} \dot{P}^{1/2} \ \mathrm{statV} \tag{2.26}$$

$$\sim 4 \times 10^{20} P^{-3/2} \dot{P}^{1/2} \ \mathrm{V} \tag{2.27}$$

In the case of the Crab pulsar, the open field line voltage is $\sim 4 \times 10^{16}$ V.

There should be a potential difference between the pulsar surface and the interstellar space, and charged particles can move along the magnetic field. Therefore, current outflows are generated from the pulsar surface. Between the pole and the last closed field line, there should be a equipotential line whose potential equals that of interstellar space. This line is called the **critical field line** (see [87]). The sign of the currents would change at this line, as shown in Fig 2.8.

2.6 Particle Acceleration within the Light Cylinder

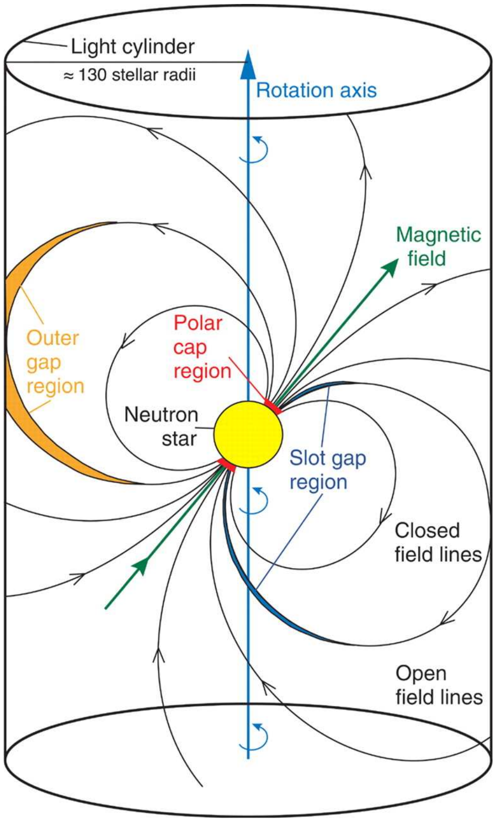

Figure 2.9: Schematic view of the particle acceleration region inside the light cylinder. The three regions, namely Polar Cap, (red) Slot Gap (blue) and Outer Gap (orange) are indicated. Figure adopted from [22].

In order to explain the observed pulsed emission up to gamma-rays, there must be places where charged particles are accelerated up to very high energies within the light cylinder. Considering the extremely strong magnetic field and the rapidly rotating star, it seems that strong electric fields are easily generated as suggested in Eq. 2.27. However, as long as the plasma distributes as Goldreich and Julian density ρ_{GJ} (Eq. 2.24), the electric field $\mathbf{E}$ parallel to the magnetic field $\mathbf{B}$ is zero within the light cylinder. Synchrotron cooling of the strong magnetic field does not allow particles to be accelerated perpendicular to $\mathbf{B}$. In other words,

- **there must be places where the plasma charge density** $\rho \neq \rho_{GJ}$

and, thus, $\mathbf{E} \cdot \mathbf{B} \neq 0$. There are mainly three models advocating such a region, namely the Polar Cap model, the Slot Gap model and the Outer Gap model. All of them are based on the same fact that

- **the current outflow from the pulsar creates a place where** $\rho \neq \rho_{GJ}$

2.6.1 The Polar Cap Model

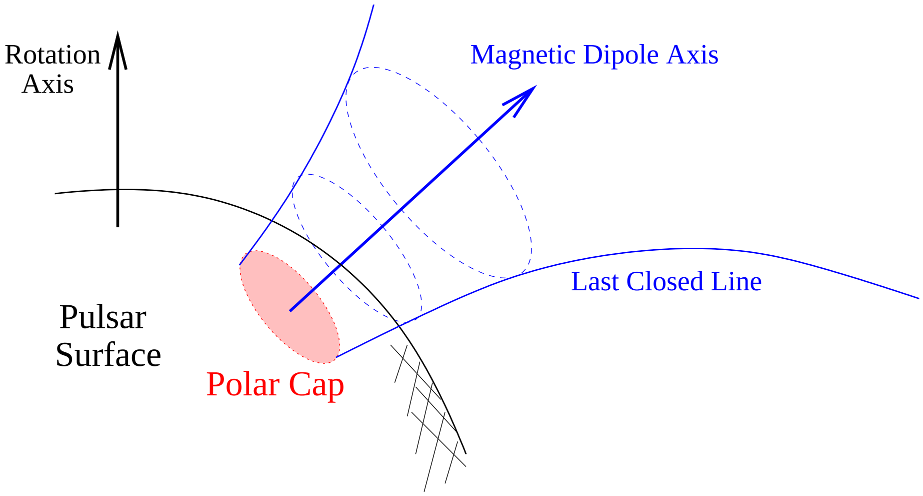

Figure 2.10: Polar Cap region. It is a region near the magnetic pole surrounded by last closed field lines.

The Polar Cap (PC) model predicts the formation of $\rho \neq \rho_{GJ}$ ($E_{||} = \mathbf{E} \cdot \mathbf{B}/|\mathbf{B}| \neq 0$) at PC. PC is defined as the region near the magnetic pole on the pulsar surface surrounded by the last closed lines, as illustrated in Fig 2.10. It was first suggested by M.A. Ruderman and P.G. Sutherland (see [157]) assuming no ion supply from the neutron star surface. Even if charged particles can escape freely from the star surface, $E_{||}$ can be developed because of the the Space-Charge Limited Flow (see e.g. [161]). It depends on the surface temperature of the neutron star T_* whether charged particles can be supplied from the neutrons star or not. If T_* is higher than $\sim 10^5$K which is the thermal emission temperature of electrons or ions, then the neutron star can emit charged particles.

The Vacuum Gap Version ($T_* <\sim 10^5$, no charge emission from the stellar surface)

There must be a current outflow near the pole. Since the star cannot provide charged particles, the lack of electrons/positrons occurs near the stellar surface, as illustrated in Fig. 2.11. Thus, a vacuum gap is created near the stellar surface. In the gap, $E_{||} \neq 0$ and difference in potential is created along the magnetic field line. If an electron and a positron are created by, for example, pair creation between thermal radiation from the surface and an external gamma-ray, then they are accelerated by $E_{||}$. The gap grows until the potential difference across the gap is so high that accelerated particles induce electromagnetic cascades ($\Delta V \sim 10^{12-13}$, see [28] and [91]). The cascade is created as follows: an accelerated electron moves along a magnetic field line, which is curved. Therefore, it emits curvature radiation. If the electron energy well exceeds 10^{12} eV, the emitted photon is energetic enough to initiate magnetic pair creation (see Sect. **??**). These created electrons and positrons, in turn, will be accelerated and produce more curvature radiation photons. In this way, the number of charged particles increase exponentially. The layer where those cascades are happening is called the pair formation front (PFF, see e.g. [30]). Above the PFF, cascading electrons and positrons feed enough charges to make $\rho = \rho_{GJ}$ $(E_{\parallel} = 0)$.

It should be noted that even if electrons can be emitted freely from the neutron star surface, as long as positive charges (ions) cannot be provided, the gap can be created in a similar manner, which was actually the basic assumption for the original polar cap model (see [157]).

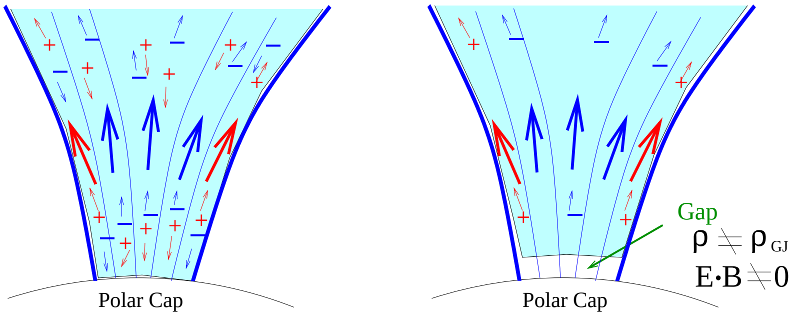

Figure 2.11: Mechanism of the generation of the gap in the Polar Cap region. Initially the neutron star is surrounded by plasma (left). However, if charge emission is not allowed from the neutron star surface, the plasma depletion region will be created by the current outflow (right). The thickness of the gap is determined by the pair formation front.

Space Charge Limited Flow Version ($T_* >\sim 10^5$, charge emission from the steller surface)

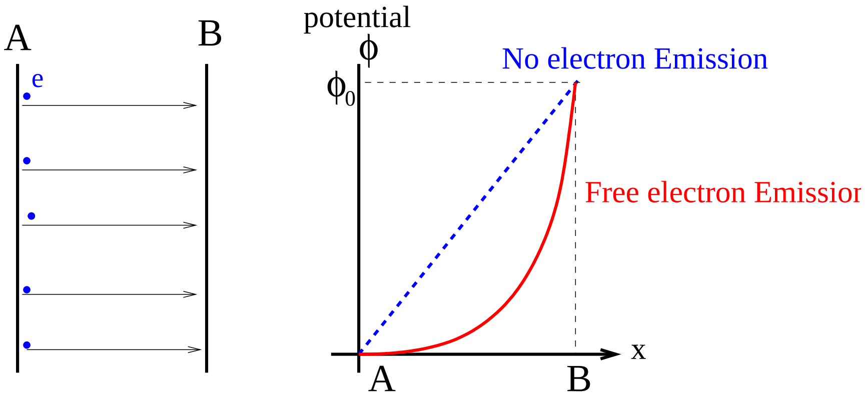

Figure 2.12: The potential distribution between the cathoed A and the anode B in the vacuum with a potential gap ϕ_0. If charge emission is not allowed from the anode A, the potential grows linearly. If charge emission is allowed, it grows quadratically. In both cases, the potential difference between A and B remains the same.

The space charge limited current flow (SCLF) was first found and studied in a completely different field, the study of thermal current flow between an anode and a cathode in vacuum. It is well described in [117]. Let us consider the two plates A (anode) and B (cathode), as illustrated in Fig. 2.12. The distance between the plates is d and the relative electric potential of plate B with respect to A is ϕ_0. If electron emission from A is forbidden, the potential $\phi(x)$ linearly grows $\phi(x) = \phi_0 x/d$, i.e. electric field is constant $-\phi_0/d$. If electron emission is allowed, currents flow between the two plates. However, electrons will be provided from the plate just as much as the electric field at the surface is compensated, so that the whole potential gap cannot be eliminated. The potential distribution between the two plates can be approximated as a parabolic function $\phi(x) = -\phi_0 x^2/d^2$ (see [117]), as illustrated in Fig. 2.12.

This is applicable to the pulsar polar cap surface. The potential gap along the magnetic field lines at PC cannot be eliminated by the ion or electron emission from the pulsar. The thickness of the gap is defined by the cascade process, as in the Vacuum Gap version. Both the Vacuum Gap model and SCLF model predict the similar features of acceleration such as the location, angular distribution and energy spectrum. The extension of the thickness of the gap is less than a few times the stellar radius.

2.6.2 The Slot Gap Model

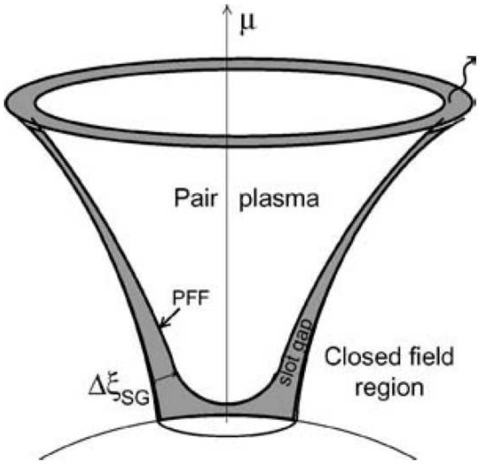

Figure 2.13: Slot Gap region. The Polar Cap model predicts the gap only close to the neutron star surface because of the pair formation front. However, near the last closed lines, the pair formation front will not be produced, resulting in the growth of the gap up to high altitude. Figure adopted from [92]

The PC model has difficulties explaining the observational results such as light curves. To overcome these difficlties, J. Arons advocated the Slot Gap (SG) model (see [29] and [30]), which is an extention of PC model.

In the PC model, the height of the region where $\rho \neq \rho_{GJ}$ is limited below PFF, where the potential gap is so large that accelerated electrons/positrons cause a cascade to screen the $E_{||}$ (see the previous section). However, Arons first noted the possibility of a high-altitude acceleration region named the Slot Gap. The potential is equal all along the last closed line even if a gap is created in the PC. This boundary condition makes $E_{||}$ near the last closed field lines weaker. Therefore, the gap can grow far from the magnetic pole (see [28], [29] and [92]), as shown in

Fig 2.13. As the altitude increases, the strength of the magnetic field decreases, which avoids the creation of the PFF. The gap can grow up to the light cylinder and the potential difference ΔV can exceed 10^{13} V. The thickness of the slot gap is estimated to be $\sim 0.04\theta_0$ in the case of the Crab pulsar, where θ_0 is the magnetic co-latitude of the last closed field line (see [93]).

2.6.3 The Outer Gap Model

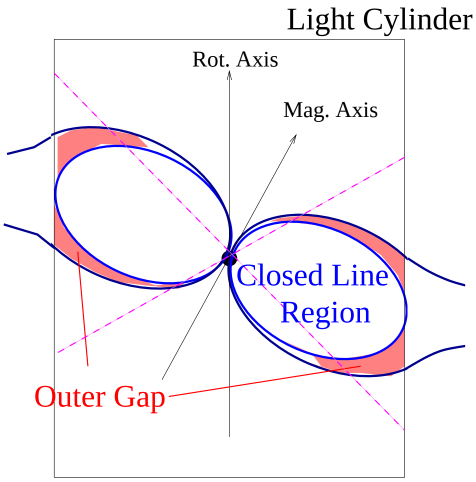

Figure 2.14: Outer Gap region. The gap is created along the last closed field lines. In the original model, the gap starts from the null surface (pink dashed lines) up to the light cylinder. On the other hand recent MHD simulation shows that it should start from below the null surface.

The Outer Gap (OG) model was first advocated by K.S. Cheng, C. Ho, and M. Ruderman in 1986 (see [52]). It points out the possibility of a gap formation along the last closed field line. The place of the gap is similar to that of the SG model but the formation mechanism is different. The basic idea of the gap formation is schematically shown in Fig. 2.15. The pink dotted lines in the figure show the null surface. If plasma distributes following the Goldreich-Julian density ρ_{GJ} and the aforementioned current continues to flow, at some point a plasma will be shorted out around the null surface, leading to $\rho \neq \rho_{GJ}$. This depleted gap will grow along the magnetic field lines. The gap cannot grow too far from the closed line regions, because high energy gamma-rays produced by the accelerated particles along the last closed line interact with ambient X-rays (the neutron star surface temperature is typically 10^6 K, see Sect. 2.2.2) to produce an electron-positron pair. They, in turn, create lots of synchrotron photons which will be good targets for the next pair creations (see Fig. 2.16 and [53]). Due to the curvature, the narrow region close to the last closed line can be free from this “pair polution” (see [52]). This thickness of the gap at the light cylinder in the case of the Crab pulsar is estimated to be $\sim 0.1R_L$ (see [200], [53], [175] and [177]). The potential difference along the field line can be $\Delta V = 10^{15}$ V (see e.g. [52]).

In the original model (see [52]), charged particles are assumed to move mainly outward which results in the gap starting from near the null surface to the light cylinder. However, this model has been challenged by Hirotani et al [103]. By solving the set of Maxwell's equations and Boltzmann's equations, they found that the inner boundary of the outer gap is significantly shifted inward from the null surface towards the stellar surface.

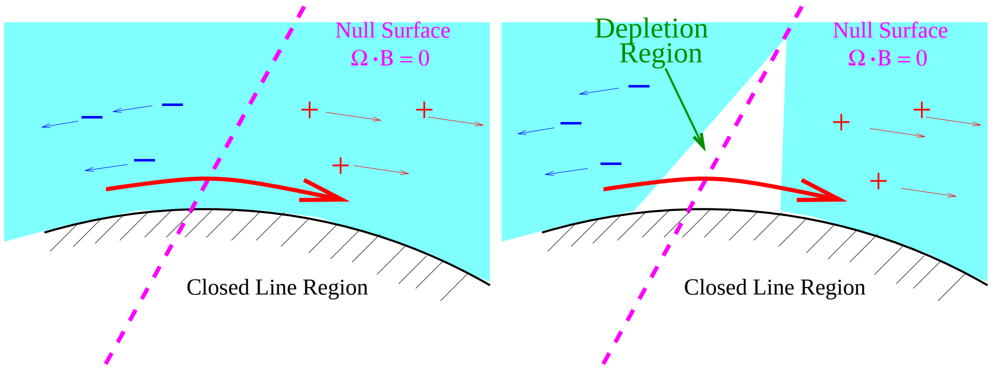

Figure 2.15: Mechanism of the generation of the Outer Gap. Initially the magnetosphere within the light cylinder is filled with plasma, which follows ρ_{GJ} (left). However, the current outflow generates a plasma depletion region starting from the null surface (right).

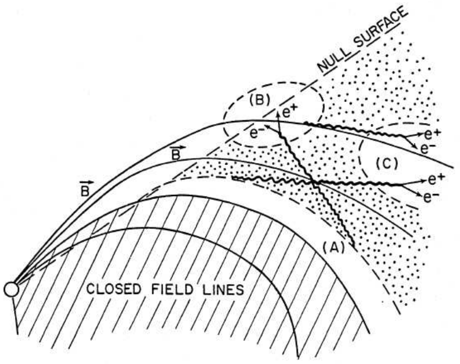

Figure 2.16: Mechanism of the limitation of Outer Gap thickness. The gap created far from the last closed field line (B) and (C) will be immediately filled by electrons and positrons created by gamma-rays. Figure adopted from [52].

2.7 Non-thermal Radiations in the Pulsar Magnetosphere

It is clear from the previous section that electrons and positrons can be accelerated up to very high energies. Here, I briefly describe how these accelerated particles produce the observed radiation from radio band to gamma-rays. Light curves and cut-off energies of the spectrum will also be explained. There are two different explanations for these depending on whether the emission region is in the inner magnetosphere (below the null surface, i.e. in the PC and in the low altitude

SG) or in the outer magnetosphere (above the null surface, i.e., in the OG and in the high altitude SG).

2.7.1 The Overall Energy Spectrum

Radio Band

As described in Sect. 2.1.1, the first pulsar was found in the radio band. A pulsar is one of the brightest classes of objects in radio astronomy. In the case of the Crab pulsar, the energy flux at 1 GHz is 100 mJy while the sensitivity of the VLA (Very Large Array, radio telescope) for this band is 0.01 mJy. About 2000 pulsars are listed in the Australia Telescope National Facility Pulsar Catalogue [124] and most of them are found in the radio band.

The natural explanation for the strong radio emission is the coherent radiation process; in other words, phases of radiation from individual particles are aligned and, hence, the total intensity is much higher than the sum of the individual particle emission intensity. The coherent emission results either from densely localized particle groups emitting curvature and synchrotron radiation or from the maser mechanism (see e.g. [84], [110] and [134]).

Optical to Gamma-rays

Although there are numerous calculations with different assumptions to explain the observed pulsar radiation energy spectrum, emission from Optical/IR to gamma-rays emission can generally be explained by synchrotron radiation, curvature radiation and inverse Compton scattering. Thermal radiation from the pulsar surface may also contribute to the X-ray band. Fig. 2.17 shows a spectral energy distribution (SED) of one of the calculations for a young pulsar assuming the emission region to be the outer magnetosphere (SG or OG) (see [155]).

The radiation above 1 GeV, the study of which is the main target for this thesis, is dominated by curvature radiation, though some models predict significant contributions from synchrotron and inverse Compton radiation as well. Assuming the Lorentz factor of the electrons to be $\Gamma = 3\times10^7$ and the curvature of the field to be 1000 km (10^8 cm), which are good approximations for the Crab pulsar, Eq. 1.62 leads to $E_c \simeq 8$ GeV.

2.7.2 The Energy Cut-off

Observational results suggest a cut-off in the energy spectrum at around $1 - 10$ GeV. The cut-off is explained differently whether emission comes from the inner magnetosphere or the outer magnetosphere.

The Outer Magnetosphere Case: Curvature Radiation Cooling

Even if the potential drop can be 10^{15} V (see Sect. 2.6.3), electrons are not necessarily accelerated up to 10^{15} eV because they lose energy mainly through curvature radiation. The maximum energy of the electron determines the cut-off energy of the gamma-ray energy spectrum in the outer magnetosphere case.

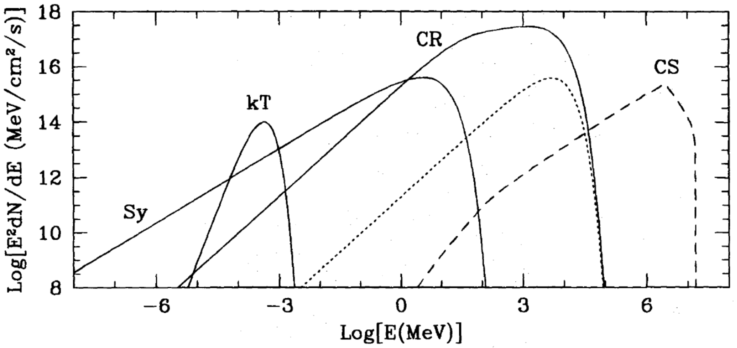

Figure 2.17: Basic energy spectra of a young pulsar. The emission region is assumed to be in the outer magnetosphere. Thermal (kT), synchrotron (Sy), and curvature (CR) radiation explain the entire energy spectrum. The dashed line (CS) is inverse Compton emission which may play a role in specific conditions. A power law spectrum was assumed for electrons, which may not be the standard case. The dotted line is the spectrum of curvature radiation from monoenergetic electrons. Figure adopted from [155].

The energy loss in unit time would be $n \cdot \bar{E}_\gamma$, where n is the number of emitted photons per unit of time and $\bar{E}_\gamma$ is their mean energy. From Eq. 1.62 and Eq. 1.64,

$$\begin{aligned} n \cdot \bar{E}_\gamma &\sim \frac{e^4 B_{curv}^2 \Gamma^2}{m_e^2 c^3} = \frac{e^2 c \Gamma^4}{R_{curv}^2} && (2.28) \\ &\sim 4 \times 10^3 \left(\frac{1}{R_{curv}/\mathrm{cm}} \right)^2 \Gamma^4 \quad \mathrm{eV/s} && (2.29) \end{aligned}$$

The maximum Γ would be derived as follows:

$$\begin{aligned} n \cdot \bar{E}_\gamma &= eE_{||}c && (2.30) \\ \Gamma^{max} &= 50 \left(\frac{eE_{||}}{(\mathrm{eV/cm})} \right)^{1/4} \sqrt{R_{curv}/\mathrm{cm}} && (2.31) \end{aligned}$$

Substituting $E_{||} = 3 \times 10^6$ V/cm, and $R_{curv} = 10^8$ cm, which are reasonable values for the Crab pulsar, one can obtain $\Gamma^{max} \simeq 2 \times 10^7$ (10 TeV). It is consistent with many other calculations (see e.g. [155], [104] and [93]). From Eq. 1.62, the energy of the curvature radiation photon from the maximum energy electron would be ~ 6.5 GeV.

It should be noted that, with $E_{||} = 3 \times 10^6$ V/cm, the electron energy of 10 TeV can be achieved with 33 km of acceleration. Considering the co-rotation radius of the Crab pulsar ($R_L = 1500$ km), accelerated electrons should be nearly monoenergetic at around the maximum energy.

Inner Magnetosphere Case: Pair Creation by Strong Magnetic Fields

In the inner magnetosphere, the maximum Lorentz factor of the accelerated electrons is similar to the one in the outer magnetosphere (see e.g. [91]). On the other hand, the curvature of the magnetic field is smaller than that in the outer magnetosphere. Therefore, one might expect even higher energy of photons via curvature radiation from the inner magnetosphere than from the outer magnetosphere. However, the strong magnetic field can absorb the high energy photons via the magnetic pair creation process, which actually determines the cut-off in the observed gamma-ray spectrum.

One photon in a field-free vacuum cannot produce an electron-positron pair even if the photon energy is higher than $2m_ec^2$, because both energy and momentum cannot be conserved at the same time. However, if the magnetic field participates in momentum and energy transfer, it becomes possible to create an electron-positron pair from a single photon. The energy E_B which has to be transferred from the magnetic field, would be estimated as follows:

$$E_B \sim 2E_e - E_\gamma \sim \frac{2m_e^2c^4}{E_\gamma} \tag{2.32}$$

assuming that the high energy photon with the energy E_γ and momentum $\mathbf{P}_\gamma$ produce an electron and a positron with the energy of E_e and the momentum $1/2\mathbf{P}_\gamma$, parallel to the photon momentum. On the other hand, the cyclotron energy states of an electron under magnetic field are discrete

$$\hbar\omega_g(N + 1/2) \tag{2.33}$$

Thus, the electron and the positron gain energy from the magnetic field by $\sim \hbar\omega_g$, where $\omega_g = eB/m_ec$ is the gyro-frequency. $\hbar\omega_g$ is equal to m_ec^2 if the magnetic field strength is the critical magnetic field strength $B_{cr} = m_e^2c^3/e\hbar = 4.4 \times 10^{13}$ G. From this argument and Eq. 2.32

$$\frac{2m_e^2c^4}{E_\gamma} < m_ec^2\frac{B_\perp}{B_{cr}} \tag{2.34}$$

would roughly be the condition for the magnetic pair creation, where $B_\perp$ is the magnetic field strength perpendicular to the electron motion. Therefore, one can define a useful dimensionless parameter χ

$$\chi = \frac{E_\gamma}{2m_ec^2}\frac{B_\perp}{B_{cr}} \tag{2.35}$$

If $\chi << 1$ then pair creation should not happen while it should happen if $\chi \sim 1$ or $\chi > 1$.

The detailed calculations were first done independently by Toll [182] and Klepikov [113] and later confirmed by many authors such as [72] and [185]. Among them, T. Erber [72] provided a useful calculation for the attenuation coefficient as a function of χ. It shows that gamma-rays can escape the pulsar magnetosphere when $\chi < 0.1$ is fulfilled throughout the propagation. In other words, from Eq 2.35, the following condition:

$$\frac{E_\gamma}{m_ec^2} < \frac{0.2B_{cr}}{B_\perp} = \frac{0.2B_{cr}}{B\sin\theta} \tag{2.36}$$

must be fulfilled throughout the trajectory in the pulsar magnetosphere, where θ is the angle between the photon propagation direction and the magnetic field. In a pulsar magnetosphere, gamma-ray photons are emitted tangentially to the magnetic field ($\theta = 0$). As long as a photon travels parallel to the magnetic fields, pair creation will never happen. However, since the dipole magnetic fields are curved, θ increases with distance. On the other hand, the magnetic field strength rapidly decreases with the distance from the stellar surface.

The maximum energy $E^{max}(r)$ of gamma-rays that were emitted at distance r from the pulsar and reach the Earth can be roughly estimated as follows: one can assume that the magnetic fields are uniformly curved with the same strength in a scale of the pulsar radius $R_0 = 10^6$ cm and that, due to the rapid decrease of the field strength, a photon which could travel up to the distance R_0 will never cause the magnetic pair creation afterwards. The radius of field curvature near the last closed line can be approximated as $\rho_c(r) = \sqrt{R_L r} = \sqrt{Pcr/(2\pi)}$ (see [34]). If a photon is emitted tangentially to the magnetic field, after traveling by R_0, then sin$\theta \simeq R_0/\rho_c$. Therefore, from Eq. 2.36

$$E_{max}(r) = \frac{0.2B_{cr}m_ec^2}{B\mathrm{sin}\theta} \simeq \frac{0.2B_{cr}m_ec^2}{B_0(R_0^3/r^3)(R_0/\rho_c)} \tag{2.37}$$

$$\simeq 7\sqrt{P}\left(\frac{r}{R_0}\right)^{7/2}\frac{B_{cr}}{B_0} \quad \mathrm{MeV} \tag{2.38}$$

Accurate calculations, taking into account the effect of general relativity can be summarized in a similar formula (see [90], [33] and [34]):

$$E_{max}(r) \simeq 40\sqrt{P}\left(\frac{r}{R_0}\right)^{7/2}\frac{B_{cr}}{B_0} \quad \mathrm{MeV} \tag{2.39}$$

In the case of the Crab pulsar, substituting $B_0 = 4 \times 10^{12}$ G and $P = 0.034$ sec, then $E_{max}(r = R_0)$ will be 0.3 GeV. This value can change depending on the emission distance r.

The photon splitting process, which is forbidden in a field-free vacuum by the Furry theorem (see [81])

$$\gamma \rightarrow \gamma + \gamma \tag{2.40}$$

is allowed in the presence of a strong magnetic field. This process, therefore, limits the attainable energy of photons. Photon splitting can dominate magnetic pair creation in a certain energy range only when $B_0 > 0.3B_{cr}$ (see [90]), which is rarely the case for pulsars except for some special ones such as PSR B 1509-58 ($B_0 \simeq 3 \times 10^{13}$G).

2.7.3 The Light Curve

Some pulsars have two pulses and others have only one. This can also be explained by both the inner magnetosphere emission model and the outer magnetosphere emission model.

Inner Magnetosphere Case: Conical Beam

The explanation of various light curves is schematically shown in Fig 2.18. If the pulsed radiation comes from near the pulsar surface, the emission region should be conically beamed. Let me define a imaginary sphere named "emission profile sphere" whose center is on the pulsar center and whose radius is infinitely long. By projecting the conical beam to the emission profile sphere and opening it like a Mercator chart, one can make a "emission profile map" as shown in the figure. The longitude of the map corresponds to the pulse phase while the latitude corresponds to the viewing angle, i.e. the angle between the rotation axis and direction to the observer (the Earth). Depending on the viewing angle, a light curve can have two peaks or one peak. The pulse width can also be any value. By adjusting the angle between the rotation axis and the magnetic dipole axis, any phase separation between two peaks can be explained as well.

It should be noted that because of the rotation of the neutron star, the magnetic field will not be a perfect dipole, especially near the light cylinder. This will cause an asymmetry in the polar cap shape when the rotation axis and the dipole axis are not aligned (see e.g. [53]), leading to different shapes between the two pulses, as shown in the right panel of Fig. 2.18.

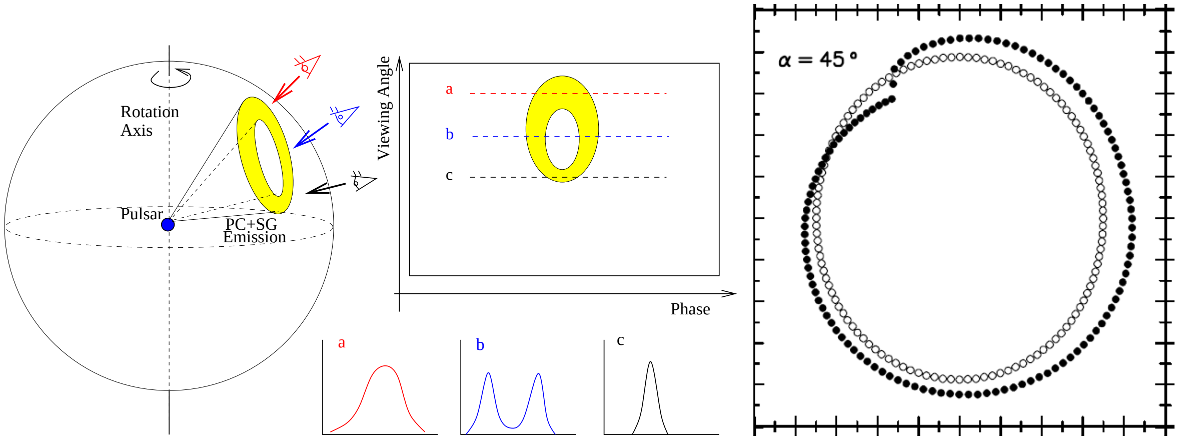

Figure 2.18: Explanation for some light curves when the emission region is in the inner magnetosphere. The mission should be a conical beam. Defining an imaginary sphere "emission profile sphere" (left) and opening it to "emission profile map" (middle), different light curves can be explained by the different view angles. Near the light cylinder, dipole approximation is not valid. Therefore, if the rotation axis and the dipole axis are not parallel, then the polar cap shape is distorted, which may cause an asymmetry between the two pulses. The right panel shows the distorted polar cap shape when the dipole axis is inclined by 45 degrees. Figure adopted from [53].

Outer Magnetosphere Case: Fan Beam

If the pulsed radiation comes from the outer magnetosphere, the light curves are explained as follows (see the left panel of Fig 2.20). Particles move along the magnetic fields near the last closed field lines. The last closed field lines in a three-dimensional view taking into account the relativistic rotation effect are shown in Fig. 2.19. All synchrotron, curvature and inverse Compton radiations are strongly beamed to the direction of the particle motions by an angle $1/\Gamma$, where Γ is the Lorentz factor of the particle. Therefore, the tangential lines of the closed lines could be projected to the "emission profile map" defined above. In the case of an emission from the outer magnetosphere, however, one has to take into account two corrections when the

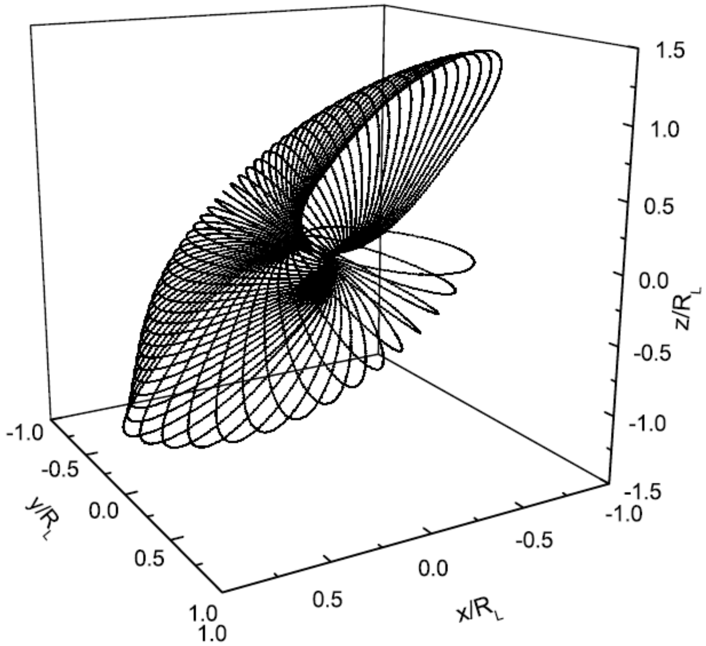

Figure 2.19: A three dimensional view of the last closed lines. The angle between the dipole and the rotation axis is 50 degrees. The effect of relativity near the light cylinder is taken into account, which makes the lines asymmetric. Figure adopted from [177].

emission profile map is created: the relativistic aberration and travel time. When the direction of the tangential line $\mathbf{u} = (u_x, u_y, u_z)$, ($|\mathbf{u}| = 1$), where z is the rotation axis direction and x is the azimuthal direction, the direction of the photon $\mathbf{u}' = (u'_x, u'_y, u'_z)$, ($|\mathbf{u}'| = 1$) would aberrate as (see [177])

$$u'_x = \frac{u_x - \beta}{1 - \beta u_x}, \quad u'_y = \frac{u_y}{\gamma(1 - \beta u_x)}, \quad u'_z = \frac{u_z}{\gamma(1 - \beta u_x)} \tag{2.41}$$

(2.42)

where $\beta = |\mathbf{r} \times \mathbf{\Omega}|/c$ and, $\gamma = (1 - \beta^2)^{-\frac{1}{2}}$. The correction for the travel time in the pulsar phase ϕ would be

$$\Delta\phi = -\frac{\mathbf{r} \cdot \mathbf{u}'}{R_L} \tag{2.43}$$

The top right panel of Fig. 2.20 shows the emission profile map assuming that the angle between the rotation axis and the magnetic axis is 65 degrees and that the emission comes only from the last closed field lines (gap width is zero, see e.g. [53]). By choosing a viewing angle such as, for example, 82 degrees, one can make a light curve as shown in the bottom right panel of the figure. Assuming that emissivity is uniform over all the field lines, the intensity of the pulsation is proportional to the density of the lines. Depending on the viewing angle, the light curve can have two peaks or one peak.

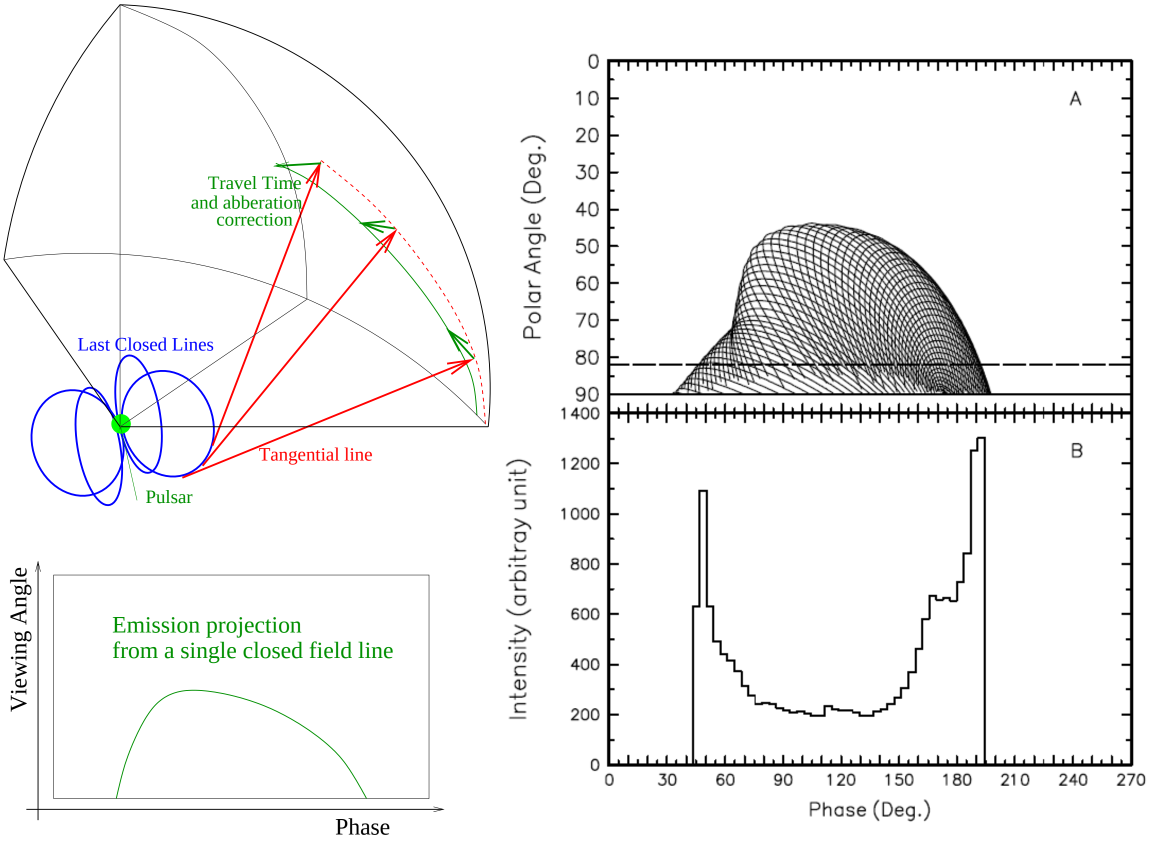

Figure 2.20: Schematic explanation of the emission profile map. Top left: tangential lines of the last closed field lines are projected onto the emission profile sphere (red arrows). Then, relativistic aberration and travel time effects are corrected (green arrows). From one closed field line, one emission profile line is drawn in this way (green line). Bottom left: The emission profile line from a single last closed line on the emission profile map. Top right: Emission profile map composed of emission profile lines from all last closed field lines. The angle between the dipole and rotation axis is assumed to be 65 degrees. Figure adopted from [53]. Bottom right: Pulsar light curve based on the above emission profile map, assuming that the viewing angle is 82 degrees and that emissivity is uniform along the lines. Figure adopted from [53].

2.8 How to Determine the Emission Region?

Both inner and outer magnetosphere emission hypotheses reasonably explain the observed energy spectrum and light curves. The best way to determine the emission region is to measure the energy spectrum around the cut-off energy, because there is a clear and robust difference between the two hypotheses, which was suggested in the previous sections and will be explicitly explained in the following sub-sections.

2.8.1 By the Highest Energy of the Observed Photons

The lower limit of the distance from the pulsar to the emission region can be obtained by applying Eq. 8.1. to the highest energy of the observed photons. This will restrict the possible emission region.

2.8.2 By the Steepness of the Cut-off

If the emission region is in the outer magnetosphere, the maximum energy of the electron determines the energy cut-off, while if it is in the inner magnetosphere the cut-off is governed by the magnetic pair creation (see Sect. 2.7.2). These two mechanisms can be distinguished by fitting the observed energy spectrum near the cut-off energy by a function

$$\frac{dN_\gamma}{dE_\gamma} = KE_\gamma^\alpha \mathrm{exp}(-(E_\gamma/E_c)^\beta) \tag{2.44}$$

where K,α, β and E_c are free parameters. If the cut-off is determined by the magnetic pair creation, due to the strong dependence of the attenuation coefficient on photon energies, β would result in ~ 2 (see [140] and [65]).

$$\frac{dN_\gamma}{dE_\gamma} \propto E_\gamma^\alpha \mathrm{exp}(-(E_\gamma/E_c)^{\sim 2}) \tag{2.45}$$

This characteristic feature is called the super-exponential cut-off (see e.g. [61]). Some of the predicted energy spectra of a pulsar assuming inner magnetosphere emission are shown in Fig 2.21.

If the cut-off is determined by the maximum electron energy, on the other hand, the higher end of the energy spectrum would be dominated by curvature radiation from nearly monoenergetic electrons. As discussed in 1.3.3 and 1.3.4, the energy spectrum of the curvature radiation from monoenergetic electrons can be expressed as

$$\frac{dN_\gamma}{dE_\gamma} \propto E_\gamma^{-0.7} \mathrm{exp}(-E_\gamma/E_c) \tag{2.46}$$

Therefore, β should be 1. It should be noted that a power law part may be affected by, for example, synchrotron radiation (see e.g. [93]) or inverse Compton radiation (see e.g. [177]), and thus, α is not necessarily -0.7. Some of the predicted energy spectra of a pulsar assuming outer magnetosphere emission are shown in Fig 2.22.

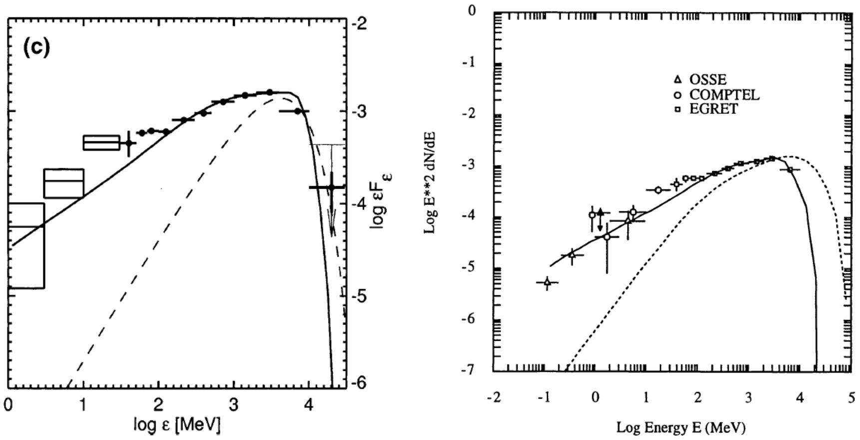

Figure 2.21: Predicted energy spectra of the Vela pulsar from two different authors, J. Dyks and B. Rudak [69] (left) and J. K. Daugherty and A. K. Harding [61], both assuming that emission occurs in PC (inner magnetosphere). The dashed and dotted lines are the curvature radiation spectra from electrons ignoring the magnetic pair creation. The very steep cut-off feature (super-exponential cut-off) caused by the magnetic pair creation can be seen.

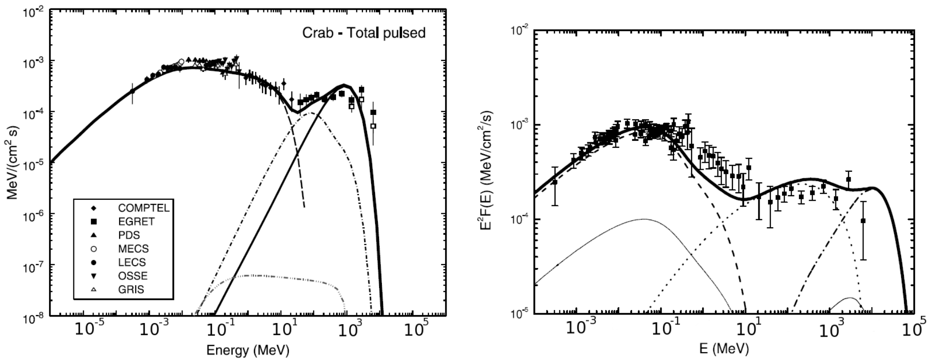

Figure 2.22: Predicted energy spectra of the Crab pulsar from two different authors, Harding et al. [93] (left) and Tang et al. [177] (right) both assuming that the emission region is in the outer magnetosphere. The highest end of the spectra are explained by the curvature radiation from monoenergetic electrons, as indicated by a solid line (left) and a dashed-dotted line (right).

2.8.3 Why was the Emission Region not Determined before 2007?

Before the *Fermi* satellite started operation, the number of known gamma-ray pulsars were only seven, all of which were found by EGRET at energies up to a few GeV. Their energy spectra from radio to gamma-rays are shown in Fig. 2.23. The vast majority of pulsars were not detected in gamma-rays because of the limited sensitivity of EGRET. Imaging Atmospheric Cherenkov Telescopes (IACTs, see Chapter 3) searched for some pulsars above ~ 100 GeV but none were detected. Flux upper limits derived from them are also shown in the same figure. As one can see, cut-off shapes were not precisely known for any of the pulsars.

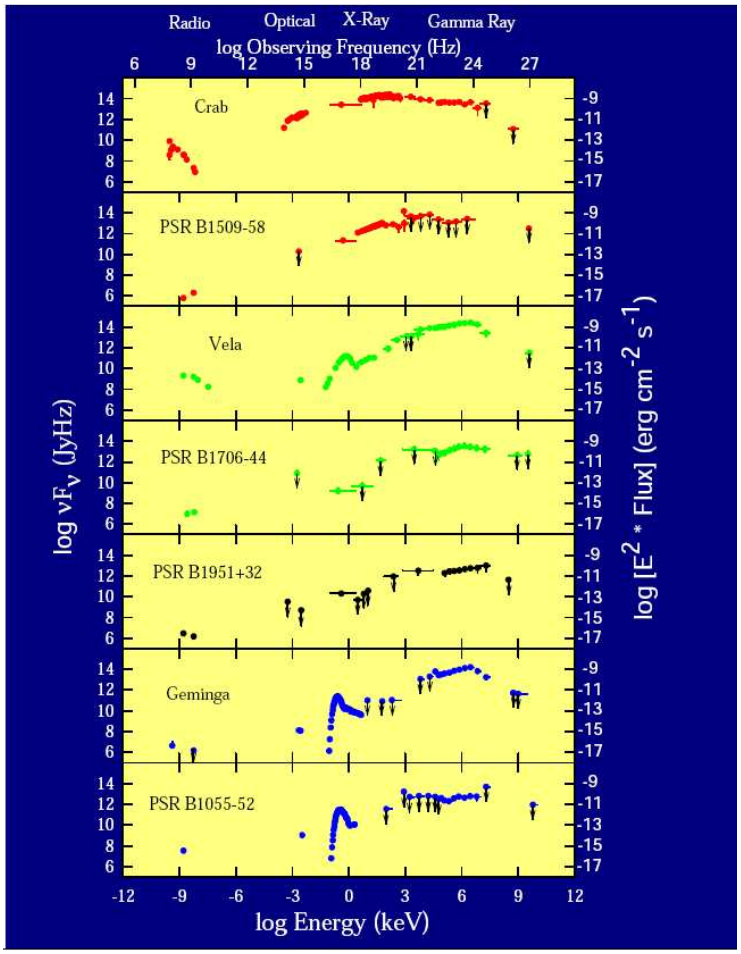

Figure 2.23: Entire energy spectra of seven gamma-ray pulsars detected by EGRET from radio (10^{-6} eV) to gamma-rays. Clear cut-off features of the spectrum in GeV region were not well measured for any of them. Figure adopted from [179].

2.9 The Crab Pulsar

Among the seven gamma-ray pulsars, which EGRET detected, Crab, PSR1951+32 and Geminga are observable by MAGIC and the Crab pulsar is the brightest of them. It is actually one of the best studied of all pulsars because of its brightness over a very wide energy range (see Fig. 2.4). Here, I will summarize the basic properties and observation status of the Crab pulsar.

2.9.1 Discovery of the Crab Pulsar and its Nebula

The Crab Pulsar was discovered in 1968 (see [171]), one year after the discovery of the first pulsar PSR B1919+21. Since then, pulsed emission from the Crab pulsar has been detected at all accessible energies up to gamma-rays (see [55] for optical , [47] for X-ray , [15] for gamma-ray below 100 MeV and [194] for gamma-ray above 100 MeV) On the other hand, the Crab nebula had been discovered much earlier, by Jone Bevis in 1731 thanks to its brightness in visible light. In the "Catalogue of Nebulae and Star Clusters" published by Charles Messier in 1781, the Crab Nebula is listed as the first object. There are several historical documents describing the supernova explosion in 1054 in the direction of the Crab pulsar/nebula. The Crab pulsar is the only pulsar whose birth is precisely documented by human beings.

2.9.2 Basic Properties of the Crab Pulsar

Basic properties of the Crab Pulsar are summarized in Table2.1.

J name	PSR J0534+2200
True Age	956 years
Spin down Age	1240 years
Mass	1.4 $M_\odot$
Radius	10 km
Co-rotation Radius	1500 km
Surface Temperature	$< 1.5 \times 10^6$ K
Pole magnetic field strength	3.78$\times 10^{12}$ Gauss
Period	33.6 msec
Time derivative of period	4.20 $\times 10^{-13}$
Spin down luminosity	4.6$\times 10^{38}$erg/s
Right ascension (J2000)	05:34:31.973
Declination (J2000)	22:00:52.06
Distance from the Earth	2.0 kpc

Table 2.1: Basic properties of the Crab Pulsar. Values are taken from [203] and [124].

As you can see from Fig. 2.6, it is one of the youngest pulsars and the spin down luminosity is also very high. Unfortunately, the surface temperature is not successfully measured but a very stringent upper limit of 1.5×10^6 K has been obtained (see [37]). The surface magnetic field strength is about 0.1 B_{cr} and magnetic pair creation would work effectively near the poles.

2.9.3 Geometry of the Crab Pulsar, the Crab Nebula and the Supernova Remnant

The geometry of the light cylinder, the unshocked pulsar wind region, the pulsar wind nebula, and the supernova blast shock front are shown in Fig. 5.3. The neutron star radius of the Crab pulsar is 10 km and the co-rotation radius is 150 times larger than that, (3×10^{10} [cm/s]) /(30Hz $\times 2\pi$) = 1500 km. The pulsar wind is highly relativistic and its Lorentz factor is thought to be higher than 10^4 (see [152] and [195]). The wind is decelerated and heated by a plasma and a standing shock wave is created at 0.1 pc (see [111] and [10]). The average speed of the plasma flow after the shock is $\sim$ 2000 km/s (see [111]) resulting in the formation of an extended synchrotron source up to $\sim$2 pc. Most of the observed radiation from radio to gamma-rays are generated in this region (see [111]) and it is called the Pulsar Wind Nebula (PWN). The blast wave of the supernova explosion propagates with an average velocity of $\sim$ 5000 km/s and now it is at $\sim$5 pc. Charged particles should be accelerated there but radiation is much weaker than the PWN.

The Crab pulsar is located at 2.0 kpc away and the radius of the PWN of 2 pc corresponds to 0.06 degrees in viewing angle. Taking into account the point spread function of typical IACTs ($\sim$ 0.1 degrees at around 500 GeV), it is not possible to resolve the pulsar emission and the nebula emission spatially by IACTs. Fig. 2.25 shows the images of the Crab nebula in different energies.

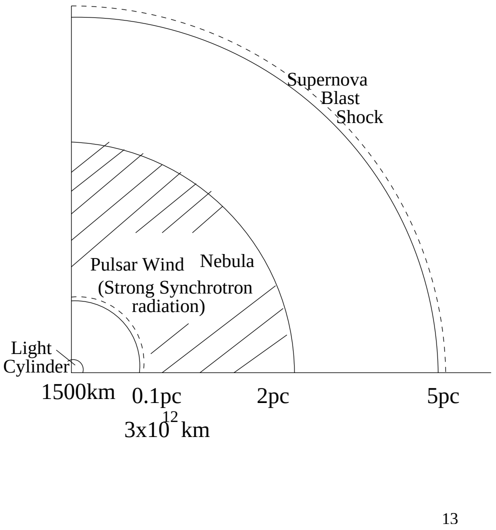

Figure 2.24: The geometry of the Crab pulsar, the Crab nebula and the supernova blast shock. The light cylinder has a radius of 1500 km. The nebula extends from 0.1 pc to 2 pc from the pulsar. The supernova blast shock is about 5 pc away from the pulsar.

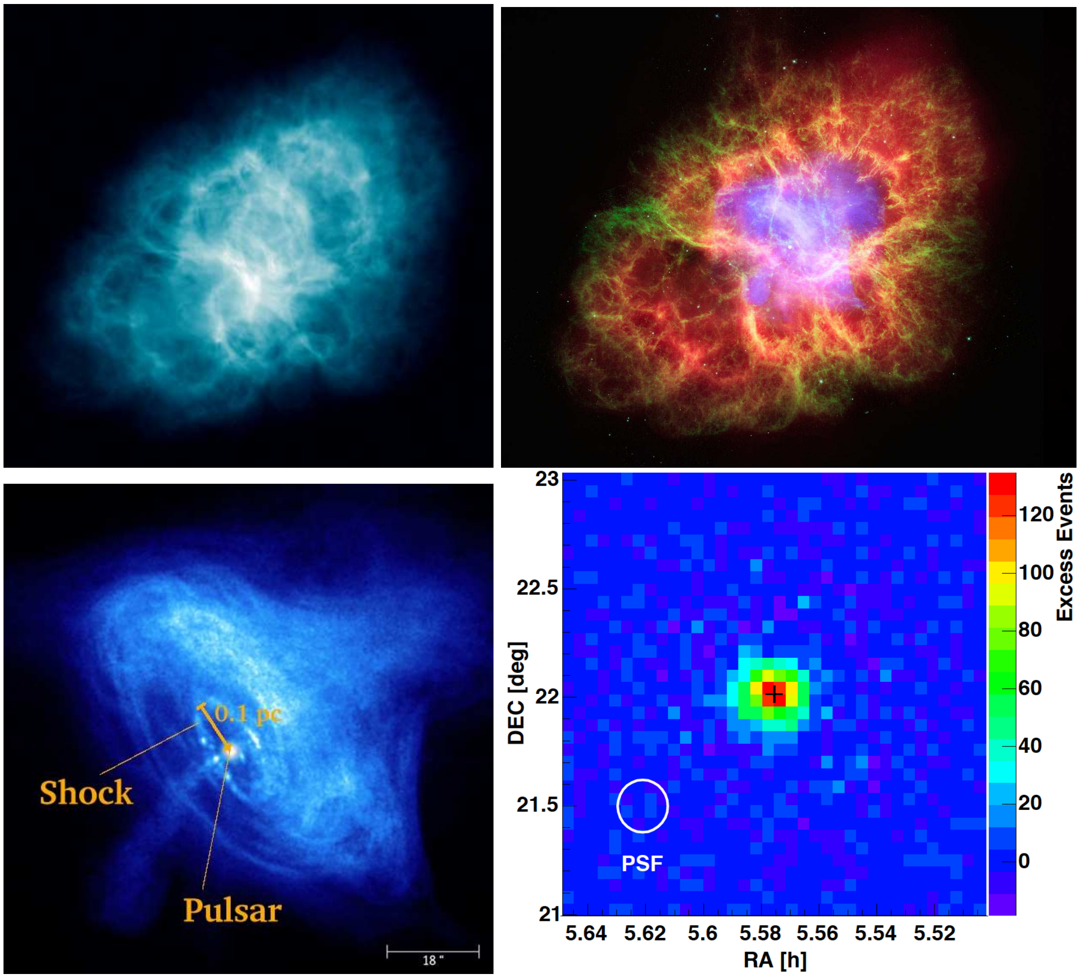

Figure 2.25: The Crab nebula in different energies. Top left: Radio image at 5 GHz. Its filament structure looks similar to the optical image. Figure adopted from [216] Top right: Optical image (red and green) overlaid with the X-ray image (blue). Figure adopted from [206]. Bottom left: X-ray image. The standing shock at 0.1 pc is indicated by an orange bar. Figure adopted from [206]. Bottom right: VHE gamma-ray image observed by MAGIC. Due to the limited angular resolution, the structure cannot be resolved. Figure adopted from [20].

2.9.4 Light Curve of the Crab Pulsar

Fig 2.26 shows pulse profile of the crab pulsar over 15 decades from radio 332 MHz (10^{-6} eV) to > 1 GeV (10^9 eV). The bottom right panel shows the X-ray (20 - 50 keV) light curve overlaid with the radio (812.5 MHz) with the phases around the first peak zoomed. One can see several interesting features.

Similar peak phases Interestingly, the phases of the two pulses are very similar over the 15 decades, which might imply the same emission region for all energy bands. Actually, this is not often the case, as one can see in Fig. 2.4.

Slight energy dependence of peak phases Although peak phases look similar at first glance, a closer look reveals the small energy dependence of the peak phases. From the left panel of Fig. 2.26, one can see that the X-ray peak is slightly advanced in time relatively to the radio peak.

Different pulse width and bridge emission The width of the pulses changes with the energy. A bridge emission between the two pulses are also seen in some of the energy ranges.

Different P2/P1 ratio The ratio of the height between the two pulses changes with the energy. It reflects different spectral shapes between the two pulses.

These features will be discussed in detail for gamma-rays in Chap. 8

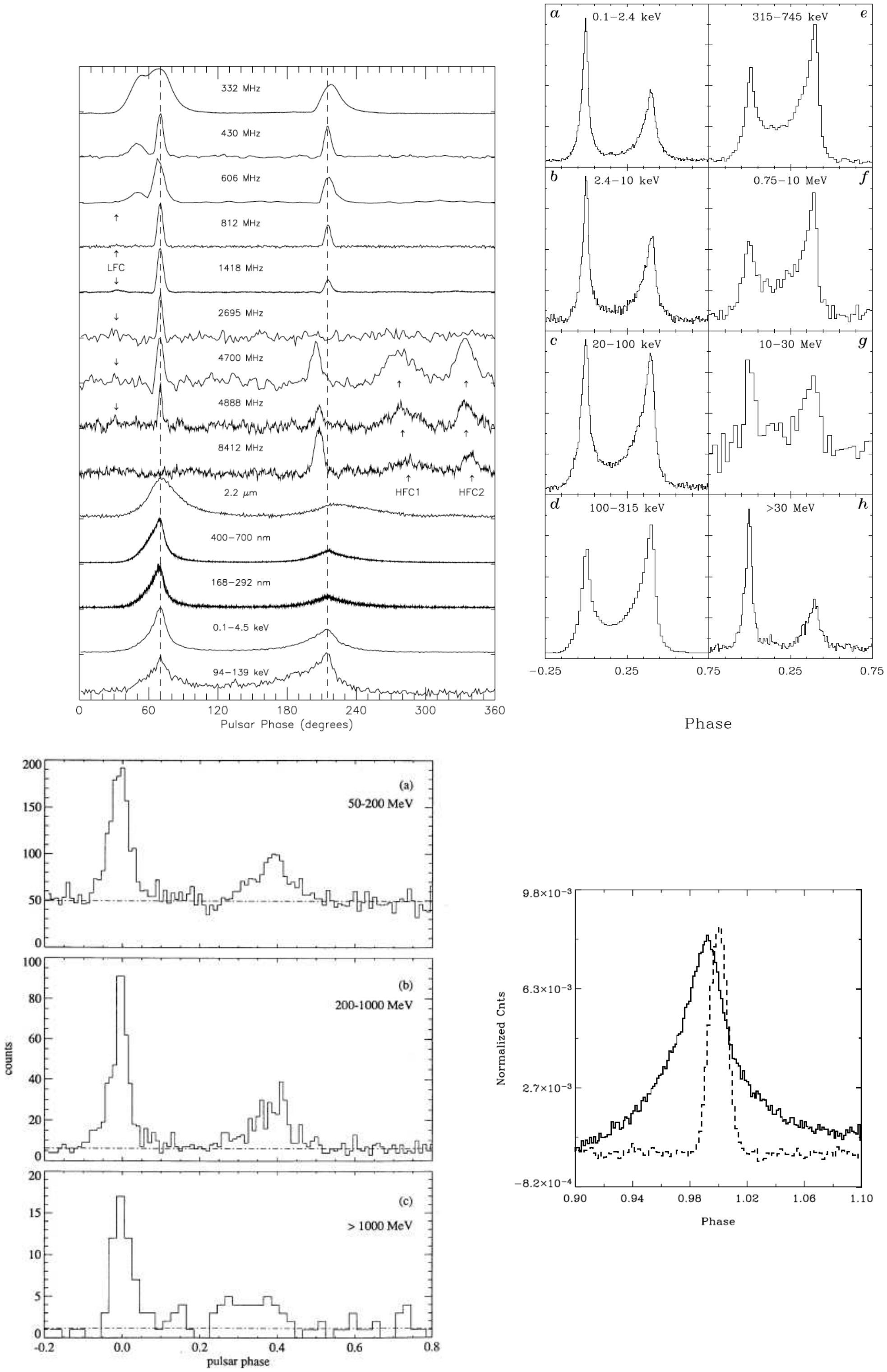

C

Figure 2.26: Light curves of the Crab pulsar measured before 2007. Top left: Radio 332 MHz to X-ray 139 keV. Figure adopted from [136]. Top right:. X-ray 0.1 keV to gamma-ray $> 30 MeV$*. Figure adopted from [114]. Bottom left: High energy gamma-ray (50 MeV to* $>$ *1 GeV). Figure adopted from [142]. Bottom right: X-ray (20 - 50 keV) overlaid with the radio (812.5 MHz) with the phases around the first peak zoomed. Figure adopted from [115].*

2.9.5 Naming of the Pulse Phases

Since the peak phases are stable for all energies, the Crab pulsar is often studied by dividing its light curve into eight phases, as shown in Fig. 2.27. In this thesis, I use the names that were first defined by Fierro et al. (see [77]).

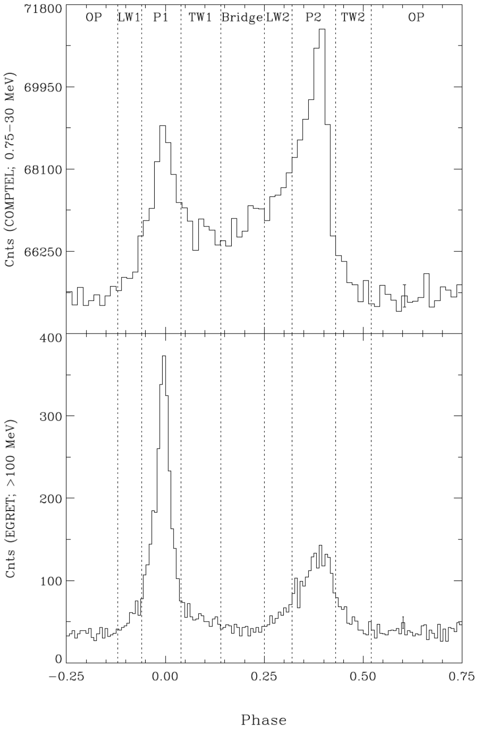

Component	Abbreviation	Phase interval	Width
Leading Wing 1	LW1	0.88−0.94	0.06
Peak 1	P1	0.94−1.04	0.10
Trailing Wing 1	TW1	0.04−0.14	0.10
Bridge	Bridge	0.14−0.25	0.11
Leading Wing 2	LW2	0.25−0.32	0.07
Peak 2	P2	0.32−0.43	0.11
Trailing Wing 2	TW2	0.43−0.52	0.09
Off Pulse	OP	0.52−0.88	0.36
Total Pulse	TP	0.88−1.52	0.64

Figure 2.27: Naming of the phases. Following [77], a light curve is divided into 8 phases. The width of the phase intervals are not the same for all phases. Figure adopted from [114].

2.9.6 The Energy Spectrum around the Cut-off Energy Measured before 2007

Fig. 2.28 shows light curves above 100 MeV measured by EGRET (top), above 5 GeV measured by EGRET (middle) and 60 to 180 GeV measured by MAGIC (bottom). EGRET clearly detected high energy gamma-ray pulsation above 100 MeV but only a small number of photons were detected above 5 GeV. On the other hand, although various IACTs (see e.g. [138], [8], [118] and [9]) and air shower arrays (see e.g. [25]) had looked for VHE gamma-rays above ~ 100 GeV, only a hint of signals (2.9 σ) was found by MAGIC above 60 GeV in 2006.

The energy spectrum of the Crab pulsar from optical to gamma-rays is shown in the upper panel of Fig. 2.29. An energy range from 100 MeV to 10 TeV is given in the bottom panel of the figure in order to show the cut-off energy range in detail. EGRET data alone could not be used to determine the cut-off because of lack of statistics. In addition, there was a big gap between the highest energy of EGRET measurements and the flux upper limits obtained by IACTs. This gap is the key energy region for studying the emission region and must be filled by measurements from the new detectors, such as the upgraded MAGIC and *Fermi*-LAT. Actually, the upgraded MAGIC detected the Crab pulsar during the observation between October 2007 and February 2008 and reported in [22], although detailed studies remained to be done with higher statistics, with more elaborate analysis methods and in conjunction with *Fermi*-LAT measurements.

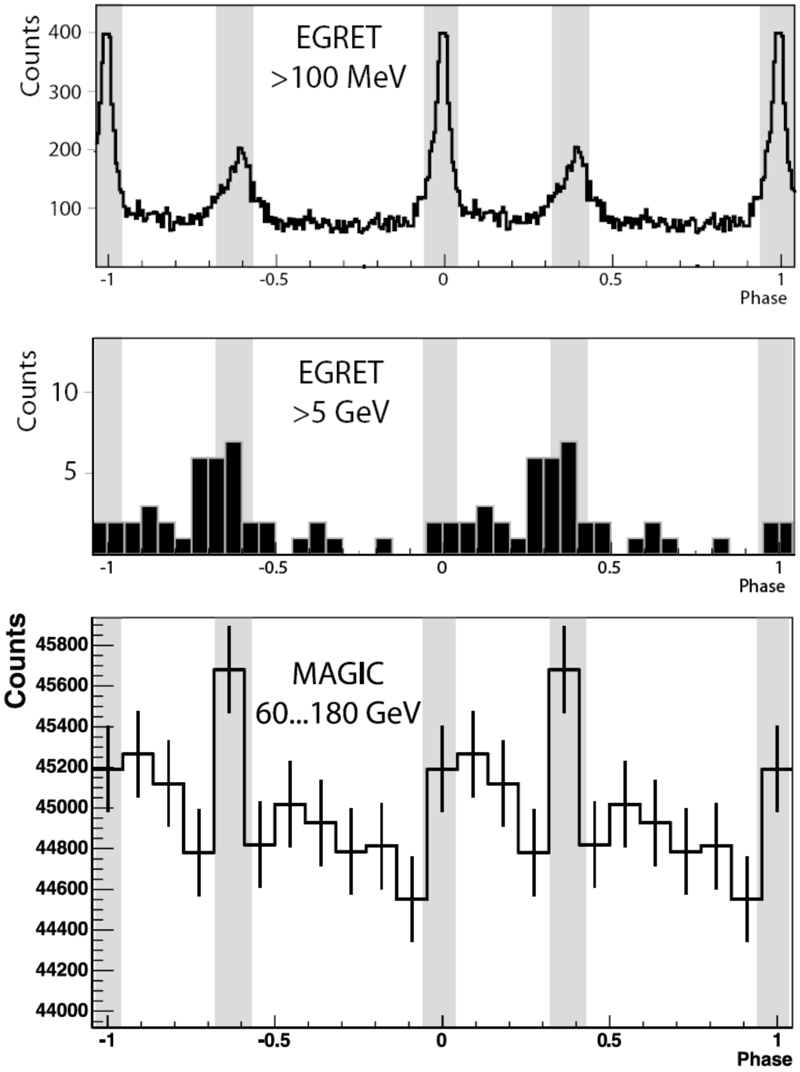

Figure 2.28: The light curve of the Crab pulsar above 100 MeV (top), above 5 GeV (middle) and 60 to 180 GeV (middle), measured before 2007. Figures are adopted from [20]. One can see that the EGRET measurement above 5 GeV was rather poor, despite being the most important energy range to determine the emission region. The MAGIC data suffer from a very high background rate.

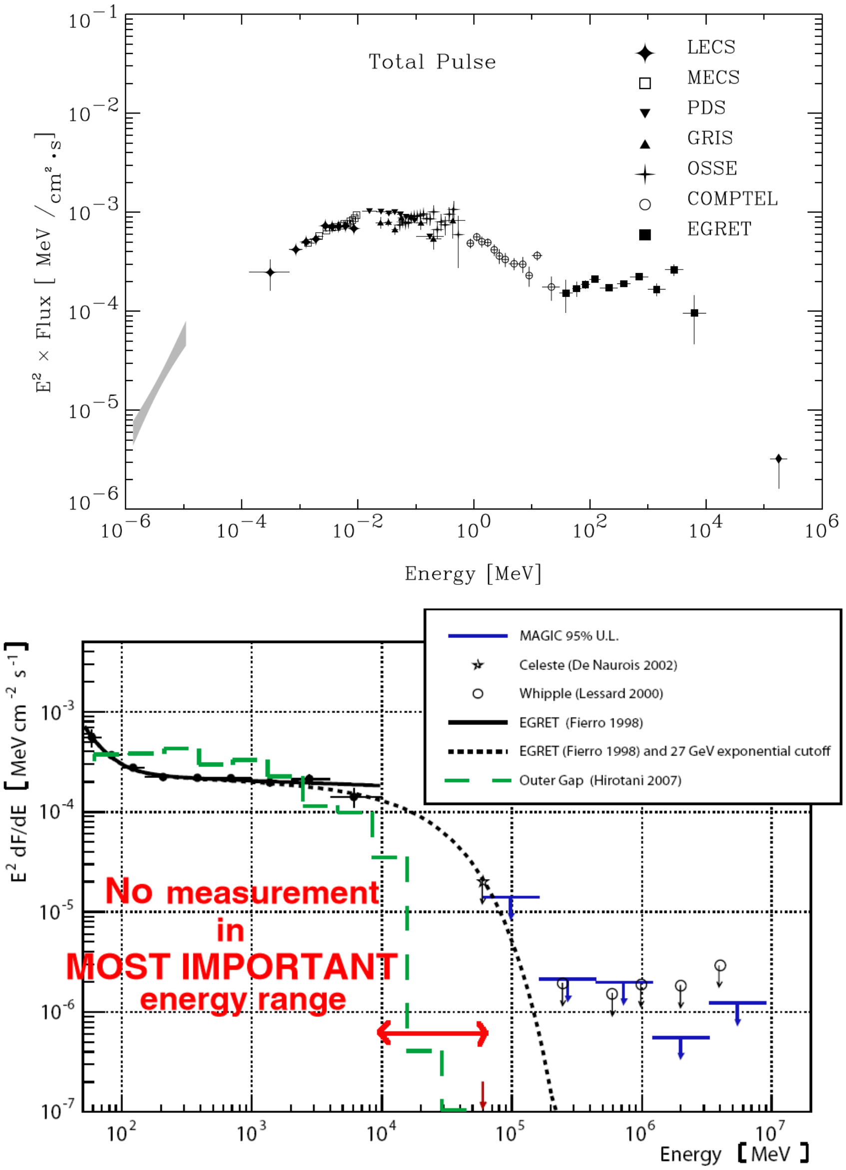

Figure 2.29: Energy spectrum of the Crab pulsar measured before 2007. Top: Optical 1 eV to gamma-ray 10 GeV. Figure adopted from [114]. Bottom: 100 MeV to 10 TeV. Figure adopted from [20]. There was no measurement between ∼ 10 *to 60 GeV, which is the most important energy range to determine the emission region.*

2.9.7 Energy Spectrum of the Crab Nebula

Contrary to the difficulty of the detection of the pulsar emission, its pulsar wind nebula, the Crab Nebula is the first source detected in VHE gamma-rays in 1989 thanks to its large flux. Since then, it has been used as a standard candle for IACTs. Also in this thesis, besides the analysis of the Crab pulsar observation by MAGIC, the nebula emission will be analyzed (see Chap. 5).

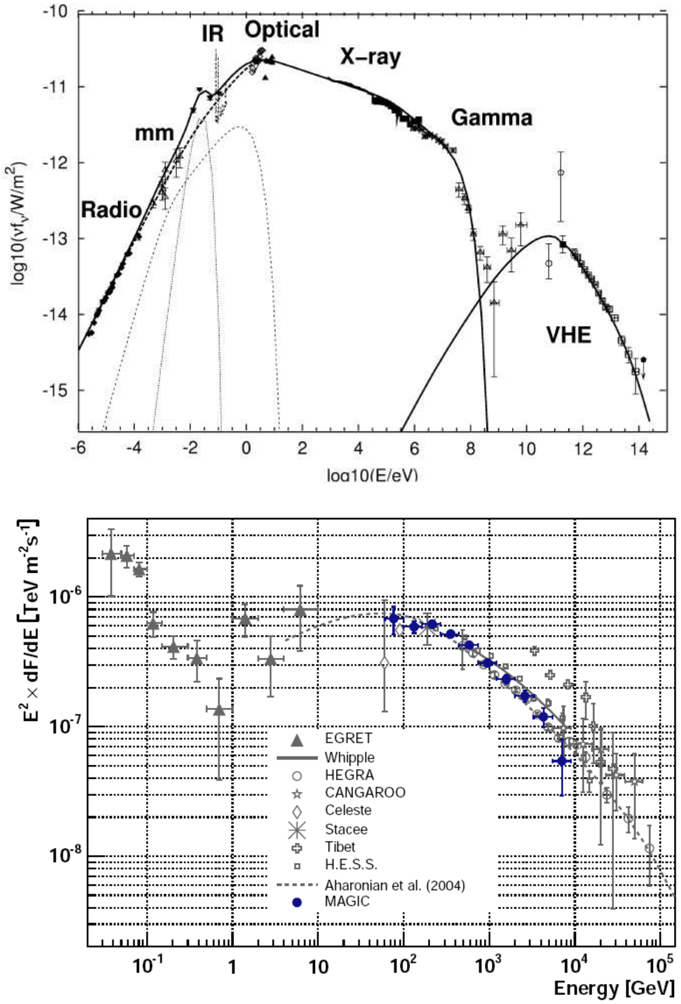

Figure 2.30: The energy spectrum of the Crab nebula. Top: Radio 10^{-6} *eV to gamma-ray 100 TeV. It can be explained by thermal emission (around* 10^{-2} *eV), synchrotron radiation (*10^{-6} *eV to 100 MeV), and inverse Compton scattering (above 100 MeV). Figure adopted from [105]. Bottom: Gamma-ray above 30 MeV. The inverse Compton component of the Crab Nebula spectrum is very useful for calibration of IACTs because of its stability and high flux. Data points from several IACTs, (Whipple, HEGRA, CANGAROO, H.E.S.S. and MAGIC) are shown. Figure adopted from [20]*

2.10 Concluding Remarks

Extremely precise periodicity and high frequency of pulsars make the magnetized neutron star interpretation undoubtable. Since the discovery in 1967, many of the observational results including pulsar wind nebulae have revealed the physics of pulsars in considerable detail.

However, both inner and outer magnetosphere emission hypotheses could explain the observational results. Therefore, the next step for the pulsar physics must come from the determination of the emission region. The best way to do that is to measure the energy spectra around the cutoff energy, which could not be done before 2007. As mentioned in Sect. 1.6, this can be done by the upgraded MAGIC telescope and the new gamma-ray detector in space, *Fermi*-LAT.

Among ~ 1800 pulsars, the Crab pulsar would be the best candidate to study the pulsation mechanism because it is the best studied pulsar in all possible energy bands and its flux is among the highest above 1 GeV. Its location in the sky is also favorable for MAGIC. The detection of the Crab pulsar was already achieved by collective efforts of some of my colleagues (names are listed in Sect. 1.6), although detailed discussions of the results remain to be done with higher statistics, with more elaborate analysis methods, and in conjunction with *Fermi*-LAT measurements.

Several interesting features of the Crab pulsar light curve are known such as similar peak phases over 15 decades in energy, the energy dependence of pulse width and the energy dependence of the ratio between the two peaks. In addition to the determination of the emission region, it would also be interesting to examine these features in the MAGIC and the *Fermi*-LAT data, which may lead to further understanding of the pulsation mechanism.

Chapter 3

Imaging Atmospheric Cherenkov Telescope Technique and The MAGIC Telescope

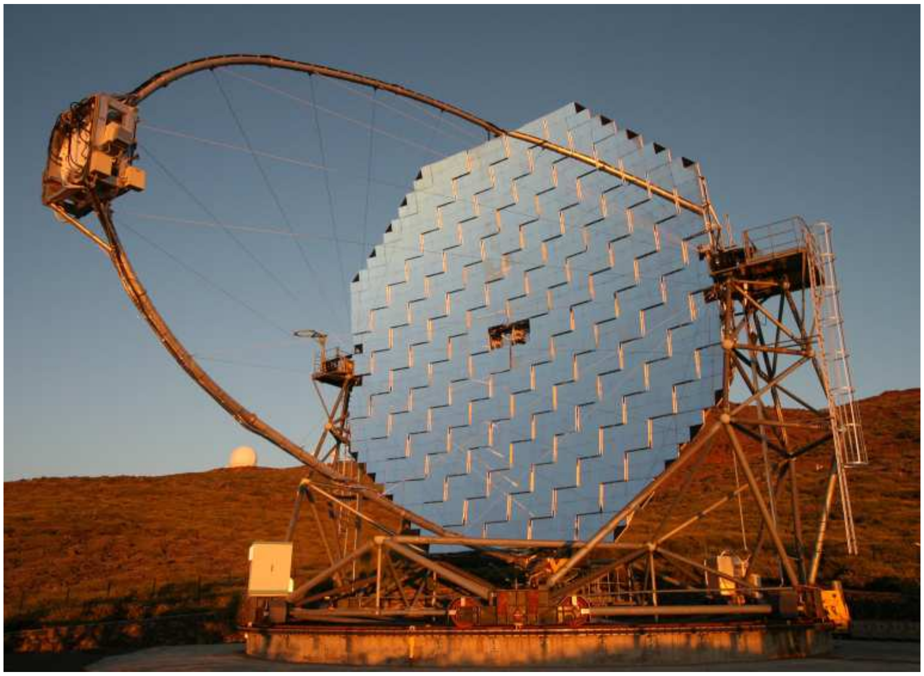

Figure 3.1: Photograph of the MAGIC-I telescope, adopted from [214]

Gamma-rays with an energy higher than $2m_ec^2$ are absorbed by the atmosphere via electron-positron pair creation. In order to detect high energy photons directly, detectors must be set up on artificial satellites (or the space station). The size of such detectors is limited (currently, the largest detector has an effective area of $\simeq 1$ m^2) and, thus, they are usually not very sensitive at high energies above 10 GeV, where the photon flux is normally very low. On the other hand, gamma-rays above 10 GeV can be detected from the ground by using the atmosphere as a part of the detector. One of - and the best of - such techniques is the Imaging Atmospheric Cherenkov Telescope (IACT) technique. Very high energy gamma-rays initiate an electromagnetic cascade when hitting the atmosphere. This cascade is called an **air shower** (Sect. 3.1). Charged, ultra-relativistic particles in the air shower produce a large number of **Cherenkov photons** (Sect. 3.2) that can reach the ground, while the charged particles themselves stop mostly high up in the atmosphere. The Cherenkov photons will be spread over approximately ~ 100 m in radius on the ground. The arrival direction and the energy of the primary gamma-ray can be estimated by sampling some of the Cherenkov photons by a telescope. This is the basic principle of the IACT technique (Sect. 3.3). The IACT technique provides a gamma-ray detection effective area more than 10^4 times larger than that of satellite-borne detectors. Although rejection of the cosmic ray background is not as easy as for satellite-borne detectors, IACTs are the only detectors that have a potential to detect the Crab pulsar signal well above its cut-off energy. This chapter describes the IACT technique and the world's largest IACT, the MAGIC telescope (Sect. 3.4).

3.1 Air Showers

The air shower phenomenon makes the IACT technique possible. First of all, I shall describe the basic features of the air shower.

3.1.1 Overview

A very high energy gamma-ray interacts with an atmospheric nucleus and the main result is an electron-positron pair creation (see Sect. 3.1.2). The created electron and positron have on average each half of the primary gamma-ray energy and, thus, are still very energetic. Subsequently, they interact with an atmospheric nucleus and emit high energy photons via bremsstrahlung (see Sect. 3.1.3). These newly generated photons again produce an electron-positron pair. This cascading process continues until energies of individual electrons and positrons are not high enough to cause the next bremsstrahlung before losing all energy by the ionization process (see Sect. 3.1.4). Eventually, the very high energy incident photon is converted into a huge number of electrons and positrons (as well as an even larger number of photons) with lower energies in this way, which is often called the **air shower** process.

Not only gamma-rays but also cosmic-rays (see Sect. 1.1) produce air showers. At the top of the atmosphere, they cause a hadronic interaction with an atmospheric nucleus to produce many hadrons, mainly pions. The charged pions either interact with an atmospheric nucleus to produce more hadrons or decay into a muon and a neutrino. This multiplication of hadrons is called a hadronic cascade (see Sect. 3.1.7). The neutral pions decay in a very short time into 2 photons. These photons are energetic enough to cause electromagnetic cascades. Therefore, in the case of cosmic-rays, the air shower consists of hadronic and electromagnetic cascades.

Fig.3.1.1 shows air shower simulations of a 100 GeV gamma-ray photon and a 100 GeV proton. Red lines indicate the particle tracks of electrons, positrons and gamma-rays, while green and blue lines indicate muons and hadrons.

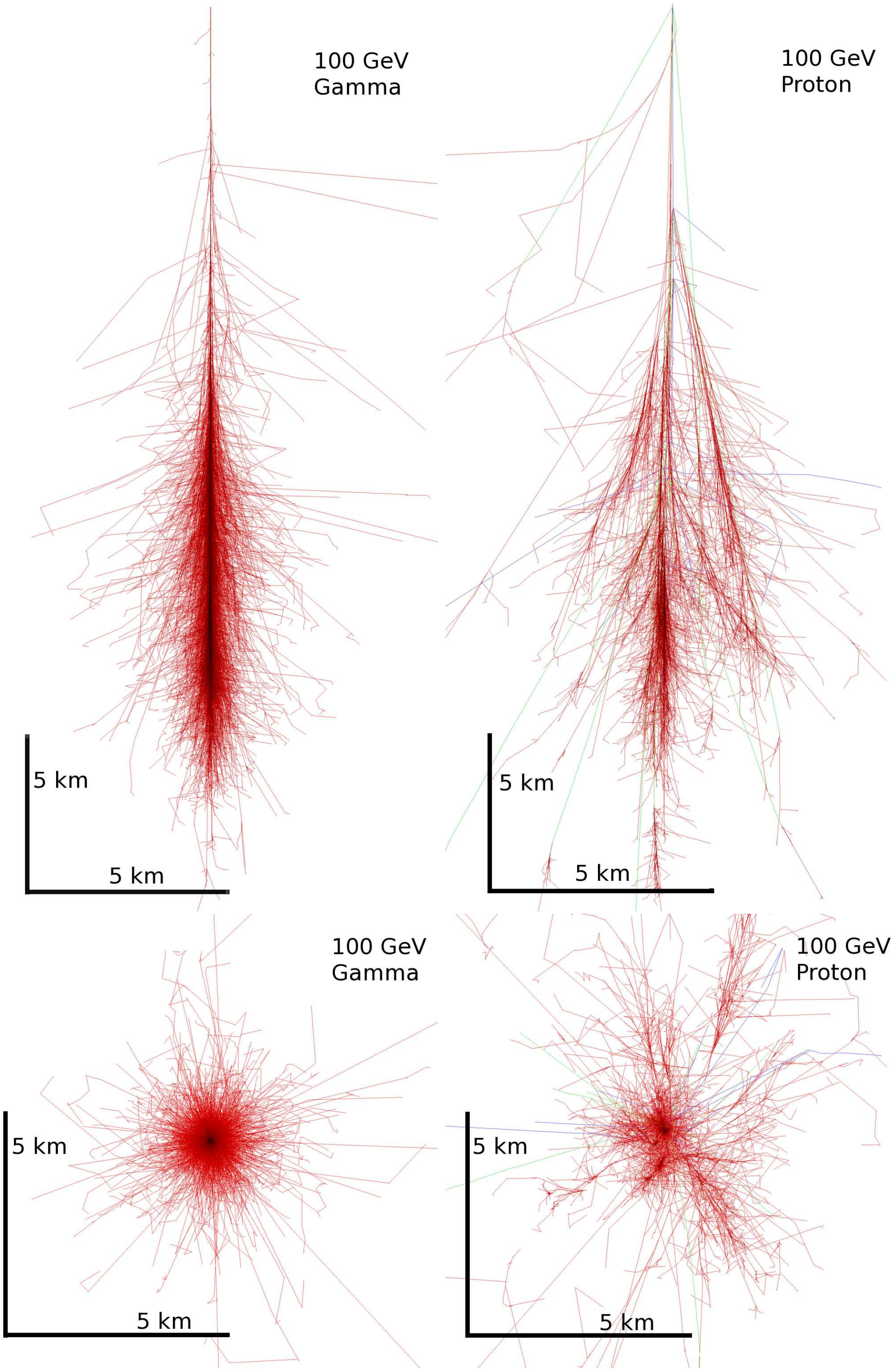

Figure 3.2: Images of an air shower caused by a 100 GeV gamma-ray (left) and a 100 GeV proton (right). A horizontal view (top) and a vertical view (bottom) are shown for each of them. Red lines indicate the track of electrons, positrons and gamma-rays, while green and blue lines in the proton shower indicate that of muons and hadrons. The scale is shown by the black bars. Figures adopted from [164].

3.1.2 Electron-Positron Pair Creation

If the energy of a photon E is more than $2m_ec^2$, it can create an electron-positron pair by interacting with atmospheric nuclei. When $E >> 2m_ec^2$, the cross-section is written as (see e.g. [96])

$$\sigma_{pair} \simeq \alpha r_e^2 Z(Z+1)\left(\frac{28}{9}\log\frac{183Z^{-1/3}}{1+0.12(Z/82)^2}\right) \tag{3.1}$$

where α is a fine structure constant (1/137.0), Z is the atomic number of the hit nucleus and r_e is a classical electron diameter (2.8 fm). The electron and positron thus produced possess a nearly equal energy of $E/2$. Their transverse momenta are roughly the mass of an electron and it is negligible compared to the one obtained by multiple Coulomb scattering (see Sect. 3.1.5). In the case of air, by substituting its effective atomic number $Z \sim 7.6$, $\sigma = 530$ mb is obtained.

The mean free path X_p in a unit of g/cm^2 is written as $A/N\sigma_{pair}$, where N is Avogadro's number 6.02×10^{-23} and A is the mass number. In the case of air, X_p = 47 [g/cm^2]. It means the gamma-rays first interact at 47 [g/cm^2] on average, corresponding to ~20 km in height (see Fig 3.4).

3.1.3 Bremsstrahlung

The differential cross-section of bremsstrahlung $\frac{d\sigma_{br}(E,\epsilon)}{d\epsilon}$, where E and ϵ are energy of the electron and emitted photon, is proportional to 1/ϵ when ϵ is close to 0, whereas it gets harder as ϵ becomes larger. Therefore, energy loss of the electron by bremsstrahlung is dominated by high energy photon emission (see [10]). When E> $100m_ec^2 \simeq 50$ MeV, the integral cross-section between $\epsilon = E/2$ and $\epsilon = E$ is

$$\int_{E/2}^{E} \frac{d\sigma_{bf}}{d\epsilon} d\epsilon \simeq \sigma_{pair} \tag{3.2}$$

Therefore, the mean free path X_0 of bremsstrahlung, which is the average length over which the electron loses energy by a factor e, should be similar to the pair creation mean free path and can be well approximated to be

$$X_0 \simeq \frac{7}{9} X_p \tag{3.3}$$

X_0 is also called the "radiation length". In air, it is $\simeq$ 37 [g/cm^2]. Transverse momenta of the electron and the emitted photon are roughly the mass of an electron and negligible compared to the one obtained by multiple Coulomb scattering (see Sect. 3.1.5).

3.1.4 Ionization and Critical Energy

When a charged particle passes through some matter, it ionizes atoms of the matter and loses its energy. In the case of electrons or positrons, energy loss per unit of length is (see [116])

$$-\frac{dE}{dX} = \frac{2\pi e^4 NZ}{m_e v^2}\left[\log\frac{\gamma^2 m_e v^2 E_{\max}}{2I} - \left(\frac{2}{\gamma} - \frac{1}{\gamma^2}\right)\log 2 + \frac{1}{\gamma^2} + \frac{1}{8}\left(1 - \frac{1}{\gamma}\right)^2\right] \tag{3.4}$$

$$E_{\max} = \frac{2\gamma^2 M^2 m_e v^2}{m_e^2 + M^2 + 2\gamma m_e M} \tag{3.5}$$

where N, Z, v, I and $E_{\max}$ are the number density of the atom, the atomic number of the atom, the velocity of the electron, the ionization potential of the atom and the maximum kinetic energy which can be transferred to the stationary electron, respectively. Since it is proportional to NZ and Z is usually about half of its mass number, the energy loss per mass length is almost independent of matters. In addition, when the electron is relativistic, it is almost energy-independent and remains at ~ 1.8 MeV/(g/cm^2). The total ionization loss ϵ_0 for an electron to travel one radiation length is called the **critical energy**. An electron with the energy ϵ_0 loses all its energy before causing bremsstrahlung in most cases. The air shower development stops when the individual particle energy reaches the critical energy. In the case of air, ϵ_0 = 84.2 MeV.

3.1.5 Multiple Coulomb Scattering

Electrons and positrons do not travel straight in the atmosphere but are scattered frequently elastically by Coulomb scattering. The deviation of direction $\delta\Theta^2$ per travel distance δX is estimated to be (see [26])

$$< \delta\Theta^2 >= \left(\frac{m_e c^2 \sqrt{4\pi/\alpha}}{E}\right)^2 \delta X = \left(\frac{21\mathrm{MeV}}{E}\right)^2 \delta X \tag{3.6}$$

where E is the energy of an electron or a positron. The scattering is more significant when the energy of the particle is lower. The transverse spread of the electromagnetic cascade can be characterized by

$$r_M = \frac{21MeV}{\epsilon_0} X_0 \tag{3.7}$$

where ϵ_0 and X_0 are the critical energy and the radiation length. This r_M is called the “Moliere unit” and $r_M = 9.5$ [g/cm^2] in the case of air. $\sim 95\%$ of the energy of the shower is deposited in a cylinder whose radius is 2 r_M around the axis of the shower (see [88]). At 10 km above sea level, where the number of air shower particles is more or less at a maximum, $r_M \sim 200$ m. (see Fig. 3.4)

3.1.6 Other Interactions

High energy electrons and positrons cause an excitation of atoms (and molecules). They lose energy by this process as well. However, compared to the ionization loss and bremsstrahlung, its effect on air shower development is negligible. Photo-production of hadrons also occurs between a gamma-ray and an atmospheric nucleus. However, since its cross-section is more than 100 times smaller (~ 0.1 mb for a proton target, see [26]) than that of electron-positron pair creation, it is a rare process. Nevertheless, it should be noted that muons can be produced after photo-production of hadrons. Not only hadron-induced showers (see Sect. 3.1.7) but also gamma-ray-induced showers might contain muons, although the number of muons in a gamma-ray-induced shower should be much smaller than that in a hadron-induced shower. Muon pair production by a high energy gamma-ray is even less frequent than photo-production of hadrons.

3.1.7 Hadronic Cascade

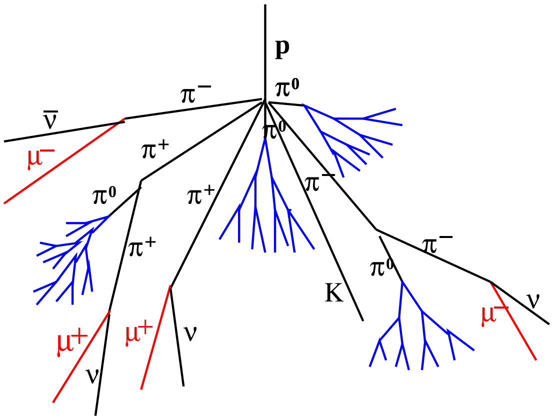

Figure 3.3: Schematic view of a hadron-induced air shower. The primary hadron first creates multiple pions and neutral pions initiate an electro-magnetic cascade, whereas charged pions produce other mesons or decay into a muon and a neutrino.

Cosmic-rays can also produce air showers. High energy nuclei first interact with atmospheric nuclei via hadronic forces and produce mesons and baryons such as pions, K mesons, protons, and neutrons. The cross-section of this inelastic interaction should be treated with Quantum ChromoDynamics (QCD) but empirical estimation of the cross-section can described as follows (see [82]):

The inelastic cross-section of proton-to-proton collision has been experimentally measured. It is $\sigma_{pp}^{inel} \sim 30$ mb and is almost constant between 3 GeV and 1 TeV of the kinetic energy of a beam proton against a steady target proton. If the target is a nucleus with A_2 nucleons, the cross-section can be described as $\sigma_{pA}^{inel} \sim 45 A_2^{0.691}$ mb. When the hitting particle is a nucleus with a mass number A_1, it is approximated as $\sigma_{AA}^{inel} = 68(A_1^{1/3} + A_2^{1/3} - 1.12)^2$ mb.

In air ($A \simeq 14.5$), the inelastic cross-section of a cosmic ray proton is about 280 mb in those energy range, corresponding to 85 [g/cm^2] of mean free path (see [82]). So the first interaction point for a proton is around 18 km a.s.l. on average (see Fig. 3.4), which is a bit lower than for gamma-rays (47 g/cm^2, 20 km). On the other hand, iron nuclei, for example, interact much earlier, the mean free path being about 10 g/cm^2. The multiplicity of the charged secondary particles N in the case of proton-to-proton collisions are estimated to be $N \simeq 2.0(E/\mathrm{GeV})^{0.25}$ (see [50]). The transverse momenta of those generated secondary particles are about 0.3 GeV (see [82]) on average. 90% of the secondary particles are pions and the numbers of π_0, π_+, and π_- are approximately equal. Neutral pions decay into two photons:

$$\pi^0 \rightarrow \gamma + \gamma \tag{3.8}$$

The life time is 8.3×10^{-17} s and quite short. Even 10 TeV π_0 can travel less than 2 mm and, thus, all of π_0 decays without any other interaction. Those high energy photons subsequently induce an electromagnetic cascade, as described in Sect. 3.1.

A charged pion decays to a muon and a neutrino.

$$\pi^{\pm} \rightarrow \mu^{\pm} + \nu_{\mu}(\bar{\nu}_{\mu}) \tag{3.9}$$

and its life time is 26 ns. The mean free path of the inelastic interaction of $\pi^{\pm}$ in air is about 110 g/cm^2 for energies between 100 GeV and 1 TeV (see [82]). If the energy of the pion is high enough, it can interact with another nucleus before decay, producing another meson. This sequence of hadronic interaction is called a hadronic cascade. It continues until all the mesons decay.

A muon also decays;

$$\mu^{\pm} \rightarrow e^{\pm} + \nu_e(\bar{\nu}_e) + \bar{\nu}_{\mu}(\nu_{\mu}) \tag{3.10}$$

and its life time is 2.2 μs. A relativistic muon with an energy $\Gamma m_{\mu} c^2$ can travel 0.66Γ km, and thus muons with an energy larger than $\sim$ 3 GeV can reach the ground on Earth without decay. Those muons are useful for the calibration of IACTs described in Sect. 4.11.

3.1.8 Differences between Hadron-induced and Gamma-ray-induced Showers

There are several major differences between hadron-induced showers and gamma-ray-induced showers, some of which are shown in Fig. 3.2.

- In nearly all cases, all the energy of the primary gamma-ray is converted into an electromagnetic cascade while significant part of the primary hadron energy is carried away by muons and neutrinos without contributing to an electromagnetic cascade.

- A hadron-induced shower is basically a collection of many electromagnetic cascades induced by different π_0s. Due to the complexity of the hadronic cascade, the resulting air showers are more disordered than gamma-ray-induced showers, producing bigger axial asymmetry and sub-cores.

- Individual π_0s have on average a transverse momentum of 0.3 GeV. Therefore, the total transverse spread of a hadron-induced shower is bigger than that of a gamma-ray-induced shower.

- Hadron-induced showers contain many muons while gamma-ray-induced showers rarely do below 1 TeV (The origins of muons in a gamma-ray-induced shower are mainly the rare photo-production processes of hadrons between gamma-rays in the shower and atmospheric nuclei.).

These differences can be detected by IACTs and are very useful for the IACT technique to reduce the background events (see Sect. 3.3).

3.1.9 Density Profile of the Atmosphere

The atmosphere on the Earth consists of 78% of nitrogen, 21 % of oxygen, 1% of argon and small fractions of other molecules. The density is not uniform but decreases in the first order exponentially with height. At sea level, it is 10^{-3} g cm^{-3} while at 100 km above sea level, it is less than 10^{-9} g cm^{-3}, as shown in the top panels of Fig. 3.4. Since gamma-ray-induced air showers are produced through the electro-magnetic cascade process, it is useful to describe the atmosphere in depth with a unit of g cm^{-2}. It also has a exponential profile as shown in the middle panels of Fig. 3.4, which is obvious from the density distribution. At see level, the depth is $\sim 10^3$ g cm^{-2}. The radiation length in the air is about 37 g cm^{-2} (see Sect. 3.1.3) and, thus, the full vertical depth of atmosphere corresponds to ~ 28 radiation lengths.

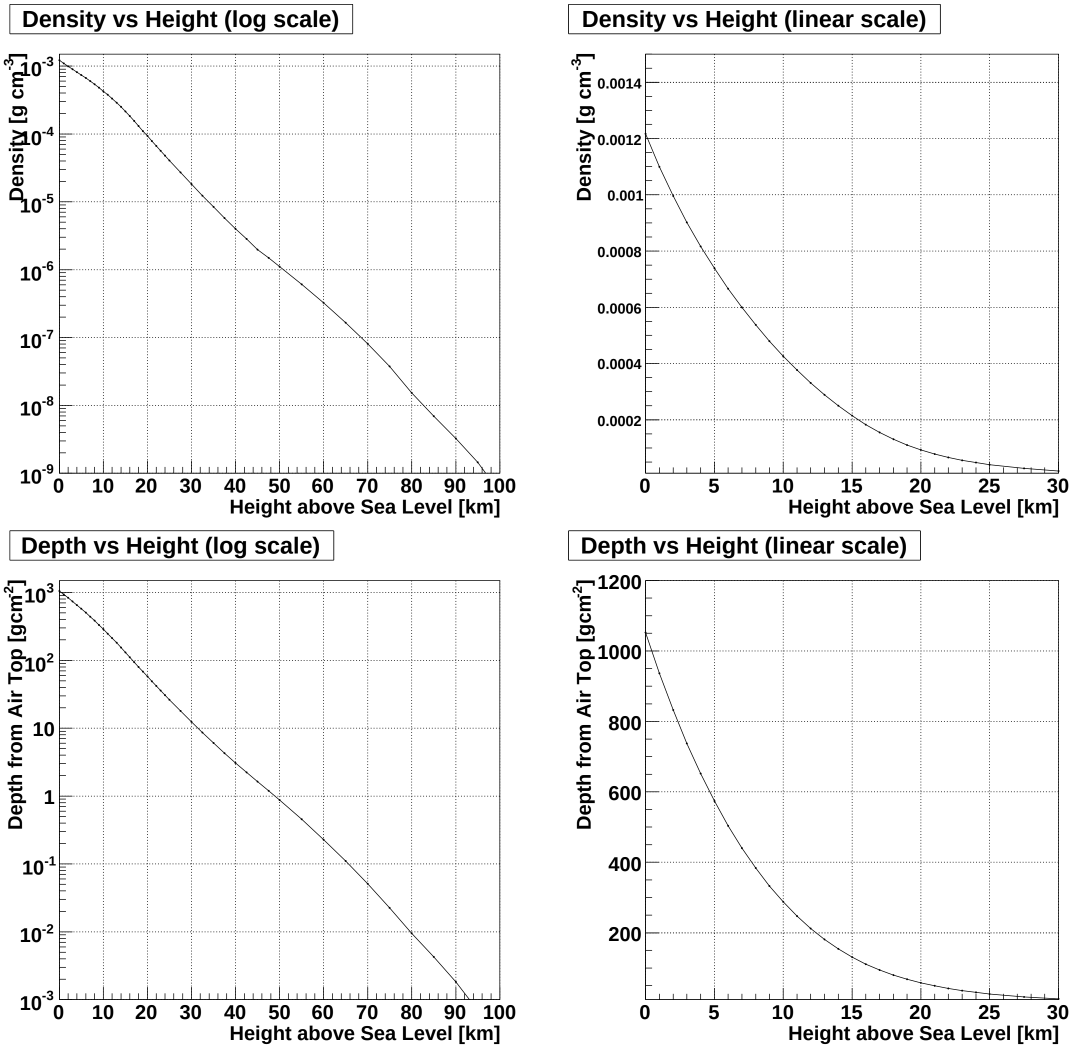

Figure 3.4: Top left: density of atmosphere as a function of height. The vertical axis is on a logarithmic scale. As height decreases, the density increases exponentially. Top right: the same as top left panel but the vertical axis is on a linear scale. Bottom left: The depth in [g/cm^2] as a function of height. The vertical axis is on a logarithmic scale. As height decreases, the depth increases exponentially, as expected from the density distribution (top left panel). Bottom right: the same as bottom left but the vertical axis is on a linear scale.

3.1.10 Characteristics of the Electromagnetic Cascade Development as a Function of Depth

.

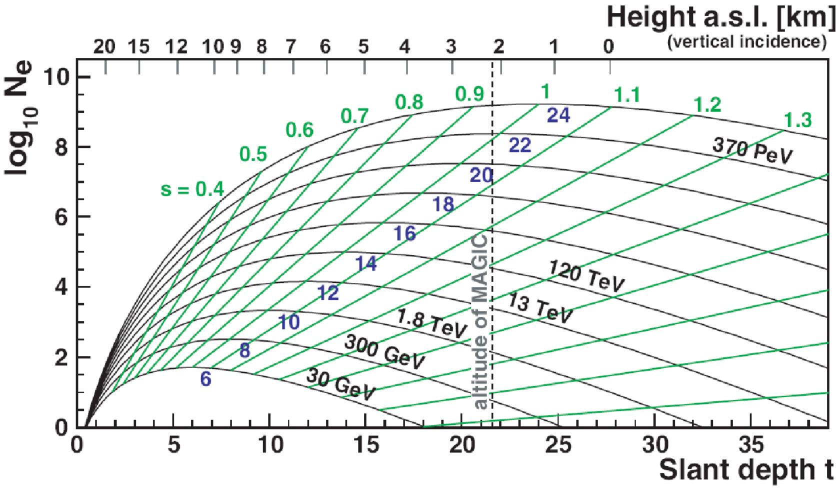

Figure 3.5: Longitudinal development of electromagnetic showers with different primary energies. The shower sizes, characterized by the number of secondary electrons in the shower N_e, are plotted as a function of the radiation length (Slant depth). The green lines denote the shower age (see [189]) which characterizes the shower developments. The energy labels indicate corresponding gamma-ray energy in the case of electromagnetic cascades in the atmosphere. The height corresponding to each radiation length is also shown by the axis at the top of the figure. Figure adopted from [189].

During the electromagnetic cascade process, first the number of particles increases until their energy reaches the critical energy, then decreases. Fig. 3.5 shows the development of the electromagnetic cascade as a function of radiation length X_0 (slant depth t in the figure). The depth at which the number of particles is maximum is called shower maximum. For a gamma-ray with the primary energy $E_0 = 10^3\epsilon_0$, where ϵ_0 is the critical energy, the shower maximum is $\sim 7X_0$. In the case of the atmosphere, $X_0 = 37$ g/cm^2 and $\epsilon_0 = 84.2$ MeV, which leads to a shower maximum at 260 g/cm^2 or ~ 10 km for a 84 GeV gamma-ray. With increasing the energy of the primary gamma-ray, the shower maximum shifts deeper into the atmosphere. From 10 GeV to 10 TeV, the maximum shifts from 5 to 12 radiation lengths, corresponding to a shift from 13 to 7 km in height (see. Fig. 3.4).

3.2 Atmospheric Cherenkov Radiation

3.2.1 Principle of Cherenkov Radiation

When a charged particle passes through dielectric matter, molecules near the track are polarized only for a short time, as shown in Fig 3.6. Focusing on the single molecule, a dipole component

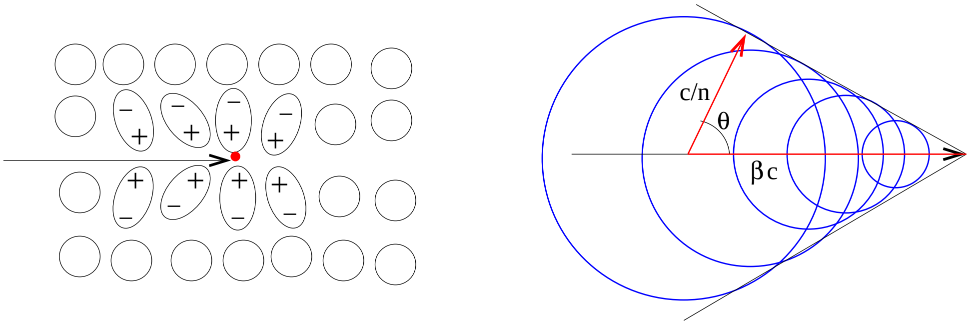

Figure 3.6: Generation of Cherenkov radiation. When a charged particle passes through some matter, molecules are polarized for a short time (left) and emit dipole radiation. When the charged particle passes slower than light through the matter, the individual emissions from molecules compensate one another. When the charged particle passes faster than light through the matter, the individual emissions from molecules become coherent and generate Cherenkov radiation. The emission angle is $\theta = cos^{-1}(1/\beta n)$

appears and immediately disappears. Change in a dipole causes dipole radiation (see e.g. [106]). However, unless the radiative emissions of individual molecules are coherent, they compensate one another and emission of electromagnetic radiation is suppressed. Only when the speed of the charged particle is faster than that of light through the matter, does coherence occur, as shown in the right panel of Fig. 3.6. As known as Huygens law, there is a line on which the phase of the individual dipole radiation is equal. A plain light wave is created on this line and propagates in a direction perpendicular to the line. In a three-dimensional space, this line creates a cone. Therefore, a charged particle moving faster than light in a matter emits a conical wave, which is called Cherenkov radiation. The threshold energy for the Cherenkov radiation E_{th} is expressed as

$$\frac{c}{n(\omega)} = \beta c \tag{3.11}$$

$$E_{th} = mc^2(1 - 1/n)^{-1/2} \tag{3.12}$$

where β is the speed of the particle divided by c, n is the refractive index of the matter and ω is radiation frequency. n is ω dependent near the anomalous dispersion frequency ω_0, while it is almost constant and larger than 1 if ω is well below ω_0. In the case of atmosphere, n can be considered as a constant value for wavelengths longer 250 nm which is relevant for the IACT technique. Therefore, hereafter I will ignore the frequency dependence of n. The angle between the track of the particle and the Cherenkov light direction is called the **Cherenkov angle**. The Cherenkov angle θ is easily calculated by the geometry shown in Fig. 3.6. In a unit of time, the particle travels by βc, while Cherenkov light propagates by c/n, Therefore,

$$\cos\theta = \frac{c/n}{\beta c} = \frac{1}{\beta n} \tag{3.13}$$

The refractive index of matter n is density-dependent. The refractive index, Cherenkov angle and Cherenkov threshold of the high energy electron are shown as a function of height in Fig. 3.7.

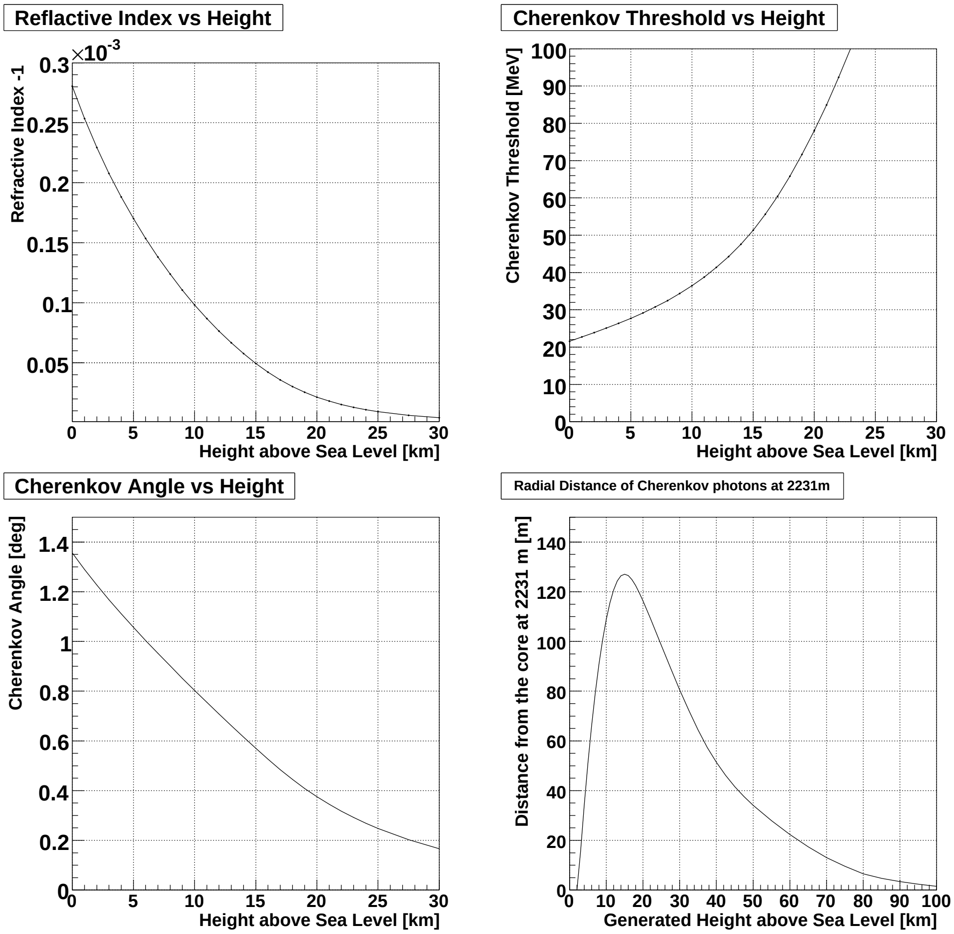

Figure 3.7: Refractive index -1 (top left), Cherenkov threshold for electron (top right) and Cherenkov angle (bottom left) as a function of height. These plots should be compared with the density of the atmosphere (top right panel of Fig 3.4). Bottom left panel shows the distance of the Cherenkov photons from the shower axis at height 2231 m, as a function of generation height. The lateral spread of the axis is ignored.

The energy loss by radiation per unit frequency per unit length is (see [106])

$$\frac{d^2I(\omega)}{d\omega dx}d\omega = \frac{e^2\omega}{c^2}\left[1-\frac{1}{\beta^2n^2}\right]d\omega \tag{3.14}$$

The total energy loss due to the Cherenkov radiation can be calculated by integrating this up to $\omega \simeq \omega_0$. It is negligible compared to, for example, ionization loss. It also shows that the number of Cherenkov photons per unit frequency interval is frequency-independent:

$$\begin{aligned} \frac{dN(\omega)}{dxd\omega}d\omega &= \frac{1}{\hbar\omega}\frac{dI(\omega)}{d\omega dx}d\omega = \frac{\alpha}{c}\left[1-\frac{1}{\beta^2n^2}\right]d\omega && (3.15) \\ &= \frac{2\pi\alpha}{\lambda^2}\left[1-\frac{1}{\beta^2n^2}\right]d\lambda && (3.16) \\ & && (3.17) \end{aligned}$$

and, hence, the number of Cherenkov photons per unit wavelength interval is proportional to $1/\lambda^2$, where λ is the wavelength of the Cherenkov photon (see Fig. 3.8). In air at 10 km, as shown in the top left panel in Fig. 3.7, $n \sim 1.0001$, leading to N(300 - 600 nm) $\simeq$ 8 photon/particle/m at 10 km.

3.2.2 Absorption of the Cherenkov Photons by Air

The atmosphere is not completely transparent for Cherenkov photons, so a certain fraction of them cannot reach the ground. Firstly, ozone exists in the atmosphere and absorbs ultraviolet photons. The absorption spectrum shows a broad peak around 250 nm (see [95]) and most of the Cherenkov photons with a wavelength below 300 nm are lost. Secondly, the air molecules cause Rayleigh scattering. It has a λ^{-4} dependency and mainly short wavelength photons are affected. Thirdly, aerosols such as dust and water droplets cause Mie scattering, which has a weak wavelength dependency ($\propto \lambda^{-(1\sim1.5)}$) and all the wavelengths are affected. The Cherenkov light spectra at 10 km (before absorption) and 2200 m a.s.l. (after absorption) are shown in Fig. 3.8.

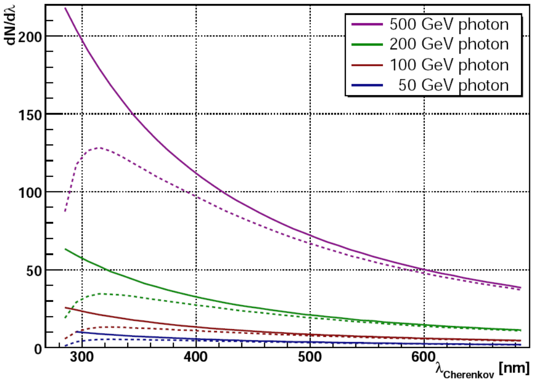

Figure 3.8: Cherenkov radiation spectrum from air showers with different primary energies. Solid lines are the spectra at 10 km. Since absorption is negligible for them, they show λ^{-2} behavior. Dotted lines are the spectra at 2200m, the absorption feature is clearly visible especially in shorter wavelengths. Figure adopted from [189].

3.2.3 Distribution of the Cherenkov Photons on the Ground

As shown in the bottom left panel of Fig. 3.7, the Cherenkov angle increases as the height in the atmosphere decreases. Due to this, a particular feature appears in the relation between the height at which Cherenkov photons are generated and the distance between the shower axis and the Cherenkov photons on the ground, as shown in the bottom right panel of the figure. It shows a peak at 15 km and the peak value is ~ 130 m. This feature, convoluted with the shower development, creates a characteristic pattern of the Cherenkov photon distribution on the ground, as shown in the left panel of Fig. 3.9. The figure shows the distribution of Cherenkov photons from air showers of 30 GeV gamma-rays (MC). A ring-like structure with the radius of ~ 120 m is visible. The area within this ring is called the **light pool**. The right panel of Fig. 3.9 shows the photon density profile on the ground as a function of a distance from the shower core. The hump seen at 120 m is the effect of the superposition of photons generated at different heights (and thus, with different emission angles), as may be understood from Fig. 3.5 and the bottom right panel of Fig. 3.7. It should be noted that for higher energies, due to the lower height of the shower maximum, the hump is less pronounced. The tail of the distribution extending up to more than 500 m is explained by the multiple Coulomb scattering of air shower particles (see Sect. 3.1.5).

The distribution shown in the right panel of Fig. 3.9 is not axially symmetric but slightly elongated in the Y direction. This is because of the geomagnetic fields in the X direction. Electrons and positrons are deflected in opposite directions, leading to this stretched distribution. For higher energies, the effect is less prominent.

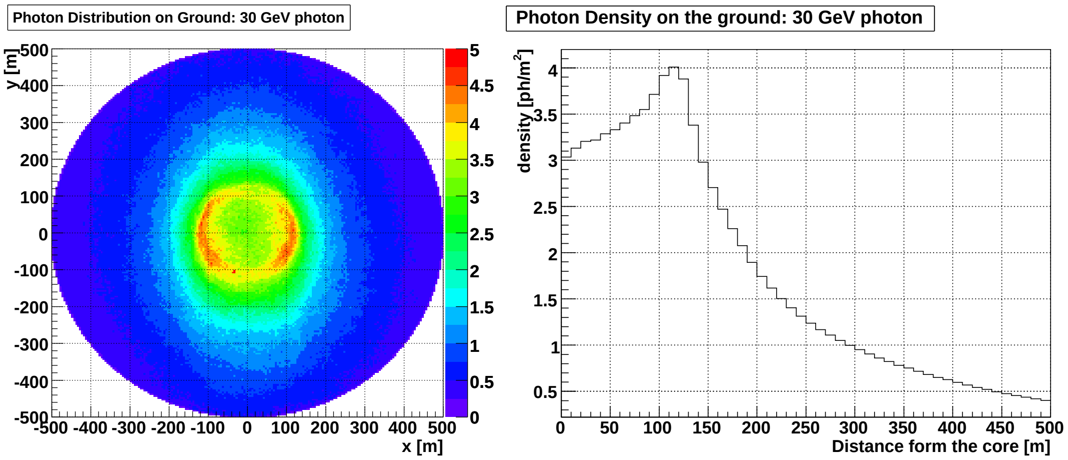

Figure 3.9: Left) Cherenkov light distribution on the ground (2200 m a.s.l.) An air shower induced by a 30 GeV gamma-ray from the zenith was simulated. The light pool with a radius of 120 m is clearly visible. The elongation in the Y direction is due to the effect of geomagnetic field. Right) Photon density on the ground as a function of distance from the core. The hump at 120 m indicates the light pool.

3.2.4 Arrival Time Spread of the Cherenkov Photon on the Ground

A shower development itself takes an order of 100 μs, and Cherenkov photons are produced at various heights. However, the downward velocity of Cherenkov photons is almost the same as for shower particles. Within about 120 m radius from the shower axis, the vertical thickness of the shower particles are less than 2 ns and the time spread of the Cherenkov photons is also of the same order. At larger distance from the shower axis, the time spread of the shower particles as well as the Cherenkov photons starts to increase.

3.3 Imaging Atmospheric Cherenkov Telescope

3.3.1 General Concept

The basic concept of the Imaging Atmospheric Cherenkov Telescope is illustrated in Fig 3.10.

As described in the previous sections, a gamma-ray air shower produce a large number of Cherenkov photons, which creates the “light pool” with a radius of ~ 120 m on the ground (see Sect. 3.2.3). The density ρ of photons with a wavelength between 300 and 600 nm falling within the light pool can be roughly expressed as $\rho = 0.1 \times E_{\rm GeV}$ [photon/m^2], where $E_{\rm GeV}$ is the primary gamma-ray energy in GeV (see [146]). Therefore, a telescope with a mirror area of ~ 100 m^2 should be able to collect$\sim 10 \times E_{\rm GeV} \times \kappa$ photons, where κ is light collection efficiency and normally $0.5 - 0.7$ [1]. The arrival angles of the photons are spread by ~ 1 degree, depending on the generated height and lateral extension. Therefore, by using a pixelized camera on the focal plane of the mirror, air shower images with an angular size of ~ 1 degree can be recorded.

From such an obtained image, the arrival direction and the energy of a gamma-ray can be estimated. From differences in the shower images, one can distinguish most of hadron-induced showers from gamma-ray-induced showers. The discrimination power increases as the primary particle energy increases. On the other hand, close to the threshold energy, the discrimination power degrades due to a small photon statistics and larger shower fluctuations.

3.3.2 Background

Cosmic-ray-induced Showers

For the IACT technique, cosmic-ray nuclei are the dominant background because they also produce air showers and their flux is usually more than 100 times higher than the gamma-ray signals (see Sect. 1.1). As discussed in Sect 3.1.8, there are several differences between gamma-ray-induced and hadron-induced showers. From recorded images of air showers, one can distinguish hadron events and gamma events by making use of these differences.

Night Sky Background Photons

Even in a moon-less clear night, the sky is not completely dark, due to the star light, zodiacal light, airglow, polar light and other (man-made) scattered light from the Earth. In the MAGIC site, for example, the flux of these night sky background (NSB) photons outside the galactic plane was measured to be $2.3 \pm 0.15 \times 10^{12}$ photons/(m^2 sr s) for wavelengths between 300nm and 600nm (see [135]), which is 0.02 photons/m^2 per 1 ns within a 0.1 degree solid angle. Considering the density (see Sect. 3.3.1) and the time spread (see Sect. 3.2.4) of Cherenkov photons, NSB is not too problematic if the photosensors used are fast enough (2-3 ns in the

---

[1] For the photon detection efficiency, the quantum efficiency and the collection efficiency of PMT must additionally be multiplied to it

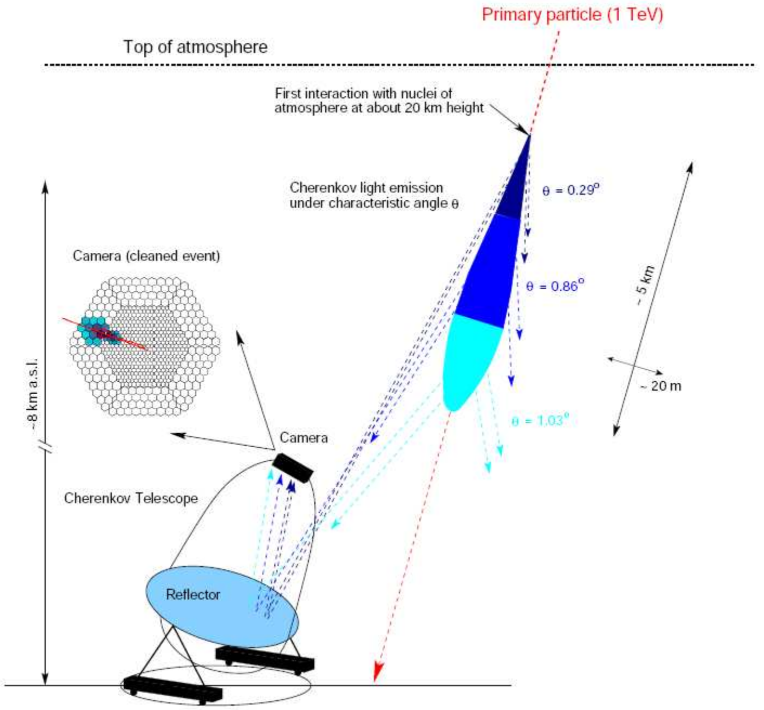

Figure 3.10: Principle of IACT technique. Figure adopted from [57]

FWHM of the signal pulse). However, NSB limits the pixel threshold of the IACTs, as will be described in Sect. 3.4.6

3.3.3 Stereo Observations

By recording a shower image with multiple telescopes, the angular resolution, the energy resolution and background rejection power are significantly improved. Although the energy threshold rises because of the coincidence trigger requirement, stereoscopic observation is nowadays the standard mode for IACT observations.

3.3.4 IACTs in the World

The first successful IACT that could detect the first TeV gamma-ray source (the Crab nebula) in 1989 was the Whipple telescope (see [193]). The HEGRA IACT array was the first stereoscopic IACT system which started observations in 1996 (see [62]). Currently four major IACTs are operational in the world.

MAGIC Located on LaPalma island in the Canary islands (2231 m a.s.l $28.45°$ north, 17.54° west). There are two telescopes and the first one started operation at the end of 2004, and the second one in 2009. The diameter of the reflectors of both telescopes is 17 m, which is currently the largest of all operational IACTs. The energy threshold of the first telescope with the SUM trigger is **25 GeV** (see Sect. 3.4.7).

HESS Located in the Khomas Highland of Namibia, (1800 m a.s.l., 23.27° south, 16.50° east). There are four telescopes operational since 2003, whose reflectors are 12 m in diameter. The energy threshold of the telescope system is **100 GeV**. One bigger telescope is under construction, whose reflector diameter will be 27 m.

VERITAS Located in Arizona, USA (1268 m a.s.l., $111.95°$ west, $31.68°$ north). There are four telescopes operational since 2007, whose reflectors are 12 m in diameter. The energy threshold of the telescope system is **100 GeV**.

CANGAROO III Located at Woomera in Australia (160 m a.s.l., $136.79°$ east, $31.10°$ south) There are four telescopes since 2004, two of which are currently operational. The diameter of the reflectors is 10 m. The energy threshold of the telescope system is **200 GeV**.

3.4 The MAGIC Telescope

The MAGIC I telescope is an IACT located on LaPalma island in the Canary islands, 2231.28 m a.s.l. The second telescope, MAGIC II, has been built 83 m away from MAGIC I and started stereoscopic operation in June 2009. In this thesis, data from MAGIC II are not used. Here, I describe each component of MAGIC I. MAGIC II is almost a copy of MAGIC I.

The major components of the telescope are:

- Carbon fiber frame
- Drive system
- Parabolic 17m diameter reflector
- PMT camera with 577 channels
- Signal transmission to the counting house via optical fibers
- Trigger system
- Data acquisition system

3.4.1 Frame and Drive System

The telescope mirror support frame is made of robust, light-weight carbon fiber tubes. The frame of the telescope, including the camera support (see the left panel of Fig. 3.11), weighs 8.5 tons.

The telescope has an alt-azimuth mount. This means that in order to track a source in the sky, the telescope has to be moved around two axes, azimuth and elevation. The azimuth axis is equipped with two 11 kW motors (see the right panel of Fig. 3.11), while the elevation axis has

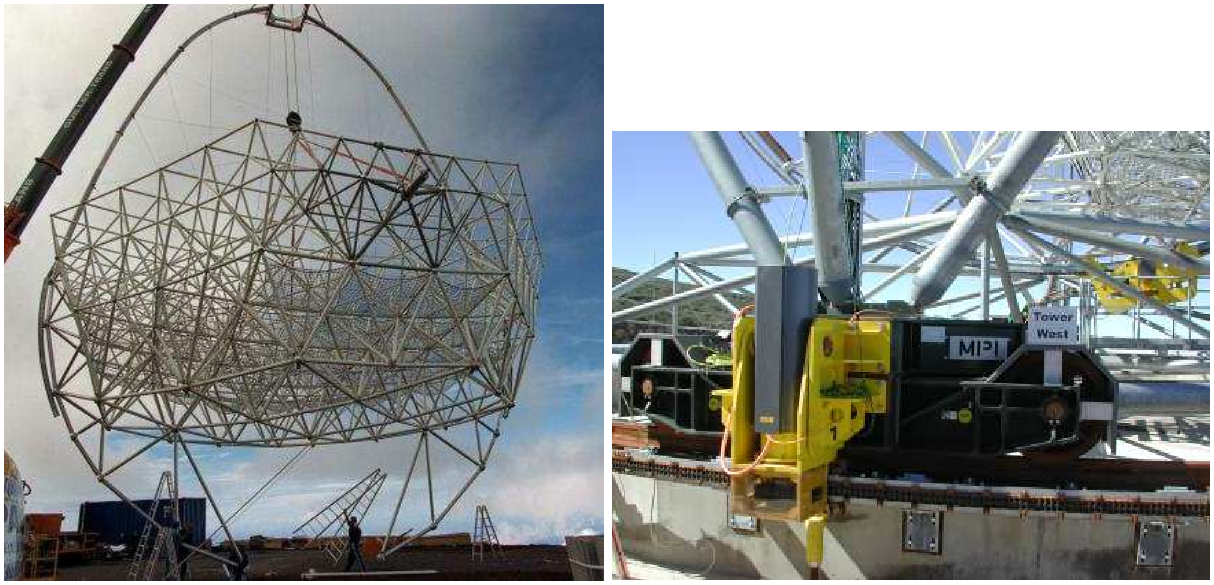

Figure 3.11: Photographs of the telescope frame (left) and the drive system (right), adopted from [214].

a single motor of the same power. The angular position of the telescope is measured by three absolute 14-bit shaft encoders. One of them is in azimuth axis and two in the declination to control twists of the mirror dish. The optical axis of the telescope is calibrated by taking pictures of stars at different azimuth and zenith angles using a highly sensitive CCD camera (SBig camera) in the middle of the reflector dish. A tracking accuracy of 0.01 degree can be achieved (see [153]). This accuracy does not include a possible irregular bending of the telescope structure. The positioning of the telescope is, therefore, constantly monitored during observations by another CCD camera (Starguider camera) mounted on the reflector frame. The entire moving part of the telescope weighs 70 tons.

3.4.2 Reflector

The diameter D of the reflector dish is 17 m which is the largest reflector among the IACTs. The total surface area is 236 m^2. It has a parabolic shape and, thus, relative arrival times of the photons on the reflector surface are conserved on the camera plane. It is important especially for the large reflector because the conservation of the very small time spread of the Cherenkov photon helps to reduce the contamination of the night sky background photons as well as to allow the best possible trigger selection. The relative arrival time information also gives the information about impact parameters (distance from the shower axis to the telescope) leading to better angular resolution and energy estimation (see [23] and [159]). On the other hand, a parabolic reflector makes a relatively large coma aberration, which makes the images extended (blurred) if looking off-axis. In the case of the MAGIC reflector, the coma aberration effect amounts to 7%, i.e. an image point which should have a distance d from the camera center, has an effective distance of $1.07d$ (see [130]). The focal distance f is equal to $D =$ 17 m, thus f/D

Figure 3.12: A photograph of the reflector adopted from [214]. Square shaped mirror panels can be seen.

= 1. Smaller f (keeping the same D) makes the aberration effect larger, while larger f forces the camera to be bigger and heavier in order to have the same field of view (FoV), which is not favorable for such a big telescope. The reflector consists of 964 square mirror elements of 49.5 cm × 49.5 cm size. Each mirror has a spherical shape but with a different radius so that whole reflector shape matches the parabolic shape. The mirrors are made of 5 mm thick AlMgSi alloy plates glued on aluminum honeycomb inside a thin Al-box. The reflectivity of the mirrors ranges between 80 and 90 % depending on the wavelength, whereas the average reflectivity is about 85%.

3.4.3 Camera

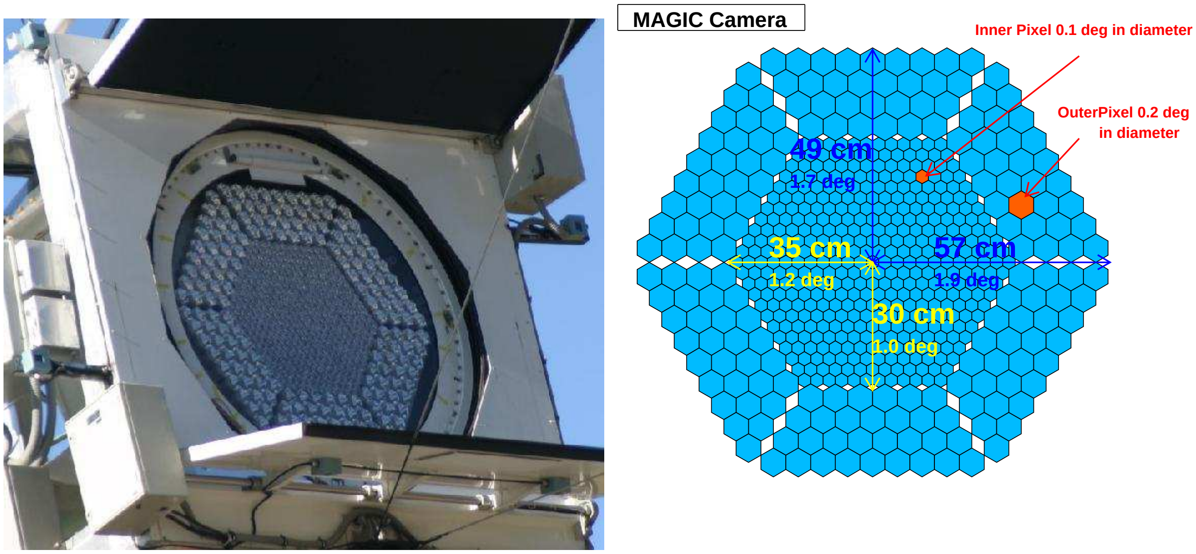

Figure 3.13: A photograph of the camera (left) adopted from [214] and the camera geometry (right)

The picture and the geometry of the camera are shown in Fig. 3.13. It has a hexagonal shape and FoV is ~ 3.5 degree in diameter. It consists of 397 inner and 180 outer pixels. The inner and outer pixels have 0.1 degree and 0.2 degree FoV in diameter, respectively. PMT ET9116 and ET9117 from Electron Tubes are used for inner and outer pixels, respectively. The hemispherical entrance window of the PMTs is coated by a diffuse lacquer doped with a wavelength shifter. The wavelength shifter enhances the QE for the UV range. In addition, the diffusive coating enhances the QE for all range by $\sim 20\%$ by increasing the possibility for a photon to cross the photocathode multiple times (see [147]). A QE curve of ET9116 after the coating is shown in Fig. 3.14, overlaid with a Cherenkov light and a NSB spectrum on the ground. The QE curve is well optimized to detect Cherenkov photons minimizing NSB photon detection. The response time of these PMTs are 1-2 ns. The size of entrance window of ET9116 and ET9117 is 1 and 1.5 inches respectively. In order to reduce the dead space between PMTs, they are coupled with a light guide, the so-called Winston cone, made of aluminized Mylar foil with a mean reflectivity of 85%. The Winston cone also helps to reduce the contamination of scattered light from the ground. Moreover, the Winston cone makes some photons cross the hemispherical photocathode twice, leading to the effective enhancement of the QE (see [147]).

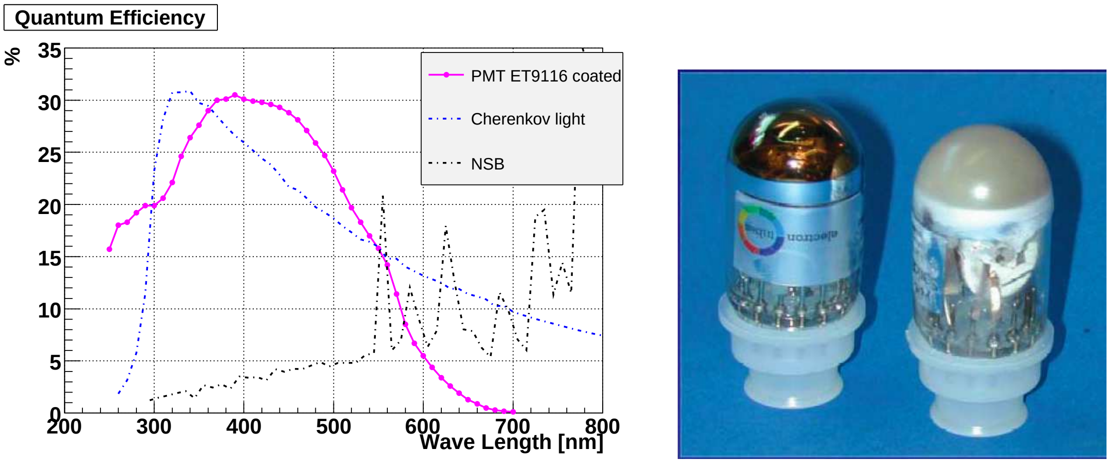

Figure 3.14: Left) Passively enhanced QE curve of PMT ET9116, overlaid with Cherenkov radiation spectrum and NSB spectrum (not in scale). The QE curve is well optimized for the Cherenkov radiation. A hump at 280 nm is due to the wavelength shifter coating. Right) Photograph of PMTs, before (left) and after (right) the diffusive coating.

3.4.4 Signal Transmission

The signal transmission from PMTs to the data storage PC is schematically shown in Fig. 3.15. The gain of the PMTs are roughly 30,000 and 20,000 for inner and outer pixels, respectively. At the PMT base, the signal is AC coupled to an ultra-fast pre-amplifier with a gain of about 6. The pre-amplified PMT signals are converted into light again using fast current driver amplifiers to Vertical Cavity Surface Emitting Laser diodes (VCSELs). The analog optical signals are then

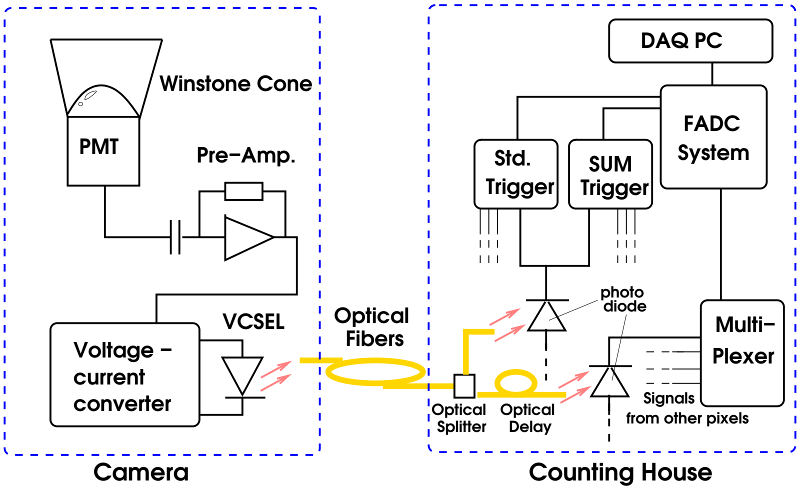

Figure 3.15: Schematics of the signal transmission from PMTs to FADC system.

transmitted from the camera over 162 m long optical fibers to the counting house. There are several advantages of using optical signals compared to electrical signals when the signal width is as short as 1-2 ns and transmission distance is so large: 1) signal attenuation and dispersion of an optical fiber are much less than that of a coaxial cable, 2)the weight of an optical fiber is much lower than that of a coaxial cable, and 3) the optical signal is free from electromagnetic pickup noises. In the counting house, each optical signal is split into two. One of them is routed to trigger branch and the other is routed to the signal digitalization branch. They will be described in the following sections.

3.4.5 Data Acquisition

In the signal digitalization branch, signals from every 16 channels are multiplexed. Multiplexing is done as follows: Each signal in a group of 16 channels is delayed by optical delay lines such that relative time difference between consecutive channels is 40 ns. The delayed signals are converted back into electric signals by fast GaAs PIN diodes and fed into a multiplexer switching in 40 ns steps from one channel to the next one. These multiplexed signals are digitized with a 13-bit flash analogue-to-digital converter (FADC) with a 2 G sampling rate and written in a ring buffer. When a trigger is issued, the digitalization is stopped and the corresponding part of the buffer is written to disk. It is known that the first and last 7.5 ns of each 40 ns FADC window are affected by multiplexer switching noises and, thus, $40 - 2 \times 7.5 = 25$ ns (50 FADC slices) of FADC information per event is finally recorded. The bandwidth of the whole DAQ chain is about 250 MHz. The Signal amplitude can be digitized linearly up to 800-900 ph.e. The deadtime of the DAQ system is ~ 16 μs, which is small enough compared to the trigger rate < 1000 Hz.

3.4.6 Standard Trigger

In the trigger branch, the optical signals are converted back into electrical signal by fast GaAs PIN diodes. Then, each electric signal is again split into two, one of which goes into the standard trigger system and the other goes to the SUM trigger branch. The standard trigger system is described in this section and the SUM trigger system is described in the next section.

The standard trigger system has three stages. However, currently only the first two are in use, namely, Level-0 and Level-1.

Level-0

Level-0 is a individual pixel trigger. Not all the pixels but only the inner 325 pixels contribute to the trigger (see the right panel of Fig. 3.17). The trigger region is about 1 degree from the camera center. Analogue signals entering to the standard trigger branch are fed into the discriminator. The threshold level is adjustable by a computer and is set such that the individual pixel rate is around 100 kHz. The level depends on, for example, the star field inside the FoV or moon condition. A individual (inner) pixel rate at a typical FoV under a dark night sky is shown in Fig 3.16.

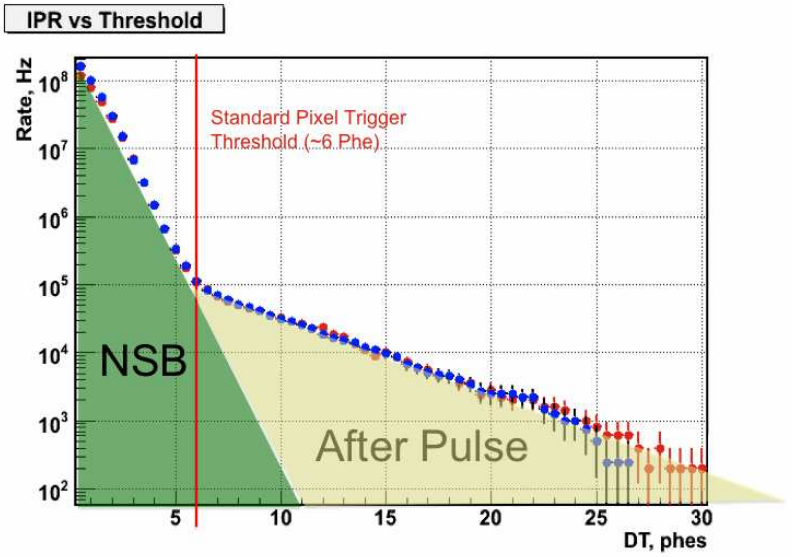

Figure 3.16: Individual pixel rate as a function of threshold. There are two component, NSB photons and after-pulsing caused by NSB photons. Blue points are data and red points are MC. Figure provided by M. Shayduk.

The NSB rate above half a photoelectron level is 150 MHz. As discussed in Sect. 3.3.2, the mean rate of NSB photon with a wavelength 300nm - 600nm is $(2.3 \pm 0.15) \times 10^{12}$ photon/(m^2 sr s). It corresponds to 1.3 $\times 10^9$ photon/s/(inner pixel) in the case of MAGIC, assuming a perfect light collection efficiency. The rate of 150 MHz is consistent with it, taking into account the quantum efficiency of the PMT and the imperfect light collection (the mirror reflectivity, loss in the Plexiglas on the camera entrance window and the light guide efficiency of the Winston cone). As the threshold increases, the rate decreases very fast following the Poisson statistics up to 6 ph.e., while the slope gets harder above it due to the after-pulsing effect. An after-pulse is a fake signal produced by ion-feedback inside a PMT, which is explained as follows: A photoelectron accelerated by an electric field toward the dynode may hit a residual molecule inside the PMT (mainly the one absorbed in the first dynode) certain probability. The hit molecule is sometimes ionized and due to its positive charge it is accelerated toward the photocathode and create multiple photoelectrons. As a result, a fake big signal can be observed after a real photon signal. The typical threshold level is set at $\sim$ 6ph.e., where NSB and the after-pulsing component is comparable.

Level-1

Level-1 is a topological logic trigger in the camera. When 4 Next Neighboring (4NN) pixels aligned in a compact region fulfill the Level 0 trigger within 6 ns, Level-1 trigger is issued. Allowed 4NN topology is shown in Fig. 3.17. However, due to too many possibilities, it is technically very hard to accept all possible 4NN conditions. Therefore Level-1 trigger is constructed as follows: 19 macrocells, each consisting of 37 pixels, are defined in the trigger region of the camera (see the right panel of Fig. 3.17). They are overlapping one another. 4NN conditions only within a macrocell are examined. It should be noted that although 4NN is the standard, the multiplicity of the next neighbor can be adjusted for special observations such as 3NN or 5NN.

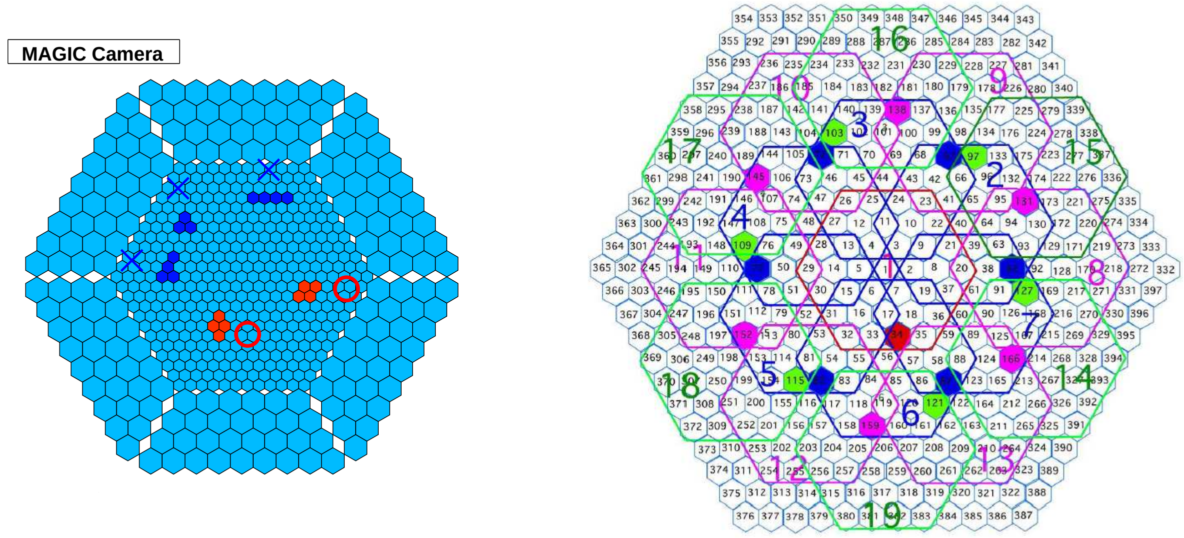

Figure 3.17: Right: 4NN topologies. Red clusters are considered as 4NN but blue ones are not. Left: 19 macrocells over the trigger region. Not all the inner pixels but only 325 pixels belonging to any of the macrocells contribute to the standard trigger.

Level-2

Level-2 is a higher level topological trigger, i.e. a further widely programmable logical trigger based on the topology of an event that passed Level-1 trigger. For example, one could discriminate images pointing to the source position from the ones pointing perpendicular to it. Up to now, the Level-2 trigger has not been used.

3.4.7 Analogue Sum Trigger

With the standard trigger, the MAGIC telescope has a energy threshold of 50 GeV (see Fig. 3.21. The peak of the energy distribution is normally defined as the threshold). MAGIC could detect a 2.9 σ signal (see [20] and Sect. 2.9.6) from the Crab pulsar with the standard trigger system but, in order to see the signal more clearly [2], it was necessary to reduce the energy threshold. Reduction of the Level-0 discriminator threshold might reduce the energy threshold but it causes a rapid increase of the individual pixel rate, as shown in Fig. 3.16, resulting in an explosion of the NSB accidental 4NN rate. Since the DAQ system cannot handle a trigger rate higher than 1000 Hz, lowering of the pixel threshold leads to the degradation of the overall sensitivity due to too much DAQ deadtime caused by accidental triggers. Therefore, a new trigger scheme was required.

Basic Concept

The new trigger system, which is called “analogue sum trigger” or simply “SUM trigger”, was developed and was installed in the MAGIC telescope in October 2007. The development is discussed in detail in [154]. It can be used in parallel to the standard trigger system. The basic scheme is as follows:

- The trigger area is restricted in a ring-shaped region on the camera with inner and outer radii of 0.2 degree to 0.8 degree from the center (see Fig. 3.19).
- Analogue signals of 18 neighboring pixels are added up before the discriminator. The discriminator threshold is 27 ph.e.
- If a signal in a pixel is larger than 6 ph.e. in amplitude, it is clipped at the 6 ph.e. level before the summation in order to minimize the after-pulse effect.

It is well optimized for low energies by selectively catching gamma-ray events and suppressing NSB accidental events based on the following two features of the shower events:

A) Image extension: Even low energy events such as 30 GeV gamma-rays have a extension with a scale of ~ 0.5 degree. On the other hand, NSB photons arrive randomly over the camera.

---

[2] in the VHE astronomy community, 5 σ is generally required to claim a detection of a source

The size of the standard 4NN topology is ~ 0.2 degree, which is good enough to find a core of a shower image above 50 GeV. However, Feature A) implies a possibility to improve the trigger for lower energies by using more information from a larger area, i.e. if the standard 4NN is fulfilled by a shower, there should be more photons around the 4NN, while if it is fulfilled by a NSB accidental event, the probability that more photons exist around the 4NN is very low. A simple increase of the multiplicity of the Level-1 trigger with lower Level-0 thresholds was tried but did not help to reduce the threshold energy, which could be explained by the fact that discriminators in Level-0 significantly lose the information of the amount of individual pixel charge. Removing Level-0/Level-1 scheme and **adding up analogue signals** from ~ 0.5 degree region before discriminators should work better. It should be noted that the time spread of the Cherenkov photons from a low energy gamma-ray is about 2 ns, which is comparable to the PMT signal width (and the minimal pulse width that the DAQ system can restore).

B) Ring shaped light pool: As shown in Fig. 3.9, a low energy gamma-ray shower makes a ring-like light pool with a radius of ~ 120 m. Therefore, low energy gamma-rays would be detected relatively easily when the impact parameter is 80-130 m.

Feature B) can be clearly shown by MC simulations. Fig. 3.18 shows in which part of the camera the low energy gamma-rays are detected with relatively large charges. It was created in the following way: Gamma-ray events with the primary energy of 10 - 40 GeV were simulated with the standard trigger system and images with more than 27 ph.e. were accumulated on the camera. The red ring-shaped region on the figure has inner and outer radii of 0.2 and 0.8 degree, which corresponds to 80 m and 130 m in impact parameter, respectively. NSB, on the other hand, illuminates the camera uniformly. **Restricting the trigger area to the ring-shaped region** reduces largely the NSB fake trigger, keeping most of the gamma-ray events.

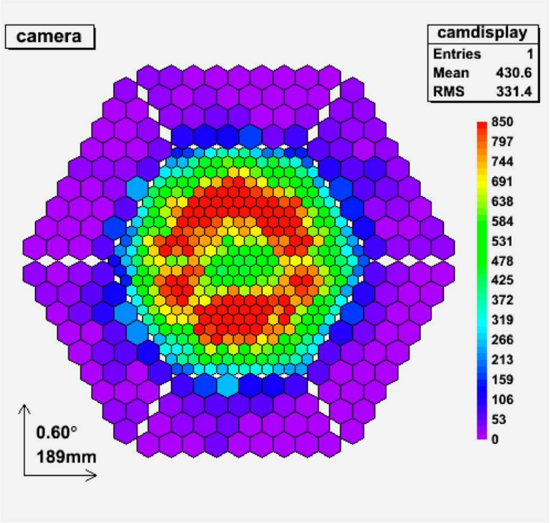

Figure 3.18: Cumulative photon distribution from images of gamma-rays between 10 and 40 GeV. A ring-like structure is seen which reflects the light pool (see Fig. 3.9)

These are the basic ideas behind the SUM trigger. However, there is an unfavorable feature of the detector which must be overcome to make the system work:

C) After-pulsing As shown in Fig 3.16, after-pulsing can create large signals. 150 MHz NSB with after-pulsing makes, for example, ~ 300Hz of pixel rates above 27 ph.e.

Feature C) is not a problem for the standard 4NN trigger because a possibility to have 4NN after-pulsing is very low. For the SUM trigger, however, it means wherever the addition is performed, the summed signal is larger than 27 ph.e. at a rate of more than 300 Hz, resulting in a total trigger rate of more than several kHz. The discriminator threshold must be much higher for the DAQ system to be able to record all the events, which makes the energy threshold even higher than the standard trigger. The solution of this problem is the clipping of the analogue signals before addition. By clipping the signal amplitude at a certain level, the contribution of the after-pulsing signal to the summed signal can be limited, although it affects the trigger efficiency of gamma-ray shower events.

The size of the summation area (18 pixels), the clipping level (6 ph.e.) and the discriminator threshold (27ph.e.) had been optimized by detailed MC studies taking into account construction feasibility (see [154]).

Sum Trigger Patches

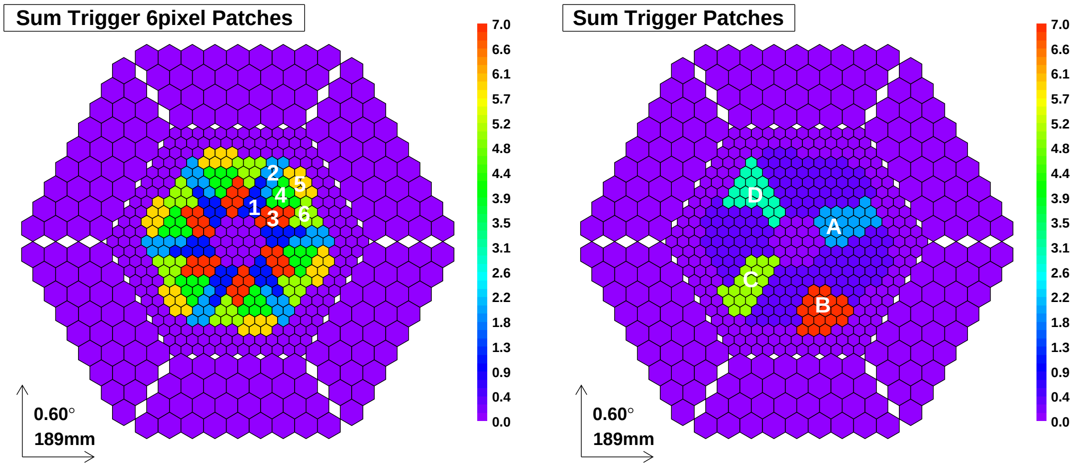

Figure 3.19: Left: 36 SUM Trigger subpatches. Each subpatch consists of 6 pixels. There are 6 different shapes. The trigger region should be compared with Fig. 3.18. Right: Examples of SUM Trigger patches. Each consists of 3 subpatches. There are 4 different shapes.

There are too many possibilities of neighboring 18-pixel areas and it is technically impossible to examine all of them. Therefore, the triggering takes place as follows: 36 subpatches consisting of six pixels are defined as shown in the left panel of Fig. 3.19. In order to fill up the trigger region, there are 6 different shapes. Three of the neighboring subpatches make up a 18-pixel sum trigger patch, as shown in the right panel of the figure. There are 4 different patch shapes: Patch type A is made from subpatch types 1,3,6; B from 2,4,5; C from 3,4,5 and D from 1,2,6. Each of subpatches participates in two patches and, thus, there are 24 of patches overlapping one another.

Hardware Overview of the System

The whole SUM trigger system is schematically shown in Fig. 3.20. First, signals entering to the SUM trigger system are clipped at 6 ph.e. level by clipping boards. The actual clipping is achieved by fast voltage limiting amplifiers (Texas Instrument: OPA 699), whose saturation voltage is adjustable and was set at 6 ph.e. level. Secondly, signals from every 6 pixels belonging to the same sub-patch are added up by summation board I. Then, three subpatch signals belonging to the same patch are added up by summation board II. Finally, outputs of the summation board II are fed into the discriminator with the threshold of 27 ph.e.. It should be noted that since one subpatch belongs to two different patches, subpatch signals are divided into two, each going to two different patch summations.

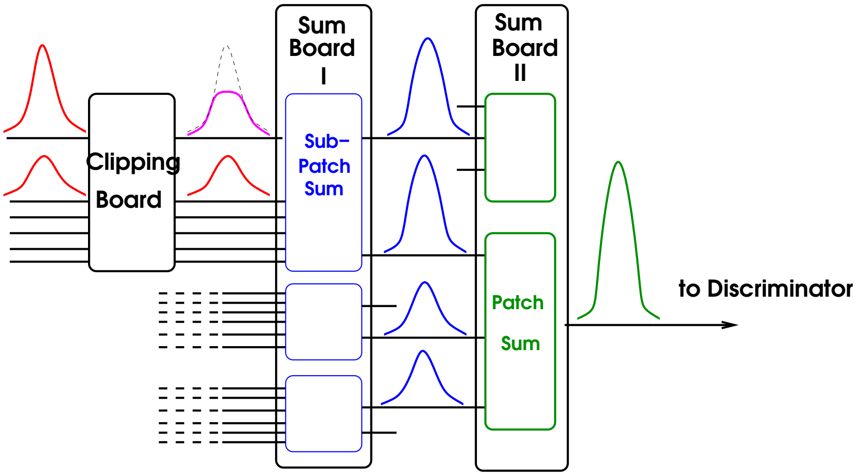

Figure 3.20: Schematics of the SUM trigger system. First, signal clipping is done. Then, signals from 6 pixels are added up in Summation board I to make a sub-patch signal. Three of the sub-patch signals are added up in Summation board II to make a patch signal, which goes to the discriminator. Two-stage addition simplifies the system because patches are overlapped, as shown in Fig. 3.19.

Comparison with the Standard Trigger

The gain of the SUM trigger with respect to the standard trigger is shown in Fig. 3.21. The left panel shows a energy distribution of triggered MC events. The gain is very remarkable at around 30 GeV. The peak of the distribution, which we normally call the threshold energy, is reduced from 50 GeV to 25-30 GeV. It should be noted that a primary energy spectrum with a power with an index of -2.6 was assumed for the MC, which is harder than the measured Crab pulsar spectrum, as will be shown later. Therefore, the peak energy of the Crab pulsar observations would be lower. The effective area is also calculated by means of MC. Below 30 GeV, which is essential for the Crab pulsar observations, the gain is a factor of more than 5. The importance of the SUM Trigger is schematically shown in Fig. 3.22.

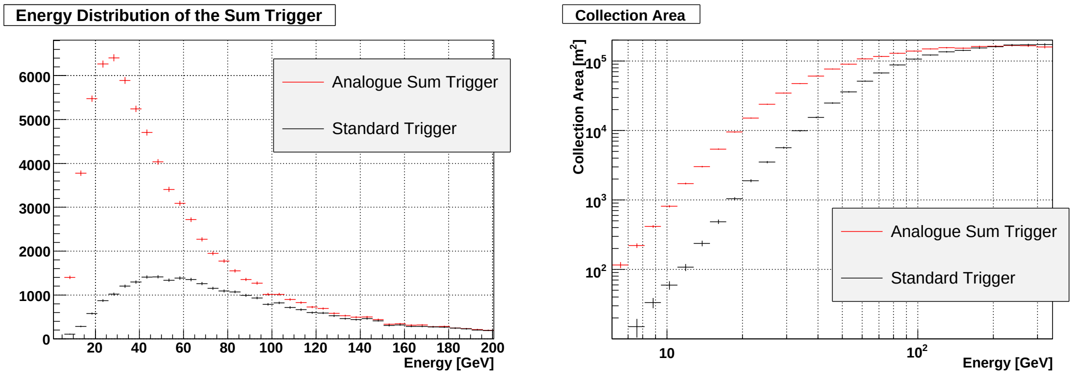

Figure 3.21: Comparison between the standard 4NN trigger and the SUM. Left) Energy distribution of triggered gamma-ray events produced by MC. Large improvement by the SUM trigger can be seen at low energies. A power law with an index of -2.6 was assumed for the gamma-ray spectrum Right: Collection area as a function of energy. Improvement amounts a factor of 5 at 30 GeV and a factor of 10 below 20 GeV.

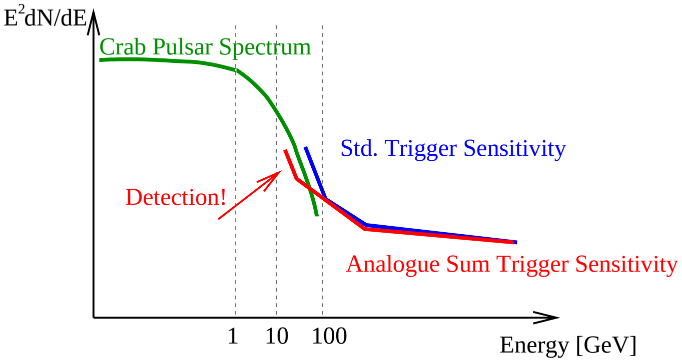

Figure 3.22: An illustration to show the importance of the SUM trigger for pulsar observations. The lowering of the threshold by the SUM trigger may make detection of the Crab pulsar possible.

3.4.8 Pyrometer

Figure 3.23: A photograph of the pyrometer adopted from [214]. It is installed at the edge of the reflector.

Most of the Cherenkov photons detected by IACTs are created at 10 to 20 km a.s.l, as described in Sect. 3.1.10. Clouds and semi-transparent haze are sometimes formed below this height and absorb Cherenkov photons strongly. We need to know whether or not our measurements are affected by the clouds or haze. It is very important for observations near the trigger threshold, which is the case for the Crab pulsar.

There is a Pyrometer installed at the edge of the reflector as shown in Fig 3.23. It measures the intensity of infrared radiation with frequencies between 8 and 14 micrometers, from which one can know the temperature of the sky. The FoV of the pyrometer is the same as for MAGIC. If there is a cloud or haze in the sky, the thermal radiation from the Earth's surface is reflected and, thus, the sky temperature gets higher. By using the sky temperature information provided by the pyrometer, a parameter called "$Cloudiness$" can be constructed. The basic concept of the calculation of $Cloudiness$ is as follows: The sky temperature with different zenith angles has been measured for many different nights, as shown in Fig. 3.24. The temperature varies depending on the sky condition but there is a lower limit at around 200 K, as indicated by a red dotted line in the figure, which should be the temperature of the sky without clouds or haze. When the sky temperature is at this limit, then $Cloudiness$ is assigned to be 0. When the temperature is higher than 280 K, which is as high as temperature on the ground, then $Cloudiness$ is thought to be 100%. $Cloudiness$ is computed between 0 and 100 linearly to the sky temperature between the lower limit and 280 K [3]. High quality data can be selected, based on $Cloudiness$. It should be noted that the pyrometer has a very limited power of determining the height of the clouds.

3.4.9 Central Pixel

The readout of the pixel at the camera center is specially designed for optical emission from a pulsar. Although the PMT itself is the same as the other inner pixels (ET 9116), it is not AC

---

[3] The effect of the humidity on the ground is also corrected empirically (see [220])

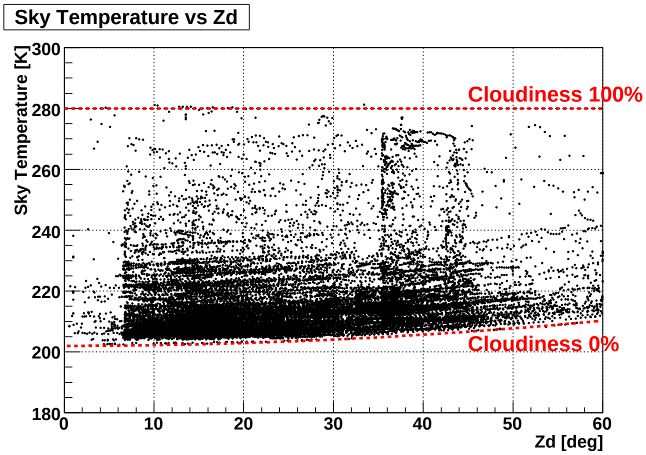

Figure 3.24: Measurements of the sky temperature with different zenith angles over many days. Data provided by J. Hose. A parameter "Cloudiness" is calculated based on this plot. The 0% and 100% cloudiness levels are indicated by red dotted lines

coupled and its DC current is read out by the DAQ system (see [120]). It does not contribute either a trigger or a shower image. When a trigger is issued the signal (current) of the central pixel is recorded by the FADC system without being multiplexed.

The information of the central pixel is very useful for Crab pulsar observations. It emits optical pulsation as well and the 236 m^2 area of the MAGIC reflector enables to detect it within 10 min. The time stamp of the data and the analysis chain for the ephemeris calculation can be checked with the optical pulsation, which will be described in Sect. 5.6.

3.4.10 Rubidium and GPS Clock

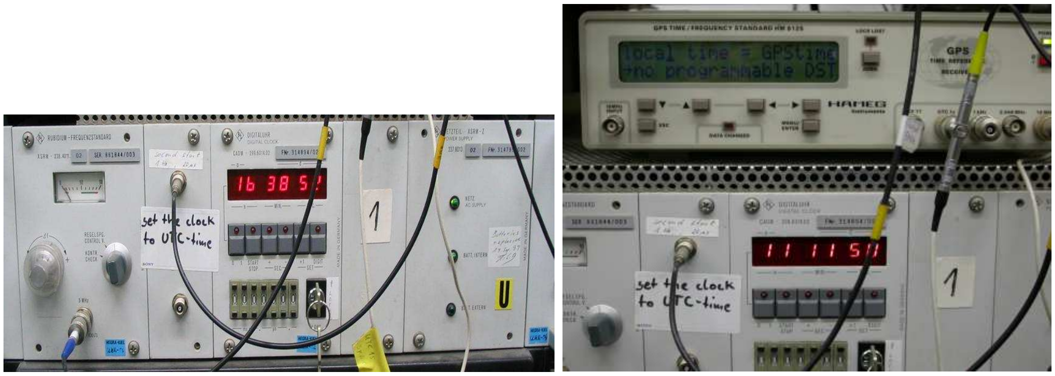

Figure 3.25: Left: A photograph of the rubidium clock, adopted from [214]. Right: A photograph of the GPS clock on top of the rubidium clock, adopted from [214].

In order to analyses pulsars, it is necessary to know for each event the time a) with a very high stability and b) with a high resolution. The time stamps of the events are generated based on the rubidium clock and the GPS clock in the counting house. The accuracy of the rubidium clock module is better than 1 microsecond for a short time scale (seconds). However, the clock drifts on a longer time scale (hours), making the precision less accurate. On the other hand, the GPS clock can generate the reference clock every second, which is very accurate for a long time scale. Therefore, the rubidium clock is synchronized with the GPS clock every second, which assures the precision of the time stamp to be better than 1 microsecond. It is good enough to detect pulsation and study the detailed pulse profile of the Crab pulsar, which has the period of $\sim$ 34 milliseconds.

3.4.11 Calibration Box for Calibrating the PMTs

There is a calibration box installed in the middle of the reflector, as shown in Fig. 3.4.11. It contains LEDs which illuminate the camera with fast light pulses of different intensity, different frequency and different wavelengths. There are also continuous light sources in four different colors to simulate star- and moon-light. A fast pulse of UV wavelength with FWHM of 2.5 ns is mainly used for signal calibration which will be described in Sect. 4.1.

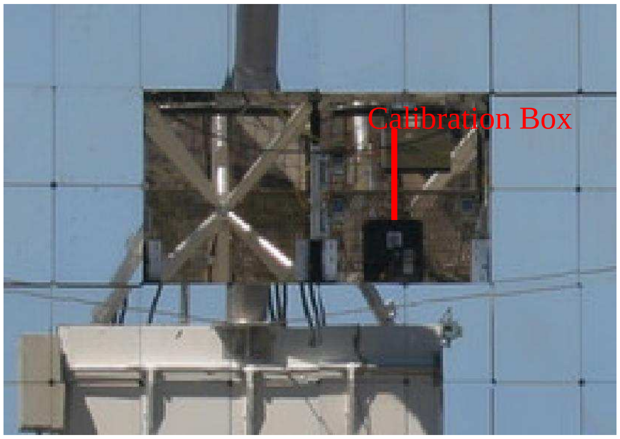

Figure 3.26: A photograph of the calibration box at the center of the reflector, adopted from [214].

3.4.12 Observation Mode

There are two types of observations, namely, ON-OFF mode and Wobble mode.

ON-OFF Mode

The telescope points to and track the source so that the source is always at the camera center. This is called the ON-mode. Additionally, OFF observations are made, pointing to a nearby sky area in which no source exists but in which the sky conditions and the declination is similar to the target source. [4] They will be used for the background estimation.

Wobble Mode

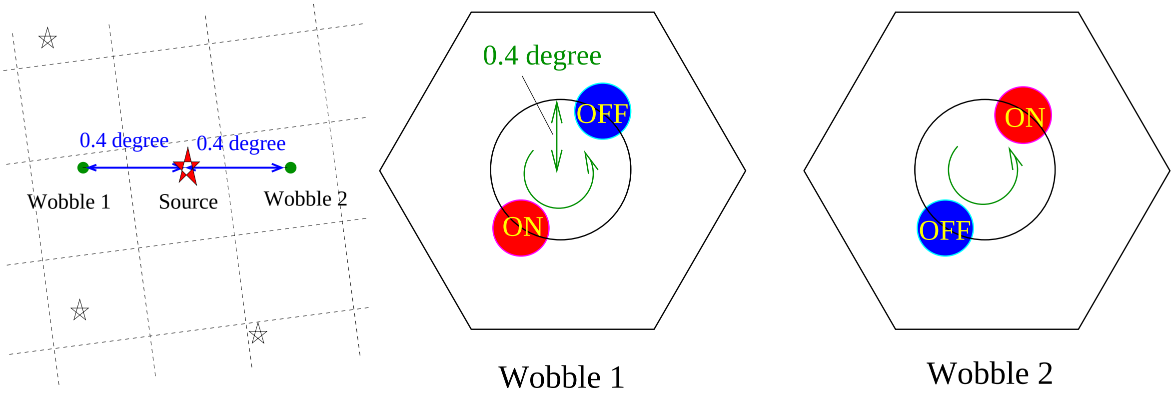

Figure 3.27: Wobble mode observation. The telescope points to two positions Wobble 1 and Wobble2, which are 0.4 degrees away from the source (left panel), wobbling between the two every 20 minutes. The source position rotates on the camera drawing a 0.4 degree radius circle. The background estimation for the Wobble 1 observation can be done with the Wobble 2 observation and vice versa (right panel).

For a target source, the telescope points to two directions, Wobble 1 and Wobble 2, wobbling between the two every 20 minutes. Wobble 1 and Wobble 2 are 0.4 degrees away from the target source and on opposite sides of it, as shown in the left panel of Fig. 3.27. Consequently, the source positions on the camera for Wobble 1 and Wobble 2 observations are 0.4 degrees away from the camera center and on opposite sides, as denoted by the red circles in the right panel of the figure. For each pointing (Wobble 1 and Wobble 2), the position opposite to the source in the camera is defined as “OFF source”, as denoted by the blue circles in the figure. The OFF source in Wobble 1 will be used for background estimation for Wobble 2 and vice versa. The camera performance is not perfectly uniform over the camera and that is why two pointing positions are required to reduce the systematic uncertainties for the background estimation. The advantage of the Wobble mode compared to the ON-OFF mode is that one can save observation time for independent OFF observations. In addition, it suppresses the systematic uncertainty caused by different ambient conditions between ON and OFF observations. For higher energy events, axial nonuniformity of the camera can be negligible. In that case, more OFF sources can be defined, such as 90 degree- and 270 degree-rotated positions with respect to the camera center, instead of only 180 degree rotation, which leads to a smaller statistical uncertainty of the background estimations. This is another advantage. The disadvantage is the reduction of camera acceptance by ~ 20 %.

---

[4] Two stars with the same declination make an identical orbit in the horizontal coordinate. Therefore, if ON and OFF pointing positions have the same declination, zenith and azimuth angle distribution would be the same, which reduces the systematic uncertainty in the background estimation

3.5 Concluding Remarks

IACTs have an effective area 10^4 times larger than that of satellite-borne detectors above tens of GeV and, thus, IACTs would be the best instruments for observing VHE gamma-ray sources. Among IACTs, the MAGIC telescope has the largest reflector area, which leads to the lowest energy threshold of 50 GeV with the standard trigger system. Moreover, the novel trigger system called SUM trigger system reduces the trigger threshold even further, down to 25 GeV. In addition to the sophisticated hardware components of the main telescope system, the subsystems such as the pyrometer, the central pixel, and the event timing system are also well designed for the pulsar observations. The MAGIC telescope would be the best detector for observing the Crab pulsar well above its cut-off energy, where very low intensity pulsed gamma-rays are expected.

Chapter 4

Analysis Method of MAGIC Data

Here I describe the methods and tools for the MAGIC data analysis. The primary goals of the analysis chain is 1) detection of gamma-ray signals, 2) calculations of the energy spectrum of the detected gamma-ray source and 3) producing a gamma-ray skymap. In the case of pulsar data, 4) production of a light curve is also important.

The standard MAGIC data analysis is done in the following sequence:

1. **Signal Calibration** The PMT signals recorded in FADC counts have to be converted into a number of equivalent photoelectrons. The arrival time of each signal is also estimated by subtracting the intrinsic relative time delay among the different channels. In the standard analysis chain, this is done by a program named Callisto.

2. **Image Cleaning** Not only Cherenkov photons from air showers but also NSB photons are recorded. By using the positional (directional) and timing information, most of the NSB photons can be removed from the images. In the standard analysis chain, this is done by a program named Star.

3. **Parameterization of Images** Each image is parametrized with about 10 parameters. This is also done by Star.

4. **Hadron/Gamma-ray Separation** The recorded images are dominated by cosmic-ray air shower events and they have to be rejected against gamma-ray shower candidates. This is done in the following way: The above three procedures (signal calibration, image cleaning and parameterization of images) are also applied to Monte Carlo (MC) gamma-ray events. Based on the difference of the image parameters between MC gamma-ray events and hadron events (observed data), a multi-dimensional hadron-gamma-ray discriminator is constructed by means of the Random Forest method. This is done by a program called Osteria. The constructed discriminator is applied to the observed data. This is done by a program named Melibea.

5. **Energy and Arrival Direction Reconstruction** From the MC gamma-ray events, the energy reconstructor and the arrival direction reconstructor based on multiple image parameters

are constructed by means of Random Forest method within Osteria. The application of these reconstructors to the data is done by Melibea.

5.1. Pulse Phase Calculation In the case of the pulsar data analysis, the pulse phase assignment for each event is done by a public program called *Tempo*. Based on the assigned phase, a pulsar light curve (phase diagram) is produced.

6. Signal Extraction A signal is extracted based on a parameter distribution ($ALPHA$ or θ, see Sect. 4.8). This can be done by a program named Fluxlc or by a simple program written by analyzers. In the case of pulsar observations, a light curve can be used for the signal extraction.

7. Energy Spectrum Calculation The energy spectrum of the detected gamma-ray sources are calculated by Fluxlc. The effect of the limited energy resolution is corrected by means of the unfolding procedure using a program called Unfold.

8. Skymap Production From the reconstructed arrival direction information, a gamma-ray skymap is produced by a program named Caspar.

For the Crab pulsar observations, because of the particular interest in the lowest energy below 50 GeV, special methods were used for the signal calibration and the image cleaning, as will be described in Sect. 4.1 and Sect. 4.2. The standard method for the rest of the procedures will be explained in Sect. 4.3 to Sect 4.10. The calibration method for the telescope reflector performance with muon events will be discussed in Sect. 4.11. Sect. 4.12 will describe the systematic uncertainties of the telescope system. Finally, concluding remark of this chapter will be given in Sect. 4.13.

4.1 Signal Calibration

The purposes of the signal calibration are 1) converting a signal recorded in FADC into a number of equivalent photoelectrons and 2) correcting the signal arrival time by subtracting the intrinsic readout time offset. In the standard analysis, Callisto is used for these signal calibration. The method and the performance of Callisto is described in [19]. For the Crab pulsar observations, a slightly different method was used in order to optimize the image cleaning for the lowest energy below 50 GeV. The major difference between this method and the one used in Callisto is the way how a signal is extracted from the FADC slices. Here I describe the method used for the Crab pulsar analysis.

4.1.1 Pedestal and Calibration Pulse Events

During data-taking, in addition to shower event triggers (the standard trigger or the SUM trigger) pedestal and calibration triggers are issued[1]. Pedestal triggers are issued periodically with a frequency of 25 Hz regardless of PMT signals. It is very unlikely that a shower image is recorded in a 25 ns FADC window when a pedestal trigger is issued while NSB contaminations are there. Thus, these events are used to estimate the pedestal of the FADC counts. The UV LED pulser in the calibration box illuminate the camera uniformly with a frequency of 25 Hz and calibration triggers are issued synchronously. The intensity of the LED pulser is stable at around the 30-40 ph.e. level. From these pedestal and calibration events, the conversion factors from FADC counts to the number of ph.e. and the relative time offsets for all pixels are calculated in ways described in the following sub-sections.

4.1.2 Conversion Factor

One data run contains 1 GB of data, which corresponds to a time duration of ~ 1 minute for the Crab pulsar observation with the SUM trigger. Since it contains ~ 1500 pedestal events, the pedestal of FADC counts for all the channels can be estimated with good precision. It also contains ~ 1500 calibration pulse events. The charge of the calibration pulse M [counts · slices] is calculated event by event by subtracting pedestals and summing up 20 slices around the pulse peak as shown in Fig. 4.1. Then, the mean value $\mu(M)$ and RMS $\sigma(M)$ of M are computed from the $\sim$ 1500 events [2]. From $\mu(M)$ and $\sigma(M)$, the conversion factor can be estimated by the so-called **F-factor method**, which is also used in the standard analysis tool, Callisto.

The F-factor method can be explained as follows: If the intensity of the LED pulser is constant, the number of photoelectrons N emitted from the PMT photocathode follows the Poisson statistics and, hence, $\sigma(N) = \sqrt{\mu(N)}$. If the gain of the PMT G defined as $G = M/N$ is always exactly the same, the resolution which is defined as $\sigma(X)^2/\mu(X)^2$ will be the same for M and N. Therefore, the mean number of photoelectrons $\mu(N)$ can be easily estimated from $\mu(M)$ and $\sigma(M)$ as,

$$\frac{\sigma(M)^2}{\mu(M)^2} = \frac{\sigma N^2}{\mu(N)^2} = \frac{1}{\mu(N)} \tag{4.1}$$

However, in reality, the gain of a PMT G is not identical for each photoelectron but fluctuates by a few percent. The resolution of M is diminished by the fluctuation of G;

$$\frac{\sigma(M)^2}{\mu(M)^2} = \frac{\sigma(N)^2}{\mu(N)^2} + \frac{\sigma(G)^2}{\mu(G)^2}\frac{1}{\mu(N)} \tag{4.2}$$

$$= \frac{1}{\mu(N)} + \frac{\sigma(G)^2}{\mu(G)^2}\frac{1}{\mu(N)} \tag{4.3}$$

---

[1] At the beginning of observations, special runs, i.e., a calibration and a pedestal runs are taken during which only calibration light pulses and pedestals are recorded. A pedestal run records 1024 events with a trigger frequency of 500 Hz. A calibration run records 4096 events with a trigger frequency of 500 Hz. They are not absolutely necessary and are not used for the Crab pulsar analysis.

[2] Contribution of the pedestal fluctuation is subtracted when $\sigma(M)$ is calculated.

The effect of the gain fluctuation on the resolution of M, i.e. the second term of the right hand side, is inversely proportional to the mean number of emitted photoelectrons (see [168]) because the fluctuation of the gain averaged over N photoelectrons decreases by $1/\sqrt{N}$. Defining the so-called F-factor F as

$$F \equiv \sqrt{1 + \frac{\sigma(G)^2}{\mu(G)^2}} \qquad (4.4)$$

From Eq. 4.3 and Eq. 4.4, $\mu(N)$ can be estimated as

$$\mu(N) = F^2 \frac{\mu(M)^2}{\sigma(M)^2} \qquad (4.5)$$

Thus, the conversion factor C from FADC counts M [counts $\cdot$ slices] to the number of photoelectrons N [ph.e.] can be obtained as $C = \mu(N)/\mu(M)$.

$\sigma(G)/\mu(G)$ (and thus, the F-factor) of a PMT can be experimentally measured by the charge distribution of single photoelectron pulses. Before installation in the MAGIC camera, the F-factors of some of the PMTs were measured in the laboratory. The average value of these PMTs was 1.15 and it is used for all pixels.

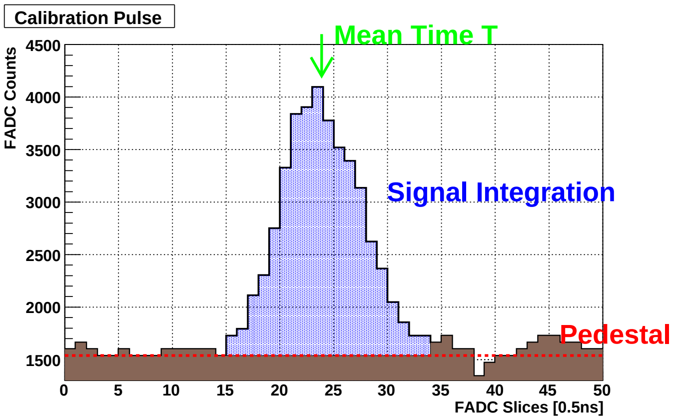

Figure 4.1: Signal extraction from the FADC slices. The brown shaded region indicates pedestal and the blue shaded indicates extracted signals. The green arrow shows the mean time of the signal.

4.1.3 Relative Timing Offset

For calibration events, the charge-weighted mean time is calculated as $T = \sum(q \cdot t)/\sum q$, where q and t are FADC counts and time, respectively. The summation is done over the 20 slices around the pulse peak. $\bar{T}$, which is the mean of T for the ~ 1500 calibration pulses, is used for correcting relative timing offsets caused by the transit time differences of different PMTs and by the readout chain. This is important for proper image cleaning and timing parameter calculation.

4.2 Image Cleaning

The rate of NSB photons from a dark sky is ~ 150 MHz per pixel (see Sect. 3.3.2 and 3.4.6). On average a PMT detects one NSB photon every 6 ns, which contaminates shower images. In order to exclude the NSB photons from images, image cleaning is applied. The method is based on the fact that Cherenkov photon signals are mostly clustered both spatially and temporally on the camera plane, while NSB signals are randomly distributed. In the standard analysis, the image cleaning is done by Star. Its method and performance are described in [23]. For the Crab pulsar observations, a more sophisticated method was used in order to optimize the image cleaning for the lowest energies below 50 GeV. Here, I describe this sophisticated method. This method was developed by M. Shayduk et al. and the basic idea and its performance are also described in [167].

4.2.1 Shower Core Search

In order to minimize the NSB contamination, charges of all pixels are calculated by integrating only 6 FADC slices around the pulse peak. Then, the core of an image is sought for over the camera. There are 3 types of core searches, 4 Next Neighbor (NN), 3NN and 2NN. They require n neighboring pixels with more than p ph.e. within a time window of t ns. For 4NN, 3NN and 2NN, (n,p,t) = (4, 2.0, 1.5), (3, 2.7, 0.8), (2, 4.7, 0.8), respectively. All the three conditions are applied to an image and pixels fulfilling any one of them are tagged as core pixels.

4.2.2 Boundary Search

Then, pixels which are not tagged as core pixels but neighboring to them are examined. If the number of photoelectron is more than 1.4 and the timing difference to the neighboring core pixel is less than 1 ns, they are tagged as boundary pixels.

4.2.3 Rejection of Pixels and Charge Recalculations

The charge of pixels tagged as either a core or a boundary are recalculated by integrating 20 slices around the peak, which is the same as for the calibration pulse charge. The charge of the other pixels are set to be 0.

4.2.4 Examples of Image Cleaning

Fig. 4.2 shows examples of image cleaning. Small $SIZE$ events are selectively shown in order to clearly illustrate the effect of the image cleaning. NSB photon contamination is clearly removed and the shower image is well restored. A sub-shower which may be produced by hadronic cascade is also restored (see the middle right panel of the figure). Sub-showers help to identify hadron events.

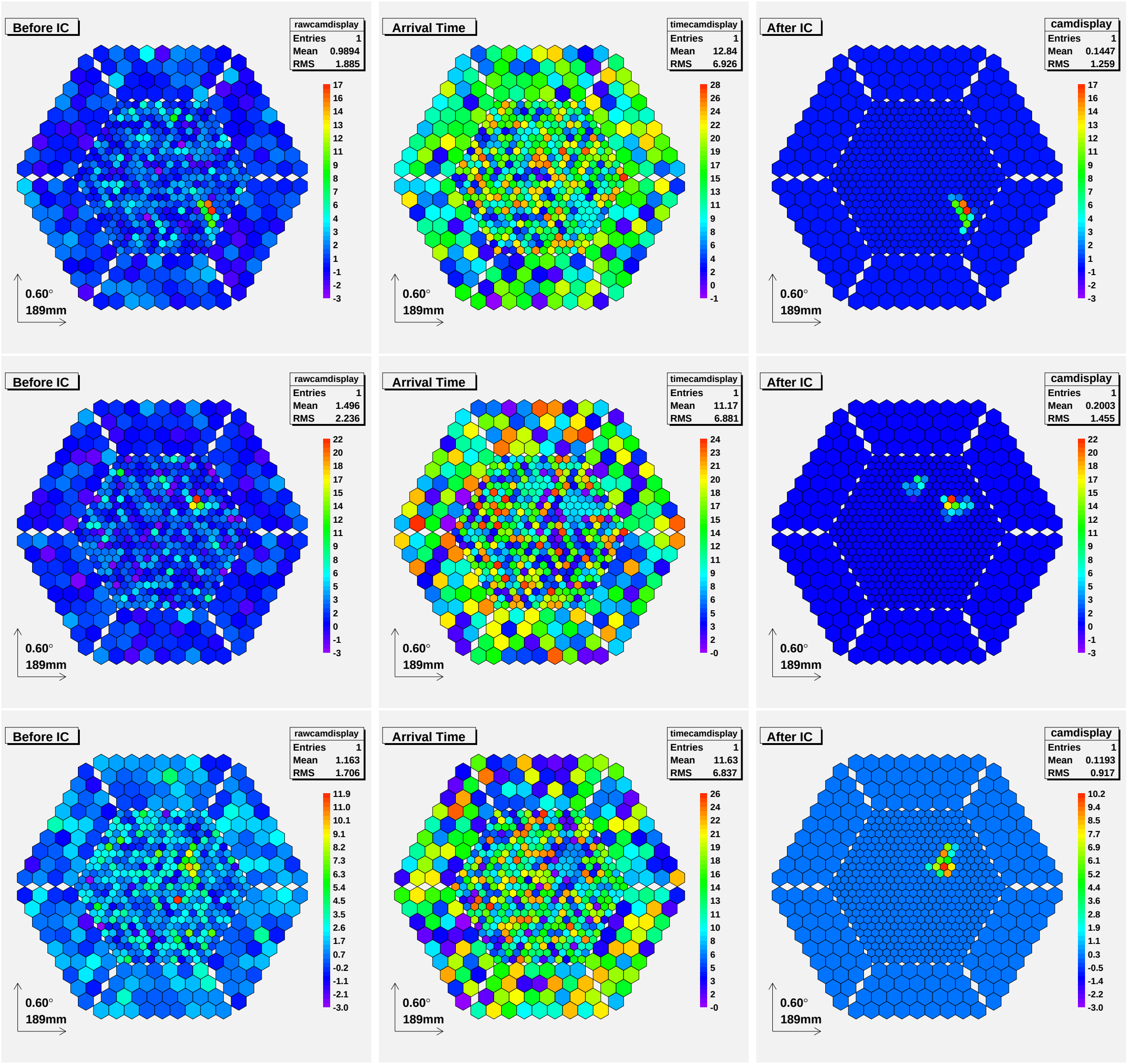

Figure 4.2: Examples of image cleaning for three small $SIZE$ events. The first and third columns show charge distributions over the camera before and after image cleaning, respectively. Colors indicate the pixel charge in ph.e.. The second column shows the distribution of arrival times of the signals. Colors indicate the signal arrival time in FADC slices (0.5 ns/slice). The first, second and third rows are a gamma-ray-like observed event, a hadron-like observed event, and a gamma-ray MC event, respectively.

4.3 Parameterization of Images

In order to process a huge number of events ($> 10^7$ events for the Crab pulsar observations), images are parameterized with about 10 parameters for further analysis. The parameters are calculated by a program named Star.

4.3.1 Example of Different Types of Images

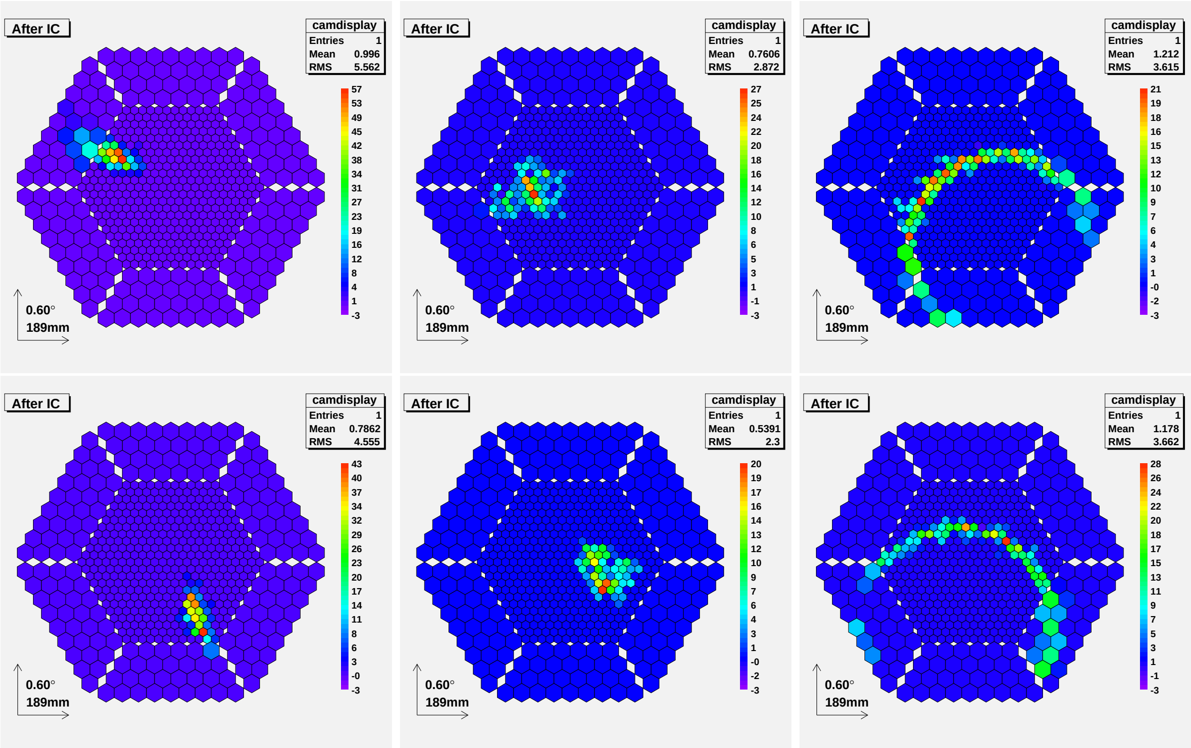

Figure 4.3: Examples of different types of images. Relatively large $SIZE$ events are chosen. The first row shows images from gamma-ray MC (left), proton MC (middle), and muon MC (right). The second row shows images from the data, gamma-like events (left), hadron-like events (middle) and muon-like events (right).

As shown in Fig. 4.3, different particles produce different types of images. A muon which hits or passes very close to the reflector produces a characteristic ring-like image, which will be explained in Sect. 4.11. Between hadron events and gamma-ray events, the clearest difference would be the ellipticity of the image, i.e. hadron events are more roundish. The concentration of the charge is also different. They are connected to the difference in the shower development (see Sect 3.1.8). There are also differences based on the fact that the gamma-rays come from the source (in most cases, it is point-like), while cosmic-rays come from any direction. The parameterization of the image is done such that these differences are well represented.

4.3.2 Parameterization of the Images

The major parameters are described below. Some of them are illustrated in Fig. 4.4. Originally, the concept of parameterization of the images was developed by M. Hillas and his coworkers (see [100]), aiming for discrimination between hadron-induced air shower images and gamma-ray-induced air shower images.

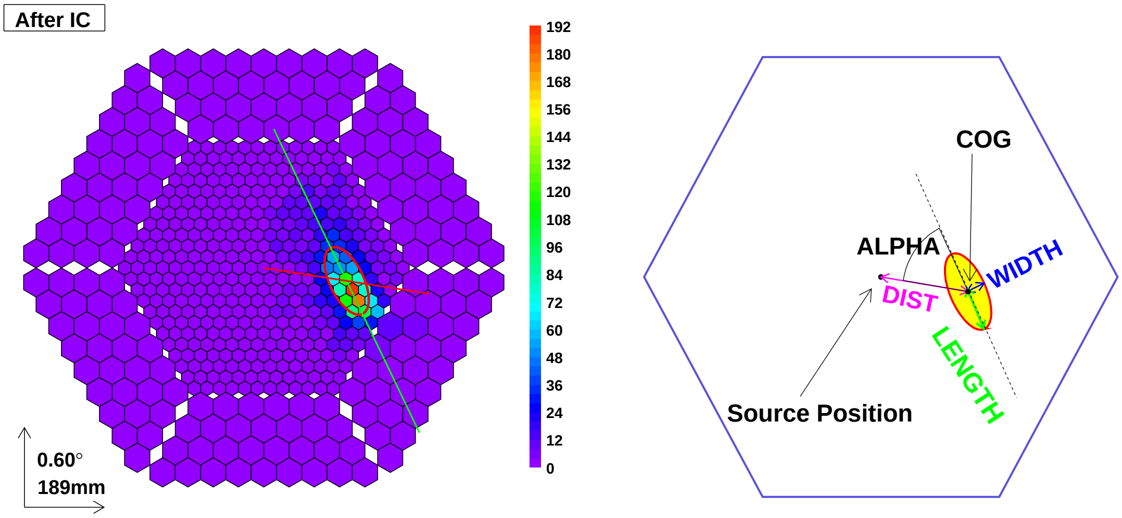

Figure 4.4: Some of major image parameters: $LENGTH$, $WIDTH$, COG, $DIST$, *and* $ALPHA$ *are shown.*

$SIZE$ The total charge contained in the cleaned image. This parameter is roughly proportional to the energy of the primary gamma-ray.

COG Center Of Gravity. The charge-weighted mean position of the image

$LENGTH$ The RMS of the charge distribution along the major axis of the image ellipse.

$WIDTH$ The RMS of the charge distribution along the minor axis of the image ellipse. $WIDTH$ is a powerful parameter to distinguish hadron-induced and gamma-ray-induced showers because of the difference in shower development described in Sect. 3.1.8.

$CONC$ The sum of the two largest pixel charges in the image divided by $SIZE$. It indicates the concentration of charges and helps to separate hadron events and gamma events.

$LEAKAGE$ The amount of charges contained in the two outermost rings of the camera divided by $SIZE$. It indicates the light content which was not recorded due to the limited FoV. Events with $LEAKAGE$ larger than 0.2 are normally discarded to ensure the validity of the image parameters.

$DIST$ The angular distance from COG to the source position on the camera. It is strongly linked to the impact distance between the shower and the telescope. Therefore, it is an important parameter for the energy and the arrival direction reconstruction of the primary gamma-rays.

$ALPHA$ The angle between the major axis of the image ellipse and the direction from COG to the source position in the camera. A small $ALPHA$ suggests that the shower comes from near the source direction.

$Time\ Gradient$ The gradient of the arrival time along the major axis. It is also a good parameter for estimating the impact distance (see [23]).

$Time\ RMS$ The RMS of the arrival time over the image. It helps to separate hadron events and gamma-ray events.

The derivation of these parameters from an image is described in [100], [196] and [23].

4.4 Hadron/Gamma-ray Separation

Because of the high flux of cosmic-rays, data of IACTs are usually dominated by hadron + muon background events. Even for observations of a strong VHE gamma-ray emitter such as the Crab nebula, the ratio between the gamma-ray signal and the background events in the data is $\sim 1/1000$. Although a cut in angular parameter such as $ALPHA$ improves the gamma-ray enrichment by a factor of ~ 10, it is still not easy to detect gamma-ray sources. Therefore, the discrimination of hadron + muon events from gamma-ray events must be done by extracting shower differences from the image parameters.

4.4.1 Differences in Image Parameters between Gamma-rays and Hadrons+Muons

Fig. 4.5 shows differences of the image parameters between the gamma-ray events and hadron + muon events. Red dots and points show the gamma-ray MC events while blue ones show events from the observed data, which are completely dominated by hadrons and muons. The top left panel of the figure shows $LENGTH$ as a function of $\log_{10}(SIZE)$. At $\log_{10}(SIZE) < 2$, no difference is visible, while at log10($SIZE$) ~ 2.5, a population of events with large $LENGTH$ is visible. This population can be explained by muon events. For arc-like images of muon events, $LENGTH$ becomes very large for a given $SIZE$ and most of them have a $\log_{10}(SIZE)$ of ~ 2.5. In addition to this muon branch, a further discrepancy is visible at $\log_{10}(SIZE) > 2.8$. This is due to the intrinsic difference between hadron events and gamma-ray events. Therefore, $LENGTH$ is a good parameter for gamma-ray/(hadron + muon) discrimination at $\log_{10}(SIZE) > 2$. The same behavior is seen in $WIDTH$ vs $\log_{10}(SIZE)$ plot in the top right panel of the figure. $WIDTH$ is also a good parameter for the discrimination at $\log_{10}(SIZE) > 2$. It should be noted that at $\log_{10}(SIZE) > 2.8$, where the intrinsic differences between gamma-ray and hadron images are shown, the $LENGTH/WIDTH$ ratio is larger for gamma-rays than for hadrons. This is reflecting the difference in the transverse spread of the air showers, as discussed in Sect. 3.1.8. The middle left panel shows distribution of $CONC$. Gamma-rays are relatively more concentrated. This is attributed to the differences in the transverse spread and the disorder of the air showers, as discussed in 3.1.8. $CONC$ is also useful for the discrimination. The middle right panel shows $Time\ Gradient$ as a function of $DIST$. Since gamma-rays come only from the source, $DIST$ is correlated with the impact parameter (see Fig. 4.10). On the other hand, $Time\ Gradient$ is also correlated with the impact parameter (see [23]). Therefore, the correlation between $Time\ Gradient$ and $DIST$ can be seen, which is not the case for hadrons and muons. The combination of $Time\ Gradient$ and $DIST$ helps to discriminate between gamma-ray events and hadron + muon events. The bottom left panel shows $Time\ RMS$ as a function of $\log_{10}(SIZE)$. At $\log_{10}(SIZE) < 2$ and at $\log_{10}(SIZE) > 2.8$, data show larger $Time\ RMS$ than for gamma-ray MC. This can mainly be explained by the hadron component, for which a larger $Time\ RMS$ is expected due to the disorder of the hadron-induced air showers (see Sect. 3.1.8). On the other hand, at $\log_{10}(SIZE) \sim 2.5$, data show a smaller $Time\ RMS$ than for gamma-ray MC. This can be attributed to the muon component, for which a smaller $Time\ RMS$ is anticipated because all the detected Cherenkov photons originate from a single particle. The ratio between the hadron component and the muon component is different at different $SIZE$s, as can be seen in, e.g., the $LENGTH$ vs $\log_{10}(SIZE)$ relation. $Time\ RMS$ is helpful for the discrimination mainly at $\log_{10}(SIZE) > 2.8$. The bottom right panel shows $ALPHA$ as a function of $\log_{10}(SIZE)$. A clear difference is seen, as can be understood by the definition of $ALPHA$.

At $\log_{10}(SIZE) < 2.5$, since the difference in each parameter (except $ALPHA$) is not very large, a simple cut in any one of the parameters does not significantly increase the signal-noise ratio. A combination of many parameters is necessary to improve the telescope sensitivity for such small $SIZE$s. Even for larger $SIZE$s, the best background rejection would be achieved by making use of differences in many parameters. Therefore, in the standard MAGIC analysis, the multi-dimensional (hadron+muon)/gamma-ray separation is applied for all $SIZE$s, based on the Random Forest method with many image parameters (see the next sub-section).

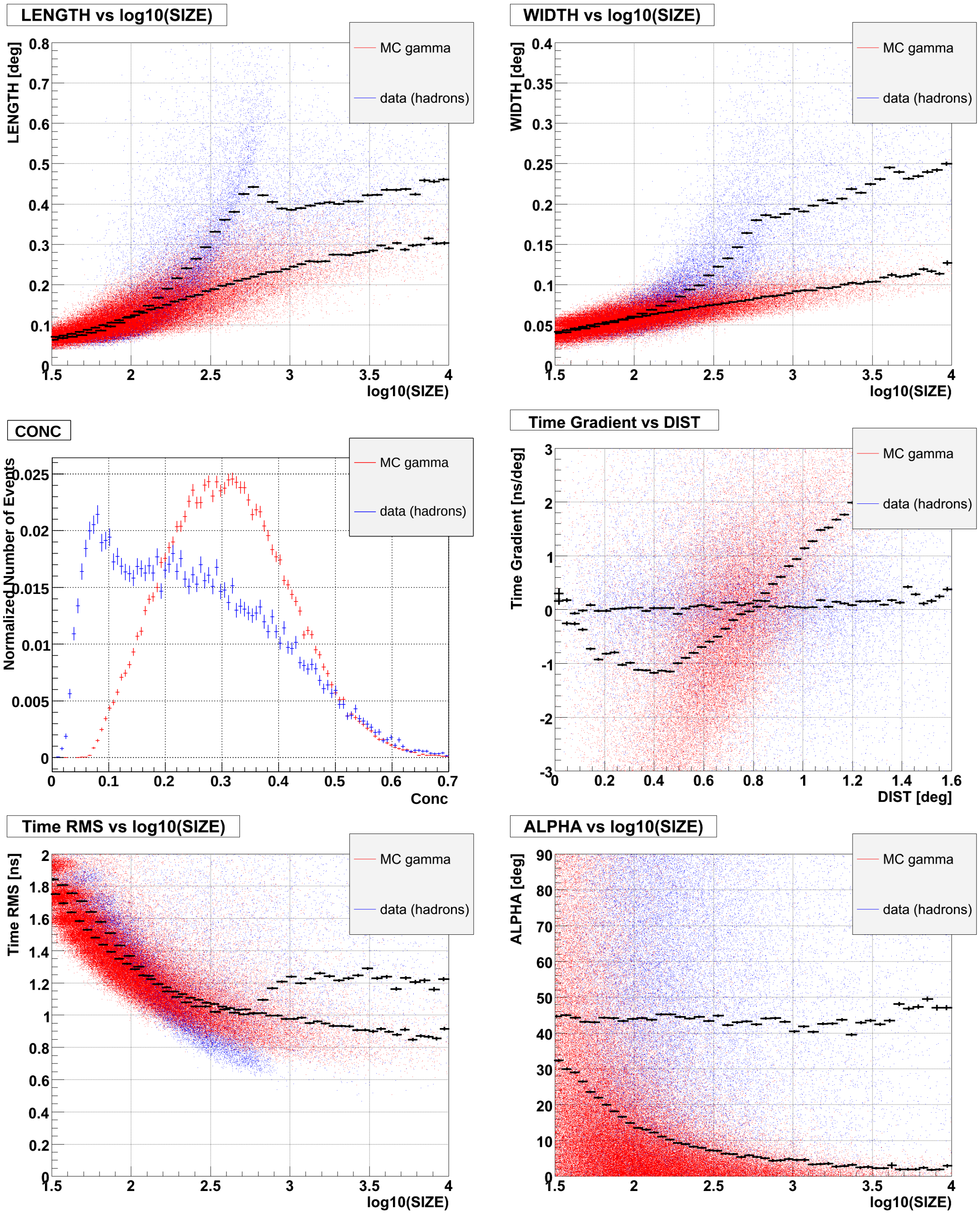

Figure 4.5: Differences of the image parameters between gamma-rays MC (red dots) and hadron + muons (blue dots). Black points show the mean values of the vertical axis parameters for each horizontal axis bins. Top left: LENGTH vs log$_{10}(SIZE)$*. Top right: WIDTH vs log*$_{10}(SIZE)$*. Middle left: Distribution of CONC. Middle right: Time Gradient vs DIST. Bottom left: Time RMS vs log*$_{10}(SIZE)$ *Bottom right: Alpha RMS vs log*$_{10}(SIZE)$

4.4.2 Random Forest Method

The details of the method and the application to the MAGIC analysis is well described in [48], [46] and [97]. Here I will describe the basic procedure. In this section, “hadron events” include the muon events as well.

First Step: Random Forest Generation

Firstly, the hadron-gamma classification trees are generated. Osteria is used for this. The generation procedure of a tree is schematically shown in the left panel of Fig. 4.6.

1. Gamma-ray and hadron event samples are prepared (S_g and S_h). Since the observation data themselves are dominated by hadron events, a part of them are used as hadron samples, while gamma-ray samples are produced by MC.

2. Several parameters to be used for the gamma/hadron separation, such as $WIDTH$, $LENGTH$, $CONC$ and $TimeGradient$ are chosen.

3. One parameter is randomly chosen from the separation parameters. S_g (S_h) is split into S_g^L and S_g^R (S_h^L and S_h^R) by the chosen parameter at the value which minimizes the Gini index Q_{Gini} defined as

   $$Q_{Gini} = 2\left(\frac{\#S_g^L \cdot \#S_h^L}{\#S_g^L + \#S_h^L} + \frac{\#S_g^R \cdot \#S_h^R}{\#S_g^R + \#S_h^R}\right) \tag{4.6}$$

   where $\#S$ is the number of events in a sample S. Each term of Eq. 4.6 indicates the impurity of the event class (hadron or gamma-ray) for each divided sample (S^L and S^R)

4. The next parameter is chosen randomly from the separation parameters. $Left$ branch (S_g^L and S_h^L) and $Right$ branch (S_g^R and S_h^R) are further split by it in the same way as process 3. This “branching” continues until the number of samples at the end of the branch is very small (normally 3) or occupied by only one class (gamma-rays or hadrons). In this way, one classification tree is produced.

5. Each end of the branches is assigned a value $\tilde{h}$, which is $\#S_h^{end}/(\#S_h^{end} + \#S_g^{end})$, where S^{end} is the sample at the end of the branch. $\tilde{h}$ indicates the purity of hadrons at the end of the branch.

6. Many (normally 100) of the classification trees are produced by repeating the above process from 2 to 5. Since branching parameters are always randomly chosen, they are not identical. The name of the method “Random Forest” comes from the fact that there are many trees produced with randomly chosen branching (separation) parameters.

Second Step: Application to the Data

Now, the produced trees are applied to each observed event. This is done by Melibea. Application of one tree to one event is illustrated in the right panel of Fig. 4.6.

1. One tree is applied to one event. According to the image parameters, the event reaches one end of a tree and obtains the value $\tilde{h}$.

2. The process 1 is done with all the trees and $Hadronness$ is calculated as

$$Hadronness = \sum_{i=1}^{N} \tilde{h}_i / N \tag{4.7}$$

   where N is the number of trees and $\tilde{h}_i$ is $\tilde{h}$ from ith tree.

As can be deduced from the definition of $\tilde{h}$, $Hadronness$ is the measure of the likelihood that the event is a hadron, ranging from 0 to 1. $Hadronness$ can also be calculated for gamma ray events generated by MC. The distributions of $Hadroness$ for gamma-ray events and data (dominate by hadrons) are compared in Fig 4.7. $SIZE$, $LENGTH$, $WIDTH$, $CONC$ and $DIST$ were used as the separation parameter for this figure. One can clearly see that for $\log_{10}(SIZE)$ $>$2.5 ($SIZE > 300$), the Random Forest method recognizes well gamma-ray events as such. Selection of events with $Hadronness$, for example below 0.1, can reject ~ 95% of the hadron background events keeping ~ 85% of the gamma-ray signal events. $SIZE$ above 300 corresponds roughly to primary gamma-ray energies above 200 GeV, which is too high for the Crab pulsar. $SIZE$ range below 100 is essential for it but separation is almost powerless. Therefore, in order to avoid additional systematic errors, $Hadroness$ is not used for the Crab pulsar analysis, whereas it is used for the nebula analysis.

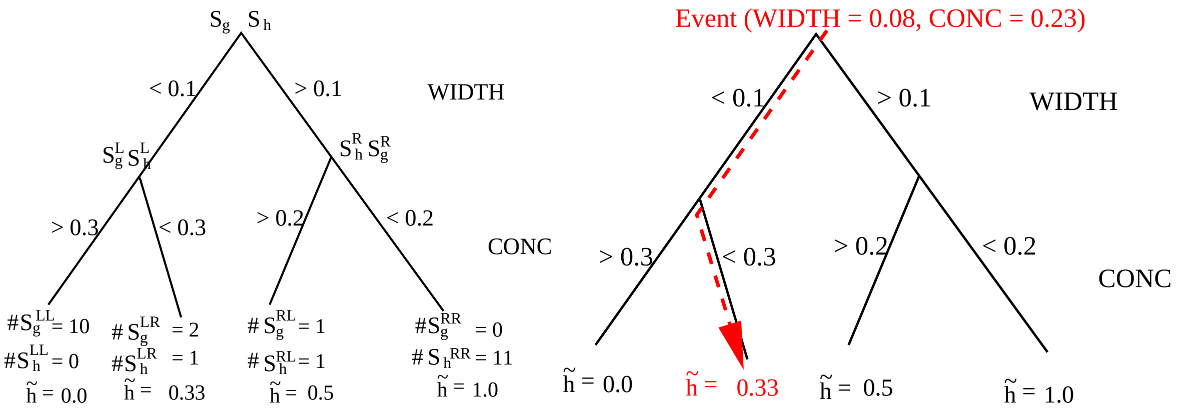

Figure 4.6: Left: A simplified example of the classification tree. WIDTH and CONC are used for the separation. For the first branching, WIDTH is used. The best separation value that minimizes the Gini index defined by Eq. 4.6 is 0.1. For the second branching, CONC is used. The best separation value is 0.3 and 0.2 for S^L and S^R, respectively. The branching stops here because the samples either are dominated by the same class or contain too few events. Then, $\tilde{h}$ is calculated for each end. Right: Application of the tree to the data. Since the event has WIDTH = 0.08 and CONC = 0.23, the tree assigns $\tilde{h} = 0.33$ for it. Many (normally 100) different trees are applied to the event and Hadronness for the event is the average of multiple $\tilde{h}$'s.

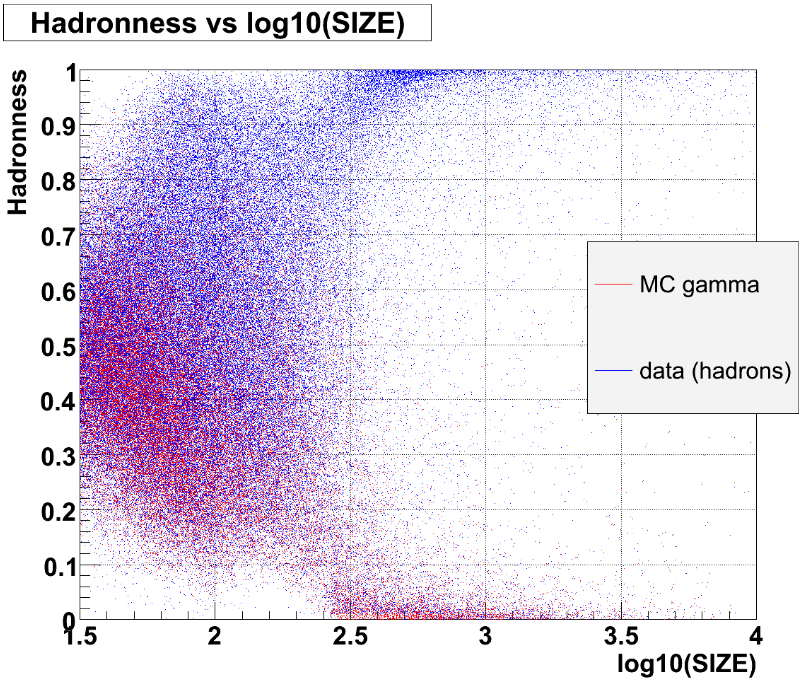

Figure 4.7: Hadronness distribution as a function of $\log_{10}(SIZE)$. Red dots and blue dots indicate MC gamma-ray events and hadron + muon events from the observed data, respectively. The separation is very good at $\log_{10}(SIZE) >\sim 2.5$ (SIZE $>\sim 300$) but it gets worse for smaller SIZE. This can be understood by the distribution of individual image parameters shown in Fig. 4.5.

4.5 Energy Reconstruction

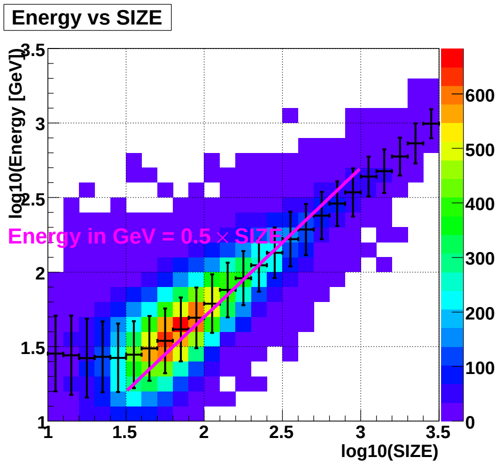

Figure 4.8: The relation between the MC gamma-ray energy and $SIZE$*. It can be roughly approximated to be Energy (in GeV) = 0.5 ×* $SIZE$ *for* $\log_{10}(SIZE) > 1.5$*. For* $\log_{10}(SIZE) < 1.5$*, this relation is not valid because of the trigger threshold and shower fluctuation. At energies below 30 GeV (*$\log_{10}(Energy[GeV]) < 1.5$*), only events with a large positive fluctuation in* $SIZE$ *are triggered (see also Fig. 4.9 and associated explanation.).*

$SIZE$ (total charge in a shower image) is a good parameter to estimate the energy as shown in Fig. 4.8. However, as discussed in Sect. 3.2.3, the $SIZE$-energy relation depends on the impact parameter. The pointing zenith angle also plays a role. Therefore, the combination of several image parameters and the zenith angle improves the energy resolution. In the MAGIC standard analysis, the Random Forest method is used also for the primary energy reconstruction. The programs used for this are Osteria and Melibea.

The procedure is almost the same as for $Hadronness$ computations except:

- Only gamma-ray samples S_g are used. They are generated by MC and, thus, energies are known.

- The Gini index is defined as

$$Q_{Gini} = \frac{1}{\#S^L + \#S^R}(\#S^L \sigma_L^2(E) + \#S^R \sigma_R^2(E)) \tag{4.8}$$

  where $\sigma(E)$ is the RMS of the energy distribution in a sample. The minimal Q_{Gini} means the minimum of the sum of two RMSs weighted by the sample size.

- $\tilde{h}$ is the mean energy of the sample at the end of a branch.

For the pulsar analysis, the energy will be reconstructed with image parameters $SIZE$, $LENGTH$, $DIST$, and the zenith angle of the source. $WIDTH$ and $CONC$, which are normally used, are excluded because they are sensitive to the point spread function (PSF) of the reflector especially when an image size is small ($SIZE < 100$). The precision of the PSF is assured to be better than 10% by muon calibration (see Sect. 4.11) but it could still cause a difference in $CONC$ and $WIDTH$ between data and MC, leading to a systematic error in energy reconstruction. On the other hand, $CONC$ and $WIDTH$ do not improve the energy resolution significantly for such small $SIZE$ events.

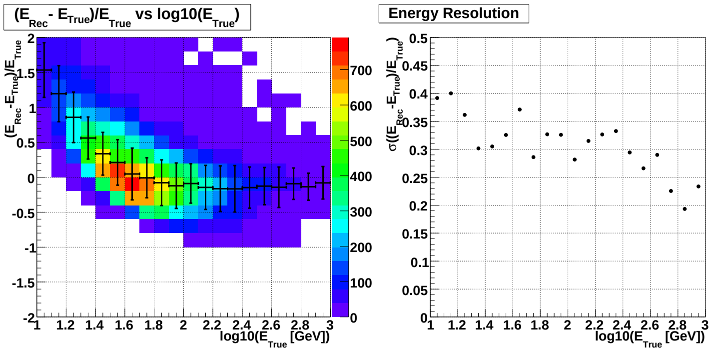

Figure 4.9: Left: The relation between the relative error of the energy reconstruction defined as $(E_{Rec} - E_{True})/E_{True}$ *and* $\log_{10}(E_{True})$*, where* E_{Rec} *and* E_{True} *are reconstructed energy and true (MC) energy. Middle: The energy resolution as a function of* $\log_{10}(E_{True})$*. Here, the energy resolution is defined as the RMS of the relative error. Right: The energy bias as a function of* $\log_{10}(E_{True})$*. Here, the energy bias is defined as the mean of the relative error.*

The energy resolution and the reconstruction bias for the pulsar analysis are shown in Fig. 4.9. The left panel of the figure shows the relation between the relative error of the energy reconstruction defined as $(E_{Rec} - E_{True})/E_{True}$ and $\log_{10}(E_{True})$, where E_{Rec} and E_{True} are reconstructed energy and true (MC) energy. In the middle panel of the figure, the energy resolution defined as the RMS the relative error is shown. The energy resolutions at 30 GeV and at 1 TeV are about 35% and about 20%, respectively. The energy reconstruction bias defined as the mean of the relative error is shown in the right panel. Below 40 GeV ($\log_{10}(E_{True}) < 1.6$), a large upward bias is seen. This is explained by the trigger bias effect and the shower fluctuation, i.e. for such low energy showers, events with a large positive fluctuated in $SIZE$ are triggered. When the energy spectrum is calculated, this bias is taken into account by the unfolding procedure (see Sect. 4.9.3).

4.6 Arrival Direction Reconstruction

As shown in the left panel of Fig. 4.10, the major axis of an image defines a plane in which the air shower axis is contained. If there are multiple telescopes, the arrival direction of the primary gamma-ray can be deduced by the crossing of planes determined by different telescopes. In the case where an image is recorded only by a single telescope, the inclination angle of the shower axis in the plane must be deduced by image parameters. In the MAGIC standard analysis, it is expressed as the $DISP$ parameter, which is the angular distance from COG to reconstructed arrival direction, as shown in the right panel of the figure.

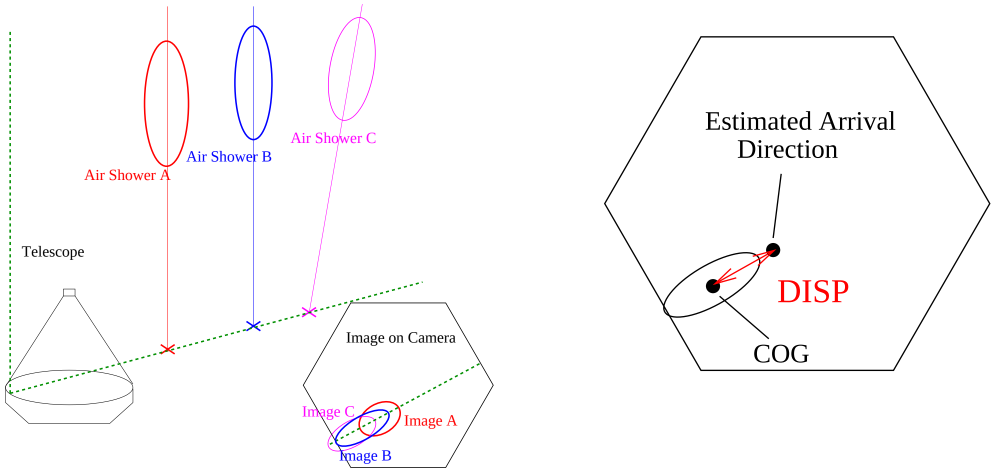

Figure 4.10: Left: The different showers whose axes are contained in the same plane. The major axis of these images is identical, as shown in the camera (a hexagon on the bottom). Right: The definition of DISP. DISP is useful to distinguish the arrival direction of the three showers shown in the left panel.

$DISP$ is strongly connected to the impact parameter, as shown in Fig. 4.11. On the other hand, the $LENGTH$-$WIDTH$ ratio is also connected to the impact parameter, as shown schematically in Fig. 4.10. Therefore, the old standard way of reconstructing $DISP$ was a following parameterization:

$$DISP = A(SIZE) + B(SIZE) \cdot \frac{WIDTH}{LENGTH + \eta(SIZE) \cdot LEAKAGE} \tag{4.9}$$

where $A(SIZE)$, $B(SIZE)$ and $\eta(SIZE)$ are a function of $SIZE$ and optimized by means of MC (see [67]). However, even though $LEAKAGE$ is taken into account, the $DISP$ reconstruction was not very precise when $LEAKAGE$ is big (> 0.1) (see [159]). In addition, $Time\ Gradient$ is a very good parameter for the impact parameter estimation but it is not easy to include it in the above equation. Therefore, together with J. Sitarek, I developed a new method to reconstruct $DISP$ by means of the Random Forest method. The method is the same as the energy reconstruction described in the previous section. It improves the angular resolution by 20-30% (see [159]). The programs used for it are Osteria and Melibea.

4.7 Pulse Phase Calculation

Because of the movement of the Earth around the Sun, the periodicity of a pulsar will show up in the event trigger time based on the rubidium and the GPS clock (see Sect. 3.4.10). In order to see the pulsation, first of all, the conversion from the trigger time to barycentric time is needed. It is done by the public and widely used program *Tempo* [218]. In addition to the time-dependent positional relation among the Earth, a pulsar and the Sun, it takes into account the “Shapiro delay” (see [165]) which is the delay in arriving time of a signal caused by the gravity of the sun.

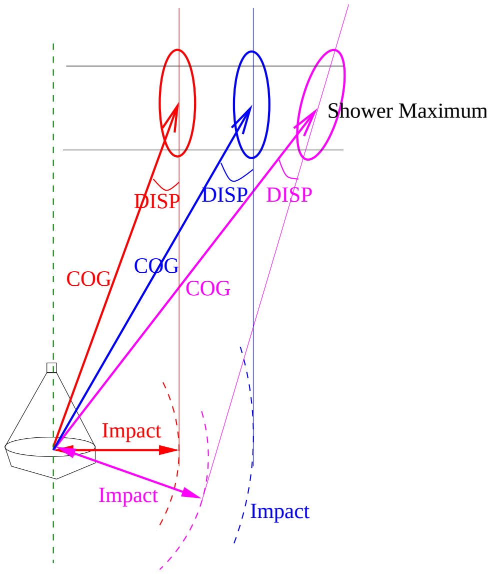

Figure 4.11: The relation between DISP and the impact parameter. The impact parameter helps to determine the direction of the shower axis.

Once the barycentric correction is done, the pulse phase can be calculated by using the precise pulsar period information obtained by lower energy bands, normally radio observation. In the case of the Crab pulsar, the barycentric time of a main pulse (P1) peak t_0, the rotation frequency ν, its first and second time derivatives $\dot{\nu}$ and $\ddot{\nu}$ at t_0 are monitored by a 12.5 m radio (610 MHz) telescope at Jodrell Bank [121]. The values are publicly reported once in a month in the "Jodrell Bank Crab Pulsar Monthly Ephemeris" [213] . This monthly monitoring is essential for young pulsars like the Crab Pulsar, because pulsar glitches occur from time to time (once in a few years in the case of the Crab pulsar), which cause discontinuous changes in these parameters (see Sect. 2.4).

With these parameters, the pulsar phase ϕ can be computed as

$$\phi(t) = \nu_0(t - t_0) + \frac{1}{2}\dot{\nu}_0(t - t_0)^2 + O(\ddot{\nu}_0) \tag{4.10}$$

where, t is barycentric time. The second and higher derivative terms of this Taylor series are negligible.

4.8 Signal Extraction

Since gamma-ray / hadron separation is not perfect, even after the separation, background must be estimated in one of the following ways.

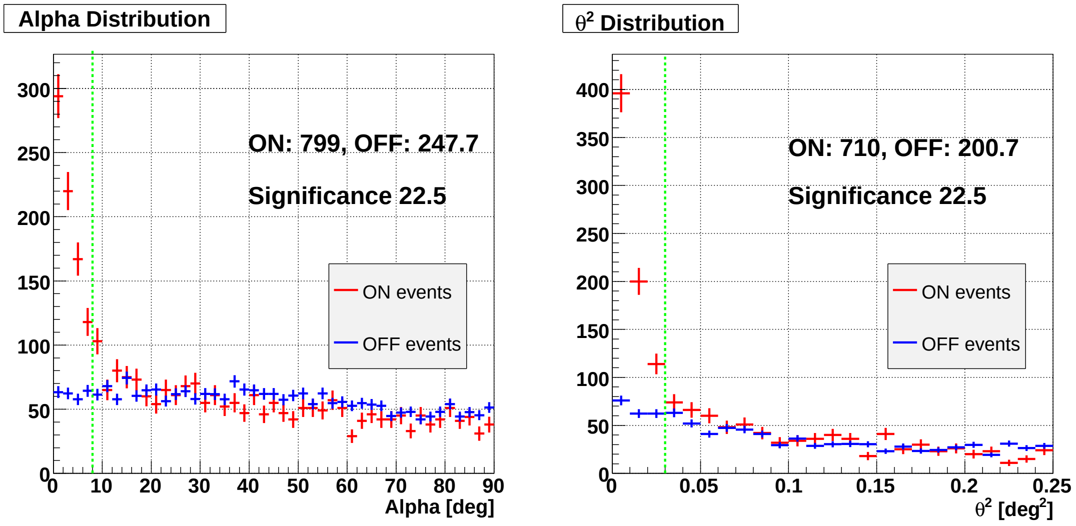

Figure 4.12: The gamma-ray signal from the Crab nebula for 1.0 hours of Wobble mode observations. Events with $SIZE > 200$ *and* $Hadronness < 0.1$ *are used. Background estimation is done with three OFF sources. Left: Alpha distribution. Signal region is defined as* $ALPHA < 8$*. The small discrepancy seen at* $ALPHA \sim 45$ *degree is due to the signals contributing to OFF sources, which does not affect the background estimation. Right:* θ^2 *distribution. Signal region is defined as* $\theta^2 A < 0.03$ *deg*^{2}.

.

4.8.1 By Using the $ALPHA$ Distribution

By definition (see Fig. 4.4), images of air showers coming from the source direction should have an $ALPHA \sim 0$. Therefore, if the source is a gamma-ray emitter, $ALPHA$ distribution should have a peak near $ALPHA = 0$ as shown in the left panel of Fig. 4.12. Because of the image resolution, the peak has a certain width. In the figure, $ALPHA < 8^\circ$ is defined as a signal region (the green dotted line in the figure). One way of estimating the number of background events in the signal region is using off-signal region of the distribution (e.g. $ALPHA > 20^\circ$), i.e. fitting a simple function to it and extrapolating to the signal region. Another way is using OFF observations, which is the standard way and is used for the figure. In the case of ON-OFF mode observations (see Sect. 3.4.12), $ALPHA$ distribution of the independent OFF observation is used, for which $ALPHA$ is calculated with respect to the tracking position where no source exists. In general, observation times of ON and OFF are different. The normalization of the two distributions is done by the off-signal region (e.g. $ALPHA > 20^\circ$), which reflect the observation time difference. In the case of Wobble mode (see Sect. 3.4.12), ON and OFF observations are simultaneously carried out and $ALPHA$ distributions with respect to the OFF source positions are used for the background estimation. Normalization is done by the geometrical factor, i.e. if only one OFF region is used, the normalization factor is one, while if three are used, the factor is 1/3. In the left panel of Fig. 4.12, data taken in the wobble mode was used and the background estimation was made using three OFF positions.

4.8.2 By Using the θ^2 Distribution

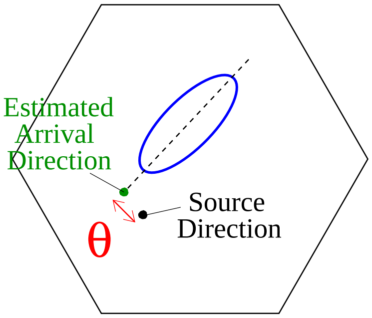

Figure 4.13: Definition of the parameter θ. It is the angular distance between the source direction and estimated arrival direction of the event.

.

Signal extraction can also be done by the reconstructed arrival direction distribution (see Sect. 4.6). This is done from the θ^2 distribution. θ is defined as the angular distance between the reconstructed arrival direction and the source direction, as shown in Fig. 4.13 (see also Fig. 4.10). For a geometrical reason, θ^2 becomes flatter than θ and that is why normally θ^2 is used as shown in the right panel of Fig. 4.12. In the figure, the signal region is defined as $\theta^2 < 0.03$ (the green dotted line in the figure). As in the $ALPHA$ case, the background estimation for the signal region can be made either by extrapolation from the off-signal region (e.g. $\theta^2 > 0.05$) or from OFF observations.

4.8.3 By Using the Pulsar Light Curve

Only in the case of pulsar observations, can a light curve be used for signal extraction, as shown in Fig. 4.14. From light curves in other energy band, pulse phases and off-pulse phases can be known a priori [3]. By estimating the background from the off-pulse phases, signals are extracted from the pulse phases.

It should be noted that, in the case of signal extraction based on a $ALPHA$ distribution or a θ^2 distribution, a possible mismatch between ON and OFF may occur due to different star fields, camera inhomogeneity or change in environmental conditions, especially in low energy regions. This mismatch causes a systematic error in background estimation and, hence, can be a problem especially for a weak source, for which the signal-to-noise ratio is very small. On the other hand, in the case of signal extraction based on a pulsar light curve, a systematic error in background estimation can be caused only by a rapid change in environmental conditions on a time scale of the pulsation period (34 ms for the Crab pulsar), which is hard to imagine. Therefore, the background estimation by using the pulsar light curve is much more robust than by using the $ALPHA$ or θ^2 distribution. Even if signal-to-noise ratio is very small ($< 10^{-2}$), a low energy signal from a pulsar can be detected, which may not be the case for other types of sources.

---

[3] For pulsars whose peak phases vary largely depending on energies, the light curve from the closest energy region should be used.

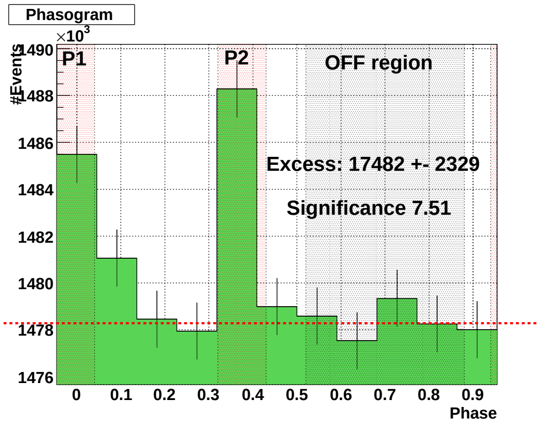

Figure 4.14: Extraction of the signal from a pulsar light curve. Pulse phases and off-pulse phases are defined by other energy ranges and background is estimated by using the off-pulse phase region.

.

4.8.4 Evaluation of Statistical Significance for an Extracted Signal

The statistical significance of the signal is calculated by the following equation (see [119]):

$$S = \sqrt{2}\left(N_{ON}\ln\left[\frac{1+\alpha}{alpha}\left(\frac{N_{ON}}{N_{ON}+N_{OFF}}\right)\right] + N_{OFF}\ln\left[(1+\alpha)\left(\frac{N_{OFF}}{N_{ON}+N_{OFF}}\right)\right]\right)^{1/2} \tag{4.11}$$

In the case of the $ALPHA$ or θ^2 approach (see Sect. 4.8.1 and Sect. 4.8.2), N_{ON} and N_{OFF} are the numbers of events in a signal region for ON and OFF observations, respectively. In the case of the light curve approach (see Sect. 4.8.3), N_{ON} and N_{OFF} are the numbers of events in pulse phases and in off-pulse phases, respectively. α is the normalization factor between ON and OFF distributions (the $ALPHA$ or θ^2 approach) or the ratio of the widths between pulse phases and off-pulse phases (the light curve approach). The equation is commonly used for the significance estimate in many physics experiments.

4.9 Energy Spectrum Calculation

In order to determine the energy spectrum of a gamma-ray source from observational data, one has to know the effective gamma-ray detection area of the observations, the observation time and the number of excess events in different energies. This is done by Fluxlc in the standard analysis.

4.9.1 Effective Area Calculation

The effective area $A_{eff}^{i,j}$ for an energy bin i, and zenith bin j is calculated by MC as $A_{eff}^{i,j} = A_{gen}^{i,j} \times N_{det}^{i,j}/N_{gen}^{i,j}$, where A_{gen}, N_{det} and N_{gen} are the area where MC gamma-rays are uniformly generated , the number of events which are detected and passed all the cuts and the number of generated MC events, respectively. The MC gamma-rays are generated uniformly in a circular area with an radius of 500 m around the telescope. The detection efficiency of a gamma-ray outside this area is $\simeq 0$. The effective area of the observation in an energy bin i is calculated as $A^i_{eff} = \sum_j w_j \cdot A^{i,j}_{eff}$, where w_j is the weight of a zenith angle bin j, which is proportional to the number of observed events in the zenith angle bin j after all the selection cuts.

4.9.2 Observation Time Calculation

The event detection is a random process in time. If the probability to detect an event in a unit time is p, the number of events detected in a time interval u follows the Poisson statistics: $Poi(n, pu) = e^{-pu} \cdot (pu)^n/n!$. Therefore, the probability that no event is detected in u is $P(u) = Poi(0, pu) = e^{-pu}$. The distribution of the time difference dt between successive events should follow the exponential function $P(\mathrm{d}t)$. By fitting an exponential function $Ae^{-dt/\tau}$ to the observed dt distribution gives an estimate of $\tau = 1/p$, which corresponds to the average value of the time needed to detect one event. The total number of events N_{all} multiplied by τ is the total observation time. Fig. 4.15 shows an example of the observation time calculation.

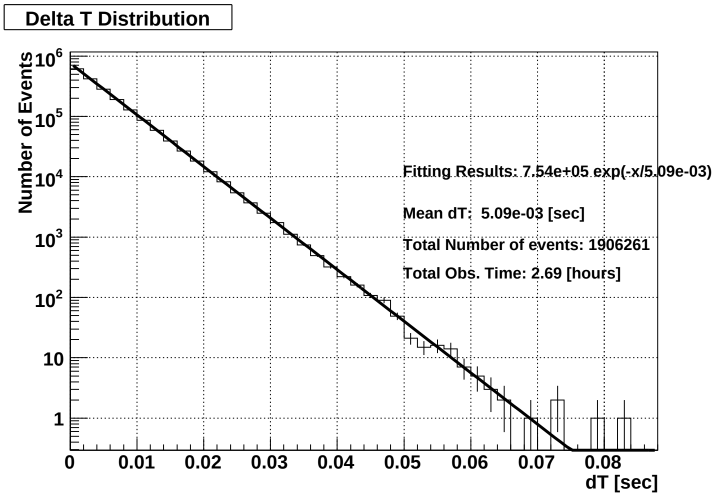

Figure 4.15: Distribution of the time difference between the successive events. It shows an exponential behavior, as explained in the text. The total number of events N_{all} is 1.91×10^6 and fitting an exponential function $Ae^{-dT/\tau}$ to the distribution gives $\tau = 5.09 \times 10^{-3}$ [s]. The effective observation time is $N_{all} \times \tau = 2.69$ hours.

4.9.3 The Number of Excess Events for Each Energy Bin

The number of excess events in the reconstructed energy bins can be obtained in the way described in Sect. 4.8. However, because of the limited energy resolution and a bias effect especially near the threshold energy (see Fig. 4.9), the excess distribution in reconstructed energy does not represent the true energy distribution of the signals. The true energy distribution must be inferred by reconstructed energy distribution by means of the unfolding method, taking into account the detector response.

Let us consider a reconstructed energy histogram of signals with a bins and a corresponding true energy histogram with b bins. A vector Y with a elements and a vector S with b elements can be defined, whose elements correspond to the number of event in each bin of these histograms. Then, the vector Y and S have a relation

$$Y = M \cdot S \quad \text{or} \quad Y_i = \sum_{j=1}^{b} M_{i,j} \cdot S_j \tag{4.12}$$

where Y_i and S_j are the ith element of Y and the jth element of S and $M_{i,j}$ is the (i,j) element of the migration matrix M. M can be calculated by MC. From the measured S, Y must be deduced based on Eq. 4.12, taking into account the statistical errors of the measurement. Even if inversion of M is possible, the solution

$$S = M^{-1} \cdot Y \tag{4.13}$$

results in large statistical errors of S due to the non-diagonal matrix M , which indicates correlation among elements of S. In order to reduce the large errors, a procedure called *regularization* is applied, which imposes additional constraints on S. The regularization can be viewed as as a smearing of the unfolded distribution with some finite resolution, which reduces the statistical correlations between the adjacent elements of S at the expense that S is no longer an unbiased estimate of the true energy distribution (see [163]). Technically, application of the regularization is as follows: χ^2 is defined as

$$\chi^2 = \frac{w}{2} \cdot \chi_0^2 + Reg(S) \tag{4.14}$$

where χ_0^2 is a normal χ square value between Y and $M \cdot S$, while $Reg(S)$ is the regularization term. w indicates the strength of the regularization, i.e. the smaller the w, the stronger the regularization. There are various options to choose the optimal w and in the MAGIC standard analysis w is chosen such that the error of S is comparable to that of Y [4]. There are also several different ways for determining the regularization term $Reg(S)$, such as the $Tikhonov$ method (see [181]), the $Bertero$ method (see [42]) and the $Schmelling$ method (see [162]). In the $Tikhonov$ method, for example, the regularization term is defined as

$$Reg(S) = \sum_{j=1}^{b} \left(\frac{d^2\tilde{S}}{dE^2} \right)_j^2 \tag{4.15}$$

where $\tilde{S}$ is the true energy distribution from which S is made. In the MAGIC software, the second derivative of $\tilde{S}$ is approximately calculated as

$$\left(\frac{d^2\tilde{S}}{dE^2} \right)_j^2 = 2.0 \cdot \left(\frac{S_{j+1} - S_j}{S_{j+1} + S_j} - \frac{S_j - S_{j-1}}{S_j + S_{j-1}} \right) \tag{4.16}$$

---

[4] More precisely w is chosen such that $Trace(K) = Trace(T)$, where K and T are covariance matrices of S and Y.

This $Reg(S)$ implies the stability of the slope of $\tilde{S}$, i.e. smoothness of the true energy distribution.

There is another way of estimating S with reasonable statistical error without using the regularization, which is called the *forward unfolding* By assuming a spectral shape a priori with several parameters (such as a power law aE^{-b}), the best parameters (a and b) that minimize the χ_0^2 (between Y and $M \cdot S$) can be found. As long as the assumption of the spectral shape is valid, the forward unfolding provides the most robust results. Moreover, it does not require a choice of w or the regularization method. Therefore, the forward unfolding is a very useful check for the reliability of other methods.

4.10 Sky Map

From the reconstructed arrival direction of the gamma-ray events, a skymap can be produced. Background estimation is done by using OFF observations (which means off-source analysis in the case of wobble mode observations). In the standard analysis, the program Caspar is used for it. Fig. 4.16 shows the skymap of the Crab nebula produced by Caspar. Events with $SIZE > 300$ and $Hadronness < 0.2$ are used. In order to produce a skymap for the Crab pulsar, the emission from the nebula must be subtracted. This function is not yet implemented in Caspar.

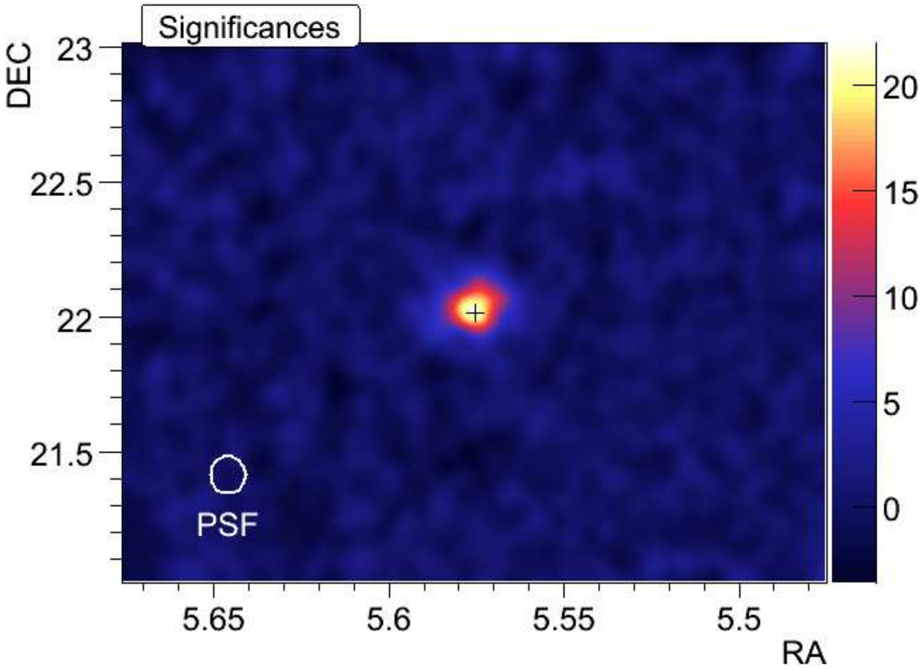

Figure 4.16: A skymap around the Crab nebula produced from 1.0 hour of wobble-mode observations. Colors indicate the statistical significance of the excess. Events with $SIZE > 300$ and $Hadronness < 0.2$ are used. Corresponding gamma-ray energies are above ~ 200 GeV. Position of the source is indicated by a cross.

4.11 Reflector Performance Calibration with Muon events

The conversion from the FADC counts to the number of detected photoelectrons can be done by the F-factor calibration method (Sect. 4.1.2). However, in order to estimate the air shower properties from the recorded image, one has to know the light collection efficiency and the focusing accuracy (PSF) of the reflector to the camera. Since the light correction efficiency and the PSF may change slightly in time because of, for example, imperfect individual mirror alignment caused by gravity (3.4.2), they must be monitored during the observations.

The monitoring can be done by using muon events. As described in Sect 3.1.7, muons produced by hadron showers can reach the ground without being scattered too much. The Cherenkov threshold of a muon below 5 km a.s.l. is around 5 GeV (Sect. 3.2.1). If a muon with an energy above 5 GeV hits or passes near the telescope reflector from a direction less than ~ 2 degree off the telescope axis, it can deposit enough photons to generate a trigger and an image on the camera. If the impact parameter of the particle is small enough, say, less than 20 m, a muon creates an arc-like or ring-like image on the camera, as schematically shown in Fig. 4.17.

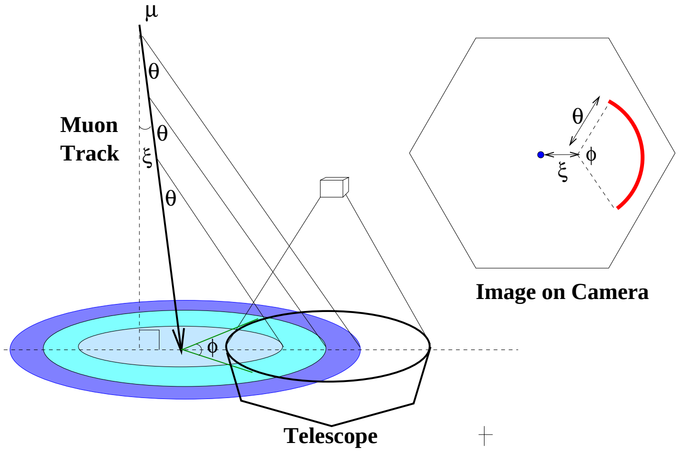

Figure 4.17: Cherenkov photon emission from a muon and a created image on the camera. The emission angle θ, the arrival direction ξ and the azimuthal angle range ϕ appear in the image.

The center of the arc/ring corresponds to the arrival direction of the muon and the radius corresponds to the Cherenkov angle. By collecting arc/ring-like images with an angle of arc larger than, for example, 90 degrees, the PSF and the light collection efficiency can be examined in the following ways.

PSF

Muon image parameters, $Radius$ and $ArcWidth$, are defined as shown in Fig. 4.18. A typical PSF of the MAGIC reflector is ~ 0.04 degrees and $ArcWidth$ is about ~ 0.05 degrees after convolution with the PSF. Therefore, $ArcWidth$ is very sensitive to changes in the PSF. ArcWidth is determined mainly by three physical processes on top of the PSF. First, along the track of a muon

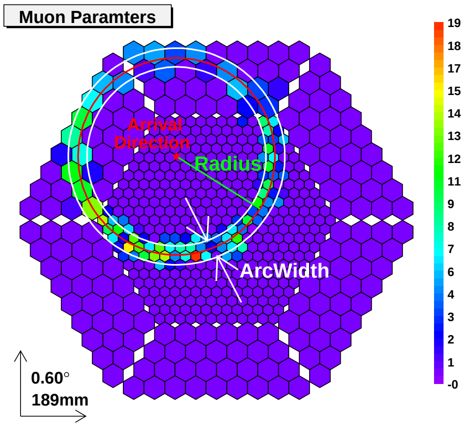

Figure 4.18: Definitions of some of the muon parameters. Radius, ArcWidth and arrival direction are shown. They are useful to estimate the reflector PSF and light collection efficiency.

through the atmosphere, the refractive index changes, resulting in change of the Cherenkov angle. Secondly, multiple scattering changes the direction of the muons slightly. Thirdly, the energy loss by ionization during the track causes a change of the Cherenkov angle. A muon loses ~ 100 MeV by ionization during the last 1000 m above the telescope. The relative divergence of the angles of the arriving Cherenkov photons caused by these three processes becomes smaller as the Cherenkov angle increases. Therefore, as the $Radius$ increases, $ArcWidth/Radius$ decreases, as shown in Fig. 4.19. The same analysis is applied to muon MC samples (see right panel of Fig. 4.19). By changing the detector PSF in the MC and comparing the $ArcWidth/Radius$ vs $Radius$ relation with observed data, the telescope PSF can be estimated. It should be noted that in order to avoid the effect of the aberration (see 3.4.2) and the larger pixel sizes (see 3.4.3), the $ArcWidth$ is calculated by a part of the arc recorded in the inner part of the camera. Since a 10% difference of the PSF significantly changes the relation, the PSF can be estimated with precision of better than 10 %.

Light Collection Efficiency

As is easily seen from Fig. 4.17, the center of the arc/ring and $Radius$ indicates the incoming direction of the muon and its energy, respectively. In addition, the charge distribution along the arc shows the impact parameter of the muon which can be understood by looking at the left panel of Fig. 4.20. The charge at an arc-angle Ψ is proportional to D in the figure. D can be expressed as

$$D(\Psi) = 2R\sqrt{1-(\rho/R)^2\sin^2\Psi} \qquad (\rho/R \geq 1) \tag{4.17}$$

$$D(\Psi) = R\sqrt{1-(\rho/R)^2\sin^2\Psi} + \rho\cos\Psi \qquad (\rho/R \leq 1) \tag{4.18}$$

where R and ρ are the radius of the reflector and the impact parameter of the muon (see the left panel of Fig. 4.20.). $D(\Psi)$ for different ρ/R is shown in the right panel of Fig. 4.20. From the recorded image, the energy, the arrival direction and the impact parameter of the muon can be

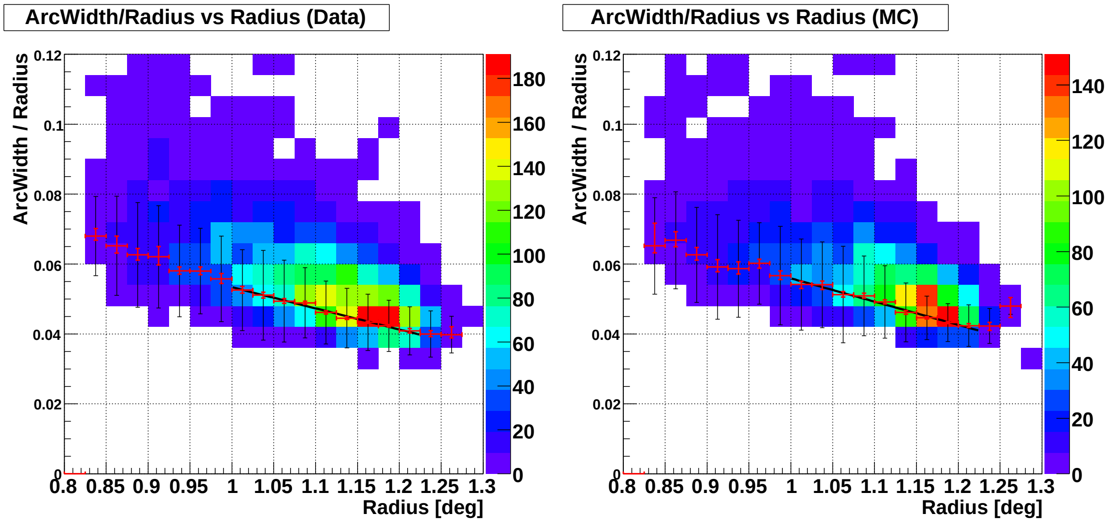

Figure 4.19: ArcWidth divided by Radius as a function of Radius. Data (left) and MC with PSF 0.032 degrees (right) are compared. The PSF of data is estimated to be 0.032 degrees from this plot. 10% difference of the PSF makes a significant difference in this relation.

determined. Therefore, from this information, the number of Cherenkov photons which should hit the reflector can be estimated. By comparing the number of the detected photoelectrons and that of the estimated photons hitting the reflector, the light collection efficiency can be deduced.

This method is very useful to monitor the reflector light collection efficiency, which may change during long term observations. On top of that, the biggest advantage of this method is that one can calibrate the absolute conversion from FADC counts to the number of Cherenkov photons hitting the reflector. The convoluted uncertainty from the mirror reflectivity, transmission of the Plexiglas at the entrance of the camera, the light guide efficiency of the Winston cones (see Sect. 3.4.3), the QE of PMTs and the accuracy of the F-factor method (see Sect. 4.1.2) can be calibrated with muon events. On the other hand, the Cherenkov photons in these ring-like images are produced within $\simeq 1$ km above the telescope. Therefore, ring-like muon events cannot be used for, e.g. the transmission calibration of the atmosphere because most of Cherenkov photons from air showers come from much higher altitude (see Sect. 3.1.10).

4.12 Systematic Uncertainties

It is not possible to calibrate MAGIC with a test beam to estimate the systematic uncertainties. Therefore, the systematic uncertainties are estimated by examining the uncertainty of each hardware component and the observational conditions. I will only discuss the major contributions and ignore uncertainties of less than 2%. This is justified because major factors can be so large that any $1-2\%$ contribution is minimal. Major factors which affect the systematic uncertainty especially for the Crab pulsar observations are the following:

Atmospheric model Atmospheric density and height distribution have a seasonal variation,

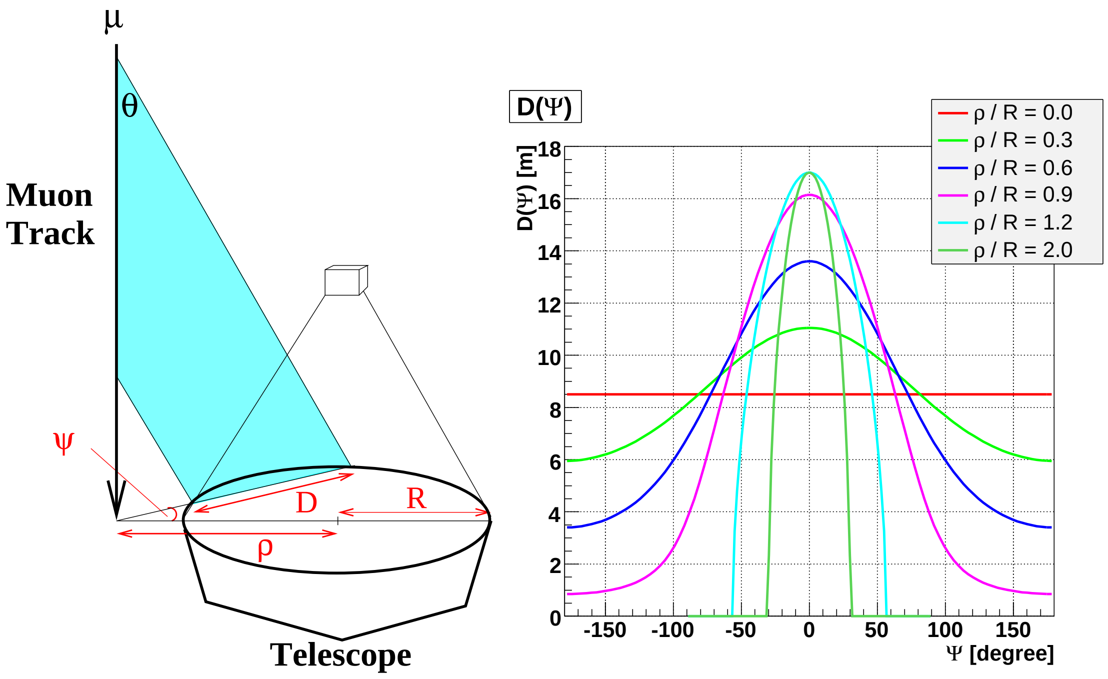

Figure 4.20: The relation between azimuthal angle ψ and crossing length D. Depending on the impact parameter ρ, $D(\psi)$ shows different behavior. For the image in the camera, ψ and $D(\psi)$ corresponds to the arc-angle and the charge. From $D(\psi)$ and ψ on the image, ρ can be estimated.

which leads to a variation in Cherenkov photon yield and transmission to the ground. The difference of the amount of Cherenkov photons reaching on the ground between summer and winter is estimated to be $\sim 15\%$ (see [41]). Since all the Crab pulsar observations were done between the end of October to the beginning of February and the atmospheric model of the MAGIC site for winter was used in MC, the uncertainty of the energy scale caused by the atmospheric model is estimated to be $\sim$ 7% (see [41]).

Atmospheric Conditions Cloud, haze, and aerosol cause a daily variation of the photon transmission. For example, data with $Cloudiness$ up to 20% were used for the Crab pulsar observations. The effect on the energy scale is conservatively estimated to be 10%

Light collection efficiency Uncertainties in the mirror reflectivity, photon loss in the Plexiglas at the entrance of the camera, the light guide efficiency of the Winston cones, QE of PMTs, the accuracy of the F-factor method etc. cause an uncertainty in the amount of detected photons. For all the Crab pulsar observations, the light collection efficiency was monitored by muon events and uncertainty of $\leq 5\%$ is guaranteed (see Fig. 5.2). Therefore, uncertainty of the energy scale caused by light collection efficiency would also be 5%.

Malfunctioning of pixels During the observation, several pixels may malfunction [5]. Uncertainty in energy scale caused by them is estimated to be 2%.

---

[5] If such pixels are within a image, the interpolation of charges is done in order to minimize the effect.

- **Discriminator threshold settings** The relevant energy region for the Crab pulsar observation is 20 to 100 GeV. For such a low energy region, the setting of the discriminator threshold affects the trigger efficiency (the collection area). Fig. 4.21 shows the $SIZE$ distribution between the proton MC events and the observed data. Below 50 ph.e. (below $\sim$ 30 GeV) the possible discrepancy is seen ($\sim 10\%$). However, this is not fully due to the discrepancy of the discriminator thresholds but mainly to the NSB + after-pulsing trigger events, which are not included in the simulation. Even though the image cleaning suppresses such events, there is still some contamination. Actually, the data taken under the higher NSB level shows a larger discrepancy only below 50 ph.e. The difference of the trigger efficiency between MC and the real observations cause an error in the energy scale too. The uncertainty of the energy scale at 20 to 100 GeV caused by this is conservatively estimated to be 15%.

- **Effective observation time estimation** The method for calculating effective observation time described in Sect. 4.9.2 has an uncertainty of 2%. This affects the flux level.

The overall systematic uncertainty in the energy scale is estimated to be 20% by adding major factors in quadrature. On top of this there is an uncertainty in the collection area (10%) and the observation time estimation (2%). Taking into account the steep spectrum of the Crab pulsar which will be discussed in the next chapter, the uncertainty in the flux estimation is dominated by the uncertainty in the energy scale.

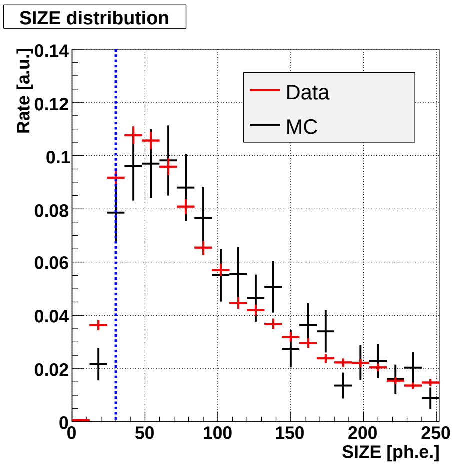

Figure 4.21: Comparison of the SIZE distribution between observed data and proton MC. Below 50 ph.e. a discrepancy of $\sim 10\%$ between the data and MC is visible. This is explained mainly by the accidental triggers caused by NSB + after-pulsing, which are not included in the simulation.

4.13 Concluding Remarks

The analysis procedures of the MAGIC data such as signal calibration, image cleaning, background suppression and energy spectrum calculation are very well developed. The method of checking the reflector performance by muon events is also a very useful tool to assure the quality of observed data. The systematic uncertainty of the energy scale is estimated to be 20% by adding in quadrature the major systematic uncertainties in hardware components and observational conditions. This should be taken into account when the spectrum of the Crab pulsar is discussed.

Chapter 5

MAGIC Observations of the Crab Pulsar and Data Analysis

The MAGIC observations are grouped in one-year long cycles and Cycle I started in May 2005. In Cycles I and II, the Crab pulsar was observed with the standard trigger. 16 hours of good-condition data showed only a weak signal of pulsation with 2.9 σ (see Sect 2.9.6). Here, I analyze the data recorded in Cycle III and Cycle IV with the SUM trigger with a much lower energy threshold and a higher sensitivity below 100 GeV.

5.1 Observations

The SUM trigger was installed in October 2007 and, subsequently, the Crab pulsar was observed in Cycles III and IV, for 48 hours (over 47 days) and 78 hours (over 36 days), respectively. All the observations were made in ON-mode, since the SUM trigger was designed for ON-mode observations. Although, as described in Sect 4.8, pulsar observations do not require OFF observations, in order to assure the validity of the analysis chain and the quality of the data sets by the Crab nebula emission, OFF observations were made in October and December 2007 for ~ 10 hours.

5.2 Sum Trigger Sub-patch Malfunction

One and five out of the 36 Sum Trigger sub-patches were malfunctioning during the Crab pulsar observations in Cycle III and Cycle IV, respectively. The effect can be seen by plotting COG of images on the camera. The regions near the broken patches show a hole in COG distribution, as shown in the top left (Cycle III data) and the middle left (Cycle IV data) panel of Fig.5.1. When a variability of the Crab pulsar flux between the two cycles is discussed, this difference must be taken into account. By deactivating the broken patches in MC, the effect can be reproduced as shown in the top right (Cycle III MC) and the middle right (Cycle IV MC). The bottom left and the bottom right panel show the difference between Cycle III and Cycle IV in data and MC, respectively. According to the MC, the differences in gamma-ray detection efficiency between the two cycles for $SIZE$ 25-50, 50-100, 100-200 and 200-400 ph.e. are about 21%, 17%, 11% and 7%. This effect will be corrected when the variability is discussed (see Sect. 5.9). The calculation of the energy spectra will also be carried out with MCs which reflect these subpatch malfunctions.

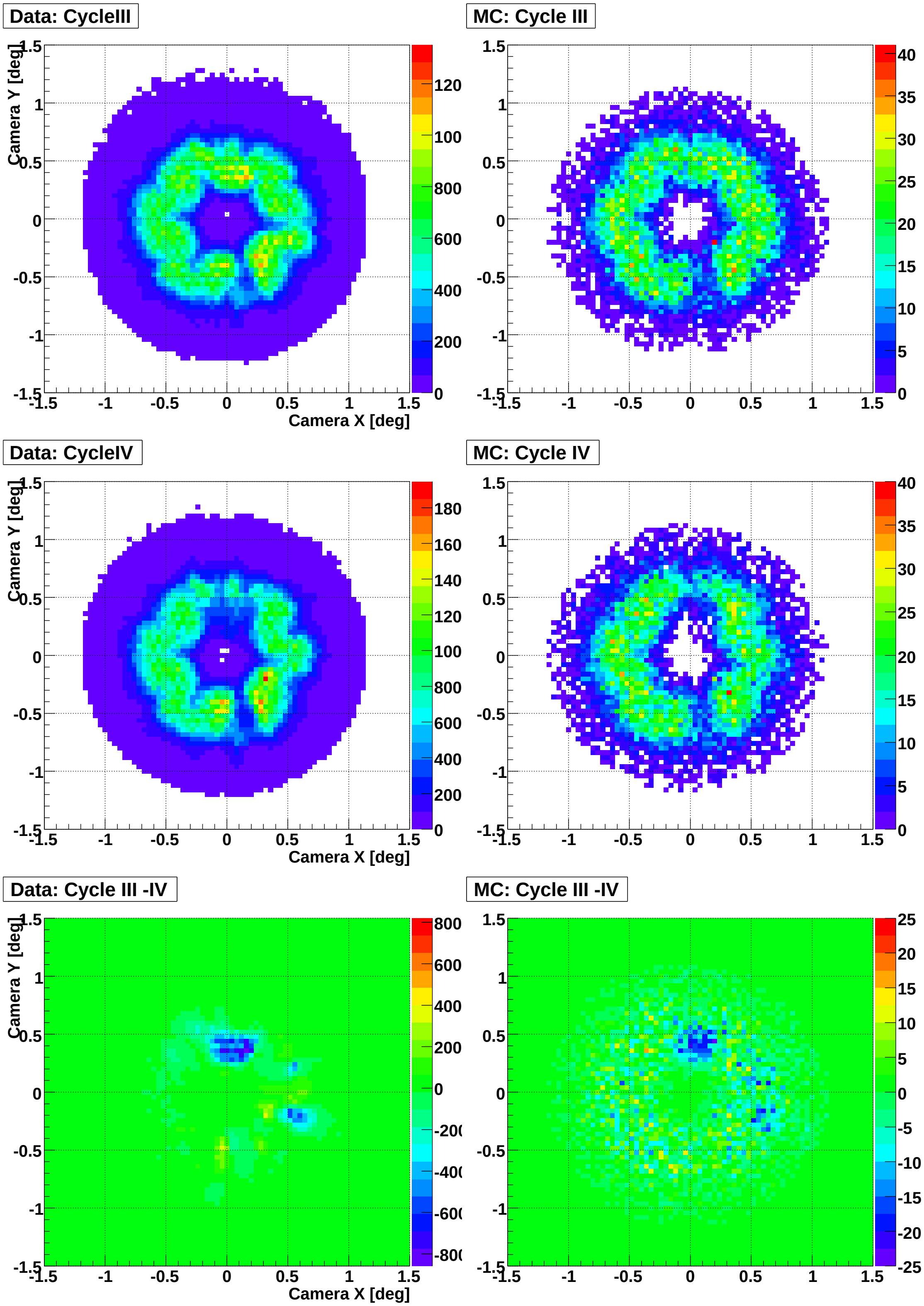

Figure 5.1: COG distributions on the camera. The left and right columns show observed data and gamma-ray MC events, respectively. The first, second and third rows show Cycle III, Cycle IV and difference between the two cycles, respectively. The effect of the subpatch malfunction is seen as holes of COG distributions. Simulations reproduce the effect reasonably well.

5.3 Data Selection

The new SUM trigger system lowers the energy threshold from 50 GeV to 25 GeV (see Sect. 3.4.7). It has a big impact on the pulsar observations because most of the signal is expected below 50 GeV (see Fig. 3.22). However, such low energy events are easily affected by the observational conditions. A slightly worse condition may result in a significant increase in the energy threshold and a worse sensitivity. Therefore, a more careful data selection than the normal observations above 50 GeV is required, in terms of both hardware and environmental conditions.

5.3.1 Reflector Performance Selection

The mirror panels of the MAGIC telescope are adjustable (see Sect. 3.4.2) and their alignment on some days can be worse than it should be. As described in Sect. 4.11, this can be checked by muon events. Blue points in Fig. 5.2 show the light collection efficiency estimated by muon events (the conversion factor from the number of photons hitting the reflector to that of the detected photoelectrons) for each observation day. The days when the efficiency is lower than 0.081 (5% lower than the average) are excluded from the analysis, since it may affect the trigger efficiency and the energy reconstruction. On average, Cycle IV has 3% lower efficiency than Cycle III, which is taken into account in the MC when the energy spectrum is calculated. The PSF was checked by fitting a linear function to the $ArcWidth/Radius - Radius$ relation (see Sect 4.11). The value at $Radius = 1.15$ degrees is used to evaluate the PSF, as shown by the red points in Fig. 5.2. From the study with MC, it was found that the PSF in Cycle IV was $\sim 5\%$ worse than that in Cycle III, which is also taken into account when the energy spectrum is computed.

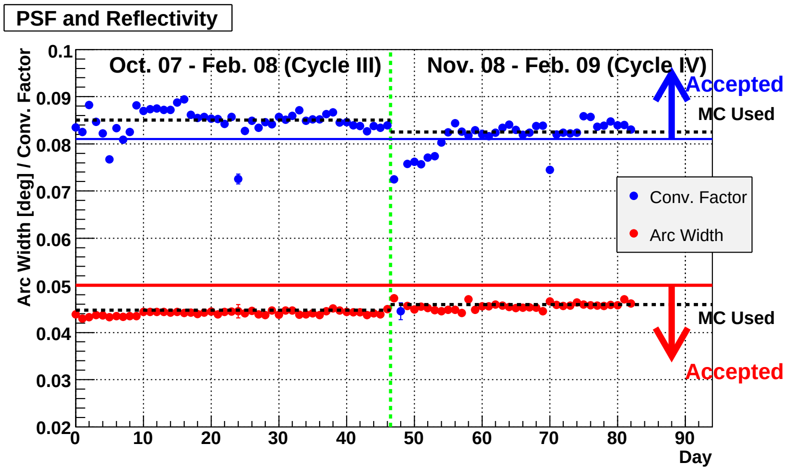

Figure 5.2: Daily monitoring of the light collection efficiency and the PSF of the reflector by muons. The horizontal axis indicates the observation day and the vertical axis indicates the mean $ArcWidth$ and the mean conversion factor. Data taken in the days when the light collection efficiency (blue points) is below the limit (a blue line) are excluded from the analysis.

5.3.2 Zenith Angle Selection

As the angular distance from the source to the zenith (Zenith Angle, ZA) becomes larger, the distance from the shower maximum to the telescope increases. The relation between the gamma-ray energy and the number of detected photons would change depending on the ZA, due to the different Cherenkov photon density on the ground [1]. Needless to say, the threshold energy is also affected. Therefore, in order to assure the lowest possible threshold and a uniform $SIZE$ – energy relation, I selected data with the ZA below 20 degrees.

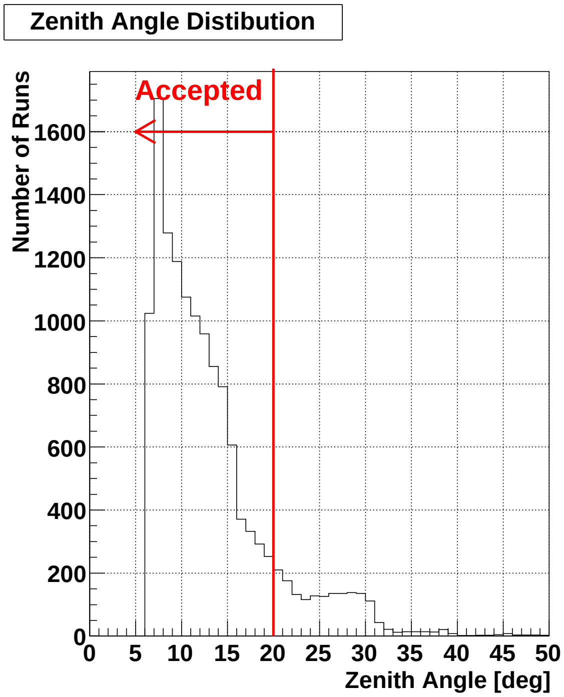

Figure 5.3: ZA distribution of the data. Most of the data are taken below 20 degrees in ZA. In order to assure the lowest possible energy threshold and the uniform $SIZE$ - energy relation, data with ZA below 20 degrees are used in the analysis.

5.3.3 Cloudiness Selection

As described in Chapter 3.4.8, haze and clouds affect the air shower images. Especially for the lowest energies below 50 GeV, the effect would be significant. Fig. 5.4 shows the event rate [2] as a function of $Cloudiness$ (see Sect. 3.4.8). A clear anti-correlation between $Cloudiness$ and

---

[1] This is a consequence of three effects: a) a higher Cherenkov threshold leading to fewer photons (see the top right panel of Fig. 3.7), b) a wider spread of photons on the ground due to the larger distance and c) increase in absorption and scattering losses (see Sect. 3.2.2).

[2] Not the trigger rate but the rate of the events which are not completely erased by the image cleaning procedure. Therefore, most of the NSB accidental trigger events are not included in the rate

the event rate can be seen. To assure that no data is affected by haze and clouds, I selected data taken with $Cloudiness$ lower than 20, as shown in Fig. 5.5. If the daily average value is more than 20, all the data taken on that day are excluded.

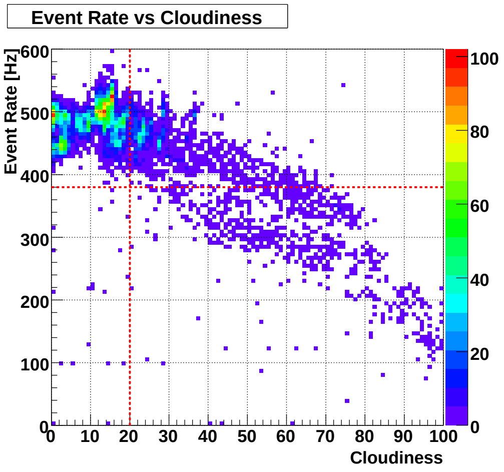

Figure 5.4: The event rate as a function of $Cloudiness$*. A clear anti-correlation can be seen. Cut values in the event rate and in* $Cloudiness$ *are indicated by the red dotted lines.*

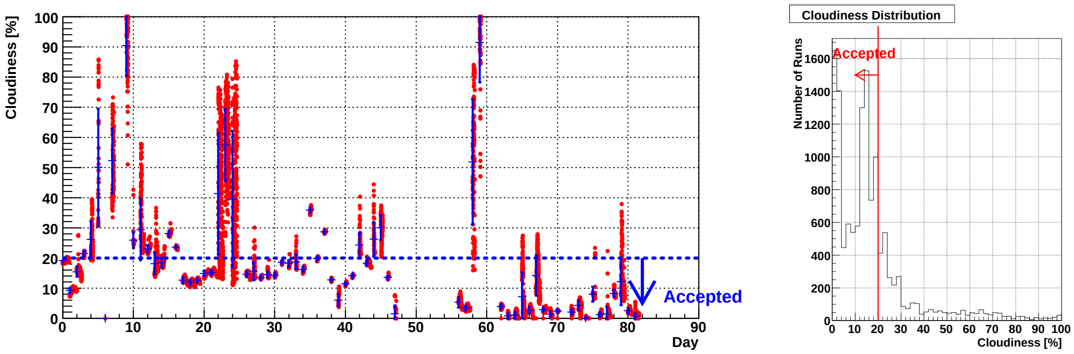

Figure 5.5: Left: $Cloudiness$ *for each run. The horizontal axis indicates the observation day and the vertical axis indicates* $Cloudiness$*. A red dot corresponds to one run (*~ 1 *minute). The mean and the RMS of the* $Cloudiness$ *for each day are denoted by blue crosses. The data with* $Cloudiness$ *larger than 20 are excluded from the analysis as denoted by the blue dotted line. Right:* $Cloudiness$ *distribution. Most of the runs have cloudiness below 20 and the data with* $Cloudiness$ *larger than 20 are excluded from the analysis.*

5.3.4 Event Rate Selection

Even if the environmental conditions and the reflector status are good, the telescope performance might not be optimal because of inappropriate DAQ settings, such as wrong threshold settings and the change in signal transmission time (length), which can happen during long-term observations. Such problems can be identified by checking the event rate. For the very low threshold observations like pulsar observations, almost half the trigger rate is due to NSB + after-pulsing accidental events and, hence, the trigger rate may not reflect improper DAQ settings. The event rate after the image cleaning would be more indicative because images of such accidental events would be completely erased by the image cleaning. As you can see from Fig. 5.6, after cutting away bad reflector days and cloudy days, almost all runs have a good rate, meaning that hardware settings had been fine. Runs with the event rate lower than 380 Hz were discarded just in case.

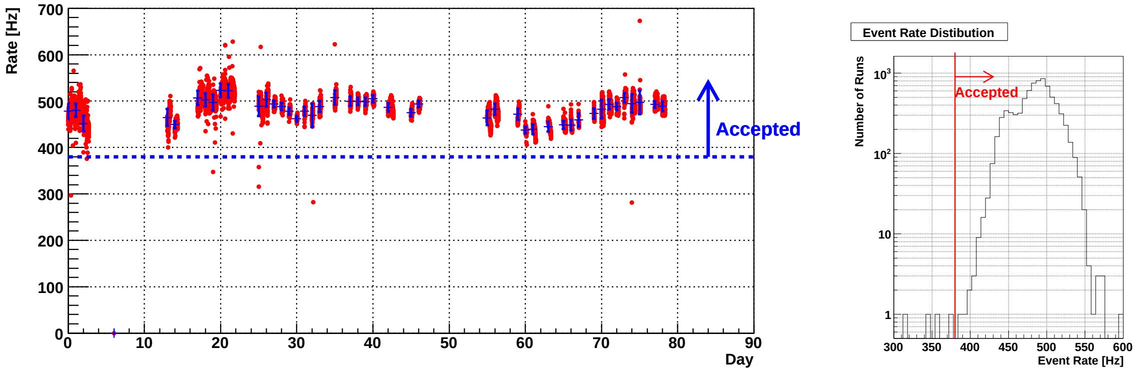

Figure 5.6: Left: The event rate for each run. The horizontal axis indicates the observation day and the vertical axis indicates the event rate. A red dot corresponds to one run ($\sim$ 1 minute). The mean and the RMS of the event rate for each day are denoted by blue crosses. The data with the event rate smaller than 380 Hz are excluded from the analysis, as denoted by the blue dotted line. Right: The event rate distribution. Only a few runs have an event rate smaller than 380 Hz and they are excluded from the analysis.

5.3.5 Nebula Measurement Selection

From the rate cut described in the previous section, it is almost guaranteed that event selection has been properly carried out. Just as an additional cross-check, the detection efficiency of the Crab nebula emission was examined. I analyzed the Crab nebula emission[3] with $SIZE$ above 300, for which $Hadronness$ cut is very powerful, i.e., the gamma-ray/hadron separation is highly efficient (Sect. 4.4) and analysis is rather easy. The $Hadronness$ cut at 0.1 is applied to the data and the excess is evaluated with the $ALPHA$ cut at 10 degrees. The background was estimated by fitting the $ALPHA$ distribution from 20 degrees to 80 degrees with a parabolic function and

---

[3] As noted in Sect. 2.9.3, the nebula and the pulsar cannot be spatially resolved by IACTs. The non-pulsed gamma-ray emission above 100 GeV is considered as a nebula emission

then extrapolating the fitted function down to 0 degree. An example of this analysis is shown

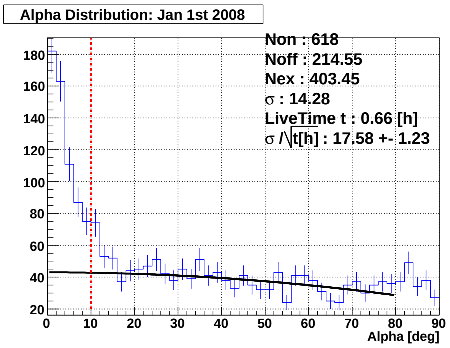

Figure 5.7: An example of the signal from the Crab nebula with $SIZE > 300$ *and* $Hadronness < 0.1$*. ALPHA analysis is used (see Sect. 4.8.1).*

in Fig. 5.7, which is for the observation on 1st January, 2008. In order to check the stability of detection efficiency, the significance of the excess for each of the observation days was scaled to one hour's observation and plotted in Fig. 5.8. They are very stable and their mean value is 16.1, which is consistent with the telescope sensitivity.

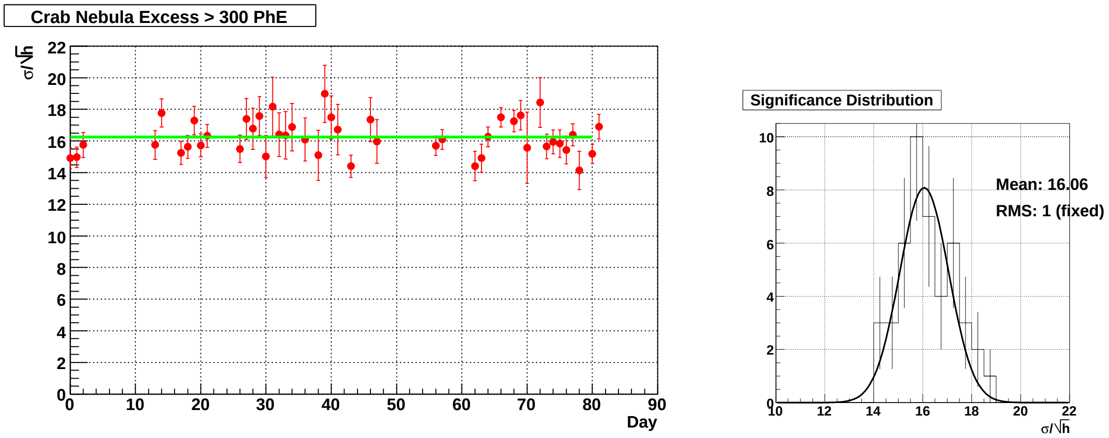

Figure 5.8: Left: Daily monitoring of the detection efficiency of the nebula emission. The horizontal axis indicates the observation day and the vertical axis indicates the excess significance normalized to one hour of observation time. Right: Distribution of the excess significance normalized to one hour. The variation is compatible with the statistical fluctuations.

5.3.6 Summary of the Data Selection

The selection of the good observation days are summarized in Table. 5.1. 26 days out of 47 days and 18 days out of 36 days passed all the selection cuts for Cycle III and IV, respectively. Within a good day, some runs were also excluded due to unfavorable ZA, $Cloudiness$ or the event rate. 25.1 and 34.0 hours of data remained for Cycle III and IV, respectively.

Date yymmdd	PSF/ Ref	Z.A.	Cloud	Used
Cycle III				
071021				yes
071022				yes
071105			Cloudy	no
071106			Cloudy	no
071107			Cloudy	no
071108	Bad			no
071109			Cloudy	no
071110	Bad			no
071111			Cloudy	no
071112			Cloudy	no
071113			Cloudy	no
071114			Cloudy	no
071115				yes
071116				yes
071117			Cloudy	no
071118			Cloudy	no
071205				yes
071206				yes
071207				yes
071208				yes
071209				yes
071210			Cloudy	no
071211			Cloudy	no
071212			Cloudy	no
071213	Bad			no
071214				yes
071230				yes
071231				yes
080101				yes
080102				yes
080103				yes
080104				yes
080105				yes
080106				yes
080107			Cloudy	no
080108				yes
080109			Cloudy	no
080110				yes
080111				yes
080112				yes
080113				yes
080126			Cloudy	no
080129				yes
080131			Cloudy	no
080201			Cloudy	no
080202				yes
080203				yes
Cycle IV				
081105	Bad			no
081107	Bad			no
081126	Bad			no
081129	Bad			no
081130	Bad			no
081201	Bad			no
081202	Bad			no
081203	Bad			no
081204				yes
081205				yes
081206			Cloudy	no
081207			Cloudy	no
081208		$> 20°$		no
081210		$> 20°$		no
081219				yes
081220				yes
081222				yes
081223			Cloudy	no
081229				yes
090101			Cloudy	no
090102				yes
090103				yes
090104				yes
090118	Bad			no
090119				yes
090120				yes
090121				yes
090122				yes
090124				yes
090125				yes
090126				yes
090127			Cloudy	no
090128				yes
090130				yes
090131		$> 20°$		no
090201		$> 20°$		no

Table 5.1: Selection of the data on daily basis based on the reflector performance, the zenith angle and $Cloudiness$.

5.4 $ALPHA$ Cut Optimization for Pulsar Analysis

For the pulsar analysis, the signal extraction can be carried out using the light curve (see Sect. 4.8.3). The image parameter $ALPHA$ is additionally used as an event selection parameter in order to increase the signal-to-noise ratio. The best cut value on $ALPHA$ changes with $SIZE$ because the larger the $SIZE$, the better the shower direction estimation. The dependency is especially strong at $SIZE < 100$, as one can see from the top right panel of Fig. 5.9. Since most of the signal from the Crab pulsar is expected at $SIZE < 100$, a $SIZE$-dependent $ALPHA$ cut is applied to the Crab pulsar data. It is optimized as follows: First, MC gamma-ray and data (mostly hadron) samples are divided into 20 of $\log_{10}(SIZE)$ bins from 1 (10 ph.e.) to 3 (1000 ph.e.), as shown in Fig. 5.9. For each of the bins, the best $ALPHA$ cut is calculated which maximizes the so-called Q-factor $Q = \epsilon_g/\sqrt{\epsilon_h}$, where ϵ_g and ϵ_h is the fraction of events which survive the $ALPHA$ cut for gamma-ray and hadron samples, respectively. Red stars in the top right panel of Fig. 5.9 indicate the best $ALPHA$ cut values for each bin. Then, those best values as a function of $\log_{10}(SIZE)$ are fitted by a function $A_{cut}(SIZE) = a(\log_{10}(SIZE) + b)^c$, obtaining $a = 3.7 \times 10^4, b = 1.674, c = -5.988$ as the best parameters. The function is shown in the same panel as a black line. In the data analysis, the events which fulfill $ALPHA < A_{cut}(SIZE)$ are considered as gamma-ray candidates. At size 25 ph.e. the cut is at 45 degrees, while at 250 ph.e. it is at 8 degrees. ϵ_h, ϵ_γ and Q are shown in the bottom panel of Fig. 5.9. Q is approximately 1.5 at 100 ph.e. and lower for smaller $SIZE$s.

It should be noted that a cut in $Hadronness$ was found not to improve the signal-to-noise ratio as much as in $ALPHA$ at $SIZE < 100$ where most of the signal from the Crab pulsar is expected. In order to avoid systematic errors in analysis, a $Hadronness$ cut is not applied.

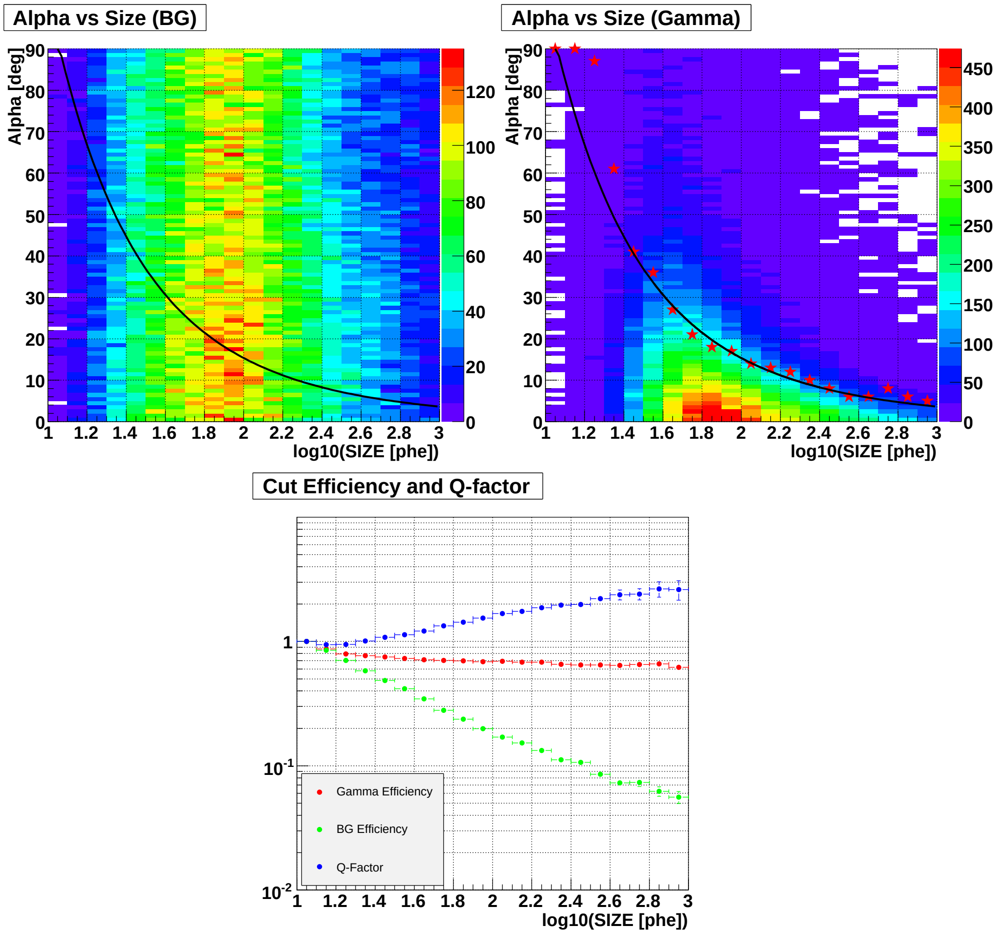

Figure 5.9: Top left: $ALPHA$ as a function of log$_{10}$(SIZE) for an observed data sample. Since the data sample is dominated by the hadron background events, $ALPHA$ distributes uniformly from 0 to 90 degree. A black line indicates the $SIZE$-dependent cut values. Top right: $ALPHA$ as a function of log$_{10}$(SIZE) for an MC gamma-ray event sample. $ALPHA$ is concentrated around 0, whereas the concentration gets weaker as $SIZE$ decreases. Red stars indicate the best cut values which maximize the Q-factor. A black line indicates the $SIZE$-dependent cut values. Bottom: The Q-factor (blue) and the survival ratios for hadrons (green) and gamma-rays (red) as a function of log$_{10}$(SIZE). Q-factor is about 1.5 at $SIZE = 100$ and 1 at $SIZE = 25$.

5.5 Analysis of the Energy Spectrum of the Crab Nebula

The Crab nebula is generally used as a standard candle for the calibration of the IACTs (see Sect. 2.9.7). It is the brightest steady point-like source above 100 GeV. Actually that is why it could conveniently be used to verify the quality of the data for the Crab pulsar analysis (see Sect. 5.3.5). It would also be very important to calculate its energy spectrum in order to assure that the analysis tool and the MC samples are appropriate before starting the Crab pulsar analysis.

5.5.1 Data Sample for the Crab Nebula Analysis

I used 17.1 hours of data (ON-data) and 5.2 hours of OFF observation data (OFF-data), both of which were taken in October and December 2007 and passed all the selection criteria described in Sect. 5.3. The conditions of the observations are summarized in Table 5.2. The pointing position of the OFF-data is on the same declination as for the ON-data but differs by 2 hours in right ascension, which results in the same trajectory on the sky between ON and OFF with a 2-hour time lag.

	ON	OFF
Dec. [deg.]	22.014	22.014
R.A. [hour]	5.5756	3.5756
Period	October 2007 and December 2007	October 2007 and December 2007
Eff. Time [hours]	17.1	5.2
Zenith Range [deg]	6 to 20	6 to 20

Table 5.2: The observation conditions for the Crab nebula data.

5.5.2 Energy Range of the Crab Nebula Analysis

For the energy range below 50 GeV, a precise background estimation is not easy in the case of the nebula observations. The reason is as follows: For the nebula analysis, the light curve cannot be used for the signal extraction and, hence, the $ALPHA$ distribution is used instead (see Sect. 4.8). However, since the images with a small $SIZE$ are easily affected by the sky conditions, $ALPHA$ distribution may slightly vary depending on the conditions, which may lead to a difference between ON-data and OFF-data. Since the observed events are strongly dominated by cosmic-ray background events, even a tiny mismatch in $ALPHA$ distributions may result in a large systematic error in the background estimation. It should be stressed that this is not the case for the pulsar analysis. Since the light curve can be used for the pulsed signal extraction, it does not require any OFF-observation. Unless the sky condition changes significantly in the time scale of a pulsar period (34 ms for the Crab pulsar), which is very hard to imagine, the background estimation can be properly carried out. For this reason, the nebula emission was analyzed only above 50 GeV.

The MC samples were generated from 6 GeV to 2 TeV. They are meant to be used for the analysis of the Crab pulsar, which is known not to have significant emission above 100 GeV. With these MC samples, it is very hard to analyze the spectrum above 1 TeV properly because no information above 2 TeV is present in MC and energy resolution is limited ($\sim 20\%$ at 1 TeV). In order to avoid any analytical bias due to the limited energy range in MC production, the spectrum was analyzed up to 700 GeV.

The results are shown in Fig. 5.10. The spectrum was unfolded using the Tikhonov regularization method. It is known that the spectrum in this energy range is better fitted by a variable power law

$$\frac{\mathrm{d}^3 F}{\mathrm{d}E\mathrm{d}A\mathrm{d}t} = f_0 (E/300\mathrm{GeV})^{[\Gamma_1 + \Gamma_2 \log_{10}(E/300\mathrm{GeV})]} \tag{5.1}$$

than a simple power law.

$$\frac{\mathrm{d}^3 F}{\mathrm{d}E\mathrm{d}A\mathrm{d}t} = f_0 (E/300\mathrm{GeV})^{\Gamma} \tag{5.2}$$

The power law fitting gives the best parameters of $f_0 = (6.6 \pm 0.7) \times 10^{-10}$ [cm^{-2}s^{-1}TeV^{-1}] and $\Gamma = -2.11 \pm 0.10$, while $\chi^2 = 4.74$ with the degree of freedom 4 (χ^2 probability = 31.5 %). On the other hand, the variable power law gives $f_0 = (7.0 \pm 0.8) \times 10^{-10}$[cm^{-2}s^{-1}TeV^{-1}], $\Gamma_1 = -2.21 \pm 0.15$ and $\Gamma_2 = -0.45 \pm 0.47$, while $\chi^2 = 3.55$ with the degree of freedom 3 (χ^2 probability = 31.4%). In this limited energy range, both functions fit well. It should be noted that the fits take into account the correlation between the spectral points which is introduced by the unfolding procedure. The spectrum measured by HESS telescopes above 500 GeV (see [11]) and the previous MAGIC measurements above 60 GeV (see [20]) are also shown in the same figure. They are consistent with one another in the overlapping range, verifying the validity of the MC samples and analysis tools used for the pulsar analysis.

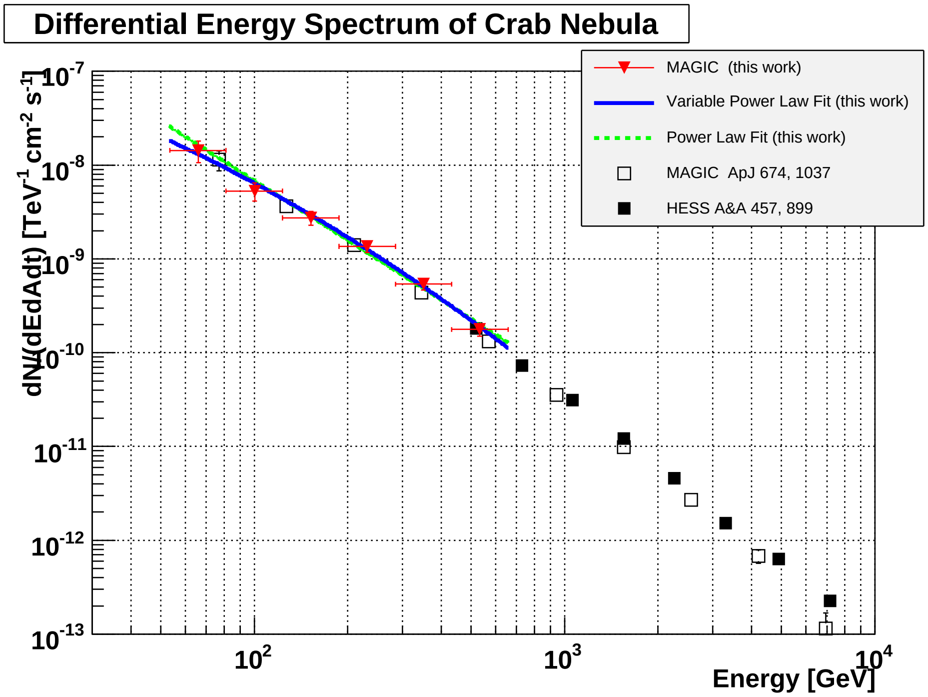

Figure 5.10: The energy spectrum of the Crab nebula. Red triangles, open squares and filled squares indicate the MAGIC observation results with the SUM trigger (this work), the published MAGIC result with the standard trigger taken in 2006 (taken from [20]), and the published HESS results (taken from [11]). They are consistent in the overlapped energy region. The power law fit (a green line) and the variable power law fit (a blue line) to the MAGIC results with the SUM trigger are also shown.

5.6 Analysis of Optical Pulsation

For the pulsar analysis, the proper barycentric correction and the accurate pulsar period information are essential. In order to check if the barycentric correction and the pulse phase calculation are correctly done, the optical pulsation of the Crab pulsar is very useful and helpful since it can be clearly detected within 10 minutes of observation thanks to the large reflector of MAGIC.

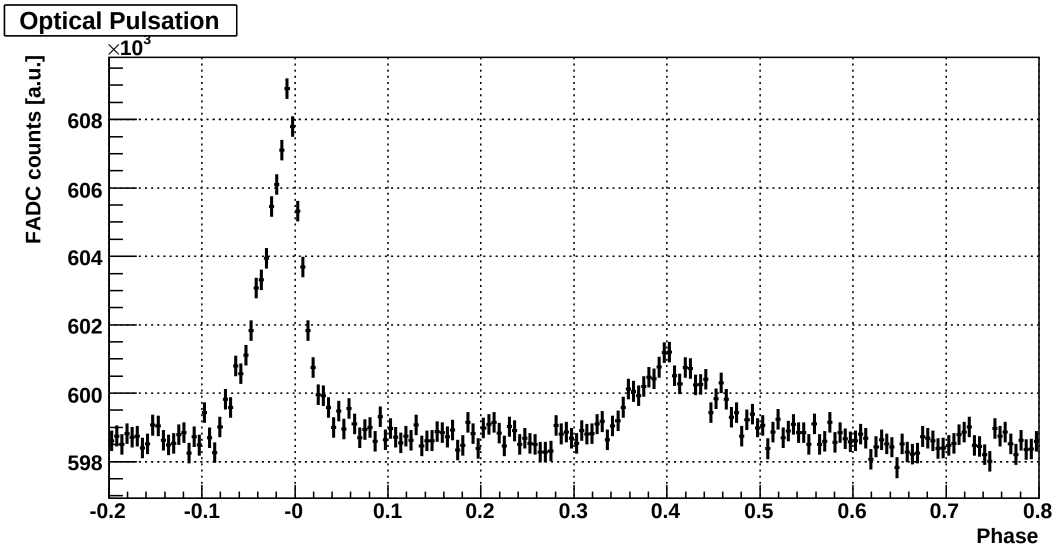

Figure 5.11: The light curve of the optical pulsation from the Crab pulsar observed by MAGIC with the central pixel (see Sect. 3.4.9). ~ 30 *hours of the observation data are used. 10 minutes is enough to see the two peaks clearly.*

Fig. 5.11 shows optical pulsation detected by the central pixel of MAGIC (see Sect. 3.4.9). ~ 30 hours of the observation data from both cycles are used. The barycentric correction was done by $Tempo$ and the period information i.e. ν, $\dot{\nu}$ and t_0, are taken from the "Jodrell Bank Crab Pulsar Monthly Ephemeris", as described in Sect. 4.7. The phase is calculated by Eq. 4.10. A glitch (see 2.4) occurred in May 2008, which is between the Cycle III and the Cycle IV observations. Since there is no Crab pulsar observation in that month and ν, $\dot{\nu}$ and t_0 are updated monthly, the glitch does not affect the phase calculations.

The peak phase of P1 is slightly shifted earlier with respect to the radio peak phase by ~ 0.01 in phase, corresponding to ~ 300 μs, which is known and consistent with other observations (see e.g. [145]). Pulse shapes are also in good agreement with other observations, although a small time variability has been reported and quantitative comparison is not easy (see e.g. [109]). Exactly the same method of phase calculation is applied to gamma-ray signals.

5.7 Detection of the Very High Energy Gamma-ray Pulsation from the Crab Pulsar

After all the selection described in Sect. 5.3, 59.1 hours (Cycle III + IV) of good data remained. The quality of the data sets, MC samples, analysis tools and the pulsar phase calculations were verified, as described in the previous sections. In this section, the analysis of the pulsed gamma-ray signal from the Crab pulsar is described.

5.7.1 The Pulsed Gamma-ray Signal

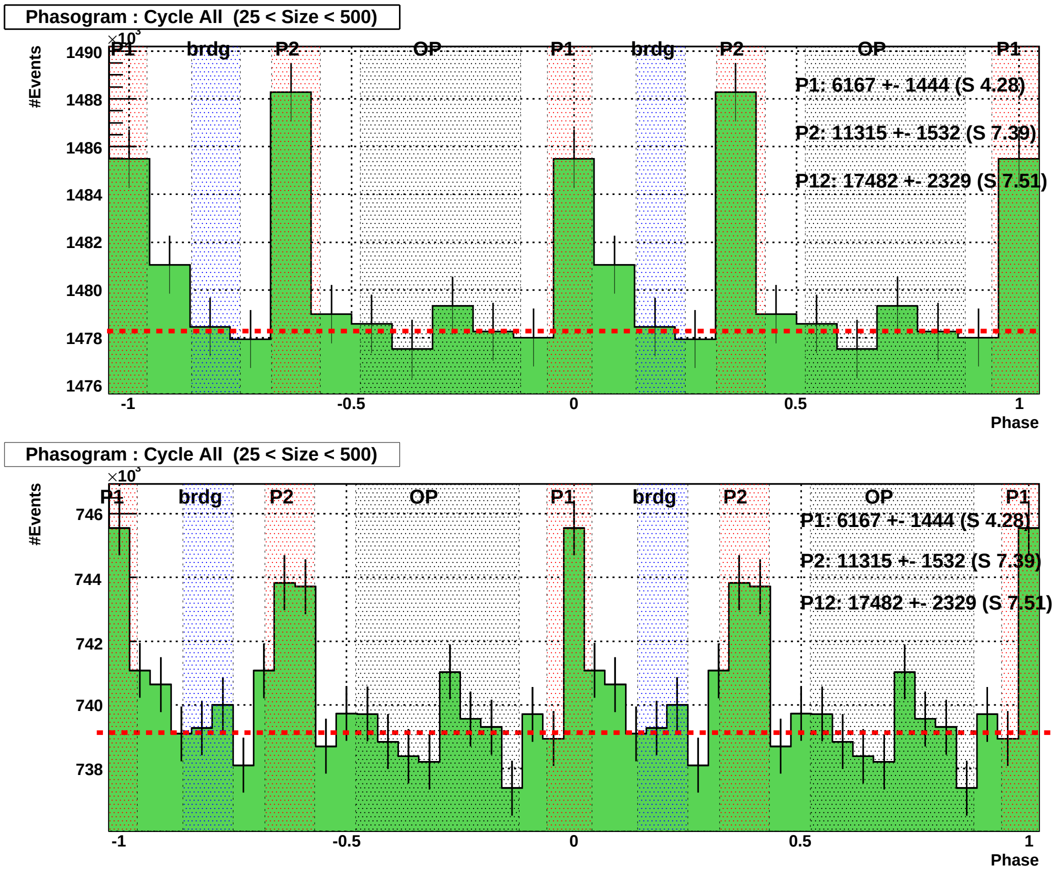

Figure 5.12: The light curves of the Crab pulsar detected by MAGIC. 59.1 hours of the observation data are used. Following the convention in pulsar analyses, the light curves are plotted from phase -1 to 1. The upper and lower panels show the light curves with 11 bins (3 milliseconds per bin) and with 22 bins (1.5 milliseconds per bin) per period. The red, shaded regions indicate the phases of P1 and P2, the blue shaded regions indicate the Bridge emission phases and the black shaded regions indicates the OP (off-pulse) phases (see Sect. 2.9.5 for the definition of these phases). The statistical significance of the excess for P1, P2, and P1 + P2 are 4.28 σ, 7.39 σ and 7.51 σ, respectively.

The light curve of all events with $SIZE$ range from 25 to 500 are shown in Fig. 5.12. A $SIZE$-dependent $ALPHA$ cut described in 5.4 was also applied. The background was estimated using the OP (off-pulse) region (phase 0.52 to 0.88). P1 (phase -0.06 to 0.04), P2 (phase 0.32 to 0.43) and the sum of P1 and P2 have 6267 ± 1444, 11315 ± 1532 and 17482 ± 2329 excess events with statistical significance of 4.28σ , 7.39σ and 7.51σ, respectively. For the definition of the phase names, see Sect. 2.9.5. The flux of P2 is twice as high as that of P1. As can be seen in Fig. 2.26, at 1 GeV, P1 has a higher flux than P2. The energy dependence of P2/P1 ratio will be discussed in Sect. 7.2. The so-called bridge emission, which is seen in some energy bands, is not visible in the MAGIC data. This will also be discussed in Sect. 7.2 As one can see the bottom panel of Fig. 5.12, although P1 is conventionally defined as 0.32 to 0.43, most of the excess is concentrated in a narrower phase interval. The precise discussion of the pulse shape will take place in Sect. 7.3.

5.7.2 Further Investigation of the Signal

Since this is the first detection of a gamma-ray pulsar by an IACT [4], it is important to assure that the signal is not an artifact of the analysis or of the instrument. A useful check is the growth of the number of excess events as a function of the number of background events. Since pulsar emission is thought to be stable in time, the excess should grow linearly. The results are shown in the left panel of Fig. 5.13 and indeed the excess grows linearly. The growth of statistical significance is also shown in the right panel.

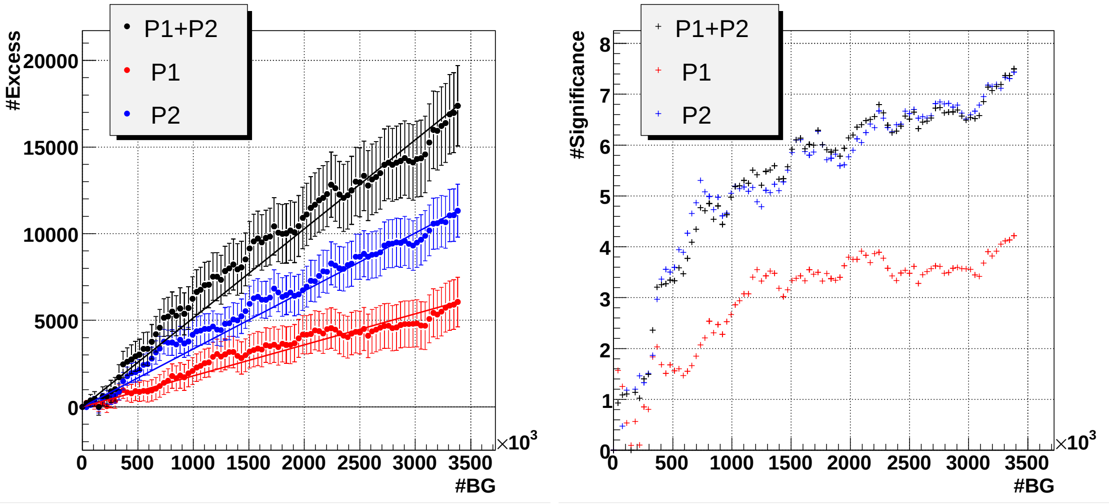

Figure 5.13: Left: the growth of the number of excess events as a function of the number of background events. Red, blue and black points indicate P1, P2, and P1 + P2, respectively. Right: The growth of the statistical significance as a function of the number of background events. Red, blue, and black points indicate P1, P2, and P1 + P2, respectively.

---

[4] The discovery of the Crab pulsar with MAGIC was first achieved by the efforts of my colleagues listed in Sect. 1.6 and reported in [22]

Another useful check is the “inverse selection” of events. If the excess is due to gamma-ray signals, events discarded by the $ALPHA$ cuts should not contain a significant excess. Figure 5.14 shows the light curve produced with events which do NOT pass the $ALPHA$ cut. Excesses are compatible with the background fluctuation.

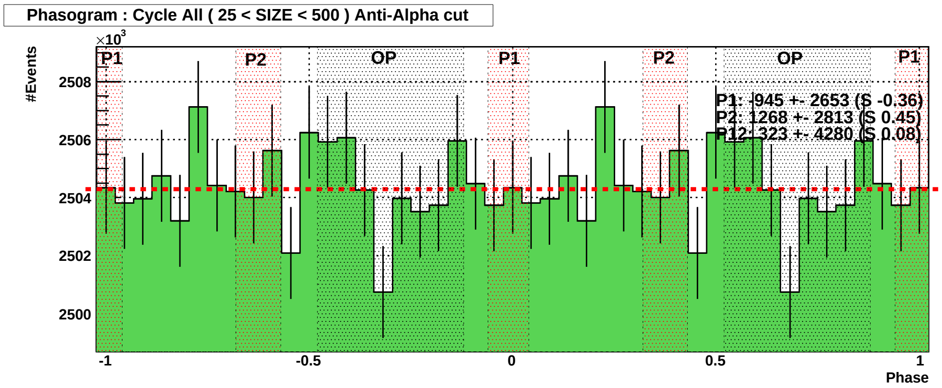

Figure 5.14: The light curve of the Crab pulsar for data which do not pass the $ALPHA$ cut. No pulsed signal is visible, as expected.

5.8 SIZE Dependence of the Pulsation

In order to roughly estimate from which energies the excess events come from, the energy dependence of the light curves should be examined. Instead of the energy reconstructed with Random Forest (see Sect. 4.5), which suffers a trigger-bias effect at these low energies as discussed in Sect. 4.5, I use $SIZE$ for this study. $SIZE$ is the total number of photoelectrons in an image and a good indicator of the primary gamma-ray energy, especially for this data set, for which the ZA range is limited up to 20 degrees. As one can see in Fig. 4.8, $SIZE$ in ph.e. corresponds roughly to two times the energy in GeV.

The data with $SIZE$ from 25 to 800 were divided into 5 bins in $\log_{10}(SIZE)$. Data with $SIZE$ above 800 were also analyzed. The light curves of these six sub-samples are shown in Fig. 5.15. The numbers of excess events for P1, P2 and P1 + P2, shown in the right upper corner of each panel, were calculated by estimating the background level with the OP region (0.52 to 0.58). Most of the excess events are in the two lowest $SIZE$ bins. The third (100 -200) and fourth (200-400) bins also show a 2 σ level excess. Above 400 ph.e., no more excess is visible. The size-dependence of the excess is shown graphically in Fig 5.16.

A detail calculation of the energy spectrum of the pulsed gamma-ray signal will take place in Sect. 5.10.

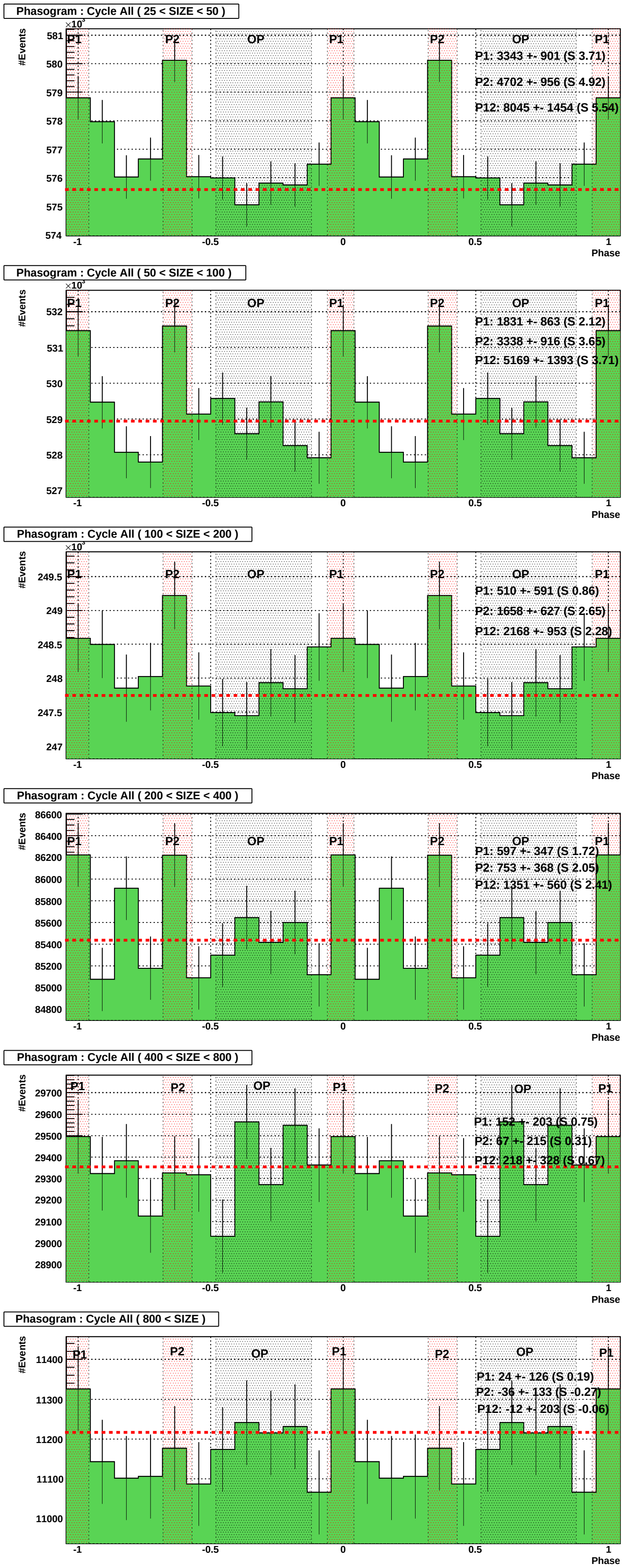

Figure 5.15: The light curves for different $SIZE$ intervals. From the top: 25 to 50, 50 to 100, 100 to 200, 200 to 400, 400 to 800 and above 800 are shown. Most of the excess events are seen at $SIZE < 100$, while some are still visible at $SIZE > 100$.

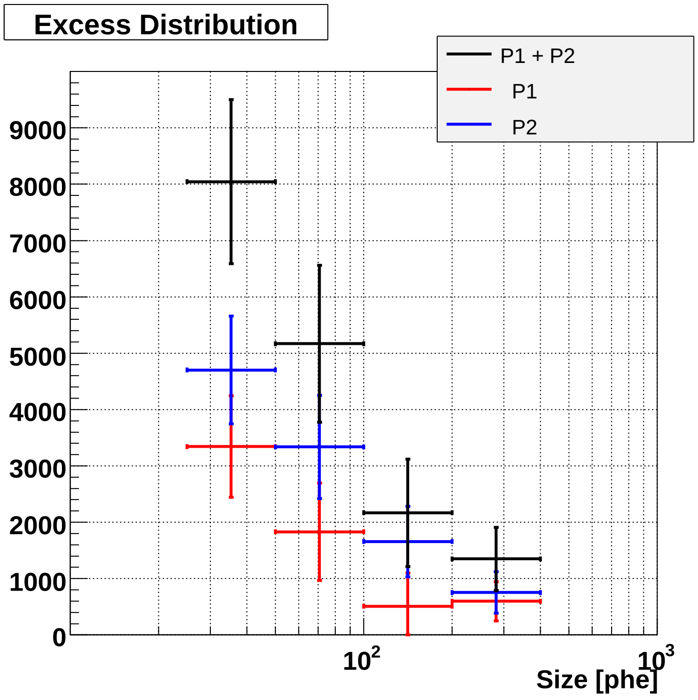

Figure 5.16: The numbers of excess events as a function of $SIZE$. Red, blue and black lines indicate P1, P2 and P1 + P2, respectively. Most of the excess events are at $SIZE < 100$, while some excess events are also visible at $SIZE > 100$.

5.9 Time Variation of the Pulsation from the Crab Pulsar

The previous study by L. Kuiper et al. (see [114]) shows the flux of the Crab pulsar at 1-10 MeV is stable in a time scale of years. However, it is still interesting to check if the flux measured by MAGIC is stable or not, especially because it is the flux beyond the cut-off energy. The growth of the number of excess events as a function of the number of background events already showed that there is no drastic change in flux (see Fig. 5.13). Here I examine the stability of the flux and the light curve more quantitatively. Due to the limited statistical significance of the excess, dividing data sample into too many subsets does not make much sense. Therefore, I only compared Cycle III and Cycle IV to search for a possible yearly variability.

5.9.1 Variability in Light Curve

Fig. 5.17 shows the light curves of Cycle III (top) and Cycle IV (bottom). The $SIZE$ range is from 25 to 500. In order to evaluate the variation in the light curve, the $\chi 2$ test was performed for the 11 bins starting from -0.0682 to 0.432 in the histograms, which is roughly from the beginning of P1 to the end of P2. The $\chi 2$ was 5.00 while the degree of freedom was 10, indicating no significant difference between the two light curves.

5.9.2 Variability in Flux

As one can see from Fig. 5.17, although Cycle IV has 30% longer observation time, it shows less excess events than Cycle III. This can be explained only by statistical fluctuation but the hardware malfunction described in Sect. 5.2 may also have played a role. $SIZE$-dependence of the number of excess events are also compared in Fig. 5.18. Left, middle and right panels are for P1, P2 and P1 + P2. The difference in observation time between the two cycles is corrected. The effect of broken sub-patches estimated by MC (see Sect. 5.2) is also corrected, such that Cycle III and IV have the same gamma-ray detection efficiency. $\chi 2$s are 1.04, 3.14, 2.46 for P1, P2 and P1 + P2, while the number of *dof* is 4 for all phase intervals. Signals observed in Cycle III and IV are statistically consistent and no significant variability is seen between Cycle III and IV.

5.10 Energy Spectra of the Pulsation from the Crab Pulsar

Here I show the energy spectra for the pulsation of P1, P2 and P1 + P2. Since the effective area is increasing rapidly from 20 GeV to 200 GeV (see Sect. 3) and the energy resolution is rather poor in this energy region (see Sect. 4.9.3), the spectra must be calculated with great care. Events with $SIZE$ lower than 30 will be excluded from the spectrum calculation in order to avoid a possible mismatch between MC and data (see Sect. 4.12). A few different methods will be tried in order to estimate the analytical uncertainty of the results.

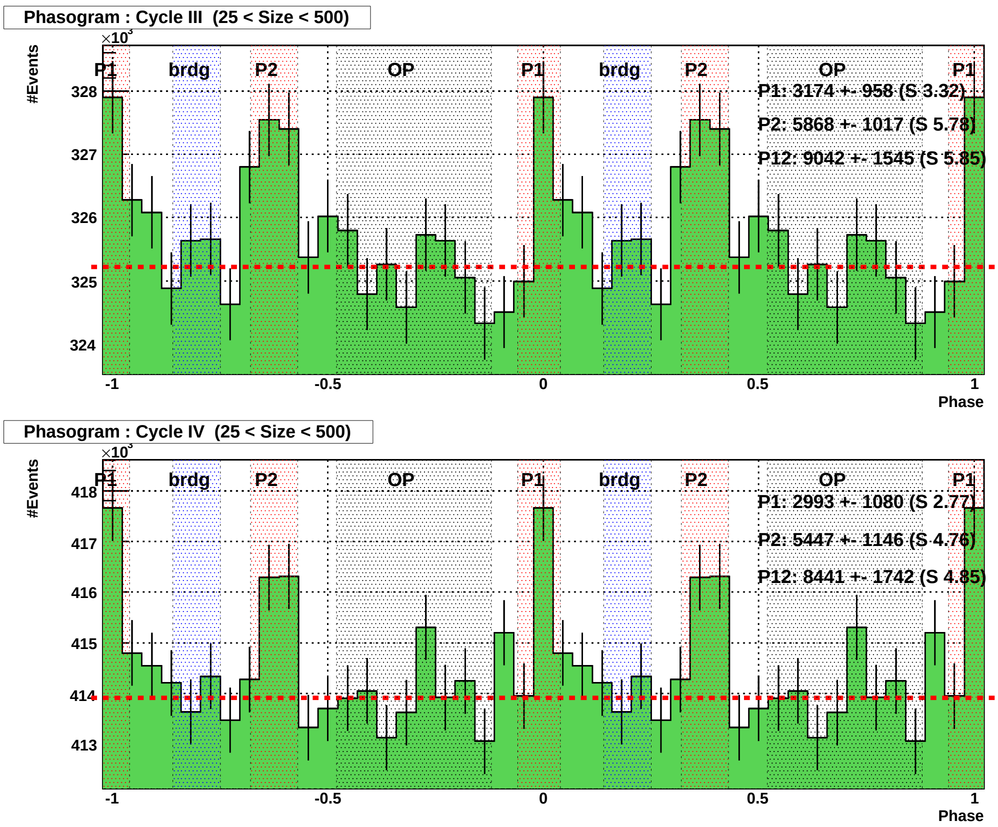

Figure 5.17: The comparison of the light curves between Cycle III and IV. Significant variation of the light curve cannot be seen.

5.10.1 Excess Distribution in the Reconstructed Energy and Size

Fig. 5.19 shows the distributions of the number of excess events as a function of $SIZE$ and the reconstructed energy. It should be emphasized again that the reconstructed energy is strongly biased by the trigger effect (see Sect. 4.9.3). The energy spectrum will be calculated from these distributions. $SIZE$ (total charge in a shower image) has less systematic uncertainty than the reconstructed energy, whereas the resolution of the energy estimation by $SIZE$ is poorer than that by the reconstructed energy. Therefore, it is important to analyze the spectrum with both and compare the results.

5.10.2 Spectrum Calculation by Forward Unfolding Assuming a Power Law

As long as the assumption of the spectral shape is valid, the forward unfolding method should provide the most robust and reliable result, as described in Sect. 4.9.3. Here, I assumed a power law spectrum with two free parameters, namely, differential flux at 30 GeV f_{30} and the spectral

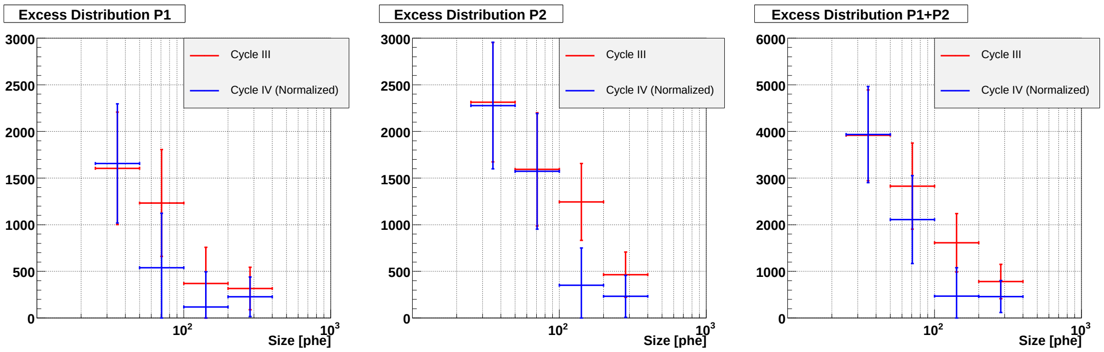

Figure 5.18: The comparison of the number of excess events as a function of $SIZE$ between Cycle III and IV. The correction for the effect of the subpatch malfunction described in 5.2 is applied for each $SIZE$ bin. In addition, the numbers of excess events for Cycle IV are multiplied by 25.1/34.0 in order to correct for the difference of the observation time.

index Γ:

$$\frac{\mathrm{d}^3 F}{\mathrm{d}E\mathrm{d}A\mathrm{d}t} = f_{30}(E/30\mathrm{GeV})^{\Gamma} \tag{5.3}$$

Due to the relatively poor statistics and the narrow energy range, even if the true spectrum is slightly curved, the power law assumption should be valid.

The results based on the $SIZE$ distribution (the left panel of Fig. 5.19) and the reconstructed energy distribution (the right panel of Fig. 5.19) are shown in Table 5.3. The obtained spectra are also graphically shown in Fig. 5.20 by green (based on $SIZE$) and red (based on the reconstructed energy) lines. Unfolded excess distributions, i.e., the expected excess distributions from the obtained spectra, are overlaid in Fig. 5.19. The χ^2 values between the unfolded excess distribution and the observed excess distribution are shown in the fifth column of Table 5.3. They are sufficiently small, assuring the validity of the power law assumption.

5.10.3 Spectrum Calculation by Unfolding with Different Regularization Methods

(Backward) unfolding does not require an assumption of the spectral shape a priori. However, as described in Sect 4.9.3, different regularization methods might give different results. The results are reliable only when all the regularization methods show consistency. Tikhonov (see [181]), Schmelling (see [162]) and Bertero (see [42]) regularization methods were used for unfolding the reconstructed energy distribution. The results are shown in Fig 5.20 as black (Tikhonov), blue (Schmelling) and pink (Bertero) points. All the results are consistent. The results with the Tikhonov method were fitted by a power law function (Eq. 5.3), shown as a black line in the figure. It should be noted that points are correlated with each other because of the unfolding procedure but that the correlation is taken into account when fitting is performed. The best fit parameters and χ^2 values are summarized in Table 5.3.

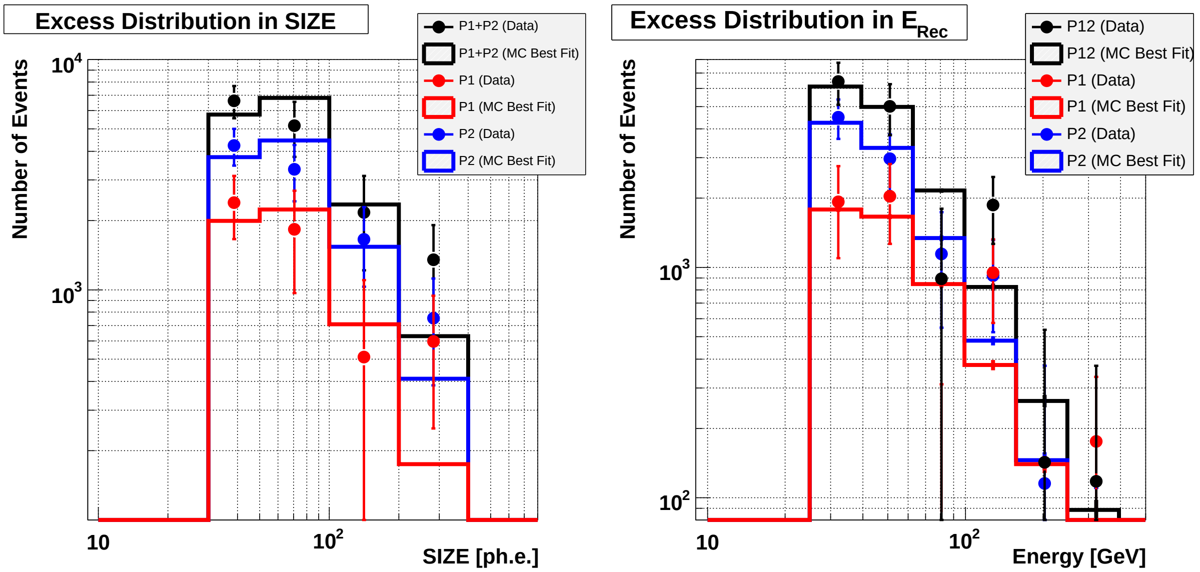

Figure 5.19: The numbers of excess events as a function of $SIZE$ (the left panel) or the reconstructed energy (the right panel). Points indicate the observed data used for the spectrum calculations, while solid lines indicate the expected number of excess events from the spectra obtained by the forward unfolding. In order to reduce the possible systematic error for the spectrum, the events with $SIZE < 30$ are excluded. Red, blue and black lines are for P1, P2 and P1 + P2, respectively.

5.10.4 Discussion of the Results

As summarized in Table 5.3, the three methods, namely, the forward unfolding with the $SIZE$ distribution, the forward unfolding with the reconstructed energy distribution and the unfolding with reconstructed energy distribution using the Tikhonov regularization method, show consistent results. The energy spectra can be well described by a simple power law, which is partially due to the limited statistics and the narrow energy range. The flux of P2 at 30 GeV is twice as large as that of P1, being consistent with the light curve. On the other hand, no difference in spectral indices between them is visible. The indices are -3.35 ± 0.52, -3.07 ± 1.04 and -3.45 ± 0.54 for P1 + P2, P1 and P2, respectively, in the case of the unfolding with the Tikhonov regularization method.

5.11 Concluding Remarks

After many careful checks, 59.1 hours of high quality data have been obtained. All the analysis tools have been carefully examined as well. From them, 6267 ± 1444, 11315 ± 1532 and 17482 ± 2329 gamma-ray signal events have been detected for P1, P2 and P1 + P2, respectively, corresponding to 4.28σ, 7.39σ and 7.51σ in statistical significance. The light curves show some interesting features compared to lower energy bands, such as very narrow P1 peak and the absence of the bridge emission. These features will be further discussed in Chapter 7 together with

Phase	Method	f_{30} [10^{-9}cm^{-2}s^{-1}TeV^{-1}]	Γ	χ^2/dof (prob.)
P1 + P2	Forward with Size	17.3 ± 2.1	-3.53 ± 0.41	3.7/2 (15.7%)
	Forward with E$_{rec}$	18.8 ± 2.4	-3.42 ± 0.34	5.1 /4 (27.7%)
	Tikhonov	14.9 ± 2.9	-3.35 ± 0.52	2.90/1 (8.9%)
P1	Forward with Size	5.7 ± 1.4	-3.67 ± 0.80	2.1/ 2 (35.0%)
	Forward with E$_{rec}$	6.0 ± 1.5	-3.06 ± 0.59	7.2 /4 (12.6%)
	Tikhonov	4.5 ± 2.3	-3.07 ± 1.04	1.20/1 (27.3%)
P2	Forward with Size	11.3 ± 1.5	-3.53 ± 0.39	2.7/2 (25.9%)
	Forward with E$_{rec}$	12.6 ± 1.6	-3.54 ± 0.32	2.0/4 (73.6 %)
	Tikhonov	10.0 ± 1.9	-3.45 ± 0.54	2.19/1 (13.9%)

Table 5.3: The parameters obtained for power law spectra (see Eq. 5.3) for different phase intervals.

lower energy observations. Most of the excess events are concentrated on $SIZE < 100$ whereas some excess events are still visible at $SIZE > 100$. The energy spectra have been calculated with a few different methods and all of them have given consistent results. All of P1, P2 and P1 + P2 can be described by a power law from 25 GeV to 100 GeV and P2 has twice as high a flux as P1 at 30 GeV. The power law indices of P1 and P2 are compatible and they are approximately -3.5. Significant time variation of the pulsation between Cycles III and IV is not seen. These results will be discussed in more detail in Chapter 7, by comparing with Fermi-LAT data from 100 MeV to ~ 30 GeV.

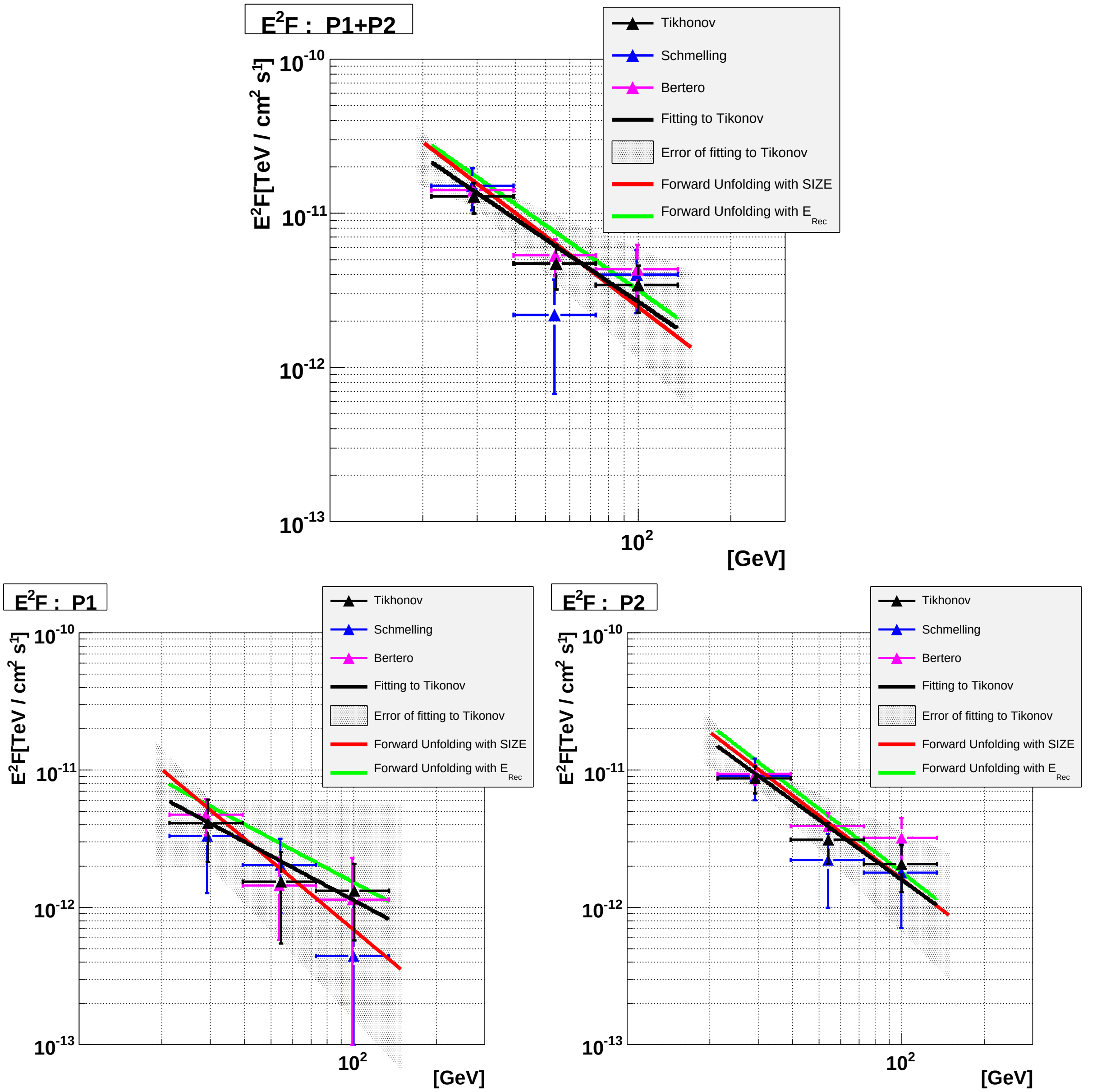

Figure 5.20: The energy spectra calculated with the various methods. Red and green lines show the power law spectra obtained by forward unfolding based on $SIZE$ distribution and the reconstructed energy distribution, respectively. Black, blue and pink points are the spectral points obtained by the unfolding with Tikhonov, Schmelling and Bertero regularization methods, respectively. Black lines indicate the power law fitting to the Tikhonov results while the shaded areas indicate the error of the fitting.

Chapter 6

Analysis of *Fermi*-LAT public Data

MAGIC could observe gamma-rays from the Crab pulsar only above 25 GeV, which is apparently beyond the spectral cut-off point. In order to make progress in understanding the emission mechanism, the MAGIC results need to be discussed in connection with the lower energies. However, even after 9 years (April 1991 to May 2000) of operation of EGRET, which was the only GeV gamma-ray detector that could detect the Crab pulsar before 2007, only ~ 20 photons above 5 GeV had been detected from the Crab pulsar (see Fig. 2.28). This gap in energy coverage between MAGIC and EGRET was soon to be filled by data from a new instrument.

The Large Area Telescope (LAT) aboard the *Fermi* Gamma-ray Space Telescope was successfully launched on June 11, 2008. It can observe gamma-rays above 100 MeV and clearly saw the Crab pulsar up to ∼30 GeV after 8 months of operation (see [4]). It is certain that the data of *Fermi*-LAT help to interpret the results of MAGIC observations discussed in the previous chapter. Therefore, I analyzed one year of its data, which was made public in August 2009.

6.1 Detector Design of *Fermi*-LAT

The *Fermi* Gamma-ray Space Telescope is equipped with the Gamma-ray Burst Monitor (GBM) and the Large Area Telescope (LAT) (see the left panel of Fig. 6.1). The GBM consists of 12 thallium-activated sodium iodide (NaI(Tl)) scintillation counters and two bismuth germanate (BGO) scintillation counters (see [131]). Each counter has an area of 126 cm^2 and energy ranges are 8 keV to 1 MeV and 200 keV to 40 MeV, for the NaI(Tl) counter and the BGO counter, respectively. The primary aim of the GBM is to detect gamma-ray bursts and its data have not been made public. The LAT comprises trackers, calorimeters, and an anti-coincidence detector (see [31]). The LAT estimates the incoming direction and the energy of a gamma-ray by converting it into an electron-positron pair, which subsequently cause electromagnetic cascades inside the detector.

Tracker: There are 16 tracker modules (see the right panel of Fig. 6.1) and each of them has 18 (x, y) tracking planes. A tracking plane consists of two layers (x and y) of single-sided silicon strip detectors (35 cm long). The 16 planes at the top of the tracker are interleaved

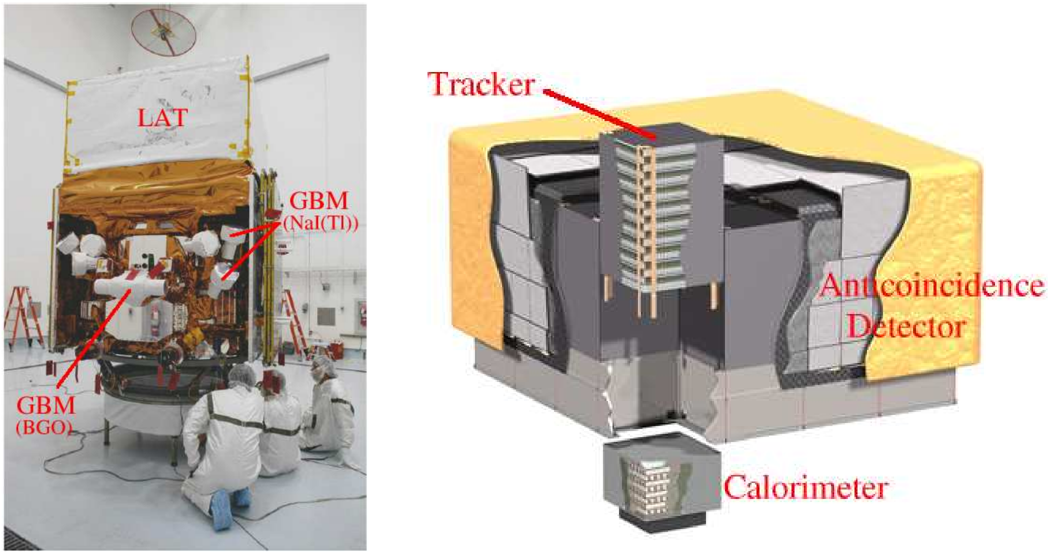

Figure 6.1: Left: A photograph of the Fermi Gamma-ray Space Telescope, adopted from [131]. The high energy gamma-ray (>100 MeV) detector LAT is seen at the top of the photograph. Six of the NaI(Tl) scintillation counters (for 8 keV to 1 MeV) and one of the BGO scintillation counters (for 200 keV to 40 MeV) which are for the gamma-ray burst monitor can also be seen. Right: The LAT detector. It consists of the tracker, the calorimeter and the anti-coincidence detector. Figure adopted from [31]. See text for details.

with high-Z converter material (tungsten) in which gamma-rays can convert to an electron-positron pair (see [31]). The total vertical depth of the tracker including support material amounts to 1.5 radiation lengths.

Calorimeter: The primary purpose of the calorimeter is twofold: 1) to measure the energy deposition due to the electromagnetic particle shower that results from the electron-positron pair produced by the incident photon and 2) to image the shower development profile, thereby providing an important background discriminator and an estimator of the shower energy leakage fluctuations. There are 16 calorimeter modules under the trackers (see the right panel of Fig. 6.1). Each of them has 96 cesium iodide crystals doped with thallium (CsI(Tl)) with a size of 2.7 cm × 2.0 cm × 32.6 cm. The crystals are optically isolated from each other and are arranged horizontally in eight layers of 12 crystals each. The total vertical depth of the calorimeter is 8.6 radiation lengths, i.e. 10.1 radiation lengths for the total instrument (see [31]).

Anti-coincidence detector: The purpose of the anti-coincidence detector is to provide charged-particle background rejection. [1] It surrounds the tracker modules (see the right panel of Fig. 6.1). High energy gamma-rays may cause a so-called "backsplash" effect in the

---

[1] The efficiency of charged particle detection is > 0.9997 (0.99999 when combined with the other subsystems). This is one of the key advantages compared to ground-based instruments, where it is impossible to install a primary hadron veto.

Parameter	Value or Range
Energy range	20 MeV - 300 GeV
Effective Area at normal incidence	9,500 cm^2
Energy resolution (equivalent Gaussian 1σ)	
100 MeV-1GeV (on-axis)	9%-15%
1 GeV-10GeV (on-axis)	8%-9%
10 GeV-300GeV (on-axis)	8.5%-18%
$>$10 GeV ($> 60^\circ$ incidence)	≤ 6%
Single Photon Angular resolution	
on-axis, 68% containment radius $\theta_{68\%}$:	
> 10 GeV	$\leq$0.15°
1 GeV	0.6°
100 MeV	3.5°
on-axis, 95% containment radius:	$3 \times \theta_{68\%}$
off-axis, containment radius at 55°	1.7 × on-axis value
Field of View (FoV)	2.4 sr
Timing accuracy	$< 10\mu$s
Event read-out time (dead time)	26.5 μs

Table 6.1: Summary of LAT Instrument Parameters and Estimated Performance.

massive calorimeter, i.e. isotropically distributed secondary particles (mostly 100-1000 keV photons) from the electromagnetic cascade can hit the anti-coincidence detector (the photons cause Compton scattering), creating false veto signals. The effect was present in EGRET and lowered the detection efficiency above 10 GeV by at least a factor of two. To minimize the false veto, the anti-coincidence detector is made up of 89 segmented plastic scintillators: A 5×5 array on the top and 4×4 arrays on each of the four sides. Each tile is read out by two photomultipliers coupled to wavelength shifting fibers. Tiles near the incident candidate photon trajectory may be considered for background rejection (see [31]).

6.2 Detector Performance of *Fermi*-LAT

The basic performance of the LAT is summarized in Table 6.1. Parameters are taken from [31]. The energy resolution is dependent on the energy and the incident angle (see the table) but it is roughly 10%, which is better than MAGIC (35% at 30 GeV, see Fig. 4.9). The large FoV (2.4 sr) would also be of great advantage to compensate for the small effective area. The timing accuracy of < 10 μs is also good enough to study the Crab pulsar. On the other hand, the angular resolution is rather poor (0.6 degree at 1 GeV), leading to large contamination of the galactic diffuse emission or nearby source emissions to the target source.

The systematic uncertainty in the energy scale was conservatively estimated to be $<$ 5% for 100 MeV to 1 GeV and $<$ 7% above 1 GeV, from the comparison between electron beam tests and their simulation (see [3] and [2]). The systematic uncertainty in effective area was evaluated by comparing Vela observation results and the simulation for them (see [3]). It is 10% below 100 MeV, decreasing to 5% at 560 MeV and increasing to 20% at 10 GeV and above.

6.3 Data Sample

After one year of operation, all the Fermi-LAT data and its analysis tools were made public in August 2009. I analyzed one year of data from 4th August 2008 to 3rd August 2009. Events with an energy between 100 MeV to 300 GeV and with an arrival direction of 20 degrees around the Crab pulsar were downloaded from the public *Fermi* website [209]. In order to have solid results, the events with a zenith angle smaller than 105 degrees and with the highest quality "Diffuse class", which means a high probability of being a photon, were selected. This event selection was performed by the Fermi official tool `gtselect` (see [209]). Events with imperfect spacecraft information and events taken when the satellite was in the South Atlantic Anomaly were also rejected. These selections were carried out by `gtmktime` (see [209]).

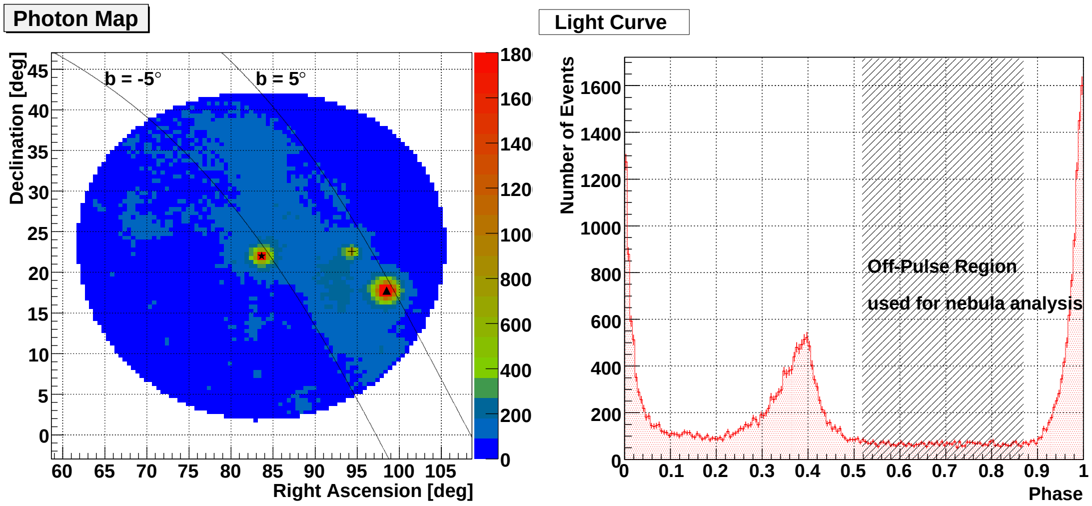

Figure 6.2: Left: An event distribution of all the Fermi-LAT data used in the analysis (100 MeV to 300 GeV) in equatorial coordinates. A star, a cross and a triangle indicate the positions of the Crab pulsar, IC 443 and the Geminga pulsar. Emissions from these sources are clearly seen. In addition, galactic diffuse emission is also visible. Right: A light curve of the Crab pulsar based on the Fermi-LAT data from 100 MeV to 300 GeV. The data between phase 0.52 and 0.87 (shaded area) are used for the nebula analysis. The nebula emission is a major background component for the pulsar analysis.

The sky map of all the data used is shown in the left panel of Fig. 6.2. The Crab pulsar is at the center of the map (star) and two more bright sources, namely, IC 443 (cross) and Geminga (triangle), can also be seen. In addition, the galactic diffuse gamma-ray emission is visible. Since the angular resolution of the LAT detector is ~ 3.5 degree at 100 MeV (see [31]), contamination from the nearby sources and the galactic diffused emission must be taken into account when the

Crab pulsar is analyzed. Moreover, emission from the Crab nebula must also be subtracted by using the pulse phase information.

6.4 The Light Curve

To make a light curve (phase diagram) of the Crab pulsar, first of all, the pulse phase must be assigned to each individual event. This is done by the official *Fermi* analysis tool, `gtpphase` (see [209]). It requires the pulsar ephemeris information and I used the "Jodrell Bank Crab Pulsar Monthly Ephemeris" for that, as I did for the MAGIC analysis (see Sect 4.7). Some of phase-resolved sky maps are shown in Fig. 2.1. Then, events from the direction around the Crab pulsar were extracted from the data set. Because the angular resolution has a strong energy-dependency, the extraction radius R [degree] should also be energy-dependent. I used the following radius R, which was also used in the *Fermi* official publication (see [4]):

$$R = \mathrm{Max}(6.68 - 1.76 * \log_{10}(E), 1.3)) \tag{6.1}$$

where E is the estimated energy which is already assigned for each event in the public data. R decreases linearly to $\log_{10}(E)$ until 1.14 GeV and stays constant at 1.3 degrees above this energy. It should be noted that the emissions from both the Crab pulsar and the Crab nebula are included within R. The angular resolution of *Fermi*-LAT does not enable a spatial resolution for the pulsar and the nebula.

The light curve obtained by all the LAT data used is shown in the right panel of Fig. 6.2. Energy-dependent light curves from 100 MeV to above 10 GeV are shown in Fig. 6.3. Below 10 GeV, the pulsations are seen with good precision. A flat continuum in the light curves is mainly from the continuous Crab nebula emission. Above 10 GeV, although the two pulses are clearly visible, the statistical uncertainties are larger than for lower energies. P1 (phases -0.06 to 0.04) and P2 (phases 0.32 to 0.43) have 12.1 ± 6.4 and 20.9 ± 7.3 excess events above 10 GeV with a significance of 2.0 and 3.2, respectively, with the background level (mainly from the nebula emission) estimated using the phases between 0.52 and 0.87.

There are several features visible in these light curves: The flux ratio between P1 and P2 is changing with the energy.The widths of the two pulses are decreasing as the energy goes higher. A hint of a possible third peak is visible at a phase around 0.75, but only above 10 GeV. These detailed features of the light curves will be discussed in Chapter 7, together with the MAGIC results and lower energy observations.

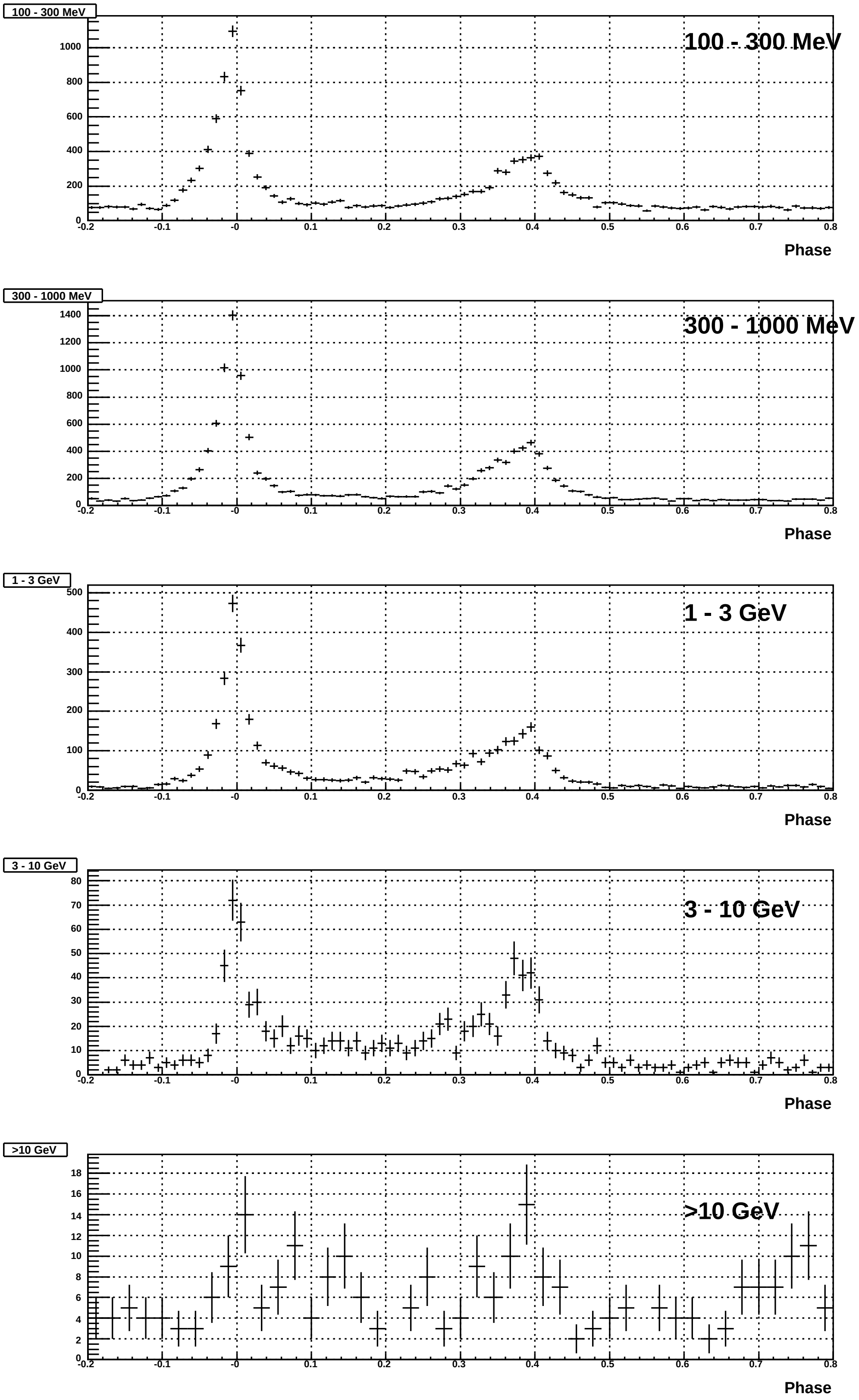

Figure 6.3: The light curves for different energies. From the top: 100 - 300 MeV, 300 - 1000 MeV, 1-3 GeV, 3-10 GeV and above 10 GeV. The energy dependence of P1/P2 ratio and the pulse width are visible. The possible third peak is also seen at a phase around 0.75, only above 10 GeV. A flat continuum in the light curves is mainly from the continuous Crab nebula emission.

6.5 The Crab Nebula Analysis

As is the case with MAGIC, the rather poor angular resolution of *Fermi*-LAT does not enable a spatial resolution for the Crab pulsar and the Crab nebula. Therefore, the nebula emission is the dominant background of the Crab pulsar emission for *Fermi*-LAT data. It must be properly analyzed by using the pulse phase information and, then, must be subtracted from the Crab pulsar emission. Fortunately, the analysis of the nebula has an important by-product: one can make sure of the analysis method by checking if the obtained energy spectrum is smoothly connected to the IACT measurements (see Sect. 2.9.7).

In order to analyze the nebula component, photons with the pulse phases from 0.52 to 0.87[2] (see the right panel of Fig. 6.2), where no pulsed emission is seen in lower energies, are assumed to be from the nebula (and other background photons such as galactic diffuse emission). The selection of the right phase events is carried out by the *Fermi*-LAT analysis tool gtselect. The effective observation time and the collection area are calculated by gtltcube and gtexpmap (see [209]). The spectrum is determined by means of the likelihood method, using the official tool gtlike (see [209]). It is done in the following way: The spectral shapes with several parameters of the sources in the FoV, the galactic and extragalactic diffuse emission models and the detector response function are assumed a priori. Then, the best parameters that maximize the likelihood of the observed data sets are determined. *P6_V3_Diffuse*, which is officially provided by the *Fermi*-LAT collaboration, was used for the detector response function, A simple power law spectrum was assumed for the IC 443 while a power law spectrum with an exponential cut-off was assumed for Geminga. For the extragalactic and galactic diffuse emission, *isotropic_iem_v02.txt* and *gll_iem_v02.fit*, which are included in the *Fermi*-LAT analysis tool package as a standard model, were used. For the Crab nebula, the spectrum based on the sum of the two power laws is assumed aiming for the synchrotron and the inverse Compton emission components, which have been suggested by the previous EGRET (see [114]) and IACT measurements (see e.g. [20], [11] and Fig. 2.30).

The spectrum of the Crab nebula calculated based on the *Fermi*-LAT data is shown in Fig. 6.4 as a red line. One can see that synchrotron spectrum is steeply falling from 200 MeV to 500 MeV and the inverse Compton component becomes dominant above 800 MeV. They can be described as

$$\frac{\mathrm{d}N}{\mathrm{d}E\mathrm{d}A\mathrm{d}T}_{sync} = (8.6 \pm 1.4) \times 10^{-11} (E/300\ \mathrm{MeV})^{-4.14\pm0.47} \tag{6.2}$$

$$\frac{\mathrm{d}N}{\mathrm{d}E\mathrm{d}A\mathrm{d}T}_{IC} = (7.3 \pm 0.7 \times 10^{-12} (E/1\ \mathrm{GeV})^{-1.68\pm0.05} \tag{6.3}$$

(6.4)

In order to make sure that the assumption of the spectral shape of the Crab pulsar is valid, the same data sets were divided into many subsets according to the energy. Then, the likelihood analysis was applied to each subset, assuming a simple power law in each small energy range.

---

[2] It is almost the same as the OP (off-pulse) phases defined in Sect. 2.9.5 but not exactly. Since the official *Fermi* publication used these phases for the nebula analysis (see [4]), I followed their example.

The red points in the figure indicate the results for the divided subsets. Instead of showing many short truncated lines, the value at the bin center and its error are shown. All the points are very well aligned along the line, showing the validity of the assumption.

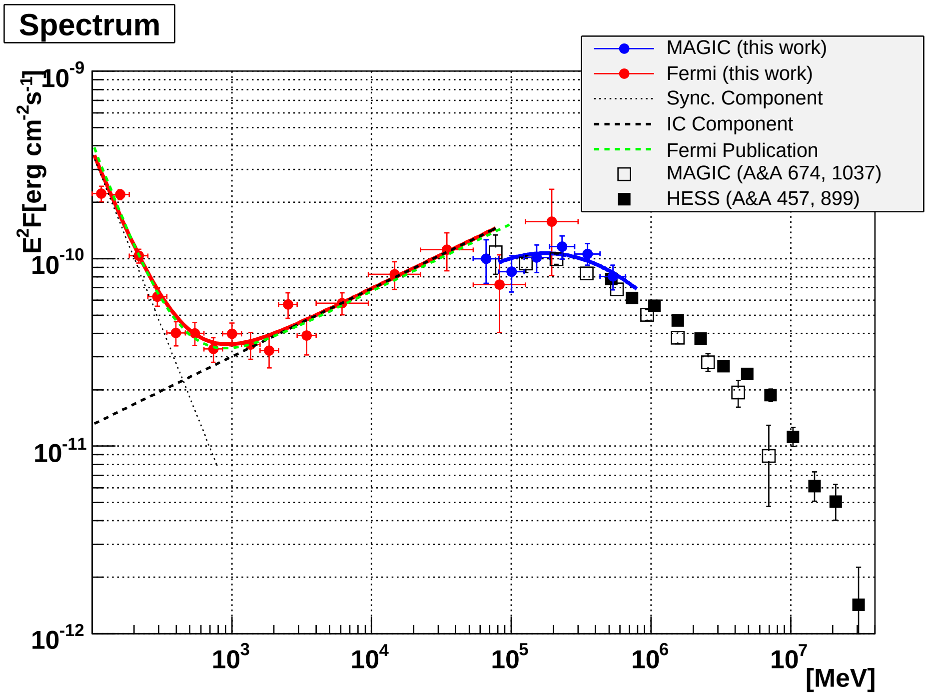

Figure 6.4: The energy spectrum of the Crab nebula. The red line and circles indicate the spectrum calculated by myself using one year of Fermi-LAT data. The green dashed line indicates the published spectrum from the $Fermi$ collaboration (see [4]). Blue circles, black open squares and black filled squares indicate the spectrum calculated by myself with the MAGIC observation data with the SUM trigger, the published spectrum from the MAGIC collaboration before the SUM trigger was installed (see [20]) and the published spectrum from the HESS collaboration (see [11]), respectively. The synchrotron and the inverse Compton components below 100 GeV are indicated by black dotted and black dashed lines, respectively.

The spectrum published by the *Fermi*-LAT collaboration with smaller data samples (8 months of data) (see [4]) are also shown in the same figure as a green dashed line, which is consistent with my analysis. The measurements by MAGIC (the published one and the one I calculated with the data samples used for the pulsar analysis) and by HESS are also shown in the same figure. The spectra are smoothly connected from 100 MeV to above 10 TeV. [3]

It should be noted that the poor statistics of *Fermi*-LAT data in the overlapped energy region from 50 GeV to 300 GeV does not allow a relative flux scale calibration between *Fermi*-LAT and MAGIC with a precision better than $\simeq 60\%$, which is larger than the systematic uncertainties of both experiments (see Sect. 4.12 and Sect. 6.2).

---

[3] The true spectrum should not be a simple power law from 10 to 100 GeV. Therefore, the $\simeq 50\%$ difference between the fitting line of *Fermi*-LAT data and that of MAGIC data at 100 GeV in Fig. 6.4 is not very meaningful.

6.6 The Crab Pulsar Spectrum

From the nebula analysis, all the background components (the nearby source emissions, the diffuse emissions and the nebula emission itself) have been determined. Keeping the spectral parameters for background components fixed, the pulsed component is analyzed with the same likelihood method. Analyses are made for four different phase intervals; TP (total pulse, phase 0.00 to 1.00), P1 (-0.06 to 0.04), P2 (0.32 to 0.43) and P1 + P2 (sum of P1 and P2). These definitions are the same as those described in Sect. 2.9.5.

6.6.1 Power Law + Cut-off Assumption for the Crab Pulsar Spectrum

Previous EGRET measurements show that the energy spectrum of the Crab pulsar can be well described by a power law between 100 MeV to a few GeV (see [114]), whereas non-detection by IACTs above 100 GeV (see [20]) imply the cut-off to be around 10 GeV as mentioned in Sect. 2.9.6. Therefore, I assumed the spectral shape as

$$\frac{\mathrm{d}^3F}{\mathrm{d}E\mathrm{d}A\mathrm{d}t} = f_1(E/1\ \mathrm{GeV})^{\Gamma_1}\exp(-(E/E_c)^{\Gamma_2}) \tag{6.5}$$

There are 4 free parameters, namely, the flux at 1 GeV f_1, the cut-off energy E_c, the power law index Γ_1 and the sharpness of the cut-off Γ_2 [4]. As discussed in Sect 2.8.2, in the case where the emission region is close to the pulsar surface, the cut-off should be sharp, i.e. Γ_2 should be significantly larger than 1, while, in the case where emission comes from the outer magnetosphere, Γ_2 should be 1. Therefore, estimation of Γ_2 is important for the investigation of the emission mechanism. However, due to the lack of statistics above 10 GeV, the likelihood analysis with four free parameters sometimes gives unstable results. Therefore, I made five analyses with three free parameters, i.e. with f_1, E_c, and Γ_1 being free parameters and with Γ_2 fixed to be 0.66, 1, 1.33, 1.66 and 2.

The results are shown in Fig. 6.5, Fig. 6.6 and Table 6.2. Hereafter, when $\Gamma_2 = 1$, the spectral cut-off shape will be called the "exponential cut-off", while when $\Gamma_2 = 0.66$, it will be called the "sub-exponential cut-off". The rest (with $\Gamma_2 > 1$) will be called the "super-exponential cut-off". In order to evaluate which assumption is more appropriate, the likelihood ratio $-\log(L/L_{ex})$ is calculated and shown in the seventh column of Table 6.2, where L and L_{ex} are the likelihood value for a given assumption and that for the exponential cut-off assumption, respectively. The eighth column shows the corresponding probability. The spectral parameters published by *Fermi*-LAT collaboration for TP under the exponential cut-off assumption [5] are also shown in the last row of Table 6.2. They are consistent with my analysis (compare with the first row).

What one can see from Fig. 6.5, Fig. 6.6 and Table 6.2 is the following:

---

[4] As can be seen in Eq. 6.5, although the flux above the cut-off energy is suppressed, a low flux can still be expected above the cut-off energy. A word "cut-off" does not mean extinction of a gamma-ray flux.

[5] *Fermi*-LAT collaboration reported these spectral parameters only under the exponential cut-off assumption in their publication [4]. In addition to the TP spectrum, they analyzed the spectrum of many narrow phase intervals (width $\simeq 0.01$). However, they did not publish the spectrum of P1 or P2, which I want to compare with MAGIC results in Chapter 7.

- No significant difference is seen in the power law index Γ_1 among different phase intervals (although Γ_1 is dependent on the sharpness of the cut-off Γ_2 due to a mathematical effect). For the exponential cut-off assumption, $\Gamma_1 \simeq -2.0$.
- The super-exponential assumptions are significantly worse than the exponential cut-off one. On the other hand, the sub-exponential cut-off assumption is as good as the exponential cut-off one.
- 80% of the total flux is from P1 + P2 at 1 GeV. P1 has twice as high a flux as P2 at 1 GeV.
- The cut-off energy is higher for P2 than for P1. The difference in the cut-off energy between TP and P1 + P2 implies a higher cut-off energy for the bridge emission than for P1 + P2.
- The flux of P1 and P2 become comparable at around 5 GeV because of the higher cut-off of P2. P2 dominates above 5 GeV.

The fact that super-exponential assumptions lead to worse fitting than the exponential one suggests that the emission region of gamma-rays is not close to the neutron star surface. This will be discussed further in Chapter 7. For the exponential cut-off model, the cut-off energies are estimated to be 6.1 ± 0.5, 4.5 ± 0.3, 3.7 ± 0.3 and 5.9 ± 0.7 GeV for TP, P1 + P2, P1 and P2 respectively.

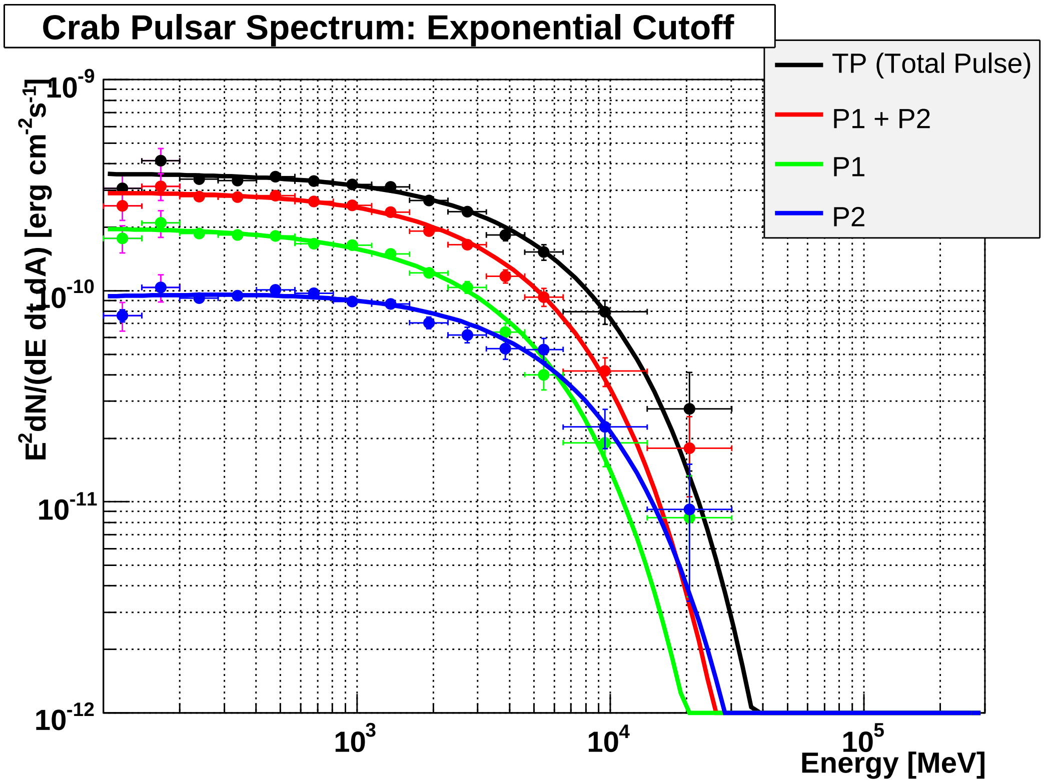

Figure 6.5: The energy spectra of the Crab pulsar for different phase intervals. The thick solid lines are determined by the likelihood analysis, assuming the spectral shape to be a power law with an exponential cut-off. The points are obtained by applying the same likelihood analysis to the small energy range, assuming a power law energy spectrum within the range (see text for details). For the the first two points below 200 MeV, where the systematic error strongly dominates the statistical error, the quadratical convolution of the systematic and statistical errors are indicated as pink lines.

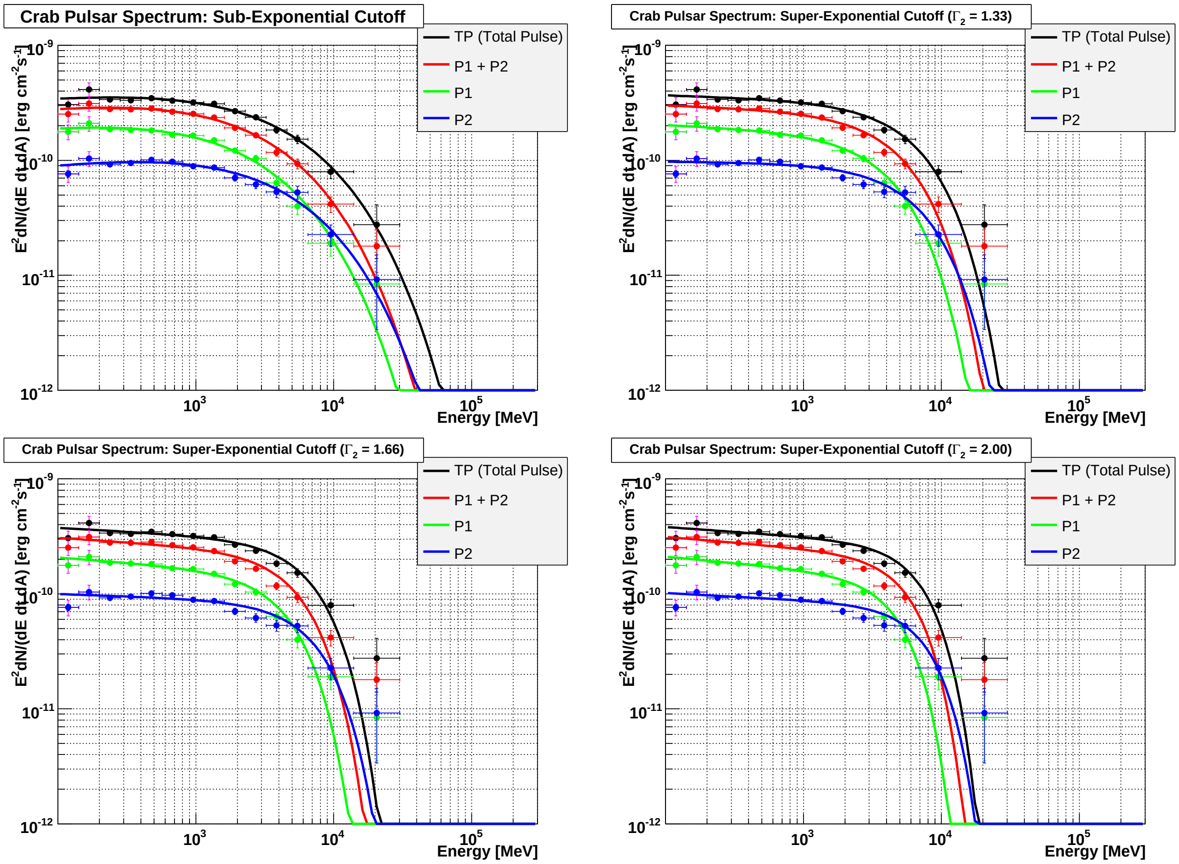

Figure 6.6: The same as Fig. 6.5 but with different spectral shape assumptions, namely, sub-exponential cut-off (top left), super-exponential cut-off with $\Gamma_2 = 1.33$ *(top right), super-exponential cut-off with* $\Gamma_2 = 1.66$ *(bottom left), and super-exponential cut-off with* $\Gamma_2 = 2.00$ *(bottom right)*

Model	Phase	f_1 [10^{-10}cm^{-2} s^{-1} MeV^{-1}]	Γ_1	Γ_2	E_c [MeV]	LR[a]	Rejection Power[b]
Exponential Cut-off	TP	2.32 ± 0.05	-1.99 ± 0.02	1	6111 ± 496	–	–
	P1 + P2	1.94 ± 0.05	-1.98 ± 0.02	1	4452 ± 307	–	–
	P1	1.29 ± 0.04	-1.99 ± 0.02	1	3682 ± 292	–	–
	P2	0.67 ± 0.02	-1.95 ± 0.03	1	5856 ± 740	–	–
Sub-exponential Cut-off $\Gamma_2 = 0.66$	TP	3.10 ± 0.13	-1.88 ± 0.02	0.66	3359 ± 379	1.6	1.9e-01 (0.9 σ)
	P1 + P2	2.80 ± 0.12	-1.85 ± 0.02	0.66	2198 ± 205	-4.8	–
	P1	1.94 ± 0.11	-1.85 ± 0.03	0.66	1791 ± 195	0.2	8.0e-01 (0.0 σ)
	P2	0.92 ± 0.06	-1.83 ± 0.04	0.66	3001 ± 511	-3.1	–
Super-exponential Cut-off $\Gamma_2 = 1.33$	TP	2.11 ± 0.03	-2.04 ± 0.01	1.33	7163 ± 493	2.7	6.6e-02 (1.5 σ)
	P1 + P2	1.71 ± 0.03	-2.04 ± 0.01	1.33	5536 ± 325	9.2	1.0e-04 (3.7 σ)
	P1	1.13 ± 0.03	-2.05 ± 0.02	1.33	4581 ± 303	3.3	3.7e-02 (1.8 σ)
	P2	0.60 ± 0.02	-2.01 ± 0.02	1.33	7272 ± 786	3.9	2.0e-02 (2.0 σ)
Super-exponential Cut-off $\Gamma_2 = 1.66$	TP	2.01 ± 0.03	-2.07 ± 0.01	1.66	7577 ± 472	7.8	4.2e-04 (3.3 σ)
	P1 + P2	1.61 ± 0.02	-2.08 ± 0.01	1.66	6085 ± 325	20.4	1.4e-09 (6.0 σ)
	P1	1.05 ± 0.02	-2.09 ± 0.01	1.66	5010 ± 296	8.6	1.8e-04 (3.6 σ)
	P2	0.57 ± 0.01	-2.04 ± 0.02	1.66	8025 ± 786	7.9	3.8e-04 (3.4 σ)
Super-exponential Cut-off $\Gamma_2 = 2.00$	TP	1.96 ± 0.02	-2.08 ± 0.01	2	7761 ± 458	14.1	7.6e-07 (4.8 σ)
	P1 + P2	1.55 ± 0.02	-2.10 ± 0.01	2	6411 ± 325	32.4	8.9e-15 (7.7 σ)
	P1	1.01 ± 0.02	-2.11 ± 0.01	2	5248 ± 286	15.1	2.9e-07 (5.0 σ)
	P2	0.55 ± 0.01	-2.06 ± 0.02	2	8496 ± 784	11.7	8.7e-06 (4.3 σ)
Fermi Publication							
Exponential Cut-off	TP	2.36 ± 0.06	-1.97 ± 0.02	1	5800 ± 500	–	–

[a] Likelihood ratio defined as $LR = -\log(L/L_{ex})$, where L and L_{ex} are the likelihood value for a given assumption and that for the exponential cut-off assumption.

[b] The probability corresponding to the LR value. It is also expressed as the corresponding deviation in the Gaussian distribution. When LR is negative, the probability is not calculated.

Table 6.2: The results of the likelihood analyses for different spectral shape assumptions. For the definition of the spectral parameters, see Eq. 6.5. The corresponding spectra are graphically shown in Fig. 6.5 and Fig. 6.6. The last row shows the spectral parameters from the Fermi-LAT publication for TP phase under the exponential cut-off assumption, taken from [4]. For other cut-off assumptions and for other phases (P1, P2 or P1 + P2), the spectral parameters were not reported in [4].

6.6.2 Power Law Extension Assumption for the Crab Pulsar Spectrum above the Cut-Off

It should be noted that the sharpness of the cut-off Γ_2 is already determined below ~ 7 GeV and the spectral shape above 7 GeV is not well determined due to the lack of statistics, as can be seen from the error bars in Fig. 6.5 and Fig. 6.6. Considering that the MAGIC results show power law spectra with an index of ~ -3.5 above 25 GeV (see Sect. 5.10), I examine a power law assumption for the spectra above the cut-off energy. The fact that the last point at 20 GeV is upwardly deviated from the exponential cut-off spectrum by $\simeq 1\sigma$ for all phase intervals (see Fig. 6.5) may support this assumption.

I selected data above 4 GeV and made a spectral analysis assuming a power law;

$$\frac{\mathrm{d}^3F}{\mathrm{d}E\mathrm{d}A\mathrm{d}t} = f_{10}(E/10\,\mathrm{GeV})^{\Gamma} \tag{6.6}$$

The results are shown in Fig. 6.7 and Table 6.3. In order to perform the likelihood ratio test with respect to the exponential cut-off assumption, the exponential cut-off assumption is also applied to the same data set. This time Γ_1 is fixed to the best value obtained by the previous analyses (see Table 6.2), so that the number of free parameters are the same (two) for the two models. The likelihood ratio (LR) and the corresponding probability are shown in the fifth and sixth columns of the table. None of the LRs are significantly large, which means that above 4 GeV the power law assumption is as good as the exponential cut-off assumption. The obtained spectral indices are $\sim -3.3 \pm 0.2$ and consistent with the ones obtained from the MAGIC data, as described in Sect. 5.10 (see Table 5.3). The spectra obtained with MAGIC data and *Fermi*-LAT data will be compared in more detail in the next chapter.

Model	Phase	f_{10} [10^{-13}cm^{-2}s^{-1} MeV^{-1}]	Γ	LR [a]	Rejection Power[b]
Power Law	TP	4.34 ± 0.42	-3.26 ± 0.15	1.3	2.8e-01 (0.6 σ)
	P1 + P2	2.55 ± 0.27	-3.35 ± 0.16	0.0	9.9e-01 (0.0 σ)
	P1	1.09 ± 0.19	-3.52 ± 0.26	-0.8	-
	P2	1.45 ± 0.20	-3.20 ± 0.21	0.6	5.5e-01 (0.0 σ)

[a] Likelihood ratio defined as $LR = -\log(L/L_{ex})$, where L and L_{ex} are the likelihood value for the power law extension assumption and that for the exponential cut-off assumption.

[b] The probability corresponding to the LR value. It is also expressed as the corresponding deviation in the Gaussian distribution. When LR is negative, the probability is not calculated.

Table 6.3: The results of the likelihood analyses assuming a power law spectrum (see Eq. 6.6) for different phase intervals. The corresponding spectra are graphically shown in Fig. 6.7

6.7 Concluding Remarks

By using one year of the public *Fermi*-LAT data, the Crab pulsar was analyzed from 100 MeV to ~ 30 GeV. Energy-dependent light curves show a few remarkable features, such as energy

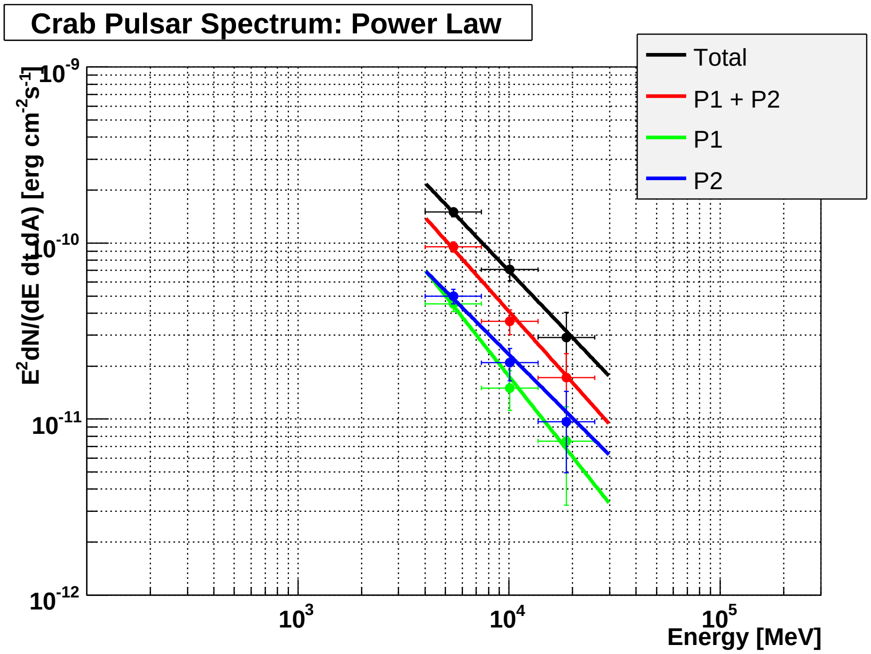

Figure 6.7: The energy spectra of the Crab pulsar above 4 GeV for different phase intervals. The thick solid lines are determined by the likelihood analysis assuming a power law spectrum. The points are obtained by applying the same likelihood analysis to the small energy range. Above 4 GeV, the spectra can be well described by a power law.

dependence of the pulse width and the P2/P1 ratio. The possible third peak is also seen only above 10 GeV. These features will be discussed in detail, combined with the MAGIC results and lower energy observations, in Chapter 7. The energy spectrum of the Crab pulsar can be well described by a power law with an exponential cut-off, indicating that the emission region is not close to the neutron star surface. The cut-off energies are estimated to be 6.1 ± 0.5 GeV, 4.5 ± 0.3 GeV, 3.7 ± 0.3 GeV, and 5.9 ± 0.7 GeV, for the TP, P1 + P2, P1 and P2, respectively. Due to the lack of statistics, the spectral shape above 7 GeV is not well determined. If data only above 4 GeV are analyzed, a power law function with an index of $\sim -3.3 \pm 0.2$ fits the data too, suggesting **the possibility that the energy spectrum is extending by a power law after the cut-off**. Actually, the spectral indices are consistent with the MAGIC results. These spectra obtained with *Fermi*-LAT data will be compared with the ones obtained by MAGIC in Chapter 7.

Chapter 7

Analysis of the Energy Spectrum and the Light Curve Combining MAGIC and *Fermi*-LAT results

MAGIC could measure the energy spectrum of the Crab pulsar from 25 GeV to 100 GeV, whereas *Fermi*-LAT could measure from 100 MeV to ~ 30 GeV. In this chapter, the energy spectrum and the light curve of the Crab pulsar from 100 MeV to 100 GeV is further investigated, by combining the results of the two experiments.

7.1 Energy Spectra of P1 + P2, P1 and P2

The energy spectra measured by MAGIC and *Fermi*-LAT are shown in Fig. 7.1. The top, the bottom left and the bottom right panels show those for P1 + P2, P1 and P2, respectively (see Sect. 2.9.5 for the definition of P1 and P2). Although the *Fermi*-LAT results are well described by a power law with an exponential cut-off or with a sub-exponential cut-off, the MAGIC results are apparently deviated from them. In Sect. 7.1.1 and Sect. 7.1.2, these deviations will be quantitatively examined, taking into account the systematic uncertainties of both experiments.

On the other hand, a power law can well describe both *Fermi*-LAT results above 4 GeV (see Sect. 6.6.2) and MAGIC results between 25 GeV and 100 GeV (see Sect. 5.10). The obtained spectral slopes from the two experiments seem similar. The power law assumption will be examined in Sect. 7.1.3, also taking into account the systematic uncertainties of both experiments.

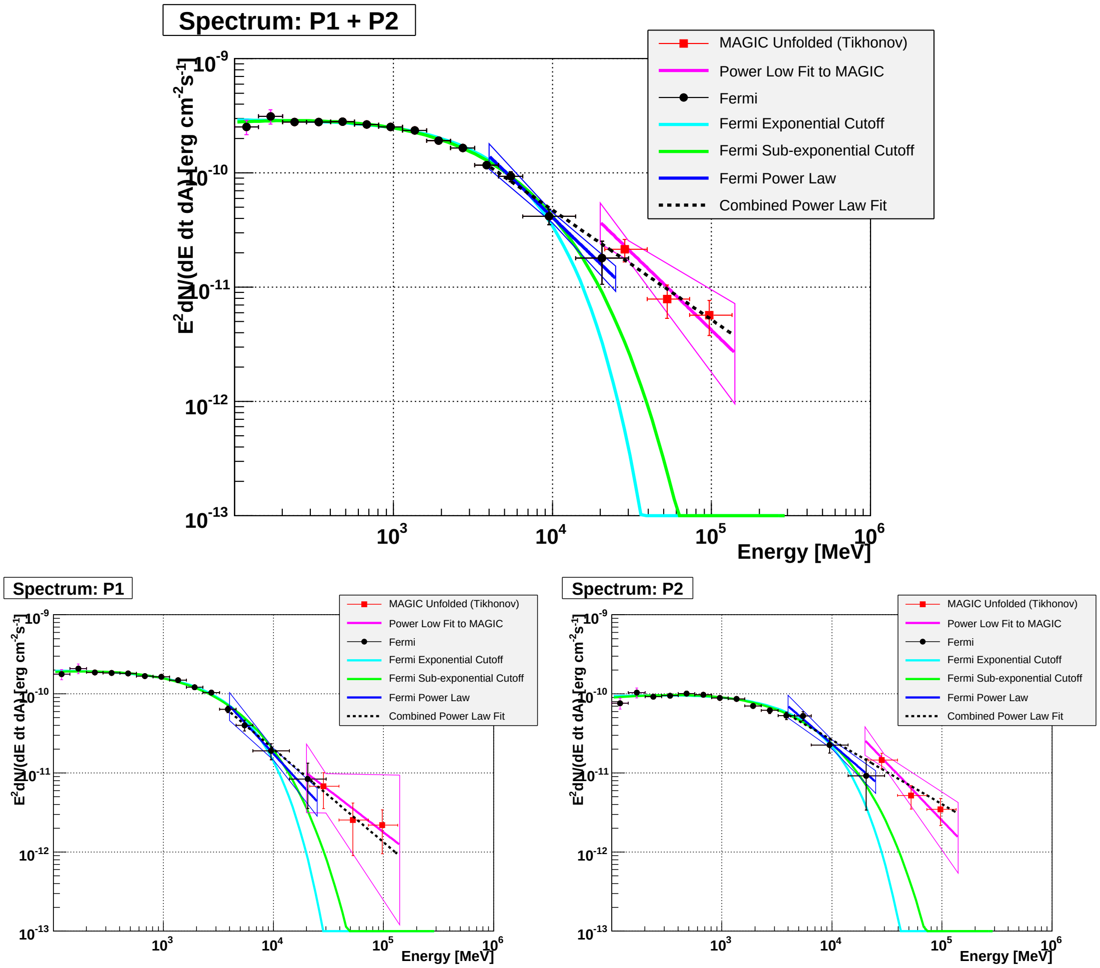

Figure 7.1: The comparison of the energy spectra of the Crab pulsar between Fermi-LAT measurements and MAGIC measurements for P1 + P2 (top), P1 (bottom left) and P2 (bottom right). The black and the red points indicate Fermi-LAT and MAGIC results, respectively. The sky blue and the green lines indicate the best fit spectra based on Fermi-LAT data, assuming a power law with an exponential cut-off and with a sub-exponential cut-off, respectively. The blue and the pink lines show the power law fits to the Fermi-LAT data above 4 GeV and MAGIC data, respectively. The statistical uncertainties of the fits are also shown by butterfly shape boxes with the corresponding color. Power law fits to the Fermi-LAT-MAGIC combined data above 4 GeV are shown by black dotted lines (see Sect. 7.1.3).

7.1.1 How Much Do the MAGIC Measurements Deviate from an Exponential Cut-off Spectrum?

In general, the theoretical calculations based on the outer magnetosphere emission hypothesis (the OG model or the SG model) predict an exponential cut-off at 1 - 10 GeV in the Crab pulsar energy spectrum, as discussed in Sect. 2.8.2, with which *Fermi*-LAT results are indeed consistent. However, as can be seen from Fig. 7.1, the MAGIC measurements seem to be deviated from the extrapolation from the *Fermi*-LAT measurements assuming that the spectra of P1, P2, and P1 + P2 above 25 GeV follow a power law with an exponential cut-off. Here, I evaluate these deviations.

Method: χ^2 Test on $SIZE$ Distributions

The power law spectra with an exponential cut-off for P1, P2 and P1 + P2 obtained by *Fermi*-LAT data (see Table 6.2) are assumed to be also valid above 25 GeV. By means of MC with these energy spectra, expected $SIZE$ distributions of excess events for P1, P2 and P1 +P2 in the MAGIC data are computed. Then, χ^2 tests are performed between these MC predictions and the actual observed distributions. The binning of the $SIZE$ distribution is $30 - 50$, $50 - 100$ and $100 - 400$, which is the same as for the spectrum calculations (see Sect. 5.10.1) except that the highest two bins are combined so that all bins have a meaningful number of excess events (with respect to the statistical uncertainty) in the data. Among the free parameters in the *Fermi*-LAT likelihood analysis, the uncertainty of the cut-off energy has the largest effect on the expected $SIZE$ distribution in the MAGIC data. Therefore, the analysis is repeated while changing the cut-off energy from 1 GeV to 25 GeV. This method is schematically shown in Fig. 7.2.

It should be noted that this method does not involve the energy reconstruction, which suffers the poor energy resolution and the trigger bias effect below 100 GeV (see Sect.4.9.3). $SIZE$ (total charge in a shower image) is one of the most reliable image parameters and a good indicator of the gamma-ray energy. Therefore, a robust evaluation of the deviation can be expected for this method.

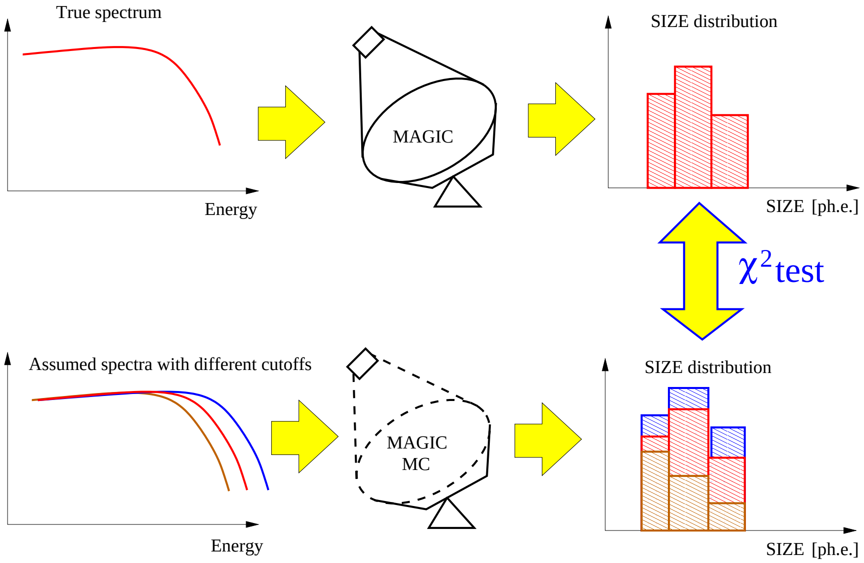

Figure 7.2: Schematical explanation of the method for evaluating the inconsistency between MAGIC and Fermi-LAT under the exponential cut-off spectrum assumption. A power law with an exponential cut-off is assumed for the spectral shape in MC. A power law part is taken from the Fermi-LAT measurements, while the cut-off energy is varied from 1 GeV to 25 GeV. A χ^2 *test is performed between the* $SIZE$ *distribution of the observed data and that of the MC for each cut-off energy. See text for details.*

Results of the χ^2 Tests on $SIZE$ Distributions

The top left panel of Fig. 7.3 shows the χ^2 value as a function of the cut-off energy. The number of degree of freedom is three. The corresponding upper probability is expressed with the corresponding Gaussian deviation and is indicated by black dotted lines. The green lines on the plot indicate the cut-off energies with statistical errors obtained from the *Fermi*-LAT data, i.e. (4.45 ± 0.31) GeV , (3.68 ± 0.29) GeV and (5.86 ± 0.74) GeV for P1 + P2, P1 and P2, respectively (see Table 6.2). The top right panel of Fig. 7.3 shows the comparison of $SIZE$ distributions between the observed data and the MC predictions for the *Fermi*-LAT-determined cut-off energies. Based on these $SIZE$ distributions, the inconsistencies between the exponential cut-off spectra determined by *Fermi*-LAT and the MAGIC measurements are estimated to be at $(6.77 \pm 0.13)\sigma$, $(3.01 \pm 0.06)\sigma$ and $(6.04 \pm 0.26)\sigma$ levels for P1 + P2, P1 and P2, respectively. The cut-off energies that minimize the χ^2 values are estimated to be (11.7 ± 0.7) GeV, (8.9 ± 0.9) GeV and (15.4 ± 1.2) GeV for P1 + P2, P1 and P2, respectively, which are also in clear contradiction with the *Fermi*-LAT-determined cut-off energies. The bottom panel shows the comparison of $SIZE$ distributions between the observed data and the MC predictions for the cut-off energies that minimize the χ^2 values. These results are summarized in Table 7.1

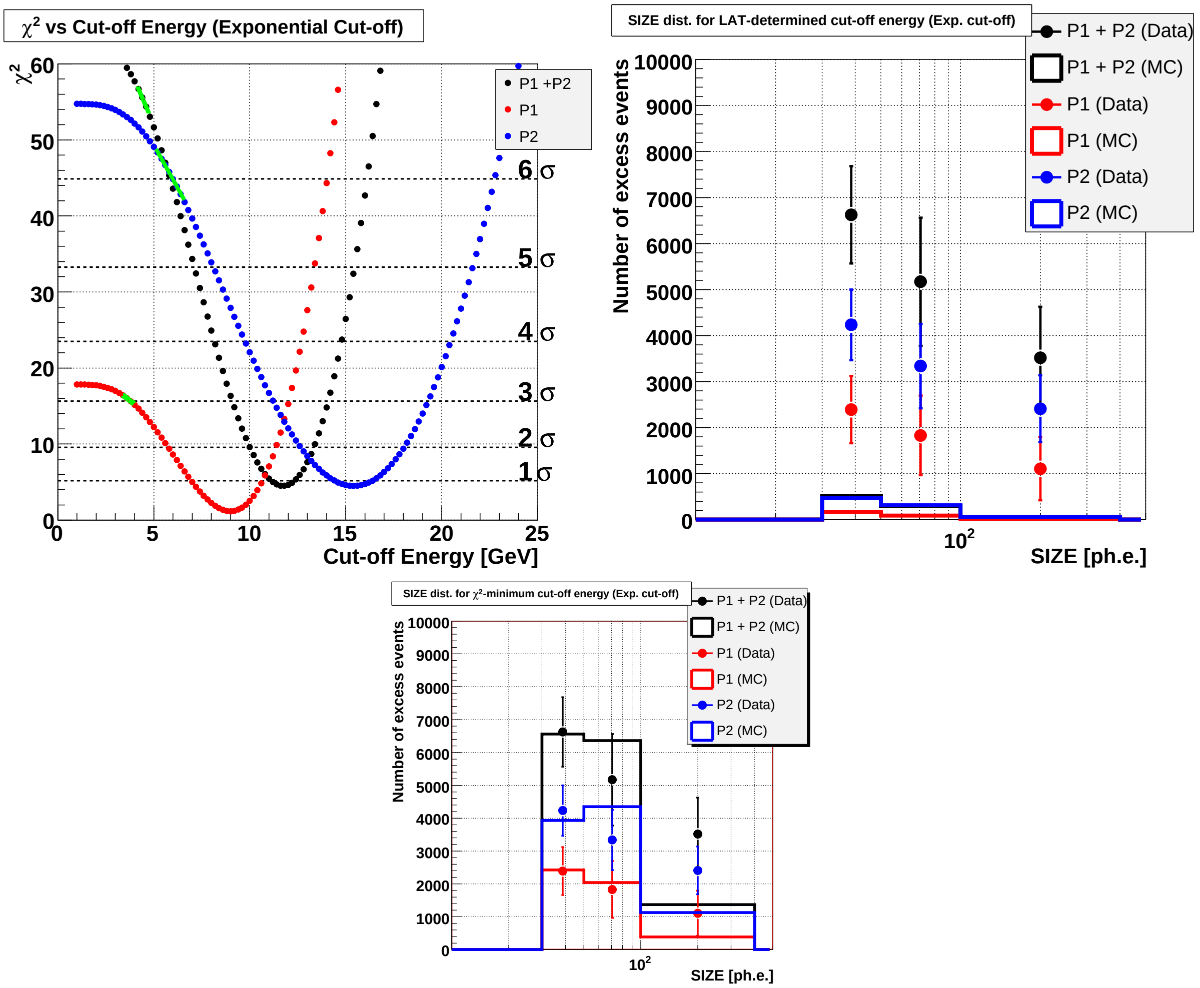

Figure 7.3: The evaluation of the consistency between the Fermi-LAT and the MAGIC results under the exponential cut-off assumption. Top left: χ^2 *value based on the* $SIZE$ *distribution of the MC prediction and that of the observed data, as a function of the cut-off energy. The number of degree of freedom is three. The corresponding upper probability is expressed with the corresponding Gaussian deviation and is indicated by black dotted lines. The black, the red and the blue points indicate P1 + P2, P1 and P2, respectively. Green bars on the plot indicate the cut-off energy and its statistical uncertainty obtained with the Fermi-LAT data. Top Right: The comparison of the* $SIZE$ *distributions between the observed data and MC predictions. The cut-off energies obtained from the Fermi-LAT data are used for MC. Bottom: The same as the top right panel but the cut-off energies which minimize the* χ^2 *are used for MC.*

Effect of Systematic Uncertainties

As mentioned in Sect. 4.12 and 6.2, the systematic uncertainties in the energy scale of MAGIC and *Fermi*-LAT above 10 GeV are 20% and 7%, respectively, while the systematic uncertainties in the effective area (including the effective observation time) of MAGIC and *Fermi*-LAT above 10 GeV are 10% and 20%, respectively. The apparent contradiction between *Fermi*-LAT and MAGIC measurements under the exponential cut-off assumption could be not due to the wrong assumption but due to these systematic uncertainties of the two experiments.

In order to examine this possibility, I made the same analysis but scaling down the energy for MAGIC by 30%, i.e., the spectrum $F_{MAGIC}(E)$ used in the MC is defined as

$$F_{MAGIC}(E) = F_{LAT}(0.7E) \tag{7.1}$$

where $F_{LAT}(E)$ is the power law with an exponential cut-off whose power law part is based on the *Fermi*-LAT measurements and whose cut-off energy is a parameter ranging from 1 GeV to 25 GeV. This 30% would be very conservative compared to the systematic uncertainties of both experiments. On the other hand, no correction for the effective area is applied because the uncertainty of the energy scale should dominate the effect on the results, due to the steep fall-off of the spectrum at MAGIC energies.

The χ^2 value as a function of the cut-off energy is shown in the left panel of Fig. 7.4. The comparison of the $SIZE$ distributions between the observed data and the MC predictions for the *Fermi*-LAT-determined cut-off energies is shown in the right panel of the figure. Even after 30% of energy scaling, the discrepancies in the $SIZE$ distributions are $(5.63 \pm 0.33)\sigma$, $(2.32 \pm 0.25)\sigma$ and $(4.86 \pm 0.60)\sigma$ level for P1 + P2, P1 and P2, respectively.The cut-off energies that minimize the χ^2 values are (8.2 ± 0.5) GeV, (6.1 ± 0.6) GeV and (10.9 ± 0.9) GeV. These values are also significantly inconsistent with the *Fermi*-LAT-determined values. These results are summarized in Table 7.1

From these discrepancies, it is evident that the exponential cut-off assumption is not valid at MAGIC energies (> 25 GeV). The extension of the pulsed gamma-ray emission observed by MAGIC requires a modification of the current pulsar models, which will be further discussed in Sect. 8.2.

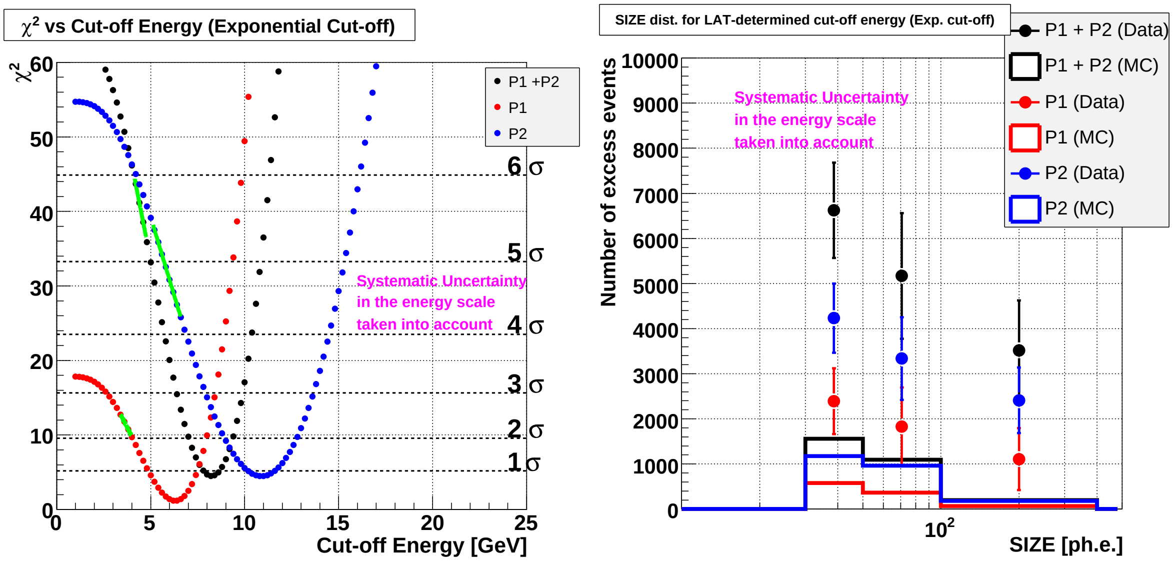

Figure 7.4: Left: χ^2 value based on the $SIZE$ distribution of the MC prediction and that of the observed data, as a function of the cut-off energy. The number of degree of freedom is three. The corresponding upper probability is expressed with the corresponding Gaussian deviation and is indicated by black dotted lines. The black, the red and the blue points indicate P1 + P2, P1 and P2, respectively. Green bars on the plot indicate the cut-off energy and its statistical uncertainty obtained with the Fermi-LAT data. The energy scale of the MAGIC data are artificially lowered by 30% in order to examine the possibility that systematic uncertainties of both experiments is the reason for the discrepancy. Right: The comparison of the $SIZE$ distributions between the observed data and the MC predictions for the cut-off energies obtained by Fermi-LAT data.

7.1.2 How Much Do the MAGIC Measurements Deviate from an Sub-Exponential Cut-off Spectrum?

As discussed in Sect.2.7.2 and Sect. 2.8.2, nearly monoenergetic electrons (as many of theoretical models assume, see e.g. [93], [177], [104] and [175]) produce an exponential cut-off, i.e., Γ_2 in Eq. 6.5 is 1. On the other hand, if Γ_2 is smaller than 1, the inconsistency between the *Fermi*-LAT measurements and the MAGIC measurements would become smaller than for the exponential cut-off assumption.

Since *Fermi*-LAT results can also be explained by the sub-exponential cut-off assumption ($\Gamma_2 = 0.66$, see Sect. 6.6.1), I examine the sub-exponential cut-off assumption. It should be noted that $\Gamma_2 < 1$ implies that the responsible electrons are not monoenergetic. In this case, no theoretical predictions for Γ_2 exist. I take the sub-exponential cut-off assumption ($\Gamma_2 = 0.66$) as one of the most extreme assumptions [1]

Method: χ^2 Test on $SIZE$ Distributions

The method is the same as the one for the exponential cut-off assumption (see Sect. 7.1.1) except that $\Gamma_2 = 0.66$ (see Eq. 6.5) is used for the steepness of the cut-off.

Results of the χ^2 Tests on $SIZE$ Distributions

The top left panel of Fig. 7.3 shows the χ^2 value as a function of the cut-off energy. The number of degree of freedom is three. The corresponding upper probability is expressed with the corresponding Gaussian deviation and is indicated by black dotted lines. The green lines on the plot indicate the cut-off energies for the sub-exponential cut-off with statistical errors obtained from the *Fermi*-LAT data, i.e. (2.20 ± 0.20) GeV , (1.79 ± 0.20) GeV and (3.00 ± 0.51) GeV for P1 + P2, P1 and P2, respectively (see Table 6.2). The top right panel of Fig. 7.5 shows the comparison of $SIZE$ distributions between the observed data and the MC predictions for the *Fermi*-LAT-determined cut-off energies. Although discrepancies are smaller than those for the exponential cut-off case because of the more gradual cut-off, the inconsistencies between the sub-exponential cut-off spectra determined by *Fermi*-LAT and the MAGIC measurements are at $(6.04 \pm 0.26)\sigma$, $(2.55 \pm 0.23)\sigma$ and $(5.35 \pm 0.58)\sigma$ levels for P1 + P2, P1 and P2, respectively. The cut-off energies that minimize the χ^2 values are (4.8 ± 0.3) GeV, (3.4 ± 0.4) GeV and (6.6 ± 0.5) GeV for P1 + P2, P1 and P2, respectively, which are also in clear contradiction with the *Fermi*-LAT-determined cut-off energies. The bottom panel shows the comparison of $SIZE$ distributions between the observed data and the MC predictions for the cut-off energies that minimize the χ^2 values.

---

[1] In the case of the Vela pulsar, the energy spectrum of the total pulse (phase 0 to 1) measured by *Fermi*-LAT shows Γ_2 in Eq. 6.5 to be 0.69 ± 0.02 (see [6]). On the other hand, the energy spectrum from each narrow phase interval (width $\simeq 0.01$) is still consistent with an exponential cut-off spectrum. In this analysis of the Crab pulsar, the widths of phase intervals are 0.1, 0.11 and 0.21 for P1, P2 and P1 + P2. Therefore, $\Gamma_2 = 0.66$ would be rather an extreme assumption.

Effect of the systematic uncertainties

The effect of the systematic uncertainties of the two experiments can be taken into account in the same way as for the exponential cut-off case, i.e. the spectrum $F_{MAGIC}(E)$ used in the MC is scaled down by 30% (see Eq. 7.1).

The χ^2 value as a function of the cut-off energy is shown in the left panel of Fig. 7.6. The comparison of the $SIZE$ distributions between the observed data and the MC predictions for the *Fermi*-LAT-determined cut-off energies are shown in the right panel of Fig. 7.6. After 30% of energy scaling, the inconsistencies in the $SIZE$ distribution are at $(4.37 \pm 0.65)\sigma$, $(1.25 \pm 0.62)\sigma$ and $(3.71 \pm 1.08)\sigma$ levels for P1 + P2, P1 and P2, respectively. The sub-exponential cut-off spectrum might explain the energy spectrum of P1 if the systematic uncertainties of the two experiments are conservatively taken into account. However, P1 + P2 and P2 are still largely inconsistent. The cut-off energies that minimize the χ^2 values are (3.39 ± 0.23) GeV, (2.40 ± 0.26) GeV and (4.77 ± 0.38) GeV. These values are still inconsistent with the *Fermi*-LAT-determined values. These results are summarized in Table 7.1.

The power law with a sub-exponential cut-off is not valid for P1 + P2 and P2 at the MAGIC energies (> 25 GeV).

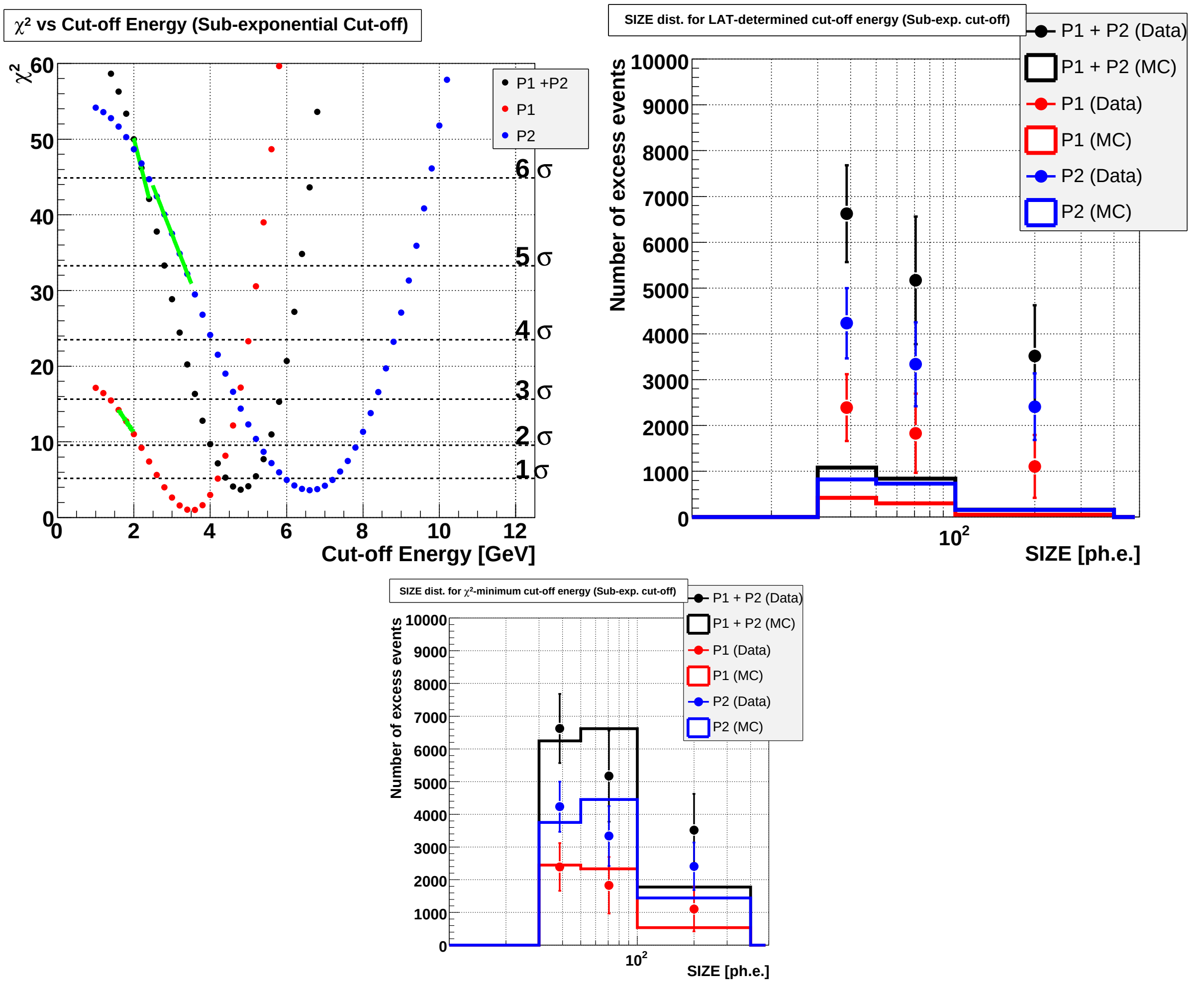

Figure 7.5: The same as Fig. 7.3 but for the sub-exponential cut-off assumption.

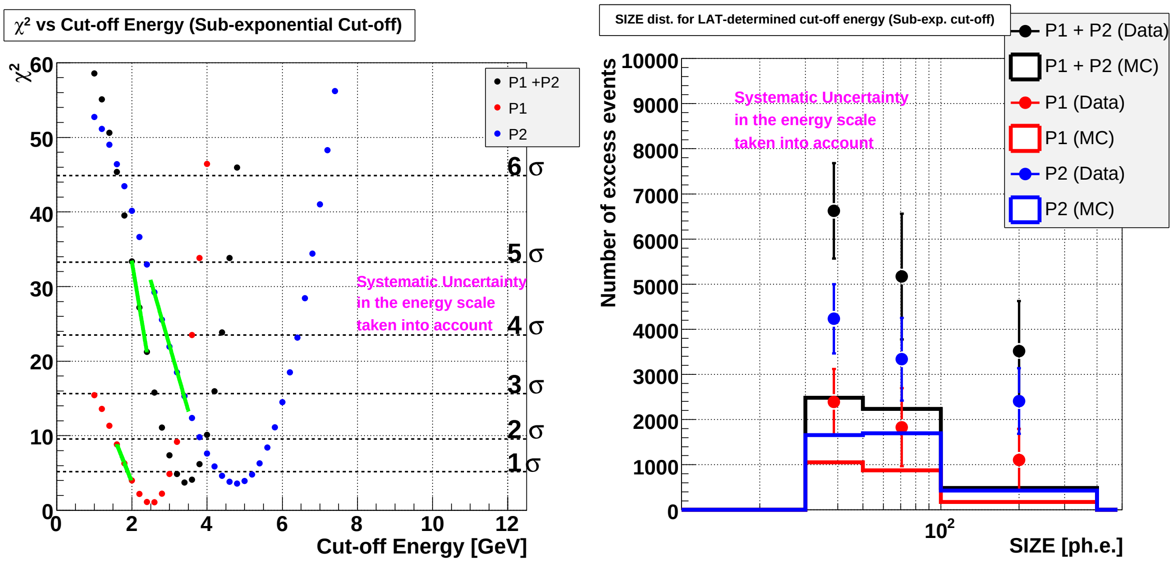

Figure 7.6: The same as Fig. 7.4 but for the sub-exponential cut-off assumption

Model	Phase	E_c^{Fermi} [GeV] [a]	E_c^{M} [GeV] [b]	Scale [c]	χ^2 from $SIZE$ [d]	Rejection Power [e]
Exponential Cut-off	P1 + P2	4.45 ± 0.31	11.68± 0.74	1	53.4 – 57.0	6.6 – 6.9 σ
	P1	3.68 ± 0.29	8.86± 0.91	1	15.3 – 16.4	3.0 – 3.1 σ
	P2	5.86 ± 0.74	15.39± 1.19	1	42.1 – 48.8	5.8 – 6.3 σ
Sub-exponential Cut-off	P1 +P2	2.20 ± 0.20	4.77± 0.31	1	42.1 – 50.2	5.8 – 6.4 σ
	P1	1.79 ± 0.20	3.43± 0.36	1	11.3 – 14.2	2.3 – 2.8 σ
	P2	3.00 ± 0.51	6.59± 0.52	1	30.8 – 44.0	4.8 – 5.9 σ
Exponential Cut-off	P1 + P2	4.45 ± 0.31	8.17± 0.53	0.7	36.5 – 44.4	5.3 – 6.0 σ
	P1	3.68 ± 0.29	6.12± 0.63	0.7	9.9 – 12.8	2.1 – 2.6 σ
	P2	5.86 ± 0.74	10.86± 0.85	0.7	25.8 – 38.3	4.3 – 5.5 σ
Sub-exponential Cut-off	P1 + P2	2.20 ± 0.20	3.39± 0.23	0.7	21.1 – 33.5	3.7 – 5.0 σ
	P1	1.79 ± 0.20	2.40± 0.26	0.7	4.0 – 8.9	0.6 – 1.9 σ
	P2	3.00 ± 0.51	4.77± 0.38	0.7	13.2 – 31.0	2.6 – 4.8 σ

[a] The cut-off energy determined by the *Fermi*-LAT data

[b] The cut-off energy estimated by the $SIZE$ distribution in MAGIC data, assuming that the power law part determined by the *Fermi*-LAT data is valid.

[c] The energy scaling factor. This factor is applied to the MAGIC energy.

[d] χ^2 value calculated from the $SIZE$ distributions of the observed data and the MC prediction. The number of degree of freedom is three.

[e] The probability that the two results are consistent, expressed in the corresponding Gaussian deviation. This is calculated from the χ^2 value.

Table 7.1: Evaluation of the inconsistency between the MAGIC measurements and the exponential/sub-exponential cut-off spectra determined by Fermi-LAT.

7.1.3 Power Law Fit above 4 GeV

The super-exponential cut-off assumption is ruled out by the *Fermi*-LAT results alone (see Sect. 6.6.1). Moreover, it is now evident that neither the exponential cut-off nor the sub-exponential cut-off can explain the observational results of *Fermi*-LAT and MAGIC consistently.

On the other hand, a power law can well describe both the *Fermi*-LAT results above 4 GeV (see Sect. 6.6.2) and MAGIC results between 25 GeV and 100 GeV (see Sect. 5.10), as can be seen in Fig. 7.1. In this section, an assumption that the spectra above 4 GeV follow a power law is examined.

Method: Combined Fit to *Fermi*-LAT and MAGIC Data

A power law function is fitted to the data points of *Fermi*-LAT and MAGIC together. In order to take into account a possible energy scale difference between the two experiments, the correction factor κ is introduced to the power law function as:

$$\begin{aligned} \frac{\mathrm{d}^3F(E)}{\mathrm{d}E\mathrm{d}A\mathrm{d}t} &= f_{10}(aE/10\mathrm{GeV})^{\Gamma} \\ a &= \begin{cases} 1 & (E \leq 25\mathrm{GeV}) \\ \kappa & (E > 25\mathrm{GeV}) \end{cases} \end{aligned} \tag{7.2}$$

Fermi-LAT points are statistically independent of each other but MAGIC data points are correlated, due to the unfolding procedure. This correlation will be taken into account when fitting is applied. Firstly, κ is fixed to 1 and then, secondly, κ is treated as a free parameter.

Results of Combined Fit to *Fermi*-LAT and MAGIC Data

The results are shown in Fig. 7.7 and Table 7.2. Even without relative energy correction, i.e. with κ fixed to 1, the fitting probability is high enough (see the fifth column of the Table). By making κ a free parameter, $\chi 2$ values are only slightly reduced and the obtained κs do not significantly deviate from 1. As a result, f_{10} and Γ do not change significantly. Γ is about 3 for all the phase intervals and a significant difference is not seen.

The physics interpretation of this result will be discussed in Sect.8.2.

Phase	f_{10} [10^{-7} cm^{-2}s^{-1}TeV^{-1}]	Γ	Scaling Factor κ	$\chi^2/dof(Prob.)$
P1 + P2	2.96 ± 0.20	-2.96 ± 0.08	1	8.09 / 5 (0.15)
P1	1.26 ± 0.16	-3.18 ± 0.16	1	1.98 / 5 (0.85)
P2	1.63 ± 0.13	-2.81 ± 0.08	1	9.29 / 5 (0.10)
P1 + P2	2.61 ± 0.30	-3.12 ± 0.14	0.83 ± 0.09	5.54 / 4 (0.24)
P1	1.16 ± 0.21	-3.29 ± 0.22	0.87 ± 0.15	1.40 / 4 (0.84)
P2	1.40 ± 0.21	-3.00 ± 0.18	0.82 ± 0.12	7.56 / 4 (0.11)

Table 7.2: The power law fit combining the Fermi-LAT data above 4 GeV and the MAGIC data

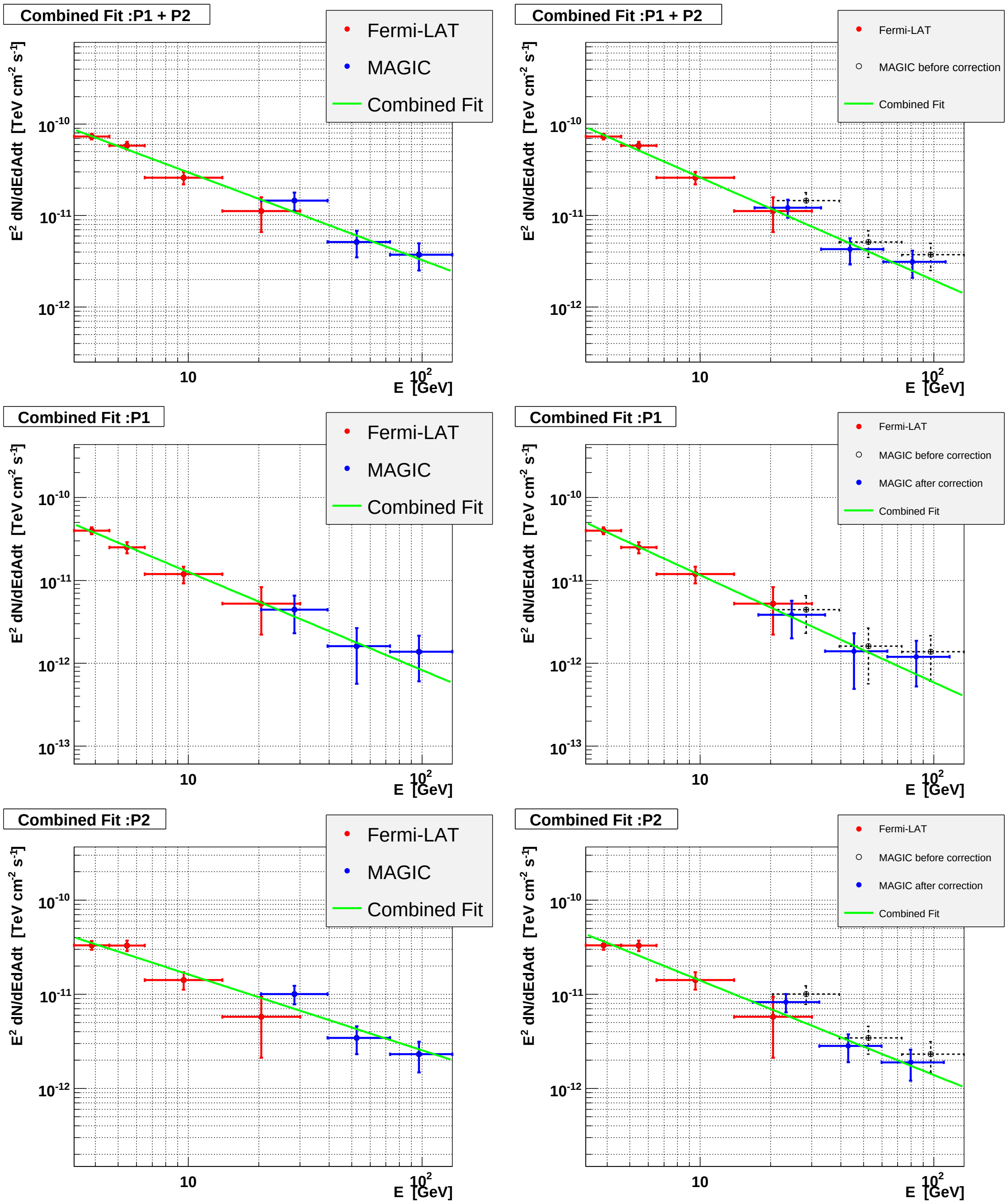

Figure 7.7: The power law fitting, combining the Fermi-LAT data above 4 GeV and the MAGIC data. The correlation among the MAGIC points is taken into account. The left panels show the case when the energy scales of both experiments are used while the right panels show the case when a shift in the energy scale of MAGIC is allowed by letting κ in Eq. 7.2 be a free parameter. Top, middle and bottom panels show P1 + P2, P1 and P2, respectively. The best fit parameters and fitting probabilities are shown in Table 7.2. The fitted lines without the energy scaling (left panels) are also shown in Fig. 7.1 as black dotted lines.

7.2 P2/P1 Ratio and Bridge/P1 Ratio

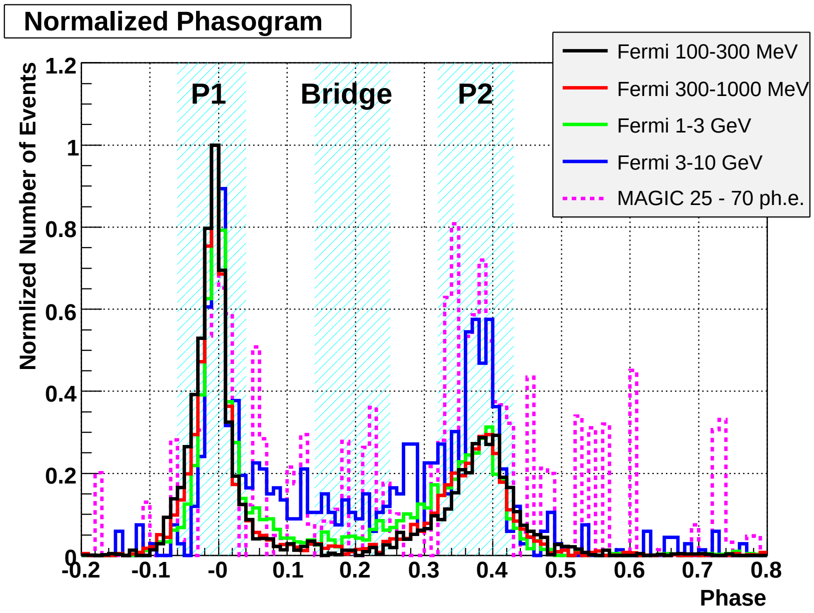

Figure 7.8: Overlaid light curves from different energies. The vertical values are normalized such that the heights of the P1 peak are equal. The energy dependence of the P2/P1 ratio and Bridge/P1 ratio are clearly seen.

Name	P1	Bridge	P2	OP
Phase Interval	-0.96 to 0.04	0.14 to 0.25	0.32 to 0.43	0.52 to 0.88

Table 7.3: The Definition of Names of Pulse Phases

The light curves for different energies such as Fig. 5.15 and Fig. 6.3 suggest that the flux ratio between P1 and P2 changes with energy. The fraction of the Bridge emission seems to be energy-dependent, too. Some of the light curves from different energies are overlaid in Fig. 7.8 in order to show the energy dependence of the P2/P1 ratio and the Bridge/P1 ratio. The P2/P1 ratio and/or the Bridge/P1 ratio have been studied by many authors such as [114], [183], [132], [126] and [127] for a wide energy range from optical to gamma-rays. On the one hand, the energy dependence of these ratios can be thought of as a consequence of the different energy spectra for different phase intervals. On the other hand, taking the flux ratio between two phase intervals cancels out the systematic uncertainty of the absolute flux scale for different detectors. Therefore, these ratios enable to study precisely the relative spectral behavior of different phase intervals for a very wide energy range using the measurements from many different detectors.

Here, I calculate the P2/P1 and Bridge/P1 ratios for *Fermi*-LAT and MAGIC data and compare them with the lower energy results.

Method: Calculation of Energy-dependent P2/P1 and Bridge/P1 Ratios from Light Curves

Fermi-LAT data sets are divided into 5 bins in energy, 100 - 300 MeV, 300 - 1000 MeV, 1 - 3 GeV, 3 - 10 GeV and above 10 GeV. MAGIC data are divided into two bins in $SIZE$, 25 - 70 ph.e. and 70 - 500 ph.e.. The number of excess events for P1, P2 and Bridge are calculated from light curves of each energy bin, by estimating background by OP phases (For the definition of P1, P2, Bridge and OP, see Sect. 2.9.5 and Table 7.3.). Then, the ratio of P2 to P1 and that of Bridge to P1 are computed.

Results of Energy-dependent P2/P1 and Bridge/P1 Ratios

The numbers of excess events of P1, P2 and Bridge as a function of energy are shown in the left panel of Fig. 7.9 and Table 7.4. In the energy ranges of above 10 GeV for *Fermi*-LAT and 70 - 500 ph.e. for MAGIC, no significant excess was found in Bridge phases. Therefore, 95% confidence level upper limits are shown for these bins. The horizontal central value of each point corresponds to the log-mean energy of each bin, taking into account the detector's effective area and the energy spectrum of the pulsar, while the horizontal error bar corresponds to 30% of the log-mean energy, which is a conservative estimation for the absolute energy uncertainty. The P2/P1 ratio stays almost constant from 100 MeV to 3GeV and rises at energies above 3 GeV. On the other hand, the Bridge/P1 ratio rises from 100 MeV to 3 GeV. Above 3 GeV, due to the lack of statistics, it is not possible to draw a conclusion in the behavior.

In Fig. 7.10, the results are compared with those at lower energies. The data points of lower wavelengths are adopted from [114]. A few common features between the behavior of the P2/P1 ratio and that of the Bridge/P1 ratio can be seen: From 1 eV to 1 MeV, they increase with energy with a power law. From 1 MeV to 100 MeV, they drop rapidly and, then, rise again above 100 MeV $-$ 1 GeV. The ratios at ~ 30 GeV may be as high as those at 1 MeV, although the uncertainty is large due to the lack of statistics.

Energy Range	Energy [a] [GeV]	P1 [counts]	P2 [counts]	Bridge [counts]	P2/P1	Bright/P1
Fermi-LAT						
0.1 - 0.3 GeV	0.156	4135 ± 71	2067 ± 55	103 ± 33	0.50 ± 0.02	0.025 ± 0.008
0.3-1.0 GeV	0.481	5219 ± 76	2885 ± 59	254 ± 28	0.55 ± 0.01	0.049 ± 0.005
1.0-3.0 GeV	1.52	1706 ± 42	974 ± 33	224 ± 18	0.57 ± 0.02	0.131 ± 0.011
3.0-10.0 GeV	4.38	248 ± 17	245 ± 17	79 ± 11	0.99 ± 0.10	0.318 ± 0.050
>10 GeV	12.7	12 ± 6	21 ± 7	< 17[b]	1.70 ± 1.05	< 1.34
MAGIC						
25 - 70 ph.e	24.0	4711 ± 1129	8233 ± 1198	1338 ± 1195	1.75 ± 0.49	0.284 ± 0.261
70 - 500 ph.e.	51.2	1437 ± 899	3096 ± 954	< 2953[b]	2.16 ± 1.50	< 2.06

[a] The representative energy, taking into account the pulsar spectrum and the detector response.

[b] 95% confidence level upper limit.

Table 7.4: The numbers of excess events of P1, P2 and Bridge and their ratios

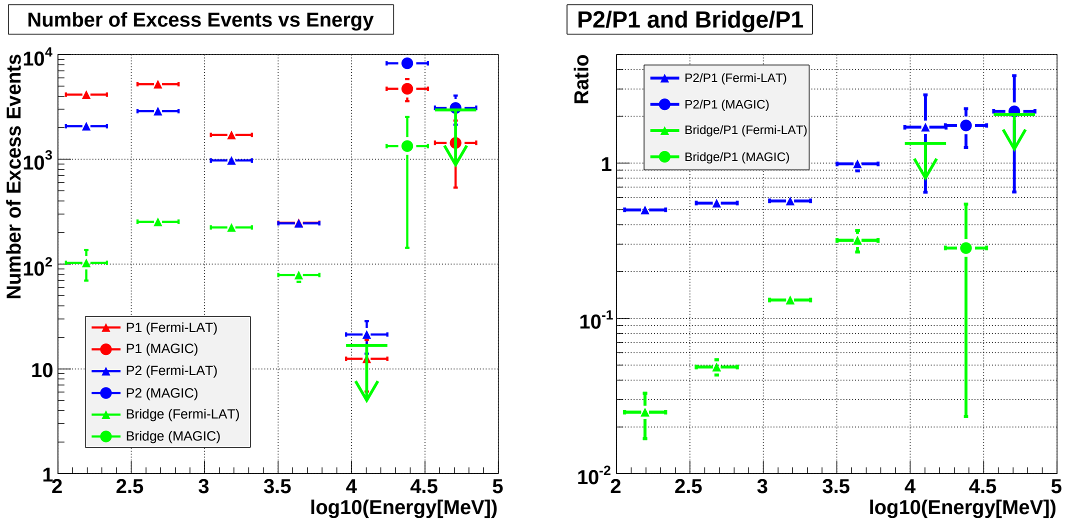

Figure 7.9: Left: The number of excess events as a function of energy. The red, blue, and green points denote P1, P2 and Bridge, respectively. The last two points above 20 GeV are based on MAGIC data, while the rest are based on Fermi-LAT data. Right: The P2/P1 ratio (blue) and the Bridge/P1 ratio (green), as a function of energy. The last two points above 20 GeV are based on MAGIC data, while the rest are based on Fermi-LAT data

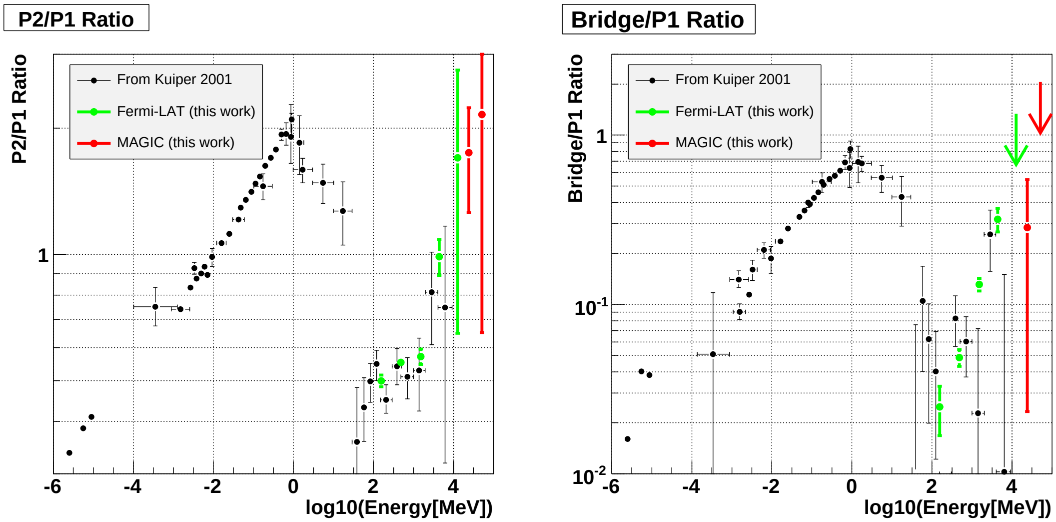

Figure 7.10: The P2/P1 ratio (left) and the Bridge/P1 ratio (right) for a wide energy range from 1 eV to 100 GeV. Black points are adopted from [114]. Green points and a green arrow are based on Fermi-LAT data, while red points and a red arrow are based on MAGIC data

7.3 Rising and Falling Edges

The energy spectra have been calculated for the specific phase intervals. They are especially important to deduce the emission regions of the pulsar on a large scale. On the other hand, as can be seen from Fig. 5.15 and Fig. 6.3, the pulse shape is not the same for all energies. A study of the change of pulse shape with energy would also be very helpful to understand the emission mechanism in more detail, i.e. on a small scale, because the pulse phase should be connected to the geometry of the emission region, as discussed in Sect. 2.7.3.

Due to the lack of statistics (with respect to the large background), it is difficult to analyze the pulse shape with MAGIC data alone. However, the fact that the pulse peak phases are very similar for all energies implies that the pulsations for all energies may originate from a common physical process. Therefore, one can also expect common features in pulse shapes. Once a common feature is found, one can statistically examine it in the MAGIC data.

In fact, I found that by plotting the light curves in log scale, some interesting features become visible. In Fig. 7.11, light curves for different energies from optical to very high energy gamma-rays are shown. The optical light curve is obtained from the MAGIC central pixel data. L. Kuiper provided the X-ray light curves, which have also been used in [114]. They are based on ROSAT HRI (100 eV to 2.4 keV, see [211]), BeppoSAX MECS (2.4 keV to 10 keV, see [204]), BeppoSAX PDS (20 keV to 100 keV, see [204]) and CGRO COMPTEL (750 keV to 30 MeV, see [207]). The gamma-ray light curves from 100 MeV to 10 GeV are produced by myself based on the *Fermi*-LAT data. The gamma-ray light curve at 20 to 200 GeV [2] are taken from my analysis of the MAGIC data with $SIZE$ between 25 to 500 ph.e.. One can see the following features:

- Both rising and falling edges show an exponential behavior.
- Slopes are not symmetric between rising and falling edges.
- Slopes change with energy.

Here, I discuss the pulse edges of P1 and P2. In the previous sections and chapters, P1 and P2 referred to specific phase intervals, P1 being from -0.06 to 0.04 and P2 being from 0.32 to 0.43, while in this section they simply denote the first peak and the second peak.

Method: Fitting Exponential Functions to Pulse Edges

An exponential function

$$F(p) = A \times \exp(\pm(p - p_0)/\tau) \tag{7.3}$$

is fitted to rising and falling edges of P1 and P2 for different energies, A, p_0 and τ being free parameters. Fitting ranges were chosen such that the bridge emission and the pulse peak do not worsen the goodness of the fit. Fitting ranges are summarized in Table 7.5. Then, the energy dependence of the rise time τ_{rise} and the fall time τ_{fall} for P1 and P2 are examined.

---

[2] This energy range is a rough estimation based on the $SIZE$ range from 25 to 500 ph.e.. No significant excess is seen at 200 GeV.

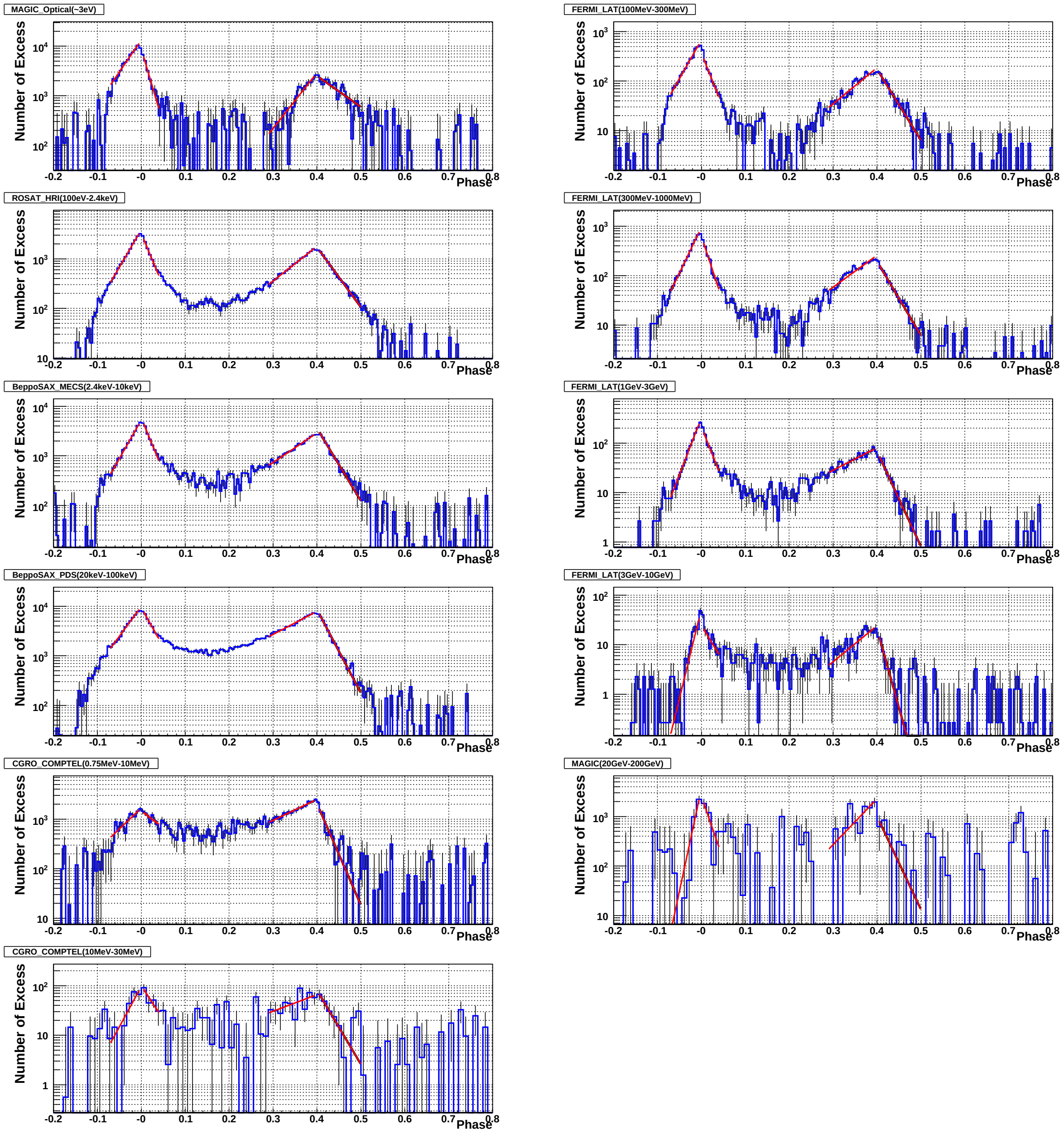

Figure 7.11: Light curves in a logarithmic scale for different energies. From the top left downward to the bottom left, optical measurements by the MAGIC central pixel (see Sect. 5.6), 100 eV to 2.4 keV by ROSAT-HRI, 2.4 keV to 10 keV by BeppoSAX MECS, 20 keV to 100 keV by BeppoSAX PDS, 0.75 MeV to 10 MeV by COMPTEL and 10 MeV to 30 MeV by COMPTEL. From the top right downward to the bottom right, 100 MeV to 300 MeV, 300 MeV to 1 GeV, 1 GeV to 3 GeV, 3 GeV to 10 GeV measured by Fermi-LAT and 20 GeV to 200 GeV (25 $< SIZE <$ 500) measured by MAGIC.

Edge	Rise of P1	Fall of P1	Rise of P2	Fall of P2
Phase	-0.07 to -0.005	0.005 to 0.04	0.29 to 0.395	0.405 to 0.50

Table 7.5: Fitting range for the rise/fall time estimation

Results of the Exponential Function Fitting to Pulse Edges

Fitted lines are overlaid on the light curves shown in Fig. 7.11. The obtained parameters and the fitting probabilities are shown in Table 7.6. Fitting probabilities are reasonably good for all energies. The energy dependence of the rise and the fall time of both peaks are graphically shown in the upper panels of Fig. 7.12. The horizontal values in Fig. 7.12 are determined in the following way: Below 100 MeV, horizontal error bars show the full energy range of the data sets and the central values are the logarithmic center of the range. Above 100 MeV, the horizontal central values and error bars are determined in the same way as the P2/P1 ratio study (see Sect. 7.2).

General behavior of the rise time and the fall time from optical to gamma-rays can be summarized as follows:

- Below 10 MeV, the rise time of both pulses and the fall time of P1 are increasing, while the fall time of P2 is decreasing.
- Above 100 MeV, the rise time of P1 and the fall time of P2 are decreasing, while the rise time of P2 and the fall time of P1 do not show clear energy dependence.

Hereafter, I would like to focus on the behavior above 100 MeV, where I have personally analyzed all the data. In the lower panels of Fig. 7.12, the energy dependence of the rise and the fall times above 100 MeV are shown. They are well described by a linear function of $\log_{10}(E)$ or a constant value, where E is the energy. By fitting a linear function to the rise time of P1 and the fall time of P2 and by fitting a constant value to the fall time of P1 and the rise time of P2, the following is obtained:

$$\tau^{P1}_{rise}(E) = (2.02 \pm 0.08) \times 10^{-2} - (9.4 \pm 1.3) \times 10^{-3} \log_{10}(E[\mathrm{GeV}]) \tag{7.4}$$

$$\tau^{P2}_{rise} = (6.46 \pm 0.24) \times 10^{-2} \tag{7.5}$$

$$\tau^{P1}_{fall} = (1.73 \pm 0.08) \times 10^{-2} \tag{7.6}$$

$$\tau^{P2}_{fall}(E) = (2.42 \pm 0.16) \times 10^{-2} - (9.6 \pm 3.1) \times 10^{-3} \log_{10}(E[\mathrm{GeV}]) \tag{7.7}$$

$\chi 2/dof$ are 2.2/3, 12.2/4, 4.6/4 and 2.4/3 for τ^{P1}_{rise}, τ^{P2}_{rise}, τ^{P1}_{fall},and τ^{P2}_{fall}, respectively.
MAGIC points and *Fermi*-LAT points can be fitted consistently. It is also interesting that the rise time of P1 and the fall time of P2 show very similar dependence on energy. The energy dependence of the pulse shape above 100 MeV is schematically illustrated in Fig. 7.13. As energy increases, the outer edges, i.e. the rising edge of P1 and the falling edge of P2 get sharper while the inner edges, i.e. the falling edge of P1 and the rising edge of P2 do not change.

The physical interpretation of these results will be discussed in Sect. 8.6.

	Rise Time		Fall Time	
Energy	τ_{Rise} [10^{-3} phase]	($\chi^2/dof, prob.$)	τ_{Fall} [10^{-3} phase]	($\chi^2/dof, prob.$)
P1				
2.0 - 4.0 eV	33.6 ± 1.2	(16.7/10, 8.0%)	14.4 ± 1.6	(2.7/4, 61.3%)
0.1 - 2.4 keV	28.6 ± 0.5	(7.7/10, 66.3%)	20.4 ± 0.7	(5.1/4, 27.6%)
2.4 - 10 keV	27.7 ± 0.8	(10.2/10, 42.5%)	20.1 ± 0.9	(8.3/4, 8.0%)
20 - 100 keV	36.0 ± 0.7	(17.7/10, 6.0%)	27.7 ± 1.0	(10.7/4, 3.0%)
0.75 - 10 MeV	51.1 ± 8.3	(15.5/10, 11.3%)	63.3 ± 27.7	(4.0/4, 40.5%)
10 - 30 MeV	26.6 ± 7.7	(5.2/4, 26.3%)	31.9 ± 14.3	(1.4/2, 48.9%)
100 - 300 MeV	27.7 ± 1.0	(11.0/10, 36.1%)	19.4 ± 1.8	(1.3/4, 86.3%)
0.3 - 1.0 GeV	23.5 ± 0.7	(4.5/10, 92.0%)	16.1 ± 1.0	(13.9/4, 0.8%)
1.0 - 3.0 GeV	18.9 ± 0.9	(3.7/10, 96.0%)	19.4 ± 2.1	(3.9/4, 41.5%)
3.0 - 10 GeV	12.0 ± 1.6	(16.2/10, 9.4%)	29.7 ± 12.4	(4.3/4, 36.3%)
20 - 200 GeV[a]	10.5 ± 4.0	(0.8/4, 93.9%)	16.8 ± 7.7	(1.4/2, 48.8%)
P2				
2.0 - 4.0 eV	38.7 ± 5.1	(10.7/17, 87.1%)	69.3 ± 10.6	(20.1/15, 16.8%)
0.1 - 2.4 keV	61.8 ± 1.4	(10.5/17, 88.0%)	35.9 ± 0.9	(16.9/15, 32.2%)
2.4 - 10 keV	72.5 ± 2.7	(14.8/17, 61.1%)	29.7 ± 1.1	(20.4/15, 15.8%)
20 - 100 keV	93.2 ± 1.9	(39.8/17, 0.1%)	25.8 ± 0.6	(29.1/15, 1.5%)
0.75 - 10 MeV	102.6 ± 9.6	(4.9/17, 99.8%)	21.2 ± 3.5	(20.9/15, 13.9%)
10 - 30 MeV	129.4 ± 60.8	(11.3/8, 18.3%)	29.1 ± 10.5	(8.0/7, 33.3%)
100 - 300 MeV	59.4 ± 3.9	(30.9/17, 2.0%)	30.3 ± 2.4	(27.8/15, 2.3%)
0.3 - 1.0 GeV	67.4 ± 3.4	(37.2/17, 0.3%)	29.0 ± 1.9	(6.4/15, 97.3%)
1.0 - 3.0 GeV	95.1 ± 11.1	(12.5/17, 76.8%)	22.6 ± 2.4	(14.4/15, 49.4%)
3.0 - 10 GeV	59.6 ± 10.0	(20.9/17, 22.9%)	13.6 ± 4.7	(16.6/15, 34.4%)
20 - 200 GeV [a]	46.8 ± 12.6	(18.0/8, 2.2%)	23.1 ± 16.1	(4.2/7, 76.0%)

[a] This energy range is a rough estimation based on the $SIZE$ range in MAGIC data from 25 to 500. No significant excess is seen at 200 GeV.

Table 7.6: Results of the rise and the fall time estimation for P1 and P2

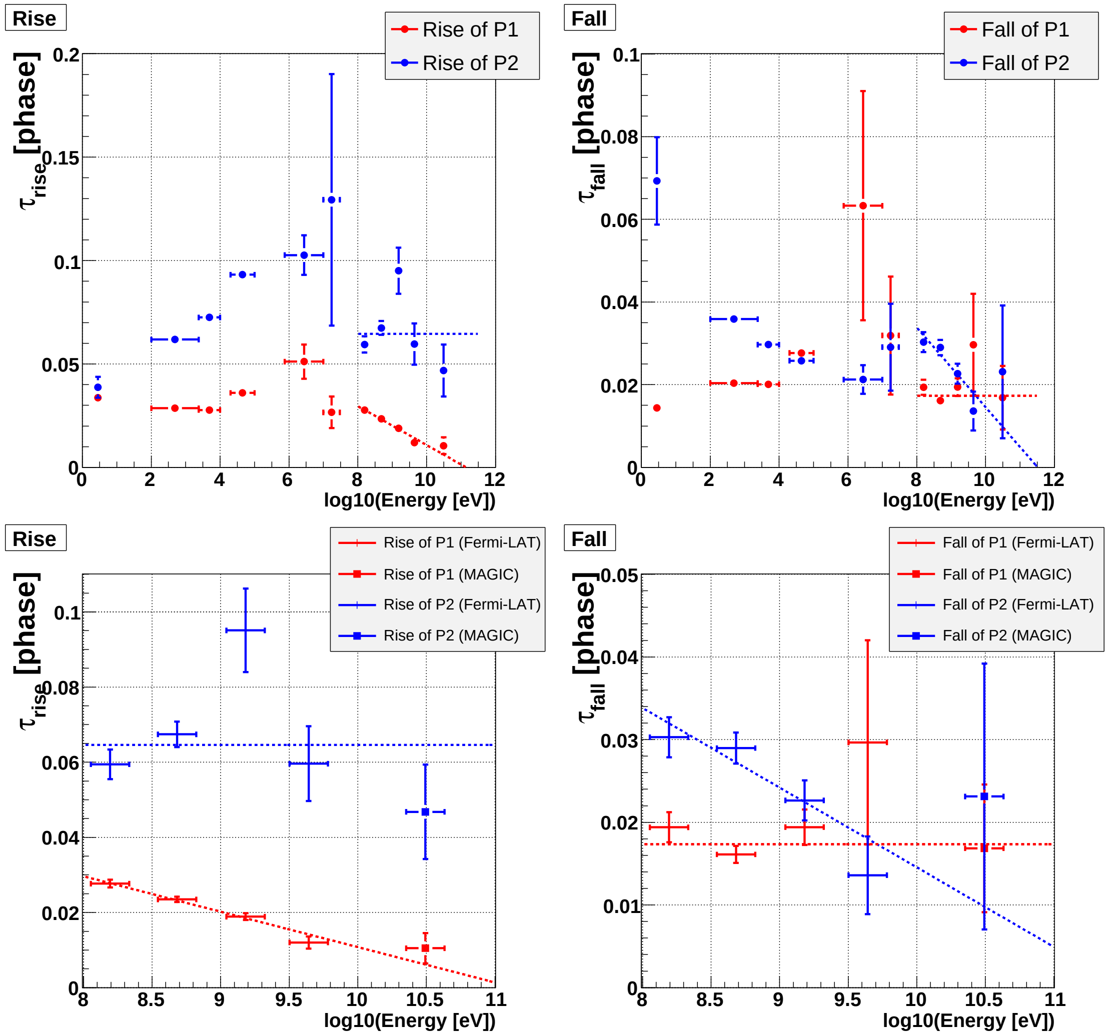

Figure 7.12: Energy dependence of the rise and the fall times. Top left: The rise time of P1 (red) and P2 (blue), as a function of energy. Top right: The fall time of P1 (red) and P2 (blue), as a function of energy. Bottom left: The same as the top left panel but the energy range from 100 MeV to 100 GeV is zoomed. Bottom right: The same as the top right panel but the energy range from 100 MeV to 100 GeV is zoomed.

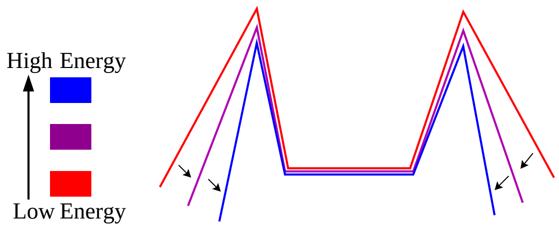

Figure 7.13: An illustration of the energy dependence of the pulse edges above 100 MeV. As energy increases, the outer edges get sharper, while the inner edges do not change.

7.4 Peak Phases

As described in Sect. 2.9.4, the pulse profiles of the Crab pulsar are very similar at all energies, while a closer look at the light curves reveals a slight energy dependence of the peak phase. For example, the first peak in the X-ray data (see Fig. 2.26) and that in optical data (see Fig. 5.11) precede the radio peak by ~ 0.01 in phase. Also, above 100 MeV, there seems to be a slight shift of the peak phase, which can be seen if the light curves based on the *Fermi*-LAT data are zoomed, as shown in Fig. 7.14.

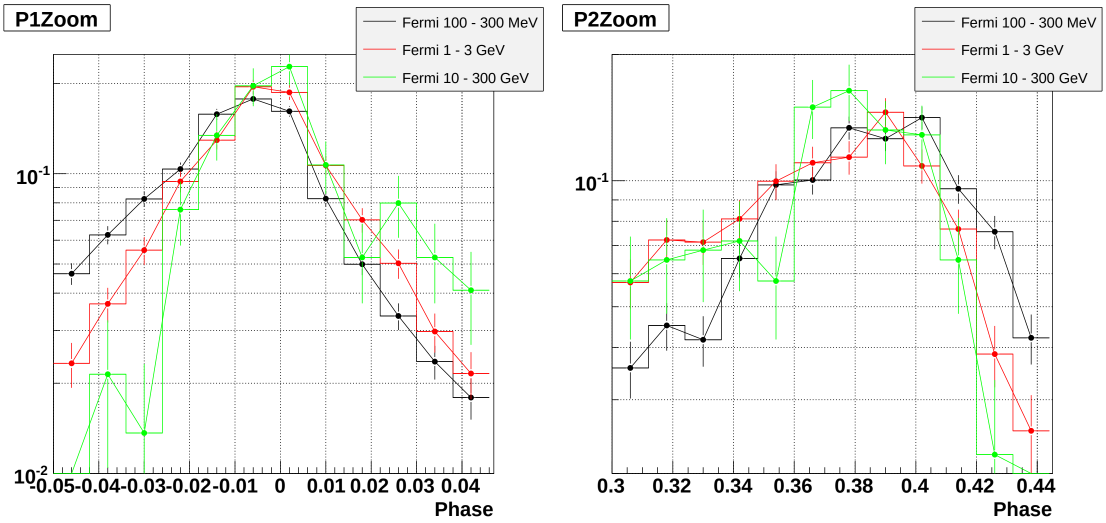

Figure 7.14: A closer look at the peak phase of P1 (left) and P2 (right). The black, red and green lines indicate the light curves for 100 MeV to 300 MeV, 1 to 3 GeV and above 10 GeV, based on Fermi-LAT data.

Here, I examine the energy dependence of the peak phase above 100 MeV by using *Fermi*-LAT and MAGIC data. Apparently, the energy dependence of the peak phases is not very strong. The precision of ~ 0.003 in phase would be required to discuss the energy dependence. In order to fulfill this requirement with the obtained data, a sophisticated method called the "Kernel density method" is used.

7.4.1 Kernel Density Method

The Basic Concept

If the statistical significance of the signal is large enough, the peak phase can be precisely determined without assuming a specific pulse shape. However, the significance of the obtained signal is not high enough to determine the peak phase with a precision of ~ 0.003, especially for energies above 10 GeV. By assuming the pulse shape a priori, the fitting of the assumed shape to the obtained data might improve the precision. In such a case, in order to achieve the best possible precision, the data should not be converted into a binned phase diagram but should be analyzed on an event-by-event basis. An event-by-event maximum likelihood method could have been used for that but, in the case of MAGIC data, which is dominated by ~ 15 million background events, it requires too much computational power.

The Kernel density method also uses event-by-event information but it does not require too much computational power. Moreover, the assumption of the pulse shape is not needed either, although a so-called "kernel estimator" must be chosen beforehand. The kernel density method is a well established statistical method for estimating the probability density function of a measured parameter, based on the observed data sample (see e.g. [80], [178] and [36]). The true pulse profile can be interpreted as a probability density function for the pulse phase of the signals and, hence, the kernel density method can be applied.

The probability density $f(p)$ as a function of phase p can be estimated as follows:

$$f(p) \quad = \quad \frac{1}{N}\sum_{i=1}^{N} K_h\left(\frac{p-p_i}{h}\right) \tag{7.8}$$

where N, p_i, $K_h(x)$ and h are the total number of events, the phase of ith event, a kernel estimator and the band width of the kernel estimator K_h. The method is schematically illustrated in Fig. 7.15. In a light curve (a phase histogram), the phase of a given event is smeared by a kernel density estimator. $f(p)$ is the sum of the smeared curves of all the events. An example of the application of the method using the MAGIC data is shown in Fig. 7.16.

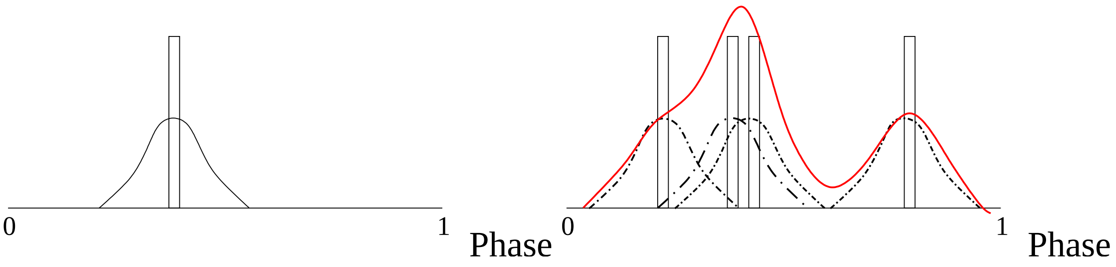

Figure 7.15: Schematical explanation of the Kernel density method. In a phase histogram, each event is smeared by a kernel density estimator, as shown in the left panel. $f(p)$ is the sum of the smeared curves of all the events, as indicated by a red line in the right panel.

The Choice of the Kernel Estimator K_h and its Width h

As a kernel estimator K_h, a normal Gaussian is commonly used in many different applications,

$$K_h\left(\frac{p-p_i}{h}\right) = \frac{1}{\sqrt{2\pi}h}e^{-\frac{(p-p_i)^2}{2h^2}} \tag{7.9}$$

On the other hand, as shown in Fig. 7.17, a Lorentzian represents the pulse shape better. The Lorentzian kernel estimator is written as

$$K_h\left(\frac{p-p_i}{h}\right) \quad = \quad \frac{1}{\sqrt{\pi}h}\frac{1}{1+\frac{(p-p_i)^2}{h^2}} \tag{7.10}$$

$$\tag{7.11}$$

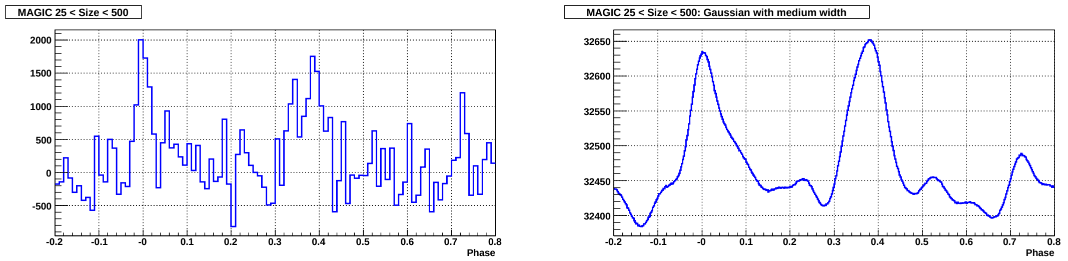

Figure 7.16: An example of the kernel density method. Left: The original light curve from MAGIC data with $SIZE$ between 25 and 500. Right: The obtained probability density function. The Gaussian kernel with $h = 0.024$ is used.

One of these estimators should be used.

Not only the shape of the estimator but also the width h must be properly chosen (see [186]). Too narrow a width will make the density function $f(p)$ too wiggly and produce many spurious features. On the other hand, too big a width will lead to too smooth a function that smears out all the structure. Since the pulse shape is not symmetric, as described in the previous section, the smearing may cause a shift in the peak phase. I chose h based on the light curve of *Fermi*-LAT data above 3 GeV, which is more or less the (logarithmic) center of the concerned energy range. First, a Gaussian and a Lorentzian are fitted to P1 and P2 independently. Results are shown in Fig. 7.17. The best fit hs are 0.016 ± 0.002 (Gaussian fit to P1), 0.031 ± 0.004 (Gaussian fit to P2), 0.011 ± 0.001 (Lorentzian fit to P1) and 0.024 ± 0.003 (Lorentzian fit to P2). The optimal h should be close to these values.

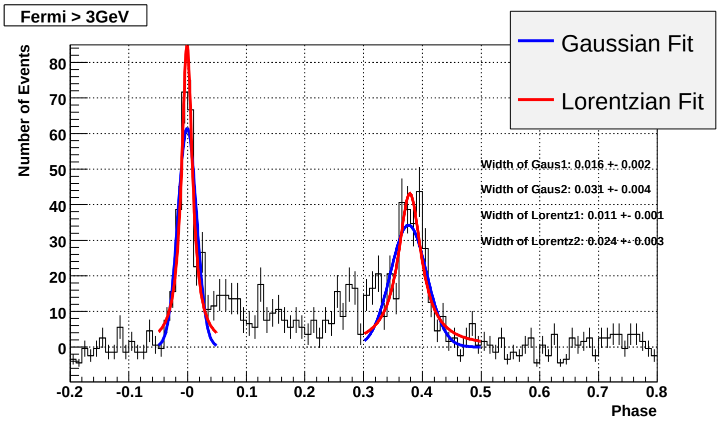

Figure 7.17: Fitting a Lorentzian and a Gaussian for a light curve of Fermi-LAT data above 3 GeV

The final choice of the shape of K_h (Gaussian or Lorentzian) and the width h was made such that the peak phase shift caused by the smearing effect is minimal. The phase shift is estimated as follows: Assuming a pulse shape to be

$$f_{true}(p) = \begin{cases} \exp(p/\tau_{rise}) & \text{if} \quad p \leq 0 \\ \exp(-p/\tau_{fall}) & \text{if} \quad p > 0 \end{cases} \tag{7.12}$$

$f(p)$ is calculated by convoluting the pulse shape $f_{true}(p)$ with the kernel estimator $K_h(p)$

$$f(p) = \int_{-0.25}^{0.25} f_{true}(p')K_h(p - p')dp' \tag{7.13}$$

Then, the difference in the peak phase Δp_{peak} between $f_{true}(p)$ and $f(p)$ is estimated. Hereafter, Δp_{peak} is referred to as the "analytical phase shift". An example of the analytical phase shift is shown in Fig. 7.18.

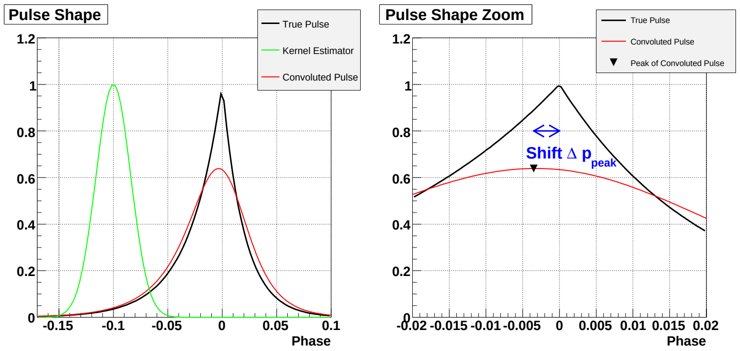

Figure 7.18: Left: An example of the convolution of a true pulse with a kernel estimator. $\tau_{rise} = 0.03$ *and* $\tau_{fall} = 0.02$ *are used for the true pulse shape* $f_{true}(p)$*, while a Gaussian kernel* $K_h(p)$ *with* $h = 0.016$ *is used for the kernel estimator. A black and a red line indicate the true pulse shape* $f_{true}(p)$ *and the convoluted pulse shape* $f(p)$*, respectively, while a green line indicates the kernel estimator* $K_h(p)$ *which is scaled such that the peak height = 1. Right: The same as the left panel but phases from -0.02 to 0.02 are zoomed. The analytical phase shift* Δp_{peak} *is indicated by a blue arrow.*

By substituting Eqs. 7.4 – 7.7 for τ_{rise} and τ_{fall} in Eq. 7.12, I estimated the energy dependence of the analytical phase shift Δp_{peak} for different K_hs, as shown in Fig. 7.19. The Lorentzian kernel estimators with $h = 0.006$ for P1 and $h = 0.012$ for P2, which are the half of the fitted values (see Fig. 7.17) have the smallest effect. Even smaller h might reduce the effect further. However, if h is too small compared to the fitted values, $f(p)$ would, in turn, produce spurious structures, as mentioned before. Therefore, in the following analysis, I use Lorentzian for K_h with $h = 0.006$ for P1 and $h = 0.012$ for P2. The residual Δp_{peak} will be subtracted from the obtained results.

Statistical Uncertainty Estimation by the Bootstrapping Method

One can estimate a probability density function $f(p)$ from observed data by the kernel density method and, then, determine the peak position from it. However, it does not give the statistical uncertainty.

The statistical uncertainty of the result can be estimated by the bootstrapping method which is well established and is used in many statistical treatments (see e.g. [70] and [63]). The procedure is explained as follows: Let N be the total number of observed events. One randomly chooses N events out of the observed N events. The same events can be chosen multiple times. Then, the

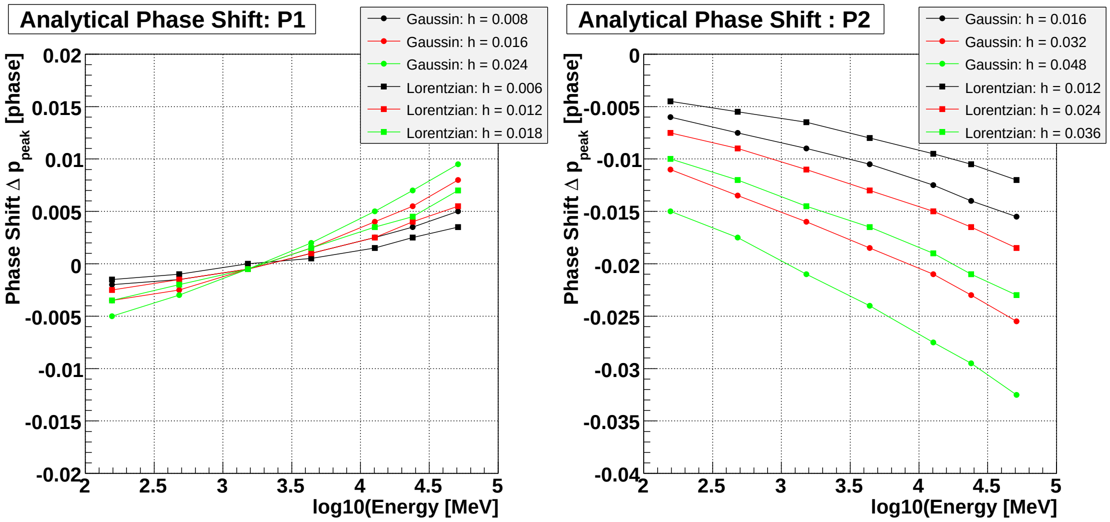

Figure 7.19: The energy and the estimator dependence of the analytical phase shift Δp_{peak} *for P1 (left) and P2 (right)*

same kernel density method is applied to the chosen data sample. By repeating this procedure M times, one obtains M different $f(p)$s. The RMS of the peak phase distribution from them is used as the statistical uncertainty of the peak phase. In this analysis, $M = 900$ is used.

7.4.2 Example of the Kernel Density for Different Energies

In Fig. 7.20 and Fig. 7.21, the original light curves and the resulting probability functions (kernel densities) are shown. The statistical uncertainty of the function estimated by the bootstrapping method are indicated by colors.

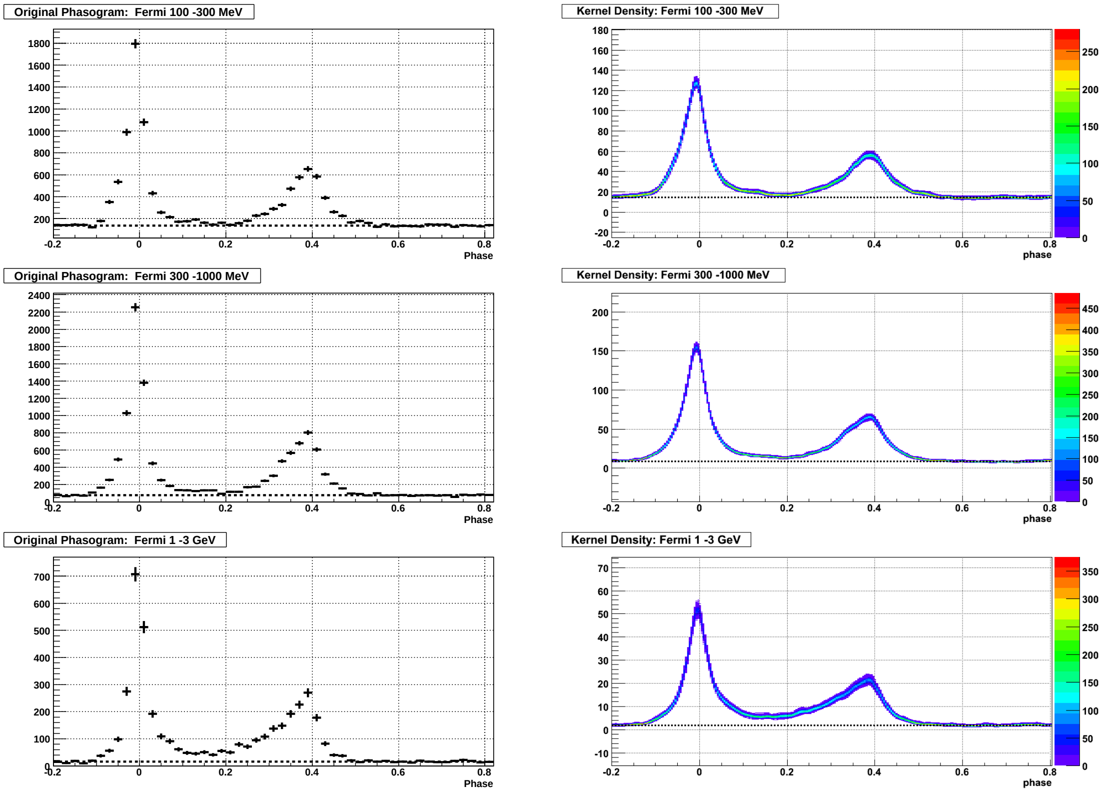

Figure 7.20: The original light curves (left) and the resulting probability density function (kernel density) by using Lorentzian kernel with $h = 0.012$ (right). This kernel density is used for the P2 peak determination, while $h = 0.006$ is used for the P1 peak. Black dotted lines indicate the background level. 900 curves obtained by the bootstrapping method are overlaid in the left panels and colors indicate their density. From the top: 100 - 300 MeV, 0.3 - 1 GeV and 1 - 3 GeV are shown, all of which are based on Fermi-LAT data.

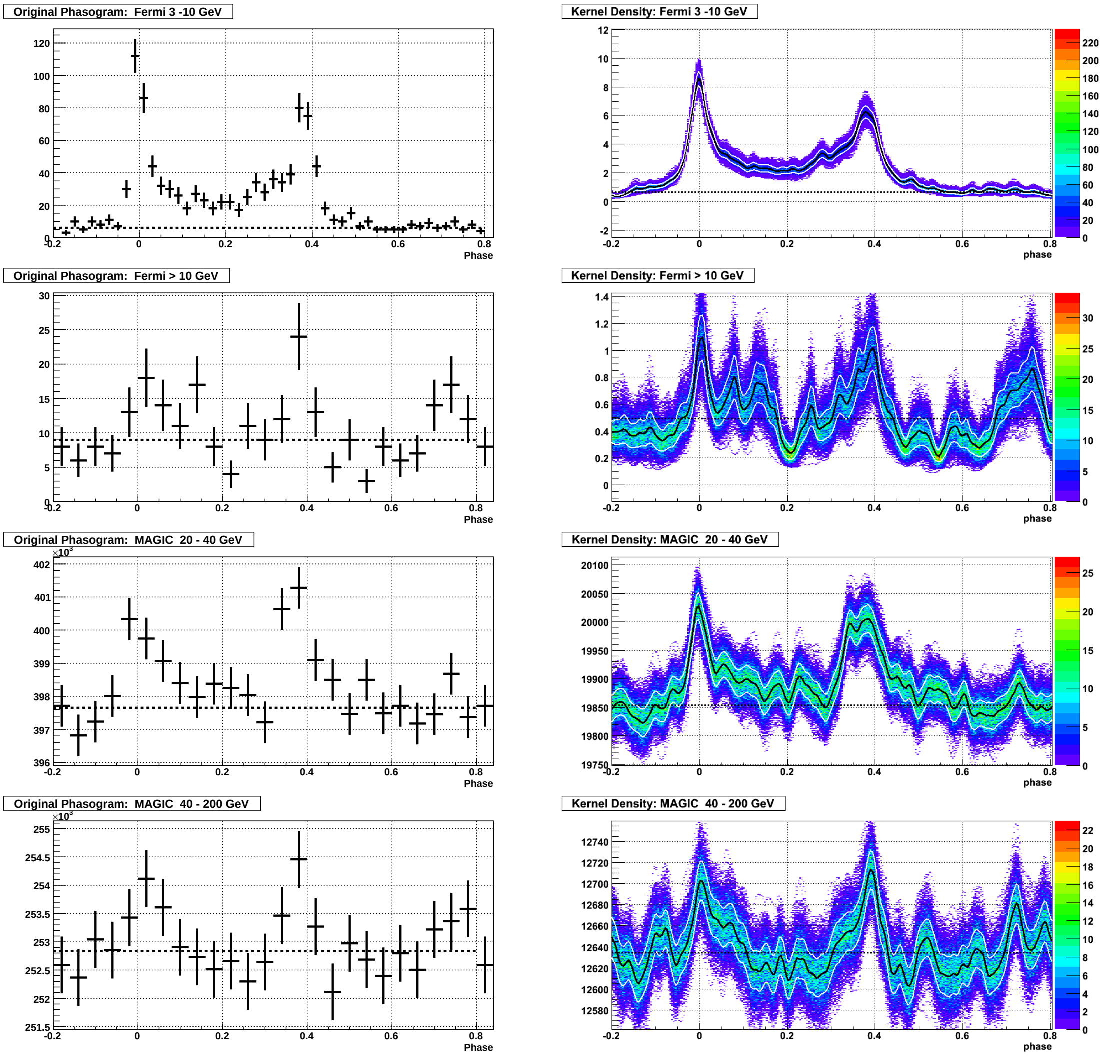

Figure 7.21: The same as Fig 7.20 but for higher energies. From the top: 3 - 10 GeV from Fermi-LAT data, above 10 GeV from Fermi-LAT data, 20 - 40 GeV (25 - 70 in $SIZE$) from MAGIC data and 40 - 200 GeV (70 - 500 in $SIZE$) from MAGIC data. These energy ranges for MAGIC data are rough estimation based on the $SIZE$ range and no significant excess is seen at 200 GeV. Because of the relatively low significance of the signals, an (acceptably) wiggly structure is visible. By using larger h in the kernel estimator, the structure will become less pronounced, while it leads to a larger analytical bias. Black lines in the left panels indicate the resulting probability density functions, while white lines are their (1 σ) uncertainty.

7.4.3 Results

Results are shown in Fig. 7.22. Open and filled squares indicate the results before and after correcting the analytical phase shift Δp_p, respectively. Horizontal values and errors are determined in the same way as the P2/P1 ratio study (see Sect. 7.2). Blue lines indicate the energy dependence of Δp_p estimated in Sect. 7.4.1 (see Fig. 7.19).

After the correction (filled squares), the energy dependence is clearly seen for P1 but it is not the case for P2, due to the large uncertainties. This difference comes mainly from the pulse width. Since P2 has twice as large a width as P1, the precision of the peak phase becomes worse. The results after the correction (filled squares) are fitted by a linear function and

$$Peak1(E) = (-3.8 \pm 0.6) \times 10^{-3} + (2.1 \pm 0.9) \times 10^{-3} \log_{10}(E[\mathrm{GeV}]) \quad (7.14)$$

$$Peak2(E) = 0.39 + (3.9 \pm 1.6) \times 10^{-3} - (0.05 \pm 2.8) \times 10^{-3} \log_{10}(E[\mathrm{GeV}]) \quad (7.15)$$

are obtained. $\chi 2/dof$ are 6.26/5 and 3.18/5, for $Peak1$ and $Peak2$, respectively.

The physical interpretation of the results will be discussed in Sect. 8.7.

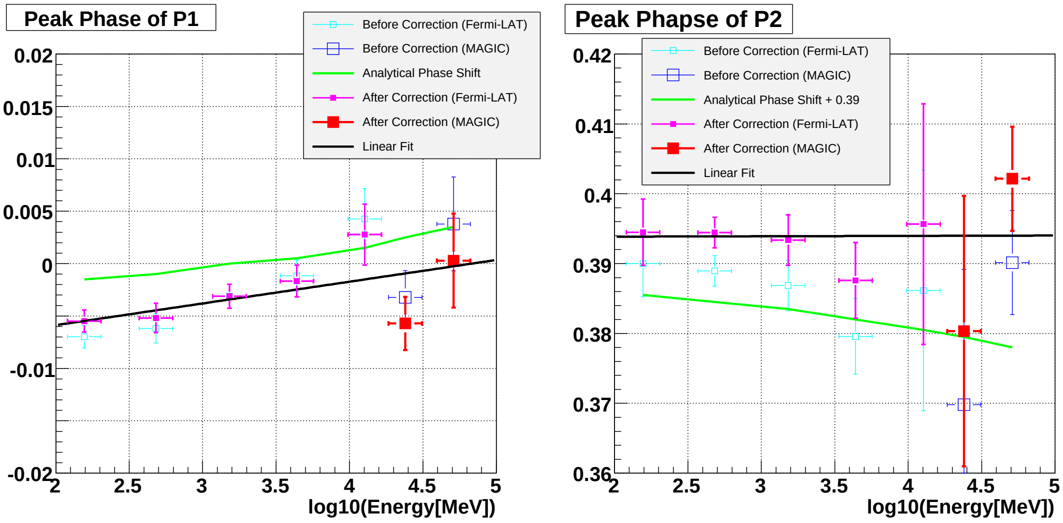

Figure 7.22: The energy dependence of the peak phase of P1 (left) and P2 (right). Open and filled squares denote the peak phase before and after correcting the analytical phase shift Δp_{peak}. Green lines indicate the Δp_{peak} (see Fig. 7.19). The peak phases after the correction as a function of energy are fitted by a linear function, as shown by the black lines.

7.5 Possible Existence of the Third Peak

As mentioned in Sect. 6.4, a possible third peak is seen above 10 GeV in *Fermi*-LAT data. Judging from the light curve (see Fig. 6.3), the flux might be as high as P1 and P2, although the large statistical uncertainty does not permit a solid argument. Here, I examine the existence of the possible third peak by using both *Fermi*-LAT data and MAGIC data.

7.5.1 Definition of the ON and OFF Phases for the Third Peak P3

The third peak has not been detected in other energies, except for specific frequencies in radio, where fourth and fifth peaks are also seen (see Sect. 2.26). Therefore, it is not possible to define the third peak phase interval (P3) a priori. I define P3 to be phases from 0.7 to 0.8. It is based on the observed result itself, which leads to the overestimation of the flux and the statistical significance, while no fine tuning of the bin-edges is carried out in order to reduce the effect. In all the previous analyses, background level had been estimated by OP phases 0.52 to 0.88 (0.52 to 0.87 for the *Fermi*-LAT nebula analysis). For P3, phases from 0.5 to 0.65 and from 0.85 to 0.9 are used for the background estimation.

7.5.2 MAGIC and *Fermi*-LAT above 10 GeV

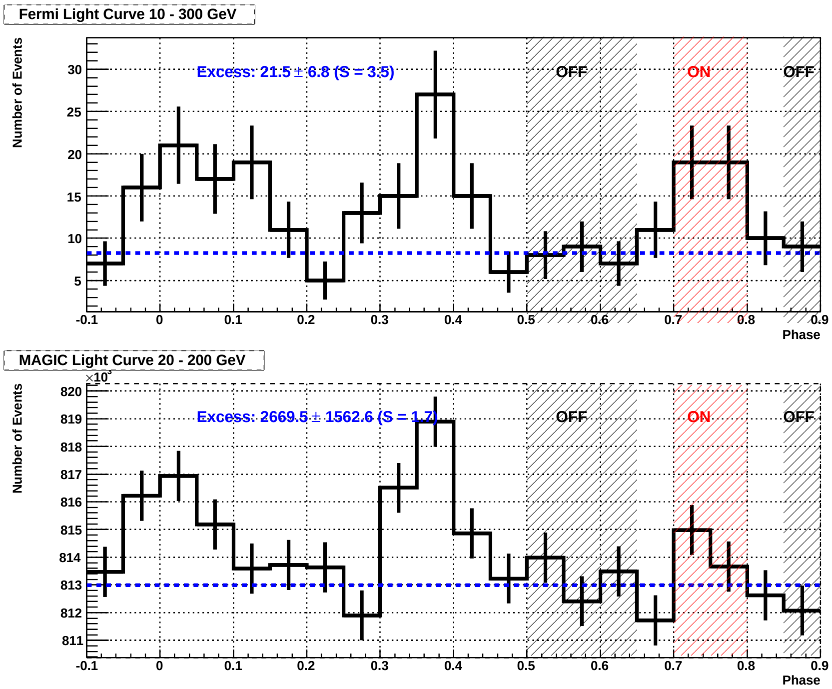

Figure 7.23: The light curves of the Fermi-LAT data above 10 GeV (top) and that of the MAGIC data with $SIZE$ from 25 to 500. P3 phases and background estimation phases are indicated by red and black shadows, respectively.

The light curves of *Fermi*-LAT data above 10 GeV and MAGIC data with $SIZE$ from 25 to 500 are shown in Fig. 7.23. *Fermi*-LAT data show 21.5 ± 6.8 excess events corresponding to 3.5σ, while MAGIC data show 2670 ± 1563 excess events corresponding to 1.7σ. More statistics are required in order to verify or refute the presence of the signal.

Although the existence of the signal is not clear, I estimated the energy spectrum of P3 based on *Fermi*-LAT data. Based on MAGIC data, the differential flux upper limit was also calculated with a 95% confidence level . They are shown in Fig. 7.24. The estimation is done in the following way: Instead of using the likelihood method for *Fermi*-LAT data and the unfolding method for MAGIC data, the number of excess events (or the upper limit on the number of excess events) in each energy bin was simply divided by the effective area and the observation time. Therefore, the spill-over effect from the adjacent bins are not taken into account. The discrepancy between MAGIC upper limits and *Fermi*-LAT measurements may imply an upward bias in the *Fermi*-LAT data analysis, probably because the P3 phases are defined based on the observed data themselves. The possibility that there is some signal, whose excess was enhanced by the background fluctuation, cannot be excluded. The time variability of the P3 excess is also another explanation.

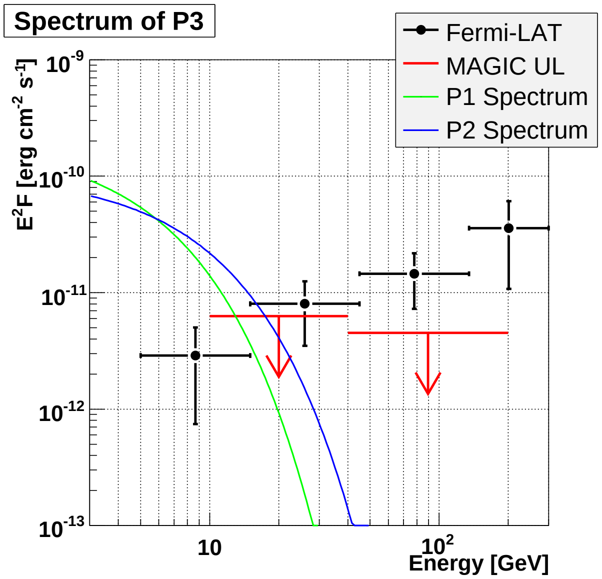

Figure 7.24: The energy spectrum of P3. Black points and red arrows indicate the measurements by Fermi-LAT and the upper limits based on MAGIC data, respectively. The flux is estimated by simply dividing the number of excess events by the observation time and the effective area. A green and a blue line indicate the exponential cut-off energy spectra of P1 and P2, respectively.

7.6 Concluding Remarks

Neither an exponential cut-off nor a sub-exponential cut-off can explain the energy spectra measured by MAGIC and *Fermi*-LAT consistently, even if the possible systematic uncertainties of both experiments are taken into account. Assuming that the energy spectrum does not roll off exponentially but extends with a power law after the cut-off energy, they can be consistently explained with an index of $\sim -3.0 \pm 0.1$ (after the cut-off). The physics interpretation of these spectral features will be discussed in Sect 8.2.

The P2/P1 ratio stays constant between 100 MeV and 3 GeV and rises above 3 GeV. On the other hand, the Bridge/P1 ratio increases by a power law between 100 MeV and 3 GeV, while the behavior above 3 GeV cannot be analyzed, due to the lack of statistics. The edges of the two pulses have an exponential shape. The rise time of P1 and the fall time of P2 have a clear energy dependence while the fall time of P2 and the rise time of P2 do not. The physics interpretation of this will be discussed in Sect. 8.6. The peak phase of P1 has a slight energy dependence while this is not clear for P2, due to the difficulty in determining the P2 peak phase. The physics discussion on this will also be presented in Sect. 8.7. The third peak seen in *Fermi*-LAT data above 10 GeV with 3.5 σ is not clearly visible in MAGIC data. In order to verify or refute the existence of the P3 signal, more statistics is required.

Chapter 8

Discussion

Several interesting features of the pulsed gamma-ray radiation from the Crab pulsar above 100 MeV have been newly found from the MAGIC and *Fermi*-LAT data analyses. Quite a few results are not in agreement with model predictions and extrapolations. Especially the following findings are remarkable:

- None of the super-exponential cut-off, the exponential cut-off and the sub-exponential cut-off can describe the measured energy spectrum.

- The measured energy spectrum extends at least up to 100 GeV.

- A power law with an index of -3.0 ± 0.1 can well explain the measured energy spectrum between 4 GeV and 100 GeV.

- The edges of the two pulses have a clear exponential behavior. The rise time of P1 and the fall time of P2 have a clear energy dependence while the fall time of P1 and the rise time of P2 do not.

- The peak phase of P1 has a small but significant energy dependence.

In this chapter, I discuss the new constraints on the pulsar emission models and possible modifications of the standard model, based on these findings. In addition, the radiation efficiency in gamma-rays above 100 MeV is discussed.

8.1 Constraints on the Emission Region

As discussed in 2.8, there are mainly two approaches to infer the emission region, namely, by the steepness of the cut-off and by the highest energy of the observed photons.

8.1.1 By the Steepness of the Cut-off

As described in 2.8.2, if the emission region is close to the star surface, a superexponential cut-off is expected. Γ_2 in Eq. 6.5 is typically 2 (see e.g. [140] and [65]). However, the analysis of Fermi-LAT data revealed that superexponential assumption ($\Gamma_2 = 2$) is less likely than exponential cut-off ($\Gamma_2 = 1$) by 4.8σ, 7.7σ, 5.0σ and 4.3σ, for TP, P1 + P2, P1, and P2 respectively. This indicates that emission region is far from the star surface and that gamma-rays do not cause magnetic pair creation. In essense, the modest steepness of the spectral cutoff allow one to reject the PC model.

8.1.2 By the Highest Energy of the Observed Photons

More quantitative estimation of the emission region can be made by the highest energy of the observed photons. As discussed in Sect. 2.7.2, the highest energy of photons E_{max} which can escape from a given height r can be estimated as

$$E_{max}(r) \simeq 40\sqrt{P}\left(\frac{r}{R_0}\right)^{7/2}\frac{B_{cr}}{B_0} \quad \mathrm{MeV} \tag{8.1}$$

where P, R_0, B_0, and B_{cr} are the period of the pulsar in second, the radius of the neutron star, the magnetic field strength at the stellar surface and the critical magnetic field ($B_{cr} = 4.4 \times 10^{13}$ G).

MAGIC detected gamma-rays up to 100 GeV. For $P = 33.6$ ms, $B_0 = 3.8 \times 10^{12}$ G $= 0.086B_{cr}$ and $E_{max} = 100$ GeV, one obtains r/R_0 = 7.8. The height of the emission region must be more than 7.8 times the pulsar radius, which is too large for the PC model.

8.2 Estimates of the Electron Spectrum and Constraints on the Acceleration Electric Field

From the argument in the previous section, it is clear that the emission region is free from magnetic pair creation process, i.e. the emission region should be in the outer magnetosphere. Since magnetic pair creation is a basic physics process, this conclusion is rather robust.

Even if the emission region is assumed to be in the outer magnetosphere, the energy spectrum observed by MAGIC contradicts the most favored theoretical models, which predict an exponential cut-off. Below, I will discuss possible modifications of the standard outer magnetosphere model. After briefly reviewing the basic equations for the electron energy spectrum within the pulsar magnetosphere and the curvature radiation spectrum from these electrons in Sect. 8.2.1, I will deduce the electron spectrum based on the observed gamma-ray spectrum of P1 + P2 in Sect. 8.2.2. Then, constraints on the strength of the acceleration electric field will be discussed in Sect. 8.2.3. Possibilities to explain the deviation of the observational results from the standard model by a imperfect dipole magnetic field will be briefly described in Sect. 8.2.4.

8.2.1 Basic Equations for the Electron Energy and the Curvature Radiation Photon Energy

As discussed in Sect. 2.7.2, the energy of the electron is set by the equilibrium between the gain in energy due to the acceleration electric field and the energy loss via the curvature radiation. The Lorentz factor of the electron Γ can be written as a function of the acceleration electric field strength $E_{||}$ and the magnetic field curvature R_{curv}:

$$\Gamma = 2.8 \times 10^7 \left(\frac{eE_{||}}{(10^7 \ \mathrm{eV/cm})} \right)^{1/4} \sqrt{R_{curv}/1000\,\mathrm{km}} \tag{8.2}$$

See Sect. 2.7.2, for the derivation of this equation,

As described in Sect. 1.3.4, the curvature radiation spectrum from a single electron with an energy $\Gamma m_e c^2$ is written as

$$\frac{dN_\gamma}{dE_\gamma dt}_{mono} \simeq KE_\gamma^{-0.7}\mathrm{exp}(-E_\gamma/E_c) \tag{8.3}$$

$$E_c = \frac{3}{2}\Gamma^3 h\nu_{curv} = \frac{3}{2}\Gamma^3 \frac{hc}{2\pi R_{curv}} \tag{8.4}$$

From Eq. 8.2 and Eq. 8.4, the cut-off energy E_c of the curvature radiation is written as a function of $E_{||}$ and R_{curv}:

$$E_c = 6.5 \left(\frac{eE_{||}}{(10^7 \ \mathrm{eV/cm})} \right)^{3/4} \sqrt{R_{curv}/1000\,\mathrm{km}} \quad [\mathrm{GeV}] \tag{8.5}$$

8.2.2 Estimates of the Electron Spectrum Based on the Measured Gamma-ray Spectrum

Here, I deduce the electron spectrum (the Γ spectrum) based on the measured gamma-ray spectrum of P1 + P2, assuming that gamma-rays above 4 GeV are generated by the curvature radiation. For simplicity, the curvature of the magnetic field is assumed to be fixed at $R_{curv} = 1000$ km [1].

0) Standard Model: Nearly Monoenergetic Electron Spectrum

In general, it is considered that $E_{||}$ and R_{curv} of the last closed field line do not change extremely largely over the emission region (see e.g. [174]). In addition, the dependency of Γ on $E_{||}$ and R_{curv} is rather weak (see Eq. 8.2). These are the reasons why a nearly monoenergetic spectrum is derived for accelerarted electrons in most of pulsar models based on the outer magnetosphere emission hypothesis.

The cut-off in the high energy gamma-ray spectrum is determined by the curvature radiation spectrum from these nearly monoenergetic electrons, in turn leading to the exponential cut-off (see Sect. 8.2.1). Examples of the theoretical explanations of the Crab pulsar spectrum observed before 2007 are shown in Fig. 8.1, which are the same as Fig. 2.22. The highest end of the spectrum is explaned by the curvature radiation from nearly monoenergetic electrons. In order to explain the power law spectrum with an index of ~ 2 between ~ 10 MeV and ~ 1 GeV, the synchrotron radiation (left panel) or the inverse Compton scattering (right panel) is considered. Below 10 MeV, the emissions from secondary electron-positron pairs created by high energy gamma-rays are considered to be responsible for the observed spectrum.

Applying the standard scenario to the observed spectrum of P1 + P2 around the cut-off energy is shown in Fig. 8.2. I made a simple calculation assuming that the Γ spectrum of the electrons has a Gaussian shape with the mean of 2×10^7 and the RMS of 10^6. This corresponds to $E_{||} = 3 \times 10^6$ [V/cm], which is consistent with, e.g. [174]. The absolute flux scale was chosen such that the predicted gamma-ray spectrum matches with the measurements.

As can be clearly seen in the figure, the measured spectrum requires modification of the standard models.

---

[1] The different R_{curv} for different emission region can be taken into account by replacing Γ with $\Gamma(R_{curv}/1000[\mathrm{km}])^{-1/3}$ (see Eq. 8.4)

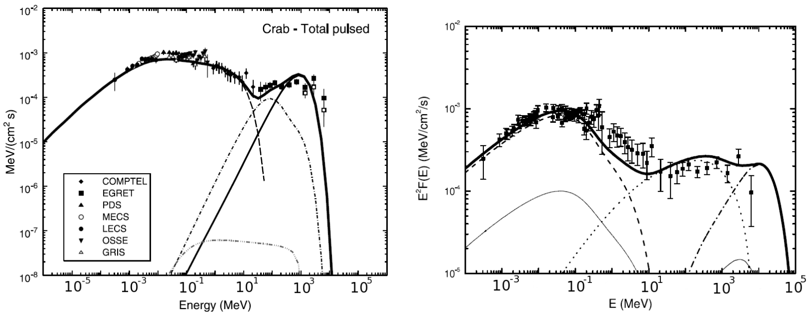

Figure 8.1: Theoretical explanations of the energy spectrum of the Crab pulsar assuming that the emission region is in the outer magnetosphere. Two models, namely Harding et al. (left, see [93]) and Tang. et al (right, see [177]) are shown. The highest end of the spectrum are explained by the curvature radiation from nearly monoenergetic electrons as indicated by a solid line (left) and a dashed-dotted line (right). The emission between 100 MeV and 1 GeV, where a power law spectrum with an index of ~ -2.0 *is observed, is explained by the synchrotron radiation (a dash-dotted line in the left panel) or inverse Compton emission (a dotted line in the right panel). Below 10 MeV, the emissions from secondary electron-positron pairs created by high energy gamma-rays are considered to be responsible for the observed spectrum.*

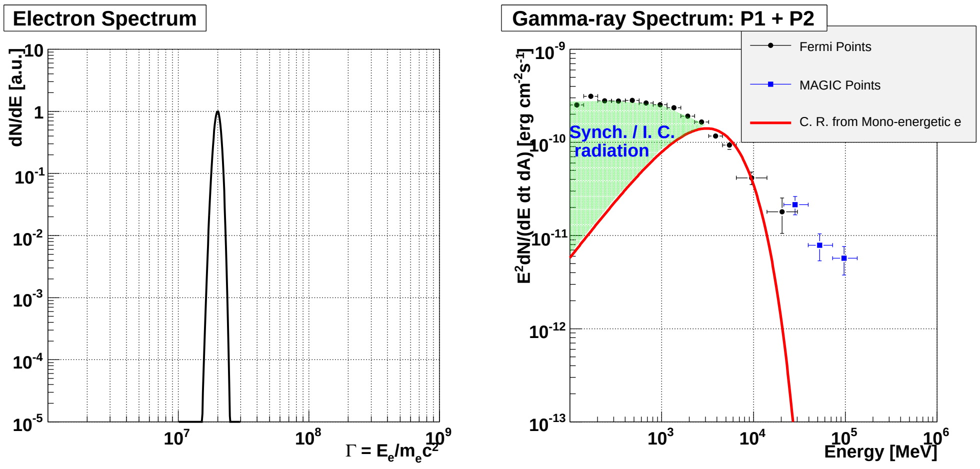

Figure 8.2: Applying the standard scenario to the highest end of the observed spectrum for P1 + P2. Left: Assumed Γ *factor spectrum for electron. It has a Gaussian shape with the mean of* 2×10^7 *and the RMS of* 10^6*. Right: The energy spectrum of the curvature radiation from the assumed electron spectrum, overlaid with the observed results. MAGIC measurements are largely deviated from the expected spectrum. The discrepancy between the curvature radiation spectrum and observed data below 3 GeV (a green shaded region) could be explained by either the synchrotron radiation or the inverse Compton scattering (see. Fig. 8.1).*

1) Steep Power Law Tail Assumption

Given the fact that the power law with an index of ~ -3 describes well the observed gamma-ray spectrum above 4 GeV, the simplest assumption for the electron spectrum would be a power law with an index of ~ -8, because if the electron has a power law spectrum with an index of $-p$, the resulting curvature radiation spectrum should show the power law with an index of $-q = -(p+1)/3$, as discussed in Sect 1.3.4. I assumed a power law with an index of -8 between 1.7×10^7 and 10^8 in the Γ spectrum. For $\Gamma < 10^7$, a Gaussian with the mean of 1.7×10^7 and the RMS of 10^6 is assumed so that the modification with respect to the standard model is only on higher energy side. The measured spectrum of P12 can well be explained by the curvature radiation from these electrons as expected (the top panels of Fig. 8.3). Obviously, the main difficulty is to find a convincing argument for the shape of the electron spectrum.

2) Log-Gaussian Assumption

It might also be possible that the observed power-law-like behavior above the cut-off energy is part of a curved spectrum, whose curvature is not visible due to the statistical uncertainty, the limited energy resolution and the limited energy coverage of the measurements.

For example, a log-Gaussian spectrum of the electrons produce a gamma-ray spectrum extending to the MAGIC energies. In the bottom panels of Fig. 8.3, the log-Gaussian spectrum of the electron with the mean of $\log_{10}(\Gamma)_{mean} = 7$ and the RMS of $\log_{10}(\Gamma)_{RMS} = 0.15$ is assumed.

$$\frac{dN_e}{d\Gamma} \propto \exp\left(-\frac{(\log_{10}\Gamma - 7)^2}{2 \cdot 0.15^2})\right) \tag{8.6}$$

The spectrum above the cut-off can be reasonably explained, taking into account that MAGIC and *Fermi*-LAT may have a relative energy scale difference of up to $\sim 30\%$. The idea behind the log-Gaussian spectrum of Γ is that the electrons are not as monoenergetic as the standard model predicts. This might originate from a small distortion of the pulsar magnetosphere structure from the standard model.

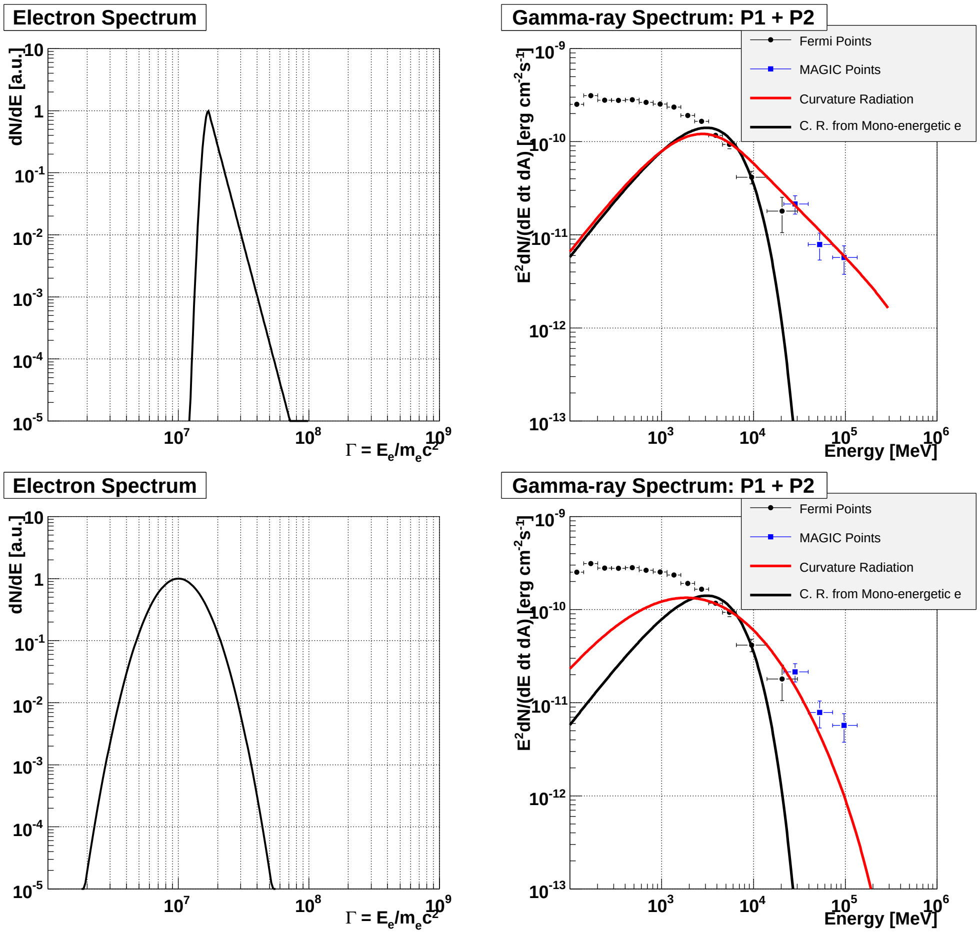

Figure 8.3: The same as Fig. 8.2 but for different Γ *spectrum. Top: A power law tail after the peak is assumed for the* Γ *spectrum. At* $\Gamma < 10^7$, *a Gaussian with the mean of* 1.7×10^7 *and the RMS of* 10^6 *is assumed, while a power law spectrum with an index of* -8 *is assumed between* 1.7×10^7 *to* 10^8. *The resulting curvature radiation reproduces the observed results very well. Bottom: A Log-Gaussian spectrum is assumed for the* Γ *spectrum. The mean of* $\log_{10}(\Gamma)_{mean} = 7$ *and the RMS of* $\log_{10}(\Gamma)_{RMS} = 0.15$ *is used. The resulting curvature radiation reproduces the observed results reasonably well taking into account the possible energy scale difference between MAGIC and Fermi-LAT up to* $\sim 30\%$.

3) Two Population Assumption

Several authors consider the possibility that the observed pulsation is the sum of the emissions from the two poles (see e.g. [174] and [177]). The two contributions to the light curve are shown in Fig. 8.4. Even though their calculations do not predict an energy spectrum extending to 100 GeV, the possibility of the contributions from the two isolated places make the two population assumption intriguing.

In fact, the model of two population of electrons can explain the measurements as well, as shown in the top panels of Fig. 8.5. Here I assumed two Gaussian spectra with the mean Γ being 2×10^7 and 4×10^7. $R_{curv} = 1000$ km is used. The RMSs of the two Gaussians are 20 times smaller than its mean. The peak flux of the second population is 200 times lower than that of the first.

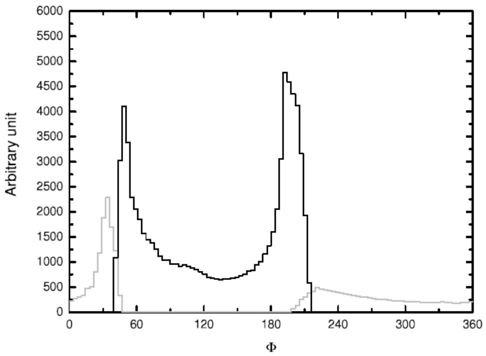

Figure 8.4: A theoretical explanation of the light curve assuming that emissions from the two poles contribute to the observed pulsation. The inclination angle of the dipole axis with respect to the rotation axis is assumed to be 50 degrees and the viewing angle is assumed to be 76 degrees. Contributions from each pole are overlaid with different intensity of the lines. Figure adopted from [177]

4) Power Law + Exponential Cut-off Assumption

The power law with an exponential cut-off for the electron spectrum produces an interesting results. By assuming a power law with an index of -3 and cut-off at $\Gamma = 0.5 \times 10^7$ for electrons, the resulting curvature radiation can explain the observed gamma-ray spectrum very well from 100 MeV to 100 GeV, if the relative energy scale difference of up to $\sim 30\%$ is taken into account (see the bottom panels of Fig. 8.5). This assumption does not require additional emission mechanisms such as the inverse Compton scattering and the synchrotron radiation in order to explain the measured spectrum between 100 MeV to 3 GeV.

It is known that the electron energy spectrum may exhibit a power law with an exponential cut-off in the case of shock acceleration in a supernova remnant taking into account either the acceleration-time limits (see [68]) or radiative-loss limits (see [192]). In order to apply a similar scheme to a pulsar, the acceleration mechanism in the pulsar magnetosphere needs to be reconsidered from scratch.

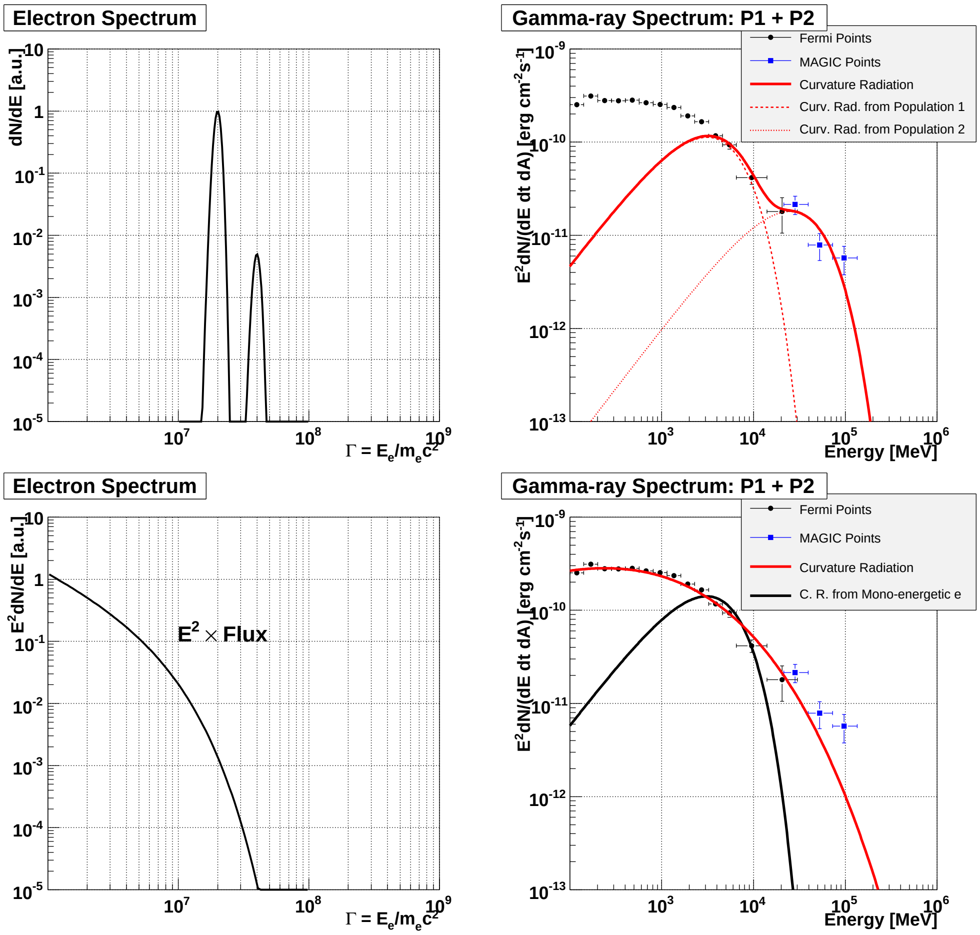

Figure 8.5: The same as Fig. 8.2 but for different Γ spectrum. Top: Two population of the Γ spectrum is assumed. Two Gaussian spectra with the mean Γ being 2×10^7 and 4×10^7 are used. The RMSs of the two Gaussians are 20 times smaller than its mean. The peak flux of the second population is 200 times lower than that of the first. The resulting curvature radiation reproduces the observed results very well. Bottom: The power law with an exponential cut-off is assumed for Γ spectrum. The power law index of -3 and cut-off at $\Gamma = 0.5 \times 10^7$ are used. The resulting curvature radiation can explain the observed spectrum very well from 100 MeV to 100 GeV, if the relative energy scale difference of up to $\sim 30\%$ is taken into account. This assumption does not require additional emission such as the inverse Compton scattering or the synchrotron radiation between 100 MeV to 3 GeV.

8.2.3 Constraints on the Acceleration Electric Field in an Ideal Dipole Magnetic Field

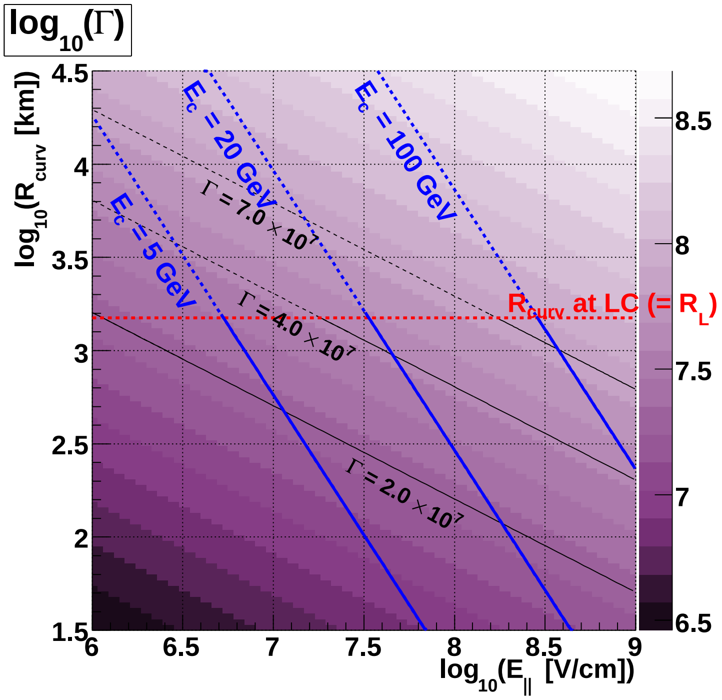

Figure 8.6: The electron Lorentz factor Γ *as a function of the field curvature* R_{curv} *and the acceleration field strength* $E_{||}$*, expressed with a color scale. Black lines indicate the contor lines for* $\Gamma = 2.0^7$*,* 4.0×10^7 *and* 7.0×10^7*. Blue lines indicate the corresponding cut-off energy of curvature radiation photons for 5 GeV, 20 GeV and 100 GeV (see Eq. 8.4.). A red dotted line indicate the co-rotation radius, which should be the upper limit in* R_{curv}*.*

Based on Eq. 8.2, Γ as a function of R_{curv} and $E_{||}$ is graphically shown in Fig. 8.6. R_{curv} as a function of $E_{||}$ for $E_c = 5$ GeV, 20 GeV and 100 GeV are shown by blue lines in the same figure.

It is known that R_{curv} of the dipole magnetic field is well approximated as $R_{curv}(r) = \sqrt{R_L r}$ (see e.g. [34]), where R_L is the co-rotation radius (see Sect. 2.5.2) and r is the distance from the center of the neutron star. Since the emission region must be within the light cylinder, $R_{curv} < R_L$ would be the reasonable upper limit on R_{curv}. Assuming that the (true) gamma-ray spectrum is extending as a power law up to 100 GeV without a cutoff, as is the case for **1) Steep Power Law Tail Assumption** in the previous subsection, there must be a place where $E_{||} > 2.9 \times 10^8$ [V/cm]. This is ~ 100 times larger than the value used in the standard model (see e.g. [174]). Assuming that the gamma-ray spectrum observed at around ~ 100 GeV is basically the tail of the curvature radiation spectrum with a 20 GeV cut-off, as is the case for **3) Two Population Assumption** in the previous subsection, the lower limit in $E_{||}$ will be $E_{||} > 3.3 \times 10^7$ [V/cm]. This is ~ 10 times larger than the standard value.

8.2.4 Possible Explanations for the High Energy Tail of the Gamma-ray Spectrum in an Imperfect Dipole Magnetic Field

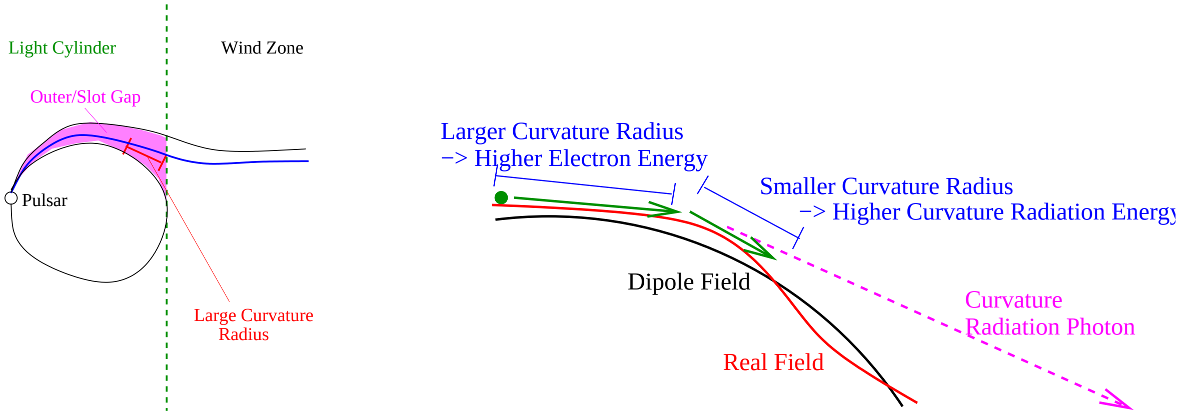

Figure 8.7: Schematical explanations of two ideas for the high energy tail of the observed gamma-ray spectrum. Left: The magnetic field curvature near the light cylinder can be much larger than that of the dipole fields, because some field lines in the gap should connect to the wind zone. Such a large field curvature may produce a high energy tail in the gamma-ray spectrum as can be understood from Eq. 8.5. Right: If the magnetic field lines are slightly wiggling along the dipole structure, there may be two radially connected regions the inner one of which has a larger-than-dipole field curvature and the outer one of which has a smaller-than-dipole field curvature. Since the curvature radiation cooling is weaker in the larger curvature field, electrons can be accelerated to higher energies. Then, these electrons subsequently enter the smaller curvature field, generating the unusually high energy curvature photons.

The high energy tail of the observed gamma-ray spectrum could be explained by the imperfect dipole structure of the magnetic field.

The thickness of the Outer Gap or the Slot Gap can be as much as $0.1 R_L$ at the light cylinder. The magnetic field lines in the middle of the gap should not close within the light cylinder and should be connected to the wind zone. Therefore, there is a possibility that the magnetic field curvature R_{curv} near the light cylinder in the middle of the gap is significantly larger than that of the dipole structure (see the left panel of Fig. 8.7). As can be seen from Eq. 8.2, the larger the curvature (R_{curv}), the higher the electron energy (Γ). Alghouth the energy of the curvature radiation photon is proportinal to R_{curv}^{-1}, it is also proportional to Γ^3 (see Eq. 8.4), resulting in the higher photon energy from the larger curvature (see Eq. 8.5).

A more efficient mechanism for producing the high energy tail could be as follows: Let us assume that the magnetic fields are slight wiggling along the dipole field in a small scale ($1 - 10$ km). There may be two radially connected regions the inner one of which has a larger-than-dipole field curvature and the outer one of which has a smaller-than-dipole field curvature (see the right panel of Fig. 8.7). Since the curvature radiation cooling is weaker, electrons can be accelerated to higher energies in the larger curvature field. These electrons subsequently enter the smaller curvature field, generating the anormally high energy curvature photons.

8.3 Inverse Compton Scattering as a Second Radiation Component

As shown in the top panels Fig. 8.5, a second emission component can explain the deviation of the MAGIC measurements from the standard model. In the previous section, a second population of electrons is assumed. By introducing the inverse Compton scattering, a single monoenergetic electron population might also explain the MAGIC measurements.

As discussed in Sect. 1.3.2, the energy of the radiated photon via the inverse Compton scattering is (see Eq. 1.37)

$$E_\gamma \simeq \epsilon\Gamma^2 \tag{8.7}$$

where ϵ is the energy of the target photon and Γ is the Lorentz factor of the electron. In order to have a radiation peak at 30 GeV for an electron population with $\Gamma = 2 \times 10^7$, ϵ should be peaked at

$$\epsilon \simeq E_\gamma/\Gamma^2 \simeq 10^{-4} \quad [\mathrm{eV}] \tag{8.8}$$

For a thermal radiation, 10^{-4} eV corresponds to 1 K, which is by far lower than the stellar surface temperature ($\sim 10^6$ K, see Sect 1). On the other hand, the CMB radiation corresponds to 2.7 K in temperature, which is actually close to $\sim 10^{-4}$ eV. However, it is known that the number density of CMB photons (400 cm^{-3}) is much lower than the radio photons emitted within the pulsar magnetosphere ($> 10^7$ cm^{-3}) (see [102]).

Therefore, in order to reproduce the inverse Compton scattering spectrum peaked at around 30 GeV, there must be a particular mechanism to produce a soft photon spectrum peaked at $\sim 10^{-4}$ eV, which is hard to imagine. Therefore, an effect of a simple inverse Compton scattering for the extended spectrum is highly unlikely.

8.4 Radiation Efficiency

The total energy loss of a pulsar, i.e. the spin down luminosity $\dot{E}$ can be estimated from the period and the time derivative of it, as described in Sect 2.3.1. For the Crab pulsar, it is $\dot{E} = 4.6 \times 10^{38}$ erg/s.

Here, I add an estimate of the radiation efficiency, which is a fraction of the spin down luminosity deposited in a given energy range. The estimation method is adopted from [4]. When the observed flux is F_{obs}, the luminosity L can be calculated as $L = 4\pi f_\Omega F_{obs} D^2$, where f_Ω and D are the beaming angle factor and the distance from the pulsar to the Earth. f_Ω depends on the inclination angle α of the magnetic dipole axis and the viewing angle ξ (see Sect 2.7.3). For the Crab pulsar, assuming the SG model or the OG model, $\alpha \sim 70$ degrees and $\xi \sim 60$ degrees well explain the light curves (see e.g. [53]), the nebula torus structure in X-ray (see [141]), and the polarization of the optical pulsation (see [169]). For α and ξ near these values, $f_\Omega \simeq 1.0$ is the good approximation according to [191]. The distance is known to be $D =$

2.0 ± 0.2 kpc (see e.g. [184]). From the measurements, F_{obs} above 100 MeV is calculated to be $(1.31 \pm 0.03) \times 10^{-9}$ erg/s.

Using $\dot{E} = 4.6 \times 10^{38}$ erg, $D = 2.0$ kpc and $f_{\Omega} = 1.0$, the efficiency η above 100 MeV is calculated as

$$\eta = \frac{L}{\dot{E}} = \frac{4\pi f_{\Omega} F_{obs} D^2}{\dot{E}} = (1.36 \pm 0.04) \times 10^{-3} \tag{8.9}$$

Only 0.13% of the total energy loss is due to the radiation above 100 MeV. As discussed in Sect. 1.2.4 and Sect. 2.3.2, the rotation energy is carried away mostly by the pulsar wind.

Fig. 8.8 shows $\eta(E)$ as a function of energy. Based on the combined analysis described in Sect. 7.1.3, η for energies between 30 and 100 GeV is $(8.4 \pm 1.1) \times 10^{-6}$. If the spectrum had shown the pure exponential cut-off, it would have been $5.1^{+2.8}_{-2.1} \times 10^{-7}$, which is a factor of ~ 10 lower than the measurement. The discrepancy between the exponential cut-off and the MAGIC measurement corresponds to $(8 \times 10^{-6})/(1.4 \times 10^{-3}) = 6 \times 10^{-3}$ = 0.6% of the radiation energy above 100 MeV.

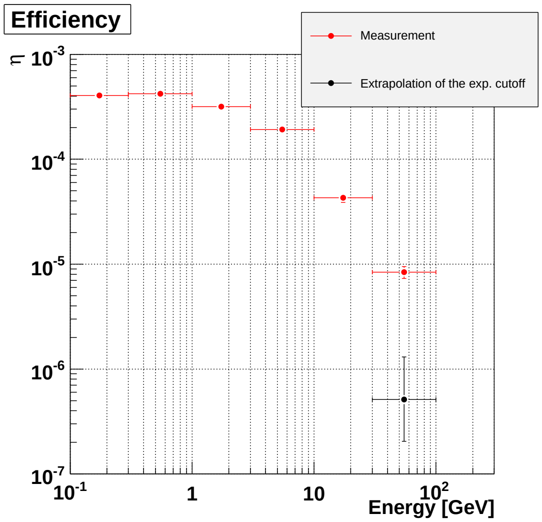

Figure 8.8: The radiation efficiency η for different energy intervals. Red points indicate the observed results. Below 10 GeV, TP spectrum with the exponential cut-off assumption is used while for the bin of 10 GeV to 30 GeV, a power law assumption above 4 GeV is used (see Sect. 6.6). For the bin of 30 GeV to 100 GeV, combined analysis with an power law assumption for P1 + P2 is used (see Sect. 7.1.3). The black point indicates the extrapolation of the exponential cut-off spectrum of TP based on Fermi-LAT measurement.

8.5 Remarks on the High Energy Tail of the Crab Pulsar Energy Spectrum

Fermi-LAT measured the energy spectrum of the Crab pulsar with good precision up to ~ 10 GeV, which is only a factor of ~ 2 higher than the exponential cut-off energy (E_c in Eq. 6.5). The *Fermi*-LAT-measured spectrum is consistent with the standard model. Therefore, the standard model is successful in explaining the energy spectrum of the Crab pulsar in the energy region where a vast majority of the gamma-ray radiation energy is deposited.

On the other hand, MAGIC observed the energy spectrum of the Crab pulsar above 25 GeV, which is a factor of ~ 5 higher than the exponential cut-off energy. Only a small fraction of the radiation energy is deposited above 25 GeV. The deviation from the standard model detected by MAGIC requires only a higher order correction for the standard model.

It should also be mentioned that, all the dedeuced electron spectra discussed in Sect. 8.2.2 eventually need to be corrected by the “smearing” of the energy due to the limited and not-perfectly-known energy resolution. While the simulations clearly showed that the observed spectrum up to 100 GeV is not just an artifact of the energy resolution (see Sect. 7.1.1), I could not determine the precise partition of genuine high energy gamma-rays and lower energy gamma-rays mismeasured with higher energy assignment. It is obvious that clarification can only come from better measurements.

8.6 Energy Dependence of the Rising and Falling Edges in the Light Curve

The basic shape of the light curve is explained by the structure of the last closed field lines, as discussed in Sect. 2.7.3. In that explanation, electrons are assumed to move parallel to the field lines, i.e. the pitch angle ϕ of electrons is assumed to be 0. Since the beaming angle of the emitted photons is $\sim 1/\Gamma \sim 10^{-7}$, all the photons are considered to be emitted tangentially to the field lines. However, this scenario explains neither the exponential behavior of the edges nor the energy dependence of the rise/fall time of the edges, which are clearly visible in the observed data.

Observed results can be explained by, for example, assuming that the emission from each field line is not beamed with an angle of $\sim 1/\Gamma$, but has an exponential angular distribution characterized by its decay constant θ_c:

$$F(\theta) = F_0 \exp(-\theta/\theta_c) \tag{8.10}$$

where θ_c is dependent on the photon energy. Then, the resulting light curve should be broadened compared with the one without a sizable emission angle , as shown in Fig. 8.9.

Here, I additionally assume that the shape of the the outer edges (the rising edge of P1 and the falling edge of P2) reflect the angular distribution of the emission along a single field line, while the shape of the inner edges (the falling edge of P1 and the rising edge of P2) are governed

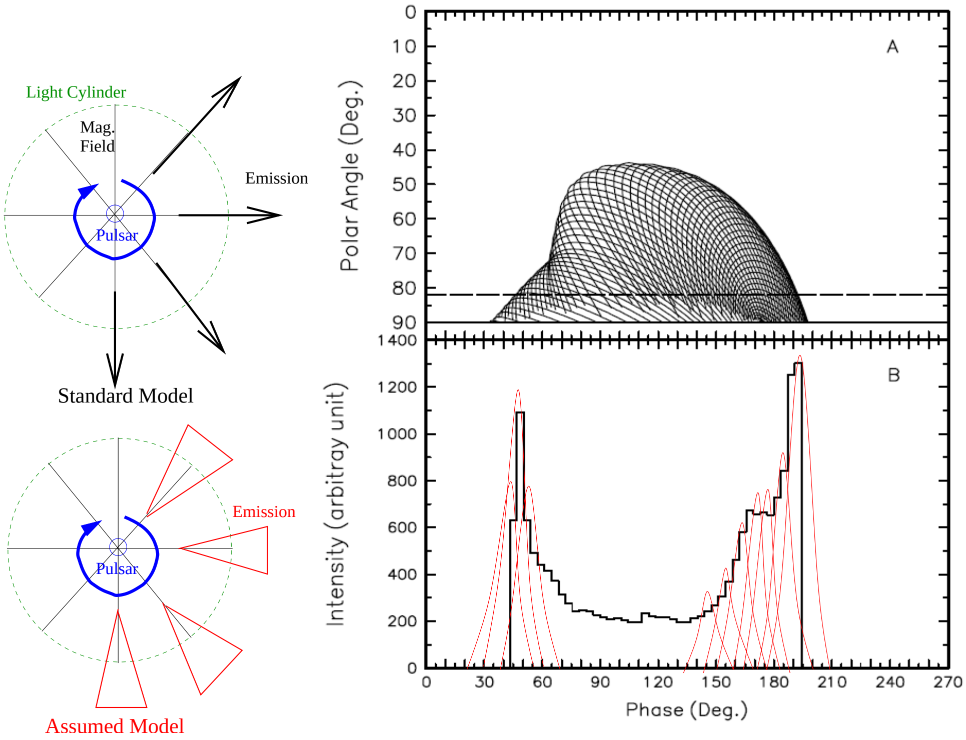

Figure 8.9: Top left: A simplified top view of a pulsar of the standard model. The emission is strongly beamed along the field lines. Bottom left: A simplified top view of a pulsar of the assumed model. The emission has an exponential angular distribution along the field lines. Top right: The emission profile map of the standard model assuming that inclination angle between the rotation axis and the dipole axis is 65 degrees. Figure adopted from [53]. Bottom right: The hypothetical light curve. A black histogram shows the basic structure of the light curve explained by the emission profile map shown in the top panel. Red lines show the hypothetical broadening effect taking into account the angular distribution of the emission Original figure is adopted from [53] and red lines are added by myself.

by the overall field line structure (see Fig. 8.9). From Eq. 7.4 and Eq. 7.7, the rise time of P1 and the fall time of P2 as a function of energy are:

$$\tau \simeq (0.022 \pm 0.0018) - (0.0095 \pm 0.0034) \log_{10}(E[\mathrm{GeV}]) \tag{8.11}$$

where the simple mean of τ^{P1}_{rize} and τ^{P2}_{fall} is adopted. Since the emission angle θ can be translated into the pulse phase p as $p = \theta/2\pi$, Eq. 8.11 leads to

$$\theta_c \simeq (0.14 \pm 0.01) - (0.06 \pm 0.02) \log_{10}(E[\mathrm{GeV}]) \quad [\mathrm{rad}] \tag{8.12}$$

$$= (7.9 \pm 0.6) - (3.4 \pm 1.2) \log_{10}(E[\mathrm{GeV}]) \quad [\mathrm{deg}] \tag{8.13}$$

This is by far larger than $1/\Gamma \sim 10^{-7}$. The large emission angle should be the consequence of the large pitch angle of the high energy electrons. These electrons with a spiral orbit should emit synchrotron radiation, which should explain the observed gamma-rays at least below 3 GeV (where the energy dependence of the edges is clearly seen as shown in Fig. 7.12.) The strength of the magnetic field at 1000 km from the neutron star is $> 10^6$G and high energy gamma-rays are therefore reasonably expected (see Sect. 1.3.3).

However, in order to realize such a large pitch angle orbit, there must exist a process which nearly instantly provides a large perpendicular momentum, because a gradual increase of perpendicular momentum cannot occur due to the strong energy loss by the synchrotron radiation itself. (This is actually the reason why the pitch angle of electrons is normally considered to be 0.)

A possibility that the pitch angle ϕ can has a large value has been discussed by, for example, S. A. Petrova (see [149] and references therein). The basic idea is as follows: The accelerated electrons efficiently absorb radio photons with a frequency corresponding to the cyclotron frequency when it is converted into the electron rest frame. This cyclotron resonance absorption of radio photons is so efficient that it can cause a large pitch angle even though electrons are continuously losing energy by the synchrotron radiation. This scenario is used in [93] to reproduce the Crab pulsar energy spectrum at around 100 MeV (see Fig. 8.1). However, this process produces neither the exponential angular distribution nor the electron-energy dependent pitch angle (see [149]).

8.7 Energy Dependence of the Peak Phase

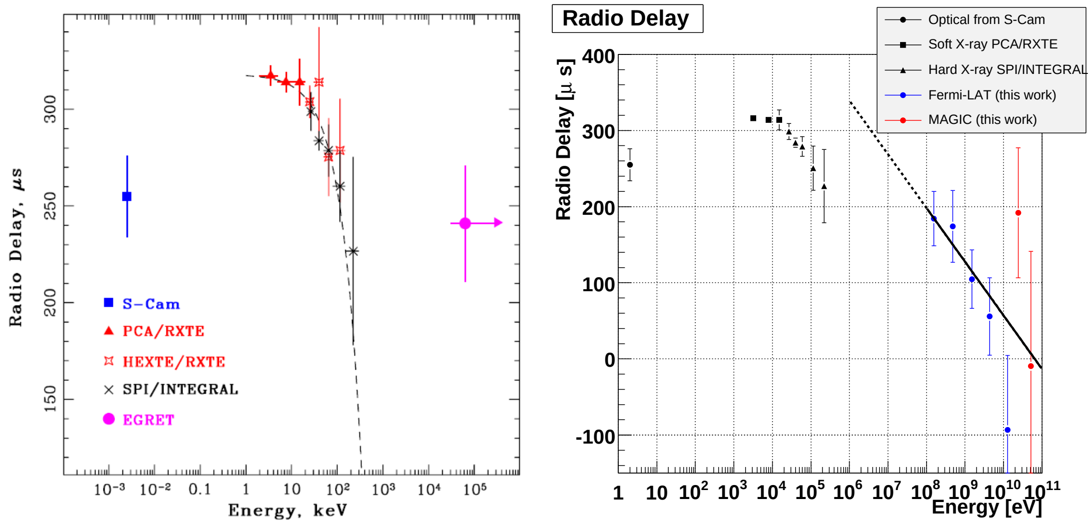

Figure 8.10: Left: Radio delay as a function of energy. A simple linear function fit to X-ray range is indicated by a dashed line. Figure adopted from [137] Right: The same as the left panel but Fermi-LAT and MAGIC results analyzed by myself are shown. The energy dependence calculated based on Eq. 7.15 is shown as a solid line above 100 MeV. The dotted line is an extrapolation of it down to 1 MeV. The points below 1 MeV are copied from the left panel by eye.

In Fig. 8.10, the first peak (P1) position as a function of energy is shown from optical to high energy gamma-rays. It is expressed as “radio delay”, which tells how much earlier the peak at a given energy occurs compared to the radio peak (Jodrell Bank, at 610 MHz). The energy dependence of the radio delay has been studied in the X-ray range. As discussed by many authors (see e.g. [115], [156] and [137]), the simplest explanation for the radio delay and its energy dependence is the difference in the emission region within the magnetosphere. i.e., the higher the energy is, the more inner of the magnetosphere the emission region is. In [137], a simple linear function was fitted to the data, deriving a shift of $0.6 \pm 0.2 \mu$s keV^{-1} (see the left panel of the figure). It corresponds to

$$L(E) \quad = \quad (180 \pm 60) \times (E[\mathrm{keV}]) \quad [\mathrm{m}] \tag{8.14}$$

where L indicate the path length difference with respect to the radio emission region. Eq. 7.15 can be rewritten as $(130 \pm 20) - (70 \pm 30)\log_{10}(E/\mathrm{GeV}) \quad [\mu\mathrm{s}]$ in radio delay, which is shown as a black line in the left panel of the figure. In path length, this corresponds to

$$L(E) \quad = \quad (40 \pm 6) - (20 \pm 9)\log_{10}(E[\mathrm{GeV}]) \quad [\mathrm{km}] \tag{8.15}$$

Considering the size of the light cylinder ($R_L = 1500$ km), Eq. 8.14 and Eq. 8.15 are reasonable. On the other hand Eq. 8.14 and Eq. 8.15 are apparently not consistent as can be seen from Fig. 8.10. Actually, the shape of the energy spectrum of the Crab pulsar (see Fig. 2.29) and the theoretical model (see Fig. 2.22) suggests different mechanisms for X-ray and high energy gamma-ray radiation. Therefore, it may be natural that the energy dependence of the radio delay is different in the two well-separated energy ranges.

It should be noted that the definition of the peak phase is different for different types of analyses. For example, A. A. Abdo et al. (see [4]), which is the official publication from the *Fermi* collaboration, determined the peak phase by fitting an asymmetric Lorentzian function to the binned light curves. In their analysis, the peak phase above 100 MeV is constant and -0.008 ± 0.001, which corresponds to 280 ± 30 μs in radio delay, though their highest energy bin of 3 to 10 GeV shows marginal deviation of -0.005 ± 0.002, corresponding to 170 ± 70 μs in radio delay.

Chapter 9

Development of High Quantum Efficiency Hybrid Photodetector HPD R9792U-40

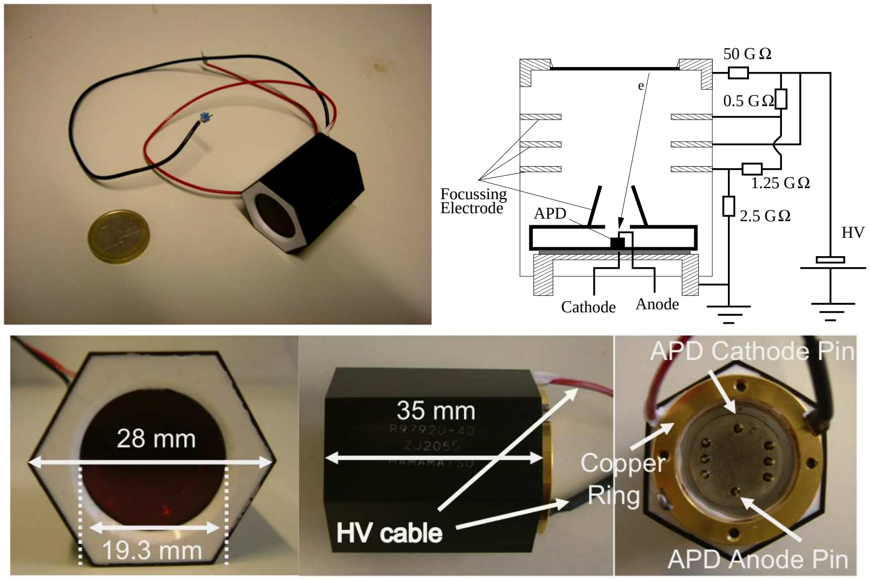

Figure 9.1: Top left: Photograph of the HPD R9792U-40. A 1 euro coin is put as a scale reference. Top right: The schematic of the electrode inside the HPD. Bottom left: The top view of the HPD. Bottom middle: The side view of the HPD. Bottom left: The bottom view of the HPD.

For better pulsar observations by MAGIC, a lower energy threshold, a higher gamma-ray detection efficiency, a higher energy resolution and an improved gamma-ray/hadron separation would be necessary. All these improvements require the detection of more Cherenkov photons. However, the diameter of the reflector of MAGIC is 17 m and it is difficult to enlarge it, considering the focusing accuracy and the total load to the telescope frame and the drive system. The better solution would be an improvement of the photodetection efficiency of the photosensors in the camera.

I participated in the second phase of the development of a new photosensor, HPD R9792U-40, together with Hamamatsu Photonics and other colleagues in the Max-Planck-Institut für Physik. HPD R9792U-40 is a so-called hybrid photodetector. This chapter describes the property and the performance of the HPD. Major results are also published in [158].

9.1 Structure and Operation Principle of the HPD R9792U-40

9.1.1 Overall Structure

The overall structure of the HPD R9792U-40 is shown Fig. 9.1. The HPD has a hexagonal cylindrical shape with the major hexagonal diameter of 28 mm and the height of 35 mm. On the top side there is a round glass window with the diameter of 19.3 mm and a semiconductor photocathode crystal (GaAsP) is attached to it from inside. The thickness of the photocathode is about 1 micrometer. To reduce the work function, cesium oxide (CsO) is evaporated onto it. Inside the tube, a 3 mm diameter cylindrical Avalanche PhotoDiode (APD, made of silicon) is located on ~ 2.5 cm distance from the photocathode and is serving as an electron bombarded anode with an additional internal gain. Its cathode and anode pins are visible in the bottom side of the HPD. There are three electron focusing rings embedded in the wall of the tube and a focusing electrode of a conical shape is located near the APD. The photocathode high voltage (HV see Sect. 9.2) is divided by the voltage dividers (see the top right panel of Fig. 9.1), and 88%, 100% and 59% of the photocathode voltage are applied to the 3 focusing rings in the wall. To the conical-shaped electrode, the same voltage as APD bias (see Sect. 9.2) is applied.

9.1.2 Operation Principle

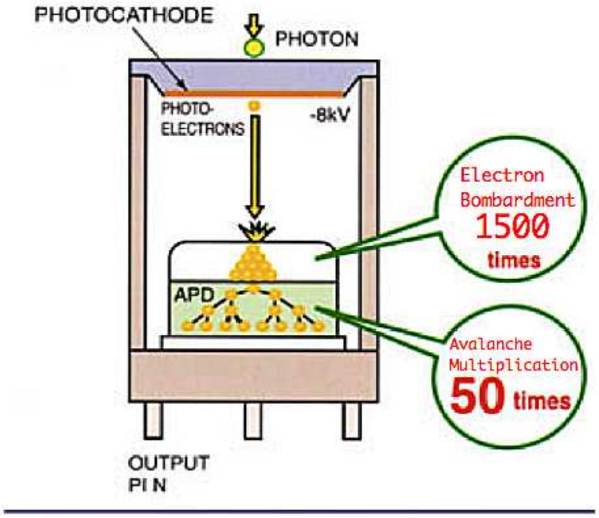

Figure 9.2: A schematical view of the working principle of the HPD. Figure adopted from [94].

Two voltages are applied to the HPD: ~ -8 kV to the photocathode and ~ 400 V to the APD anode (inverse bias voltage). When photons hit the photocathode, ph.e.s are produced. They are accelerated in the high electric field and bombard the APD. This bombardment produces ~ 1500 electron-hole pairs per one ph.e. (in the case of ~ -8kV photocathode voltage, see Sect 9.3.1) in the depleted layer of the APD. The secondary electrons are subsequently accelerated in the high electric field of the pn structure of the APD and initiate avalanches, providing an additional gain (see Sect. 9.3.2).

9.2 Photodetection Efficiency

The sensitivity of a photosensor can be described by the photodetection detection efficiency (PDE). The PDE is the product of the quantum efficiency (QE) of the photocathode and the ph.e. collection efficiency (CE), i.e., PDE = QE × CE.

9.2.1 Quantum Efficiency

The quantum efficiency (QE) have been measured in the following way. A HPD is set up in a dark box where a HV cable and a current readout cable are inserted. A laser (Spectral Products: ASTN-D1-W150) and a monochromator (Spectral Products: CM 110) are also connected to the dark box, with which HPD photocathode can be illuminated by light with a specific (less than 10 nm in resolution) wavelength. The measurement setup is shown in the left panel of Fig. 9.3. For the HPD photocathode, -2 kV is applied, which is enough to focus all the ph.e.s onto the APD [1]. The anode and the cathode of the APD are shorted as shown in the right panel of Fig. 9.3. First, changing the wavelength of the illuminating light from 250 nm to 800 nm, the current from the APD to the ground, which is equal to the photocathode current, is measured with a current meter (KEITHLEY: 6485 picoamperemeter). And then, the same current measurement is repeated replacing the HPD with a calibrated PIN photodiode (Hamamatsu Photonics, S6337-01), whose QE is known with an accuracy of 2%. The ratio of the output currents corresponds to the ratio of the quantum efficiencies. Therefore, the QE of the HPD is measured as

$$QE_{HPD}(\lambda) = QE_{PIN}(\lambda) \times I_{HPD}(\lambda)/I_{PIN}(\lambda) \tag{9.1}$$

where λ is the wavelength of the light and I denotes measured current.

The QE curves of four HPDs are shown in the left panel of Fig. 9.4. The QE curve of the currently used PMT, the Cherenkov light spectrum of an 80 GeV gamma-ray shower from the zenith and the NSB spectrum are also shown in the same figure. The QE drops at the wavelengths below 400 nm, while the peak of the Cherenkov spectrum is at around 330 nm. In order to enhance the QE below 350 nm, the wavelength shifter (WLS) coating was studied by M. Hayashida (see [94]). The improvement by the WLS coating is also shown in the same figure. Convoluted with the spectrum, the HPD (with the WLS coating) can detect ~ 1.9 times more Cherenkov photons than currently used PMT, while it also detects ~ 3.4 times more NSB photons.

9.2.2 Collection Efficiency

From the simulation, the collection efficiency (CE) of the HPD is known to be more than 99%[2], while that of the currently used PMT is typically about 80%. It must be noted that in the case of

---

[1] As described in 9.5.2, at a certain probability, the ph.e.s escape from the APD after bombardment due to backscattering effect. However, these ph.e.s will end up in the conical electrode which is electrically connected to the APD anode. Therefore, the photocathode current can be properly measured in this method.

[2] Based on the simulation performed by Hamamatsu Photonics

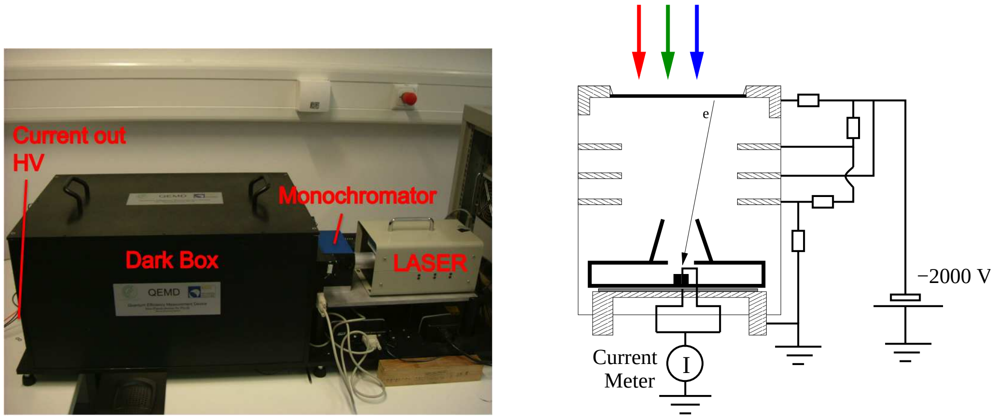

Figure 9.3: Left: A photograph of the QE measurement setup. Right: The schematic of the circuit for the QE measurement. The anode and the cathode of the APD are shorted. Then, the current from the APD to the ground is measured. This current is equal to the photocathode current.

the HPD, a fraction of the charge ($\sim 10\%$) may be lost due to the backscattering effect as will be described in Sect. 9.5.2.

9.2.3 Improvement in PDE Compared to PMTs

Compared to the currently used PMTs, the number of detected Cherenkov photons (from the zenith) will be raised by a factor of 2.1 (1.9 in QE × 1.1 in CE). This helps to improve the energy threshold, the energy resolution, the gamma-ray detection efficiency and the gamma-ray/hadron separation, even though the gain in the NSB photon detection efficiency is larger (3.8). A precise estimation of these improvements must rely on a detailed simulation.

It should be noted that as the zenith angle of the gamma-ray incoming direction increases, the peak of the Cherenkov light spectrum on the ground shifts to longer wavelengths due to the absorption (see Sect. 3.2.2). For example, for the shower coming from the zenith angle of 60 degrees, the gains are 2.4 and 3.8 in the number of detected Cherenkov photons and that of NSB photons, respectively.

9.2.4 Uniformity of the photocathode

The uniformity of the PDE of the photocathode was measured in Hamamatsu Photonics with a light beam of 1 mm diameter spot size. As shown in the right panel of Fig. 9.4, it is uniform, i.e., the variation is less than 10% over 16 mm diameter area and less than 20 % over 18 mm diameter area. It should be noted that, the QE curves shown in the left panel of Fig. 9.4 have been measured in the center of the photocathode with a spot size of ~ 5 mm. Since the uniformity is rather high, it represents the average QE over the photocathode with a good precision.

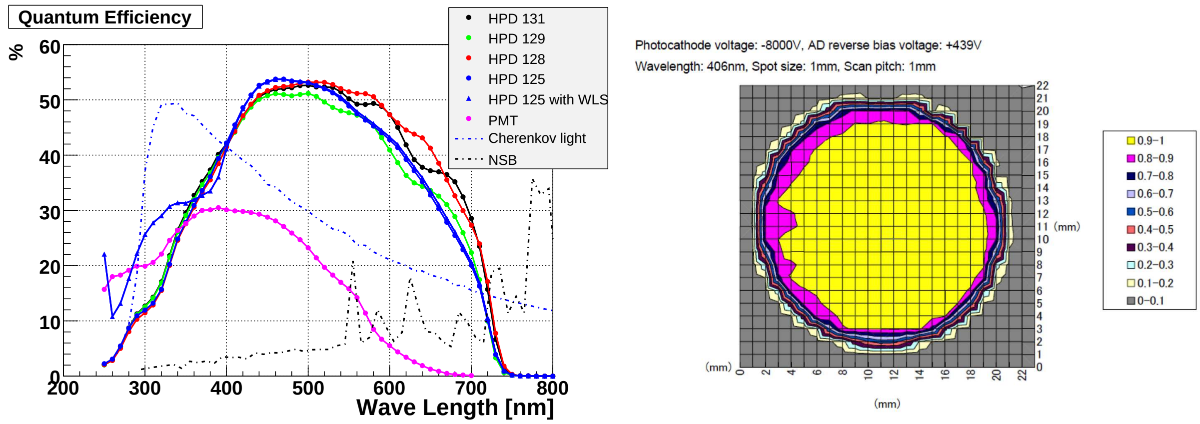

Figure 9.4: Left: The measured QE curves of some of HPDs (Black, green, red and blue lines). As a reference, the QE curve of the currently used PMT is also shown (the pink line). A blue line with triangles show the QE curve of an HPD coated with wavelength shifting material, which enhance the QE below 350 nm. The Cherenkov spectrum and the NSB spectrum measured on the ground are also shown by a blue and black dotted lines, respectively. Right: The uniformity of QE (PDE) over the photocathode area measured with light of 406 nm wavelength. The PDE normalized to its maximum value is shown by colors. The right figure provided by Hamamatsu Photonics.

9.3 Gain

9.3.1 Bombardment Gain

A ph.e. bombardment creates a number of electron-hole pairs in the APD (silicon). 3.6 eV is necessary for creating a single pair in silicon. The energy of the accelerated ph.e. (e.g. 8 keV) is consumed to create those pairs in the APD. However, not all energy can be detected as output charge because some of electron-hole pairs generated in the non-depleted region can not propagate into the depletion layer. Such pairs recombine without producing any avalanche.

Based on this feature, the bombardment gain has been measured in the following way. Inside a dark box, the HPD is illuminated by a LED (603 nm). For the APD bias voltage, 30 V is applied, under which the avalanche gain should be 1 (no gain) and the leakage current (see Sect. 9.3.2) is negligible. Changing the photocathode HV from 0 V to -8 kV, output current was measured by a current meter (KEITHLEY: electrometer 6517). The output current should be proportional to the bombardment gain. When the absolute value of the applied HV is less than 200 V, the current stays almost constant. Assuming that this current corresponds to the HV gain of 1, the bombardment gains for different HVs are calculated.

The results for three HPDs are shown in the left panel of Fig. 9.5. As expected, it is not linear but curved as shown in Fig. 9.5. Up to 3 keV, the gain is small and afterwards it increases linearly to the applied HV. The linear part can well be represented by a function $Gain$ = 290×(HV/[kV]-2.9), meaning that the energy loss at the SiO_2 layer and the non-depleted region is approximately 2.9 kV and that $1000/290 = 3.4$ eV is needed for creating an electron-hole pair. The small difference of the energy needed for a single pair with respect to the literature value (3.6 eV) could be attributed to the ph.e. energy dependence of the energy loss in the non-depleted region.

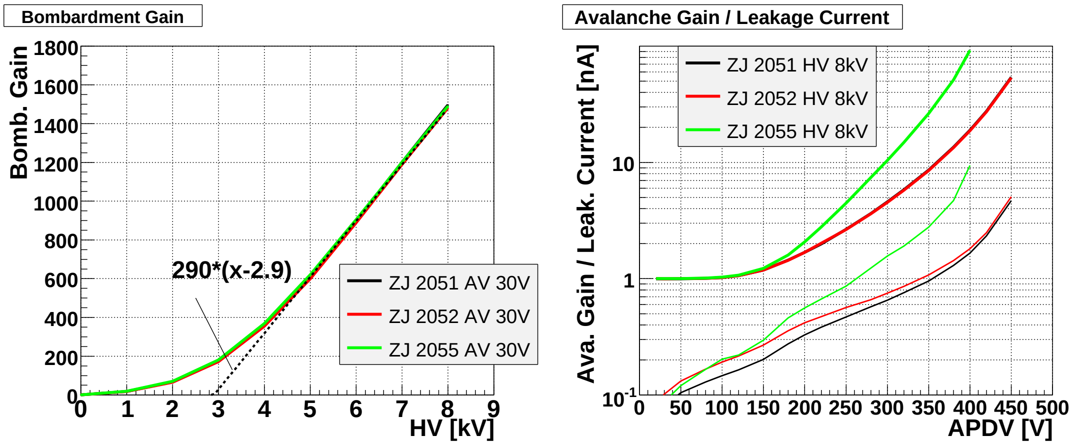

Figure 9.5: Left: The bombardment gain as a function of the photocathode HV. Right: The avalanche gain (thick lines) and the leakage current (thin lines) as a function of APD bias voltage (ZJ 2051, ZJ2052, and ZJ2055 denote the serial number of the HPDs.).

9.3.2 Avalanche Gain and Leakage Current

In the depletion region of the APD, electrons produced by the bombardment are accelerated by the bias electric field and create electrons (electron-hole pairs). Newly created electrons will also be accelerated to create more electron-hole pairs, resulting in the avalanche process. The APD is operated with a bias voltage lower than the breakdown voltage. and there is a finite resistance between the anode and the cathode. The avalanche process is very fast (< 1 ns). The multiplication of the pairs depends strongly on the bias voltage.

Even without an initial creation of the pair by the bombardment, when the bias voltage is applied, a small current flows across the APD due to the thermally generated electron-hole pairs in the depletion region [3]. This current is called the leakage current. The leakage current is also strongly dependent on the bias voltage. Before measuring the avalanche gain, the leakage current had been measured by setting an HPD in a dark box without any light source and applying various bias voltages to the APD from 0 V to the maximum applicable voltage (10 V less than the breakdown voltage). The results for three HPDs are shown in the right panel of Fig. 9.5. The leakage current increases exponentially. Near the breakdown voltage, the increase is especially rapid. The leakage current at the maximum applicable voltage is $5 - 10$ nA. The leakage current differs by a large factor from HPD to HPD.

Then, the avalanche gain is measured in the following way. Inside the dark box, the HPD is illuminated by a LED (603 nm). For the photocathode, -8 kV is applied. Changing the bias voltage from 0 V to the maximum applicable voltage, the output current is measured. The

---

[3] In addition, there is a contribution from a surface current

output current with the leakage current subtracted is proportional to the avalanche gain. When the voltage is less than 50 V, the current (with the leakage current subtracted) doesn't change. This current is assumed to be the one with the avalanche gain of 1 and the avalanche gain with higher voltages is calculated based on the output current. Avalanche gain as a function of the bias voltage is shown in the right panel of Fig. 9.5. There is a difference in the avalanche gain curve among different HPDs but the typical gain is $20 - 80$ at 400V.

9.4 Pulse Shape

Taking into account that the time spread of the atmospheric Cherenkov light reaching the ground is about 3 ns (for gamma-ray showers below 100 GeV) and that there is a constant NSB, the needed pulse width of the HPD should be below 3 ns in order to minimize the contamination of the NSB photons to the triggers and the shower image.

9.4.1 Standard Readout

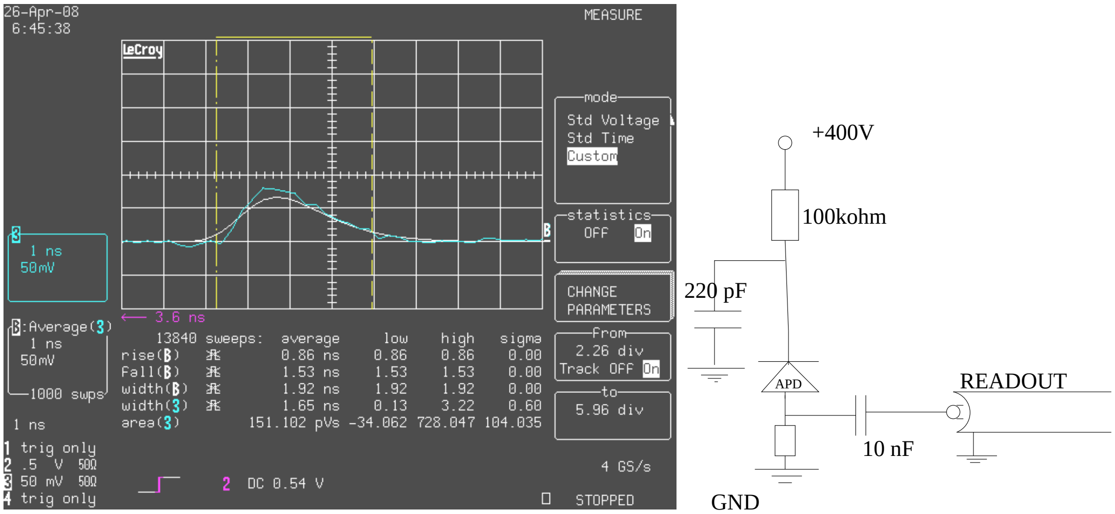
```
        13840 sweeps:   average     low     high    sigma
rise(B)    ⌘         0.86 ns    0.86    0.86     0.00
fall(B)    ⌘         1.53 ns    1.53    1.53     0.00
width(B)   ⌘         1.92 ns    1.92    1.92     0.00
width(3)   ⌘         1.65 ns    0.13    3.22     0.60
area(3)          151.102 pVs -34.062 728.047 104.035
```

Figure 9.6: Left: The pulse shape with the standard circuit. The rise time, the fall time and the FWHM are 0.9 ns, 1.5 ns, and 1.9 ns, respectively. Right: The readout circuit for the standard operation.

The pulse shape of the HPD and the standard readout circuit are shown in Fig. 9.6. This HPD is designed to provide a positive pulse polarity. The rise time, the fall time and the FWHM of the pulse is 0.9 ns, 1.5 ns, and 1.9 ns, respectively.

9.4.2 Inverted Polarity

By changing only the readout circuit, the polarity of the pulse can be inverted to the negative, as shown in Fig. 9.4.2. In this readout circuit, the rise time, the fall time and the FWHM of the pulse

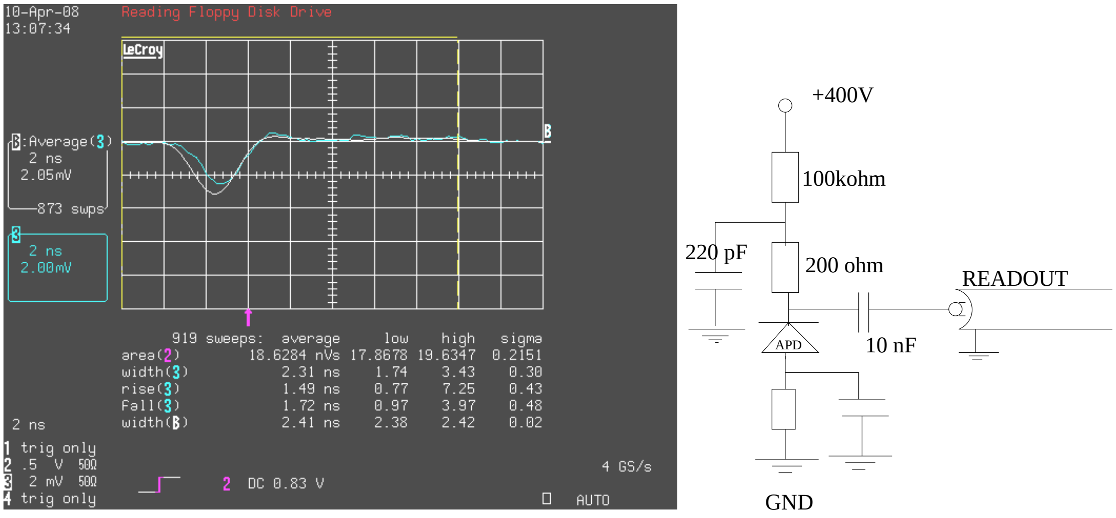

```
      919 sweeps:   average      low     high    sigma
area(2)        18.6284 nVs 17.8678 19.6347  0.2151
width(3)            2.31 ns     1.74     3.43     0.30
rise(3)             1.49 ns     0.77     7.25     0.43
Fall(3)             1.72 ns     0.97     3.97     0.48
width(B)            2.41 ns     2.38     2.42     0.02
```

Figure 9.7: Left: The pulse shape with the polarity inverted readout circuit. The rise time, the fall time and the FWHM are 1.3 ns, 1.6 ns, and 2.4 ns, respectively. Right: The readout circuit for the polarity inverted operation.

are 1.3 ns, 1.6 ns, and 2.4 ns, respectively. The degradation of these timing properties compared to the positive readout result from the additional 200 Ω resistance. Since the pulse polarity of the currently used PMTs is negative, a negative readout of HPDs could be of advantage. For example, the same amplifier used for the current PMTs could also be used for the HPDs if a negative readout circuit is used.

9.5 Charge Resolution

9.5.1 Photoelectron Resolution

As described in [168], the gain fluctuation is mainly determined by the first stage of multiplication, which is the bombardment gain in the case of this HPD and the multiplication at the first dynode in the case of PMTs. Since the first stage multiplication of the HPD is quite large (~ 1500) compared to the conventional PMTs (~ 10), the charge resolution of the HPD should be much better than that of the conventional PMTs. I measured the charge resolution in the following way: an HPD is set up in a dark box and an LED pulser ($\simeq 2$ ns in pulse FWHM and 603 nm in wavelength) illuminates the HPD via an optical fiber with an average intensity of ~ 3 ph.e.. The output signal is integrated for 6 ns and recorded by an oscilloscope (LeCroy: LC684 DXL) making use of its FADC function. The trigger for the oscilloscope is provided by the LED pulser. The left panel of Fig. 9.8 shows the output charge distribution. The bombardment gain and the avalanche gain was 1550 and 50, respectively. Clear peaks are visible up to 5 ph.e. The peak at 0 ph.e. corresponds to the pedestal.

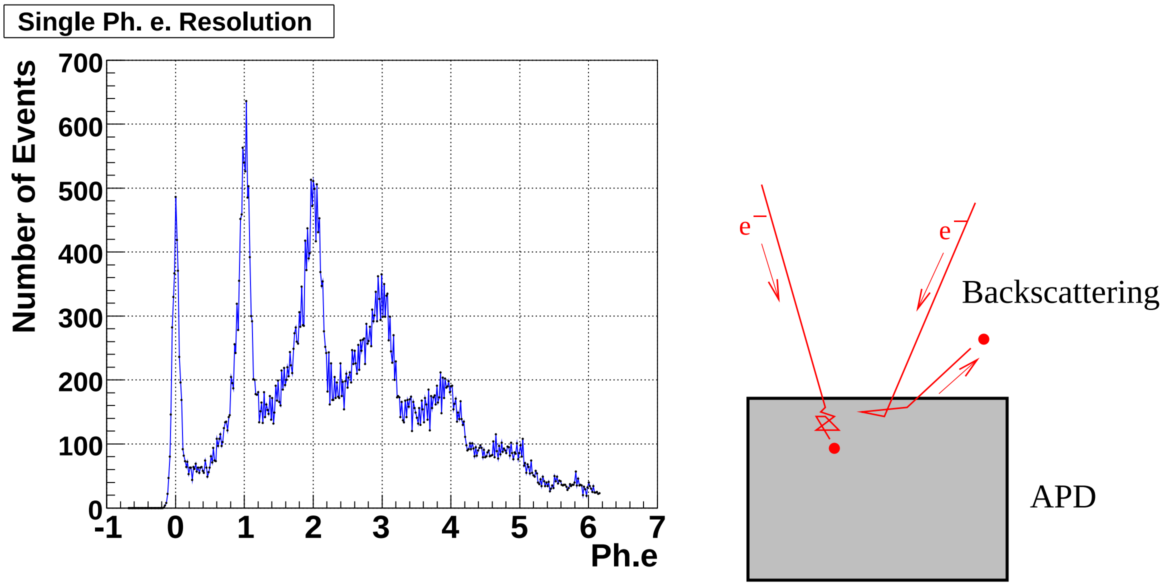

Figure 9.8: Left: Output charge histogram for light pulses inducing ~ 3 ph.e.s on average. Peaks for up to 5 ph.e. are clearly visible. The peak at 0 ph.e. corresponds to the pedestal. Right: Schematical explanation of the backscattering effect.

9.5.2 Backscattering of Electrons

All peaks except for the pedestal one in the left panel of Fig. 9.8 have a tail going to lower values. This can be explained by the backscattering effect. When an accelerated ph.e. is impinging onto the APD, it experiences multiple Coulomb scattering and at a certain probability, it can escape

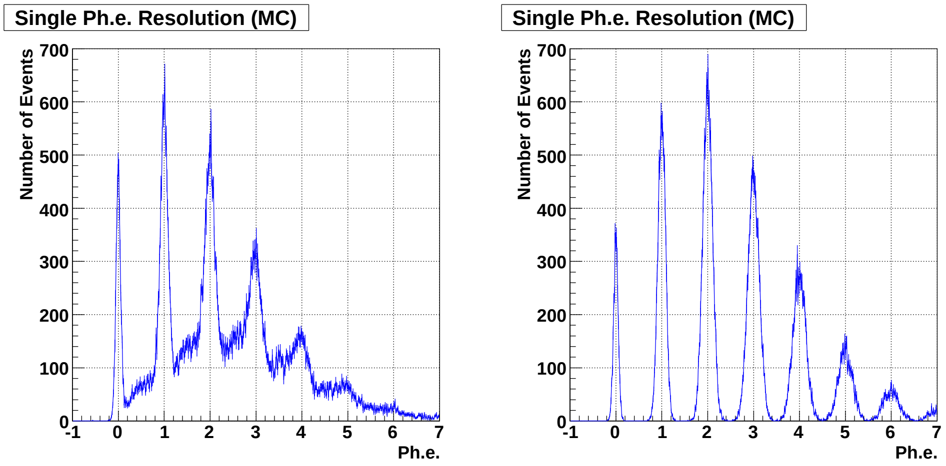

Figure 9.9: Output charge simulation for 2.7 ph.e. level light pulses with (left) and without (right) the backscattering effect taken into account.

from the APD (see the left panel of Fig. 9.8). This phenomenon is called backscattering. Once a backscattering occurs, only a part of the ph.e. energy is deposited in the APD.

In order to examine this backscattering effect, I performed a simple simulation assuming that:

- The number of ph.e.s emitted from the photocathode follows the Poisson statistic with a mean value of 2.7.
- The backscattering probability is 30%.
- The deposited energy distribution of backscattered electrons follows $0.23 \times (q - \frac{4}{5}q^2 - \frac{1}{75}q^3)$, where q is a fraction of the initial electron energy $0 < q < 1$. On average, a backscattered electron carries away 43% of the initial energy.
- The fluctuation in avalanche gain follows a Gaussian statistics with an RMS of 0.06 ph.e..
- The readout noise follows Gaussian statistics with an RMS of 0.05 ph.e..

The backscattering probability and the deposited energy distribution of the back-scattered electrons were chosen such that the simulation result reproduce the measurement. Indeed, the simulation well reproduce the measurement, as shown in the left panel of Fig. 9.9.

There are detailed studies about the backscattering effect. For example, according to [60], for the ph.e. energy of $10 - 25$ keV, backscattering in silicon happens at a probability of 20% and the scattered electron possesses 65% of the initial energy on average. The reason for the discrepancy between these values (20% and 65%) and the used values (30% and 43%) could be attribute to the electric field around APD produced by the positive potential conical electrode, which may attracts low energy electrons. In order to demonstrate the effect of the backscattering, the simulation results with the same settings except for the backscattering probability being 0 is shown in the right panel of the same figure.

9.6 Dynamic Range

The dynamic range of the HPD had been measured by M. Hayashida in Max-Planck-Institut für Physik (see [94]). As shown in Fig. 9.10, the output is proportional to the input from 1 ph.e. to at least ~ 5000 ph.e.. This dynamic range is more than enough for MAGIC.

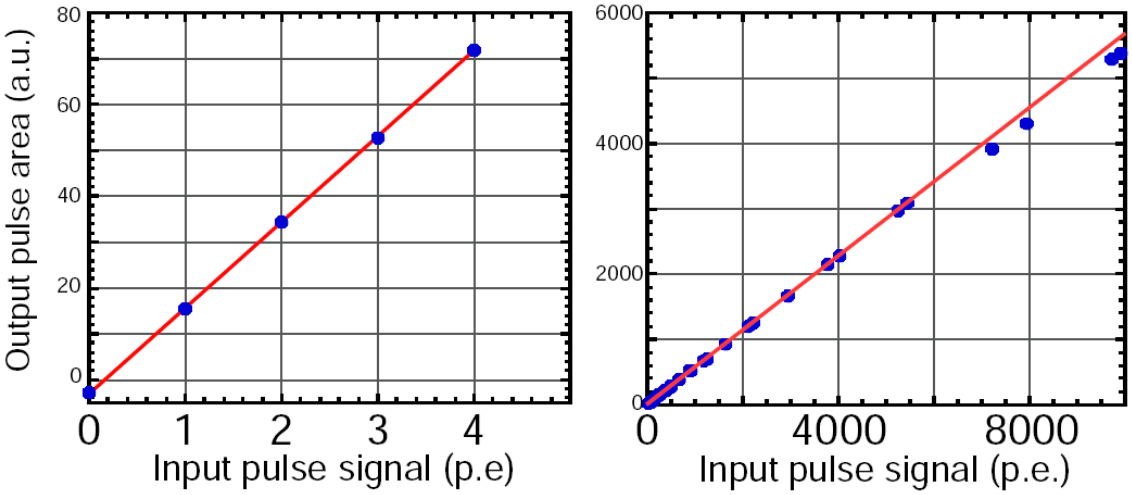

Figure 9.10: The measurement of the dynamic range. Figure adopted from [94].

9.7 Afterpulsing

During operations of PMTs or HPDs, shortly after a signal pulse, another delayed pulse could be seen. This effect is called afterpulsing. Afterpulsing is generally explained by molecules ionized by accelerated ph.e.s. Even if the vacuum inside a PMT or HPD is very high, still some molecules remain. They are mainly absorbed on the surface of the dynodes and the anode but some are present as residual gas. When a ph.e. hits a molecule and ionizes it, the electric field accelerates the positive ion toward the photocathode. When the ion hits the photocathode, many electrons are knocked out from the photocathode, usually resulting in a big and delayed output pulse (see Fig. 9.11). The amplitude of an afterpulse can be up to ~ 30 ph.e. As discussed in Sect. 3.4.7, this makes the signal clipping inevitable in the SUM trigger system, which reduces the collection area by 50%. at 30 GeV. In the case of HPD R9792U-40, in addition to the ion-feedback afterpulsing, two other types of afterpulsing effects have been found, which will be described in this section.

9.7.1 Afterpulsing Probability

I measured the afterpulsing probability of an HPD in the following way: An HPD is set up in a dark box and an LED pulser ($\simeq 2$ ns in pulse FWHM and 603 nm in wavelength) illuminates

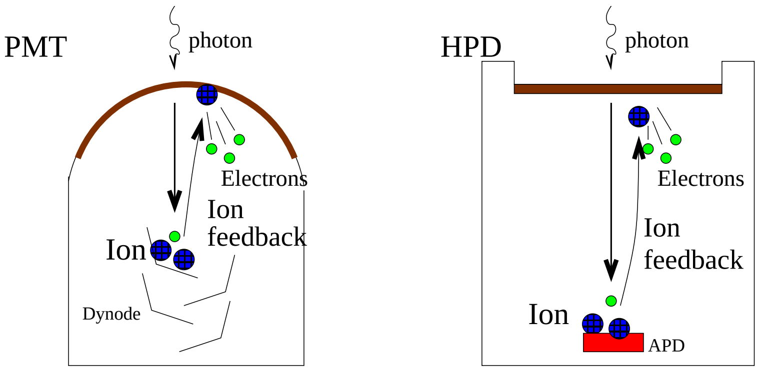

Figure 9.11: Explanation of the ion-feedback for the afterpulsing effect. Both the PMT case (left) and the HPD (right) case are shown.

the HPD via an optical fiber as shown in Fig. 9.12. The output signal is recorded by a 2 G Sample/s FADC (Acqiris cc103) for 500 ns. The trigger for the FADC is provided by the LED pulser. The afterpulses are searched for from 33 ns to 450 ns after the main pulse. Two different LED light pulse intensities are used, namely ~ 3 ph.e. and ~ 90 ph.e. levels. Because every single impinging ph.e. can produce an afterpulse, the afterpulsing probability P_{AP} is computed by using the following formula,

$$P_{AP} = \frac{N_{AP}}{N_{MP} \times M_{MP}} \tag{9.2}$$

where N_{AP}, N_{MP}, and M_{MP} are the number of afterpulses, the number of main pulses, (signals caused by the LED light pulse), and the mean number of ph.e.s in the main pulses. The measured afterpulsing probability as a function of the threshold level is shown in Fig. 9.13. As a reference, the afterpulsing probability of the currently used PMT is also shown.

The two measurements with different light intensities (~ 3 ph.e. and ~ 90 ph.e. level) agree well. When the threshold level is larger than 1 ph.e., the afterpulsing probability of the HPD is $\sim 3 \times 10^{-6}$, which is ~ 500 times lower than that of the currently used PMTs. Therefore, the clipping in the SUM trigger system may not be necessary for HPDs, leading to 50% larger collection area, even without taking into account the improvement in photodetection efficiency. However, a detailed MC study has not yet been done. If the threshold is set at 0.5 ph.e. level, the afterpulsing probability of the HPD suddenly increases by a factor of ~ 200. This cannot be attributed to the misidentification of the pedestal because the charge of the pedestal and a single ph.e. are clearly separated, as shown in Fig. 9.8. The dark count rate of the HPD on the single ph.e. level is known to be less than 100 kHz and it cannot explain the high probability either. Although such a low charge afterpulsing should not cause any problem in the telescope system (0.1% increase in NSB rate), since HPDs have never been used in any IACTs, the detector properties should be understood in detail.

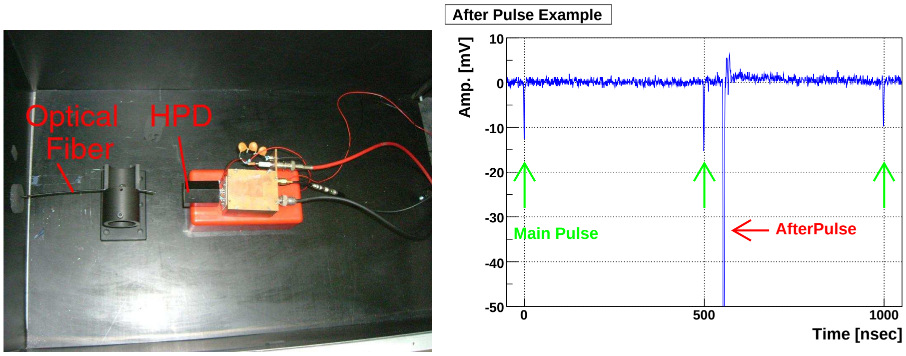

Figure 9.12: Left: A photograph of the afterpulsing measurement setup inside the dark box. An optical fiber that guides the LED light pulse can be seen on the left side. Right: An example of the recorded pulse traces in the FADC. Three main pulses can be seen (∼ 3 ph.e. level), where the second main pulse is followed by a large afterpulse (> 10 ph.e. level)).

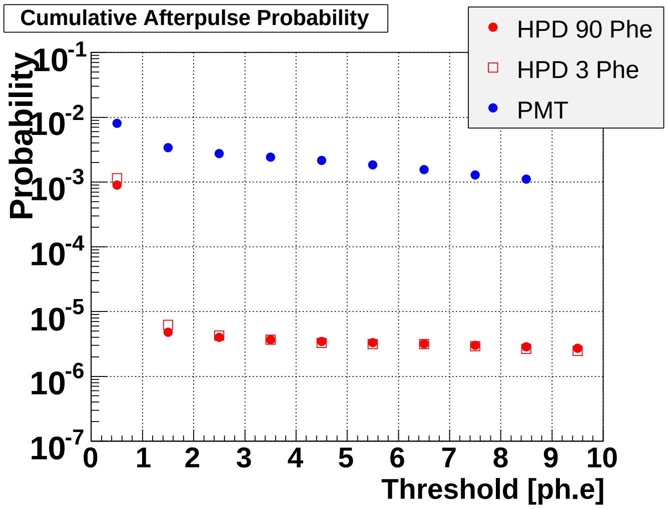

Figure 9.13: The probability of the afterpulsing as a function of the threshold level. Red open squares and red filled circles denote the results for the HPD measured with 3 ph.e. and 90 ph.e. level light pulses, respectively. The blue circles denote the results for the currently used PMTs, provided by C.C. Hsu.

9.7.2 Timing Properties of Afterpulses

In order to identify the cause of the high-probability single ph.e. afterpulses and also in order to understand other afterpulses better, I studied the timing property of the afterpulsing. The timing property of the afterpulsing above 0.5 ph.e. (strongly dominated by the single ph.e. afterpulses) and that above 1.5 ph.e. are studied separately because it is very likely that they have different origins.

Arrival Time Distribution of > 1.5 ph.e. Afterpulses

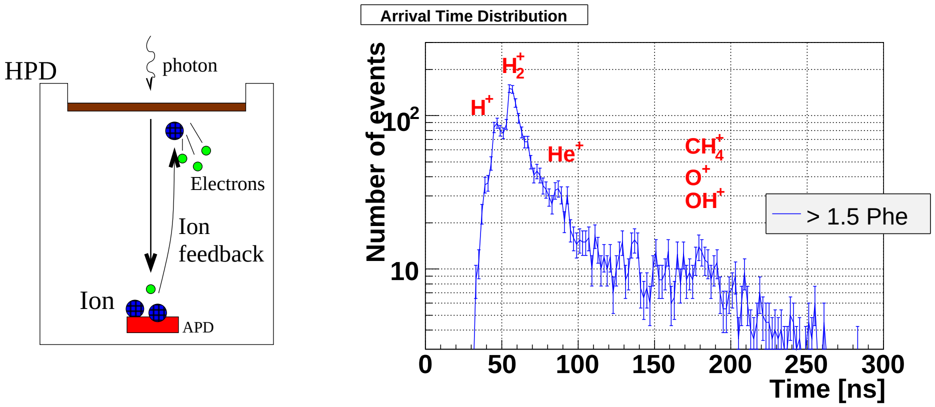

Figure 9.14: Left: Schematical view of the ion-feedback, which create peaks in the distribution of the time difference between the main pulse and the afterpulse. Right: The distribution of the time difference between the main pulse and the afterpulse with the amplitude larger than 1.5 ph.e. Several peaks can be seen. They can be explained by the travel time of the ions of different masses from the APD to the photocathode.

The arrival time distribution of afterpulses with an amplitude larger than 1.5 ph.e. is shown in the right panel of Fig. 9.14. Several peaks can be seen at ~ 45, ~ 60, ~ 90, ~ 135, and ~ 180 ns, some of them are not pronounced, though. They can be well explained as molecules absorbed on the surface of the APD which are ionized at a certain probability by impinging 8 keV ph.e.s and accelerated toward the photocathode. The delay time from the main pulse to the afterpulse can be roughly estimated since the dimensions of the HPD and the applied voltage are known. Basically, the set-up resembles a simple time-of-flight mass spectrometer. Assuming that the electric field is uniform with 8 kV of potential difference and that the distance of 2.8 cm between the photocathode and the APD, the delay time can be estimated as $\sim 45\sqrt{M/M_p/Z}$ ns, where M, M_p, and Z are the mass of the ion, the mass of proton, and the charge of the ion (in unit of electron charge), respectively. Peaks seen at ~ 45, ~ 60, and ~ 90 in the right panel of Fig. 9.14 may reflect feedbacks of ions with $(M/M_p)/Z$ = 1, 2 and 4, where protons, hydrogen molecular ions and helium ions are the likely candidates. The responsible ions for the peak at ~ 135 ns, if it is genuine, is not clear but $(M/M_p)/Z$ should be ~ 9. Unresolved complex between 150 and 200 ns are likely to originate from methane, nitrogen, oxygen and hydroxide ions, for example. There is also some contribution from gas ionization adding to the continuum under the peaks.

The very low ion-feedback rate compared to the PMTs is partially attributed to the higher vacuum. But the conical electrode would also play an important role. From the arrival time distribution, it is clear that most of the ion-feedback are from the surface of the APD. The conical electrode (see the top right panel of Fig. 9.1) around the APD has positive electric potential. Therefore, the only ions which initially possess a large momentum toward the photocathode can reach the photocathode and the rest would land somewhere around the APD. Therefore, the conical electrode, whose primary purpose is focusing the ph.e.s, serves as an ion-feedback suppression electrode [4]

Arrival Time Distribution of Single ph.e. Afterpulses

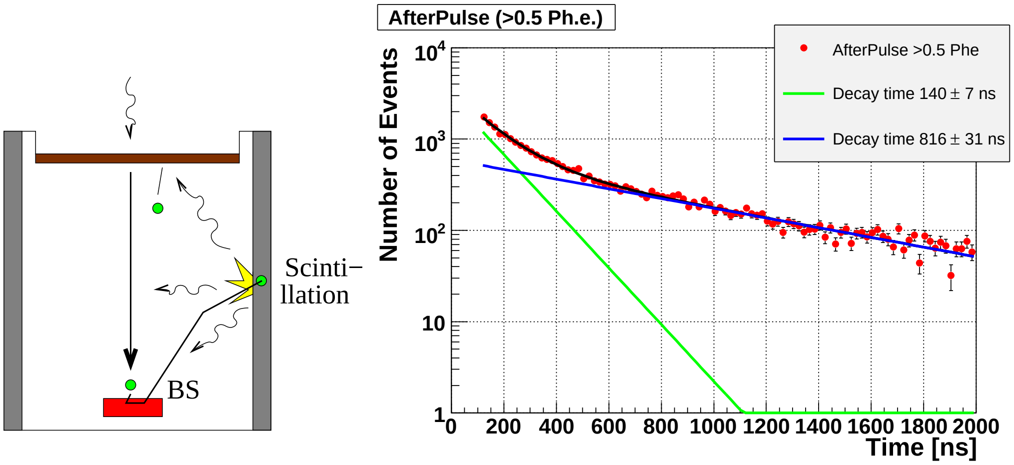

Figure 9.15: Left: Schematical view of the scintillation photon-feedback, which creates an exponential decay in the distribution of the time difference between the main pulse and the afterpulse with an amplitude of single ph.e.. Right: The distribution of the time difference between the main pulse and the afterpulse with the amplitude larger than 0.5 ph.e. As can be seen from Fig. 9.13, it is strongly dominated by single ph.e. afterpulses. It shows two components of exponential decays. They could be explained by the scintillation light caused by the backscattered ph.e. inside the HPD.

For investigating the arrival time distribution of the single ph.e. afterpulses, the recording time window of the FADC has been increased from 500 ns to 2 μs. The result is shown in the right panel of Fig. 9.15. The distribution can be fitted by the sum of two exponential functions

$$R(t) = A_1 \exp(t/\tau_1) + A_2 \exp(t/\tau_2) \tag{9.3}$$

obtaining $A_1 = 283 \pm 13$, $A_2 = 59.5 \pm 34$, $\tau_1 = 140 \pm 7$ ns, and $\tau_2 = 816 \pm 31$ ns. Given the fact that always single ph.e. afterpulses are created and that exponential decays in arrival time are seen, one of the reasonable explanations would be scintillation light created inside the HPD. The ph.e.s may undergo backscattering in the APD as described in Sect. 9.5.2. Such a ph.e. may subsequently hit the ceramic wall of the HPD tube at a certain probability. The energy of

---

[4] The original idea of suppressing the ion-feedback by an electrode was presented by D. Ferenc [74]

scattered electrons is high enough (some keV) to produce scintillation light. In order to explain the two time constants τ_1 and τ_2, there may be two different components responsible for the single ph.e. afterpulses.

9.7.3 Fast-and-huge afterpulses

As mentioned before, the afterpulsing probability was calculated from the time range between 33 ns and 450 ns after the main pulse. As one can see from Fig. 9.14, it seems that most of the afterpulses (> 1.5 ph.e.) are well included in this range. However, during some measurements, unusual afterpulsing events were found in the oscilloscope display. They appeared ~ 3 ns after the main pulse and their amplitude was huge. They appear so early that they are not counted in the afterpulsing probability calculation.

I studied this "fast-and-huge" afterpulsing, using the oscilloscope. By flashing the HPD with the 3×20000 light pulses with intensities of 3 ph.e, 10 ph.e and 20 ph.e. levels, the number of fast-and-huge afterpulses were counted. The results are shown in the left panel of Fig. 9.16. As the light intensity increases, the number of fast-and-huge afterpulses linearly increases, which means its rate is proportional to the original ph.e. rate. By fitting a linear function, the probability for a single ph.e. to produce a fast-and-huge afterpulsing is estimated to be $(7 \pm 1) \times 10^{-5}$, which is one order of magnitude higher than ion-feedback afterpulsing.

There is another interesting feature. In most of the cases, the amplitude of the fast-and-huge afterpulses is similar and at ~ 200 ph.e. level. The right panel of the Fig. 9.16 is the photograph of the oscilloscope display showing 776 of fast-and-huge afterpulsing. It was taken in the following way: the HPD was put in a dark box and the trigger of the oscilloscope was set at 100 ph.e. level. The thermal ph.e. emission from the photocathode (dark count) can make very small signals, but not on the level of 100 ph.e.. However, the 776 events were triggered within 20 minutes due to the fast-and-huge afterpulsing. (~ 10 kHz of a dark count rate) $\times$ (~ 1200 second of operation) $\times$ ($\sim 7 \times 10^{-5}$ of the fast-and-huge afterpulsing probability) would explain the 776 events. Most of the pulses have an amplitude of ~ 200 ph.e.

This fast-and-huge afterpulsing might be explained in the following way. Silicon can emit characteristic X-rays at 1.74 keV (L shell to K shell) or 1.84 keV (M shell to K shell). The bombardment of the 8 keV electron may trigger these emissions. If this X-ray hits the photocathode, all the energy of the X-ray will be transfered to a single electron in the GaAsP via a photoelectric effect. Then, this energetic electron will cause (photo)electron emission from the photocathode. In the case of Gallium, the attenuation coefficient of the 1.8 keV X-ray (determined by photoelectric effect) is $\sim 2 \times 10^4$ cm^{-1} (see [219]), which corresponds to 0.5 μm in mean free path. Since the thickness of the photocathode is 1μm, it is very likely that the photoelectric effect happens inside the photocathode. Then, the scattered electron causes an emission of more ph.e.s. 1.8 keV electron lose 36 MeV in every 1 g/cm^2 of Gallium (see [217]), which corresponds to ~ 2 keV per 0.1 μm. Nearly all the energy of the electron should be lost within the photocathode. Therefore, it is reasonable that this fast-and-huge afterpulsing has an almost constant amplitude, although the ph.e. production efficiency 1.8 keV / 200 ph.e. = 9 eV/ ph.e. should still find an explaination. The reason why this afterpulsing is much faster than the ion-feedback one is that, unlike the ions, the X-ray can reach the photocathode within 0.1 ns The ~ 3 ns delay could be explained by the travel time of the ph.e.s. from the photocathode to the APD.

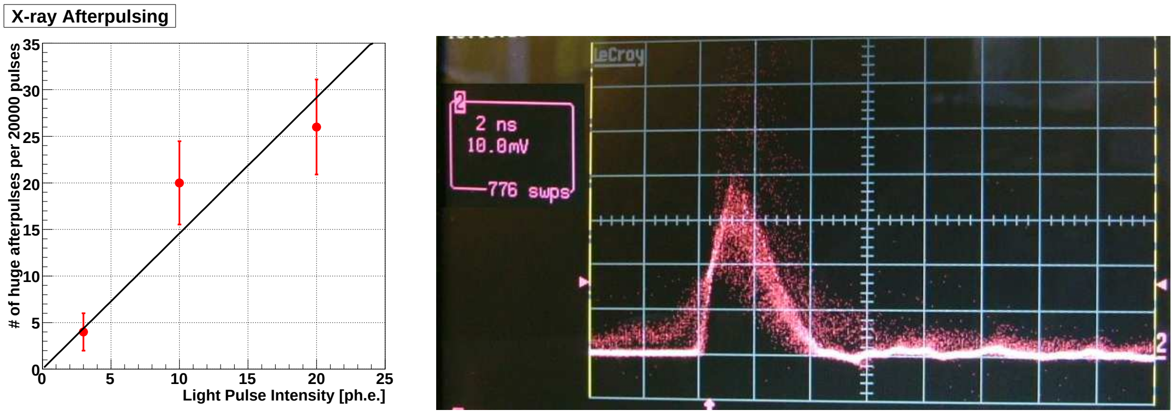

Figure 9.16: Left: The number of fast-and-huge afterpulses per 20000 main pulses as a function of the light pulse intensity. Right: A photograph of the display of the oscilloscope showing 776 *fast-and-huge afterpulses. The oscilloscope was operated at a self-trigger mode with the threshold level of 100 ph.e.. Most of the pulses have an amplitude of* ~ 200 *ph.e..*

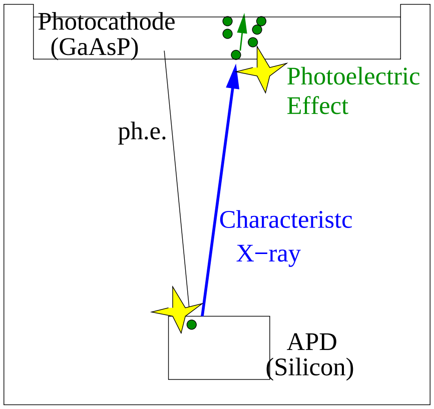

Figure 9.17: A possible interpretation of the fast-and-huge afterpulses. The ph.e. bombardment causes a characteristic X-ray emission from silicon (~ 1.8 *keV). The X-ray hit the photocathode and all the energy is transferred to an electron via a photoelectric effect. Nearly all the energy of the electron should be deposited within the* 1μ*m thick photocathode, producing a roughly constant number (*~ 200*) of ph.e.s.*

9.8 Lifetime

A GaAsP photocathode is known to have a very high quantum efficiency, as shown in Sect. 9.2.1. At the same time, it is also known to have a very short lifetime. The reason for the short lifetime is as follows: In order to reduce the work function of a photocathode, in general, cesium is evaporated to the photocathode. However, this cesium (CsO) layer attached to a GaAsP photocathode is more fragile than that attached to, for example, a bialkali photocathode. Therefore, the ion feedback breaks the cesium layer on a GaAsP photocathode more easily, leading to a relatively short life time. On the other hand, as mentioned in Sect. 9.7.2, this HPD has an extremely low ion feedback rate. Therefore, one can expect a sufficiently long lifetime. Hamamatsu Photonics measured the lifetime of four HPDs and I measured that of three HPDs in the following way: The three HPDs, a white LED, and a PIN diode are set up in a dark box (see Fig. 9.18). The LED illuminates the HPDs with an intensity corresponding to ~ 40 times brighter than the NSB intensity in LaPalma. The current from the PIN photodiode was continuously monitored to ensure the stability of the LED intensity. The relative output currents form the three HPDs were monitored for ~ 20 days to see the degradation of the photocathode QE.

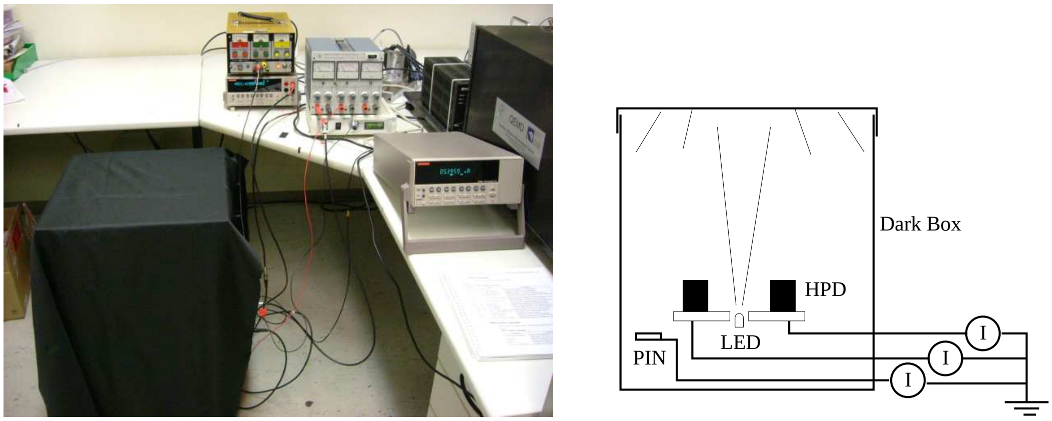

Figure 9.18: Left: A photograph of the experimental setting for the aging measurement. Right: Schematical view of the setup inside the dark box. HPDs, a PIN photodiode and a white LED are pointing upward. The inner side of the lid of the box is painted white and the light from the LED are scattered, uniformly illuminating the HPDs. Output current of the HPDs and the LED are measured outside the box.

The results are shown in the left panel of Fig. 9.19. The horizontal axis is the operation time normalized to the true NSB rate and the vertical axis is the relative output current with respect to the initial current. In one year (one cycle), the MAGIC telescope is operational for approximately 1000 hours in dark time. The figure shows the HPD can hold more than 80% of the initial QE for 10 years, which should be long enough. The right panel of Fig. 9.19 shows the QE degradation map over the photocathode after aging tests measured in Hamamatsu Photonics. The ratio between the initial value and the value after 68% degradation in average QE is shown. The closer to the center, the larger the degradation. This is a clear evidence that QE degradation is caused by ion-feedback. As discussed in Sect. 9.7.2, due to the the conical electrode (see top right panel of Fig. 9.1), the ions which could reach the photocathode must have passed the center of the conical electrode. Such ions should hit the photocathode around the center.

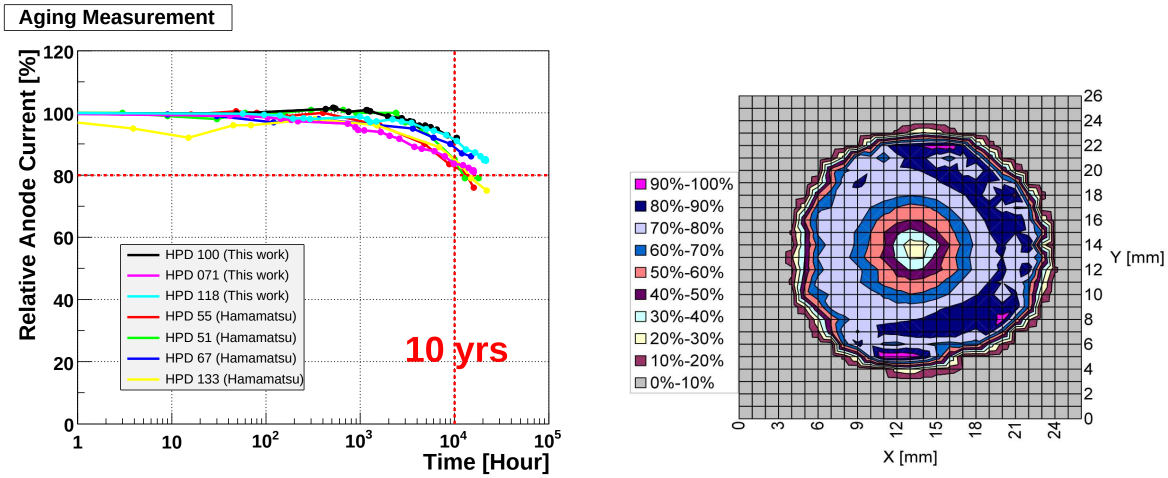

Figure 9.19: Left: Relative output currents with respect to the initial value as a function of the operation time. The operation time is scaled to the nominal NSB intensity. Assuming there is 1000 hours of observation in one year, the QE holds 80% of the initial value for more than 10 years. Right: The degradation of the QE over the photocathode measured by Hamamatsu Photonics. The ratio to the initial value is indicated as colors. The closer to the center, the larger the degradation. Figure provided by Hamamatsu Photonics.

9.9 Temperature Compensation

The avalanche gain has a strong temperature dependence. I measured the dependence of the avalanche gain in the following way. The HPD is set up in a temperature regulation box (Heraus Vötsch: VMT 04/30, see the left panel of Fig. 9.20). The LED pulser (603nm) illuminates the HPD via an optical fiber with a dim light (~ 2 ph.e. level) and an output charge histogram (similar to the left panel of Fig. 9.8) is produced. The peak charge of the single ph.e. is used to estimate the change in avalanche gain. The bias voltage of the APD is set such that the gain at 25°C is 30. In order to make sure that the temperature in the chamber is well stabilized and there is no hysteresis, the measurement is done twice, i.e. at first the temperature is raised from ~ 20°C to ~ 40°C and then lowered back to ~ 20°C. The result is shown in the right panel of Fig. 9.21 as a blue line. The temperature coefficient of the gain change amounts to ~ -2%/°C. During the operation of the MAGIC, the temperature of the camera might change easily by ~ 5°C and hence, this strong temperature dependence of the gain is not acceptable for being used in the MAGIC camera. I developed a temperature compensation circuit based on three resistors, a DC/DC converter (Systems Development & Solutions, APD 5P501201) and a thermistor (Ishizuka Electronic Corporation, 103AT-2) [5], as shown in the right panel of Fig. 9.20. The DC/DC converter requires the operation voltage of 5 V and a control voltage from 0 V to 2.5V. The output is 200 times larger than the control voltage. Additionally it provides a reference voltage of 2.5 V, which is a part of the compensation circuit and shown in the right upper corner of the right panel of Fig. 9.20. The resistance of the thermistor is expressed as

$$10 \exp(3435 \left(\frac{1}{273.15 + T} - \frac{1}{273.15 + 25} \right)) \quad \mathrm{k}\Omega \tag{9.4}$$

which is shown also in the left panel of Fig. 9.21. As the temperature increases, the resistance of the thermistor decreases, which leads to the higher bias voltage. Thus, the reduction of the avalanche gain is compensated by the higher bias voltage. With this compensation circuit, the temperature dependence of the avalanche gain is measured in the same way as without the circuit. The results are shown in the right panel of Fig. 9.21 as a red line. The temperature dependence of the avalanche gain was reduced to the level of ~ 0.3%/°C from 25° to 35°, which is the same level as that of the PMT gain [6] . The numerical calculation of the avalanche gain is shown as a green line in the same figure, which agrees well with the measurement. It should be noted that I tuned the system for a mean temperature of 30°, which shall be the nominal temperature inside the MAGIC camera, but that it is easy to shift the optimal temperature range by changing the resistors of the circuit.

---

[5] The idea of using a thermistor was given by M. Hayashida.

[6] Typically, the temperature dependence of the PMT gain is ~ 0.2%/°C

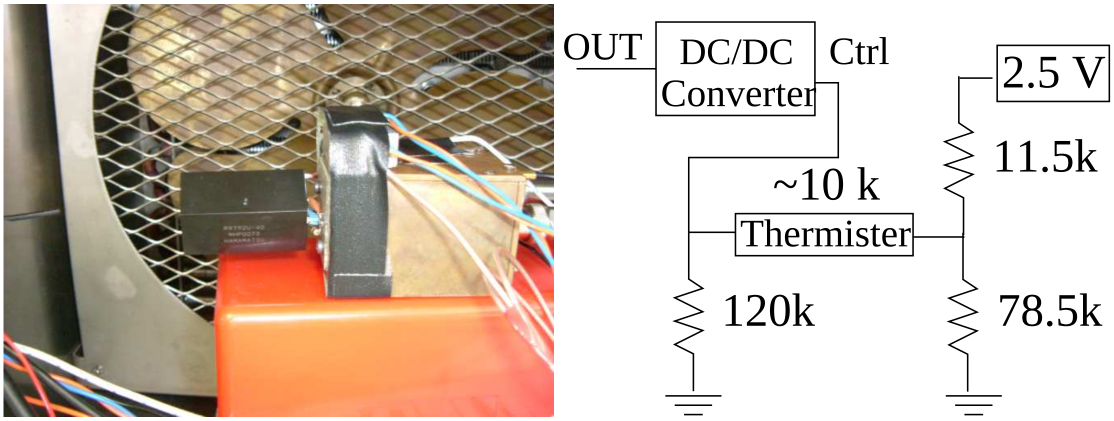

Figure 9.20: Left: A photograph of the experimental setup for the temperature compensation of the APD gain. Inside the copper box, readout circuit and an amplifier are set up. On top of the copper box, the compensation circuit is seen. Right: A schematic of the temperature compensation circuit. As the temperature increases, the resistance of the thermistor decreases, leading to the higher bias voltage. In this way, the reduction of the avalanche gain by increase of temperature is compensated.

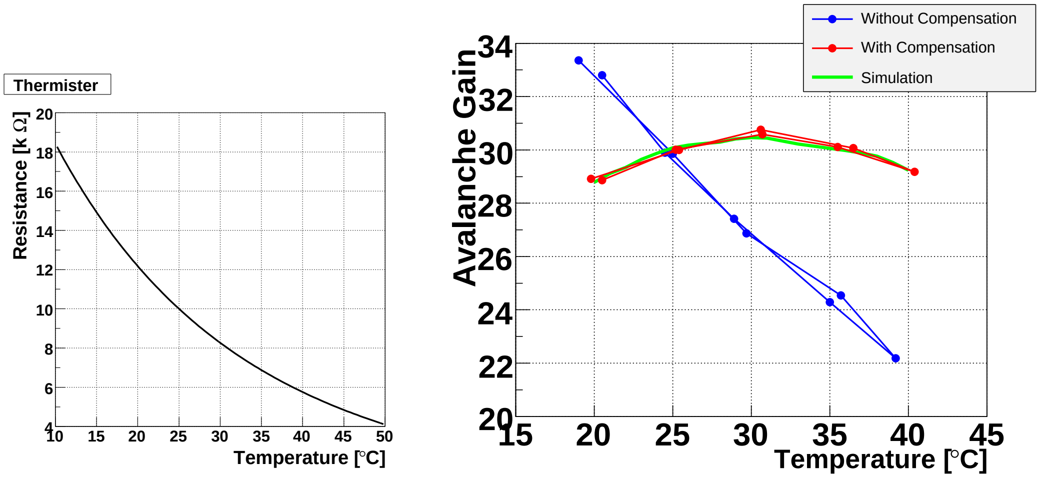

Figure 9.21: Left: The resistance of the thermistor (Ishizuka Electronic Corporation, 103AT-2) as a function of temperature. It is 10 kΩ at 25°C and has anti-correlation with temperature expressed as Eq. 9.4. Right: The avalanche gain as a function of temperature. The blue and the red line show the gain without and with the compensation circuit, respectively. The temperature dependence is suppressed from $-2\%/^\circ C$ *to* $0.3\%/^\circ C$ *between 25 degree and 35 degree. The green line is the numerical calculation for the temperature compensation. It agrees very well with the measurement.*

9.10 Safety Circuit

9.10.1 Limitation of the Photocathode Current

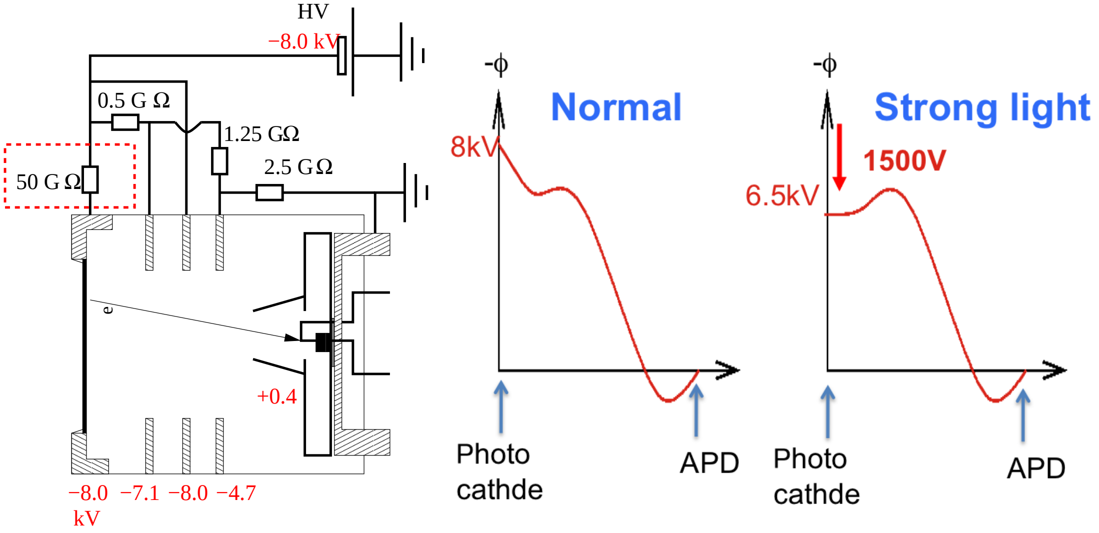

Figure 9.22: Left: The schematics of the voltage distribution across the electrodes inside the HPD. The $50\ \mathrm{G}\Omega$ resister for the photocathde protection is indicated by the red dotted box. Middle: The (inverted) electrical potential distribution at the center of the HPD tube as a function of the distance from the photocathode, under nominal light condition. There is a hump produced by the second ring. Right: The same as the middle panel but under the strong light condition. If photocathode currently is large, due to the $50\ \mathrm{G}\Omega$ resistance indicated in the left panel, the photocathode potential drops signicantly. If the drop amounts to 19% of the initial value, no ph.e. can overcome the hump and hence, photocathode current is saturated at the value that causes 19% of the potential drop.

During operation, an unwanted strong light such as car flash and star light might shine onto the photodetectors of the MAGIC camera, which shorten the lifetime of the photocathodes significantly. In order to avoid this problem, a $50\ \mathrm{G}\Omega$ resister is inserted in the connection of the HV supply and the photocathode after the voltage divider chain across the HPD, as shown in the left panel of Fig. 9.22. It works as follows: The electric potential at the center of the tube as a function of the distance from the photocathde is schematically shown in the middle panel of Fig. 9.22. Due to the potential of the rings, there is a hump at the second ring. If a large photocathode current is generated by intense illumination, the $50\ \mathrm{G}\Omega$ resister cause a potential drop at the photocathode. When the potential of the photocathode drops by more than 19%, none of the ph.e. can overcome the hump. Therefore, the photocathde current is satulated at the value that causes 19% of the potential drop.

In the case when -8 kV is applied to the photocathode, the 19% corresponds to 1.5 kV, for which 30 nA is needed. In the dark night, the NSB ph.e. rate would be 500 MHz, which corresponds to 0.08 nA. However strong the intensity of an illuminating light is, the photocathode current is less than 400 times the one caused by NSB. In this way, the fast degradation of the QE by a very strong light can be prevented.

9.10.2 Limitation of the APD Current

The 50 GΩ protection resister is meant for the strong constant light. For a fast and very strong pulsed light (less than 100 ms in duration), it does not work. The reason is as follows: The capacitance of the photocathode with respect to the ground material is estimated to be 1 pF. When -8 kV is applied, a charge of 8 nC is stored on the photocathode. If a strong and fast pulsed light illuminates the photocathode, these charges will be emitted from the photocathode and accelerated toward the APD. Until 1.5 nC leave the photocathode (potential drops by 1.5 V), the current flows.

When the bombardment gain is 1500 and the avalance gain is 40, in total $\sim 10\ \mu$C of charge goes through the APD. If the light pulse is as short as 0.1 microsecond, the current amounts to 100 A, which may cause a damage on the APD. To protect the APD from such an event, the feeding capacitance shown in the left side of Fig. 9.23 has relatively small capacitance (220 pF). For short time scales, the current flowing throuth the APD is provided by this capacitance but only 88 nC (220 pF × 400 V = 88 nC) is available. Thus, the current is limited by this capacitance.

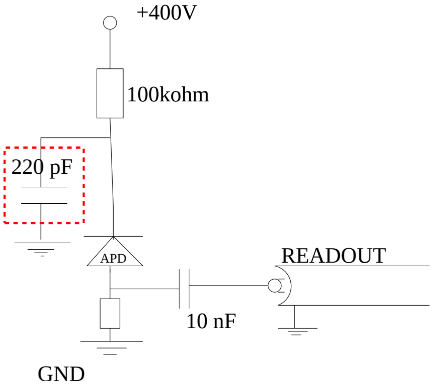

Figure 9.23: The small feeding capacitor for limiting the APD current. With 220 pF of the capacitance, only 220 pF $\times \sim 400$V = ~ 88 nC is charged to the capacitor. This can limit the APD current however strong a light pulse illuminate the photocathode.

9.11 Installation to MAGIC

After studying the basic properties of the HPD described in the previous sections, I requested the engineers in the Max-Planck-Institut für Physik (O. Reimann, D. Fink, et al) to produce some HPD clusters which consist of 7 HPDs and can be exchanged for the PMT clusters currently used in the MAGIC camera.

The cluster design is shown in the bottom left panel of Fig. 9.24. Right behind the HPDs, there is a print circuit board (PCB) with amplifiers, temperature sensors, the APD bias voltage supplies, and test pulse injection circuits. The copper ring of the HPD has thermal contact with an aluminum plate whose temperature is regulated by the cooling system. The plate serves as a shield for the amplifier, too. Behind the aluminum plate, there are 7 PCBs which carry an amplifier bias voltage supply, a VCSEL and a DC/DC converter for the APD bias voltage. The DC/DC converter for the photocathode HV is placed inside an aluminum box at the bottom of the cluster.

Currently, a prototype with 6 HPDs (the central pixel is missing) is installed to the edge of the MAGIC-II camera (see the top left panel of Fig. 9.24. The detailed check of the performance will be carried out in the following months.

Figure 9.24: Top left: The completion drawing of the HPD cluster. Figure provided by D. Fink. Top right: Current status of the installation of a prototype cluster at the edge of the MAGIC-II camera. The central pixel is still missing. Three HPDs are not equipped with a Winston Cone in order to study the possible spark effect between the PMT and the HPD photocathode. Figure provided by D. Fink. Bottom: Essential components of the HPD cluster. Figure provided by D. Fink.

The next goal of the HPD camera development would be the installation of 61 clusters (427 pixels) in the central region of the MAGIC-II camera (see Fig. 9.25). Considering the price (~ 10 times more expensive than PMTs), filling up whole camera with the HPDs may only be realized after the gain in sensitivity from the central region has been proven.

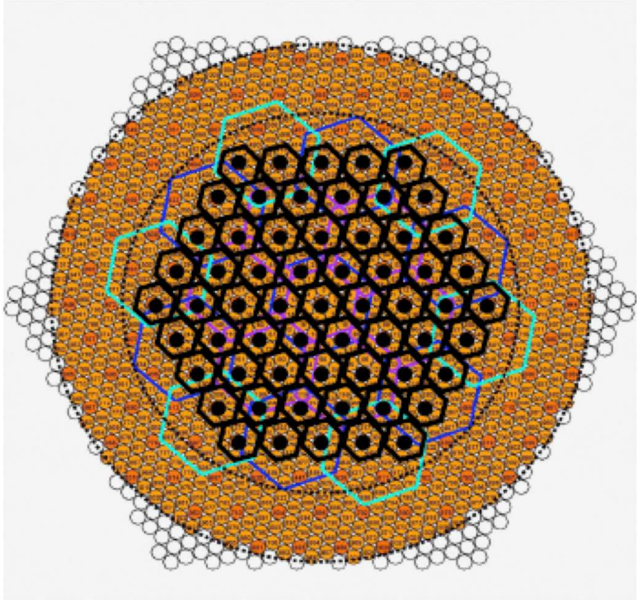

Figure 9.25: The future plan of the HPD installation in place of PMTs in the MAGIC II camera. Brown colored area are currently occupied with the PMTs. The black hexagons indicate the planned area for the 61 HPD clusters. Figure provided by M. Teshima.

9.12 Concluding Remarks

I participated in the development of a new photosensor HPD R9792U-40 together with Hamamatsu Photonics and colleagues in Max-Planck-Institut für Physik, aiming for better observations of pulsars and other sources below 100 GeV with MAGIC. Its high quantum efficiency of about 50% between 450 and 550 nm and its high photoelectron collection efficiency provides more than twice as many photon detections as the currently used PMTs. The width of the output pulse in the case of a delta light flash is ~ 2 ns in FWHM, which is favorable for the IACT technique. The polarity of the pulse can be both positive and negative depending on the readout circuit. It also has an excellent charge resolution, which enables to resolve up to 5 ph.e.s, even though the backscattering effect worsens the resolution. The rate of ion-feedback of the HPD which causes afterpulsing is 500 times less than that of the currently used PMTs, although it has two other different types of afterpulsing, which are possibly explained by scintillation light and the characteristic X-ray inside the HPD. The lifetime of the HPD is long enough to be used in MAGIC for 10 years. The temperature dependence of the avalanche gain can be successfully suppressed by a simple compensation circuit. The protection of the HPD against the strong light is done by a 50 GΩ resistance connected to the photocathode and a small feeding capacitance at the APD cathode. The mechanical and electronic design for the first prototype of the 7-HPD cluster have been done by the engineers in Max-Planck-Institut für Physik and one cluster has already been installed in the MAGIC-II camera. The performance study is going to be done in the near future.

Chapter 10

Conclusions and Outlook

10.1 Conclusions

Before 2007, the energy spectrum of the Crab pulsar had been measured only up to ~ 5 GeV by the satellite-borne detector, EGRET, while IACTs had set flux upper limits only above 100 GeV. There existed no sufficient measurement at around the cut-off energy, i.e, at energies between a few GeV and a few tens of GeV, while the spectral shape at around the cut-off energy is essential to constraining the emission region of the pulsation,

The MAGIC telescope with the newly implemented SUM trigger successfully detected emission from the Crab pulsar above 25 GeV during the observations between October 2007 and February 2008 thanks to the collective efforts of my colleagues, T. Schweizer, M. Lopez, A. N. Otte, M. Rissi and M. Shayduk. However, an in-depth analysis and detailed discussion in comparison with the adjacent energy range had not yet been performed. Also, a new satellite-borne detector, *Fermi*-LAT, became operational in August 2008 and the observational data were made public in August 2009.

In this thesis, the Crab pulsar has been studied in detail in the previously (almost) unstudied energy gap between 5 GeV and 100 GeV. For the analysis, I used the data from both the upgraded MAGIC telescope and the public *Fermi*-LAT data. The main results are summarized as follows:

- MAGIC observations between October 2007 and January 2009 resulted in the detection of the Crab pulsar above 25 GeV with a statistical significance of 4.3 σ, 7.4 σ and 7.5 σ for the first peak (P1), the second peak (P2), and the sum of the two peaks (P1 + P2), respectively.

- **The energy spectrum of the Crab pulsar is consistent with a power law with an index of $\sim -3.5 \pm 0.5$ between 25 GeV and 100 GeV for P1, P2 and P1 + P2. At 30 GeV, the flux of P2 is twice as high as that of P1.**

- A variation of the flux and the light curve of the Crab pulsar on a yearly time scale were not found in the MAGIC data.

- One year of *Fermi*-LAT data showed a clear detection ($> 100\ \sigma$) of the Crab pulsar from 100 MeV to ~ 30 GeV. Between 100 MeV and ~ 30 GeV, the energy spectrum is consistent with a power law with an exponential cut-off, for total pulse (TP), P1, P2 and P1 + P2. The cut-off energies are estimated to be 6.1 ± 0.5 GeV, 3.7 ± 0.3 GeV, 5.9 ± 0.7 GeV and 4.5 ± 0.3 GeV for TP, P1, P2 and P1 + P2, respectively. Due to the small detector area of ~ 1 m^2, the statistical uncertainty of the spectrum above ~ 10 GeV is rather large and it is not possible to detect any pulsed signal above 30 GeV.

- **From the *Fermi*-LAT observations, the superexponential cut-off assumption ($\Gamma_2 = 2.0$ in Eq. 6.5) is ruled out by 4.8 σ, 5.0σ, 4.3σ and 7.7σ for TP, P1, P2 and P1 + P2, respectively.**

- **The combination of the results from MAGIC and *Fermi*-LAT revealed that the exponential cut-off spectra determined by *Fermi*-LAT are inconsistent with MAGIC results above 25 GeV by $> 2.1\sigma$, $> 4.3\sigma$ and $> 5.3\sigma$ for P1, P2 and P1 + P2, respectively, even if the possible absolute energy scale difference between the two experiments is carefully taken into account (up to 30%)**.

- The flux ratio of P2 to P1 and that of Bridge to P1 increase rapidly with energy between 100 MeV and 100 GeV. This behavior is similar to that in the energy range below 1 MeV but contrary to that in the energy range between 1 MeV to 100 MeV.

- **Both edges of the two peaks show a clear exponential behavior. In addition, the outer edges, i.e., the rising edge of P1 and the falling edge of P2 become sharper as the energy increases, while the inner edges, i.e. the falling edge of P1 and the rising edge of P2 have no energy dependence.** The rise time of P1 (τ^{P1}_{rise}) and the fall time of P2 (τ^{P2}_{fall}) can be expressed as
  $\tau^{P1}_{rise}(E) = (2.02 \pm 0.08) \times 10^{-2} - (9.4 \pm 1.3) \times 10^{-3}\log_{10}(E[\mathrm{GeV}])$
  $\tau^{P2}_{fall}(E) = (2.42 \pm 0.16) \times 10^{-2} - (9.6 \pm 3.1) \times 10^{-3}\log_{10}(E[\mathrm{GeV}])$

- **The phase of the first peak has a slight but significant energy dependence.** This shift can be expressed as
  $Peak1(E) = (-3.8 \pm 0.6) \times 10^{-3} + (2.1 \pm 0.9) \times 10^{-3}\log_{10}(E[\mathrm{GeV}])$. As the energy increases, the peak position shifts to a later time in the light curve. For the second peak, because of the broader width, the peak phase is determined with a worse precision, and no significant energy dependence has been found.

- In the *Fermi*-LAT data above 10 GeV, a hint of the third peak is seen at phase ~ 0.75 with a significance of 3.5 σ. However, in the MAGIC data, only a 1.7 σ excess has been found and the flux upper limit based on the MAGIC data is in marginal contradiction with the *Fermi*-LAT results.

- Aiming for better observations of pulsars and other sources below 100 GeV with MAGIC, I participated in the development of a new photodetector, the Hamamatsu hybrid photodetector HPD R9792U-40. Compared to the currently used PMTs, its photodetection efficiency is twice higher and its ion-feedback rate is 500 times lower. Its charge resolution is excellent, too. The lifetime of the photocathode was proven to be long enough to allow a ten year observation time without significant degradation. A compensation circuit for the correction of the temperature dependence of the gain and safety circuits against the strong light were also successfully developed.

Based on these results, the following physics conclusions have been drawn:

- The extension of the pulsed gamma-ray emission up to 100 GeV observed by MAGIC sets a lower limit in height of the emission region at 7.8 times the neutron star radius. This rules out the inner magnetosphere emission scenario, i.e. the Polar Cap model, for the pulsation mechanism. Strong rejection of the super-exponential cut-off assumption by *Fermi*-LAT also favors the outer magnetosphere emission scenario, i.e. the Slot Gap model or the Outer Gap model.

- The rejection of the exponential cut-off assumption by the combined analysis of *Fermi*-LAT results and MAGIC results requires modifications of the standard outer magnetosphere model. If the magnetic field has an ideal dipole structure, there must be a place where the acceleration electric field is more than 10 times larger than that of the standard model ($> 3.3 \times 10^7$ [V/cm]). A distorted dipole structure of the magnetic field is another possible explanation.

- It is unlikely that the contribution of the inverse Compton scattering is the reason for the discrepancy between the standard outer magnetosphere model and the observed results, considering the energy of accelerated electrons and that of possible target photons.

- The radiation efficiency above 100 MeV is estimated to be $(1.36 \pm 0.04) \times 10^{-3}$ from the *Fermi*-LAT measurement while that above 30 GeV is estimated to be $(8.4 \pm 1.1) \times 10^{-6}$ from the MAGIC measurement. The discrepancy in the radiation energy above 30 GeV between the standard outer magnetosphere model and the MAGIC measurement amounts to 0.6% of the radiation energy above 100 MeV.

- The exponential behavior of the pulse edges can be explained by assuming that the emission angle with respect to the magnetic field line has an exponential distribution. Under this assumption, the energy dependence of the exponential decay constant θ_c can be expressed as $\theta_c = (7.9 \pm 0.6) - (3.4 \pm 1.2)\log_{10}(E[\mathrm{GeV}])$ [deg], $E < 100$ GeV.

- The simplest explanation for the energy dependence of the peak phase is that the emission region shifts inward toward the neutron star. The energy-dependent difference in path length $L(E)$ with respect to the radio emission region can be written as
  $L(E) = (40 \pm 6) - (20 \pm 9)\mathrm{log}_{10}(E/\mathrm{GeV})$ [km], $E < 100$ GeV.

10.2 Future Prospect: Observations of Other Gamma-ray Pulsars

The power-law-like extension of the gamma-ray energy spectrum of the Crab pulsar beyond the cut-off energy is a new discovery and currently there is no concrete theoretical explanation for it, except the discussions presented in this thesis. It would be necessary to check if this feature is unique for the Crab pulsar or common for all/some of the other pulsars. Although *Fermi*-LAT detected 46 gamma-ray pulsars, it is not possible to study the spectral behavior well beyond the cut-off energy with *Fermi*-LAT data due to the limited effective area of the detector. MAGIC is currently the only detector that can study pulsars at energies well beyond the cut-off energy. The next target of observation for MAGIC could be the Geminga pulsar, which is the second brightest above 1 GeV (next to the Crab pulsar) among the pulsars in the sky region which MAGIC can observe. Above 10 GeV, its flux is comparable to that of the Crab pulsar, according to the *Fermi*-LAT observations.

10.3 Future Prospect: Improvement of the Telescope Performance

The Crab pulsar is the only pulsar that has up to now been detected by an IACT. Other pulsars have never been detected from ground despite tremendous efforts. Even for the Crab pulsar, the energy spectrum could be determined only with the moderate statistical significance after 59.1 hours of observations, which is relatively long for IACT observations. The measured energy spectrum of the Crab pulsar is consistent with a power law above 25 GeV. However, if the statistical uncertainty of the measurements is smaller and the energy resolution is better, a possible curvature of the spectrum might become visible, which surely helps to understand the reason for the spectral extension after the cut-off.

In order to detect more pulsars and determine the energy spectrum with higher precision, one needs to meet the following requirements:

- A lower energy threshold.
- A larger effective area below 100 GeV
- A better (hadron+muon)/gamma separation below 100 GeV
- A better angular resolution below 100 GeV
- A better energy resolution below 100 GeV

For meeting these requirements, several improvements might be explored, as described in the following subsections.

10.3.1 Installation of the HPD R9792U-40

The replacement of the PMTs in the camera with the HPDs described in Chapter 9 would improve the telescope performance. The HPDs will double the number of detected Cherenkov photons from air showers. One can record shower images with higher precision, which will lead to a better (hadron+muon)/gamma separation, a better angular resolution and a better energy resolution. The energy threshold will also be lowered. The effective area should also increase largely, not only thanks to the higher photodetection efficiency but also due to the lower ion-feedback rate, allowing a more efficient trigger. However, the effect of the fast-and-huge afterpulsing, which may be attributed to the generation of characteristic X-rays inside the HPD, should be carefully studied.

10.3.2 Stereoscopic Observation with the MAGIC Stereoscopic System

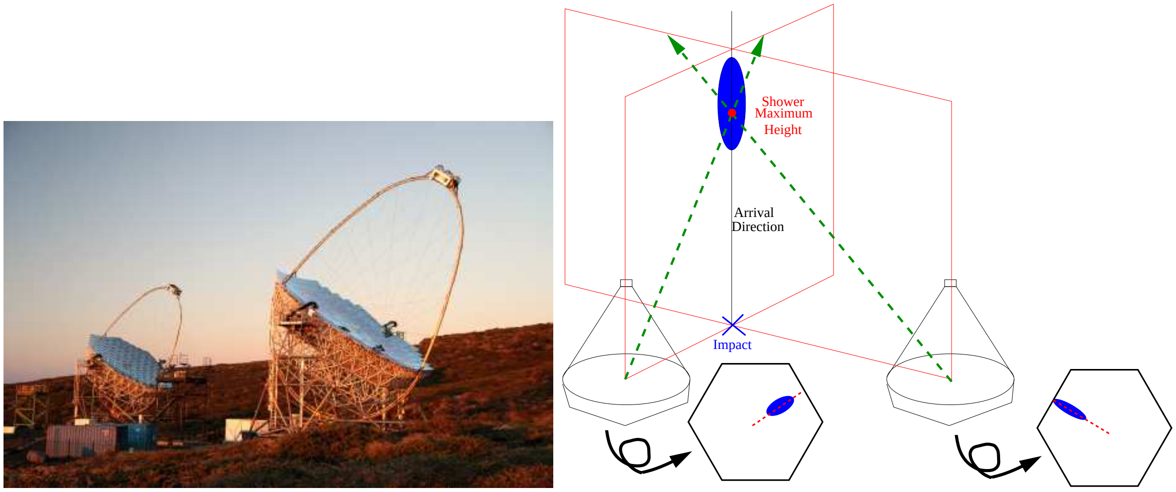

Figure 10.1: Left: A photograph of the two MAGIC telescopes adopted from [214]. Right: Concept for the stereo observations. Using two images recorded by the two telescopes, the arrival direction, the shower maximum height and the impact point of an air shower can be reconstructed with a much higher precision than with a single telescope.

In October 2009, MAGIC started stereoscopic observations with two telescopes. As schematically explained in the right panel of Fig. 10.1, if an air shower image is recorded by the two telescopes, the arrival direction can be reconstructed better than by a single telescope. In addition, the impact point of the shower and the shower maximum height can be determined with higher precision. This leads to a better energy resolution. The information of the shower maximum height has another advantage. A muon image may look like a low energy gamma-ray image if the impact distances from both telescopes are large (> 80 m). However, the majority of muons can be identified by the reconstructed shower maximum height (a muon does not produce a shower but can create a shower-like image). In the case of muon images, the height should be reconstructed to be ~ 5 km, which is unusually low for low energy gamma-rays (see Fig.

10.2). Also, Hadron/gamma-ray separation will improve simply due to the double amount of information from the two telescopes.

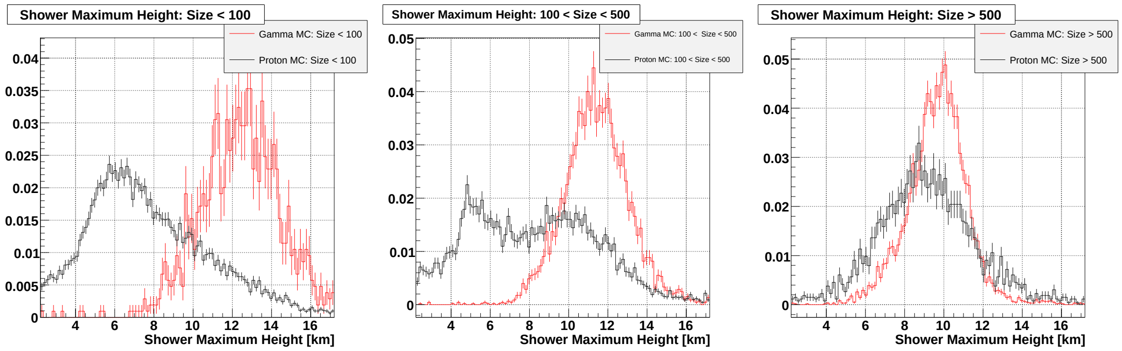

Figure 10.2: The shower maximum height distributions for observed data (black histograms) and gamma-ray MC (red histograms). $SIZE < 100$ *(left),* $100 < SIZE < 500$ *(middle) and* $SIZE > 500$ *(right) are shown. At* $SIZE > 500$*, two distributions are not clearly separated. At* $100 < SIZE < 500$*, two peaks can be seen for the observed data. The first peak at* ~ 5 *km can be explained by the the contribution from large-impact-distance muons (see text for detailed explanation). At* $SIZE < 100$*, only one peak can be seen at* ~ 6 *km for the observed data, suggesting that most of the events are large-impact-distance muons. Consequently, the distribution of the observed data is clearly separated from that of the gamma-ray MC. Therefore, the shower maximum height, which can precisely be estimated only with the stereo observations, is a powerful parameter for the gamma-ray/hadron separation for very low energies.*

However, the requirement for a coinciding signal from the two telescopes reduces the effective area especially for low energies. Below 50 GeV, the reduction can be as large as a factor of ~ 5. The energy threshold also increases. The trigger condition, i.e. whether or not the coincidence condition is fulfilled, must be carefully studied taking into account the advantage and the disadvantage of stereoscopic observation.

10.3.3 Pulsar Observation with CTA

A new project in VHE gamma-ray astronomy named Cherenkov Telescope Array (CTA) was recently proposed and a large international collaboration was formed (see [208]). The basic concept of CTA is an array of a large number of IACTs spread over a square kilometer area.

The telescope configuration would be as follows;

- The array consists of 3 different sizes of telescopes, $3-5$ large size ones, $20-30$ middle size ones, and $20-30$ small size ones.
- The large size telescopes have a reflector diameter of ~ 23 m with a FoV of 5 degree.
- The middle size telescopes have a reflector diameter of ~ 12 m with a FoV of 8 degree.

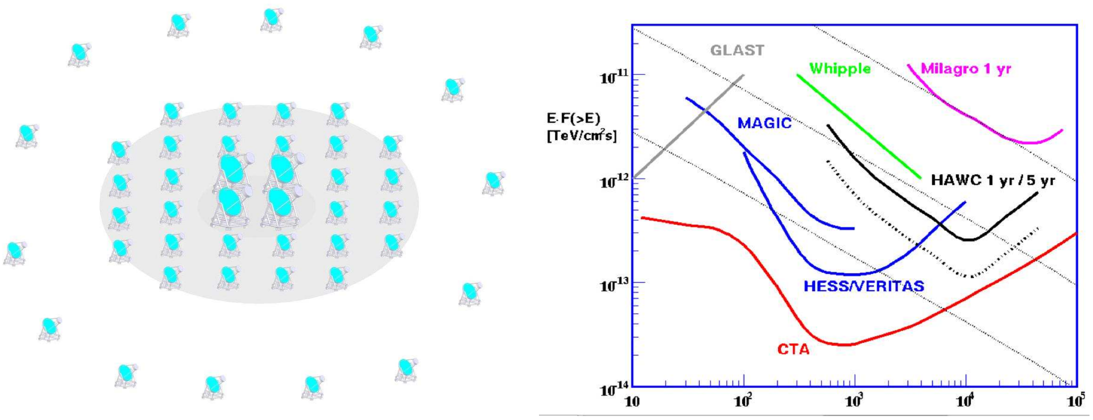

Figure 10.3: Left:An illustration of the CTA project. Figure adopted from [208]. Right: Sensitivity curves for currently operational experiments (GLAST(Fermi-LAT), MAGIC, HESS, VERITAS and Milagro) and expected sensitivity curves for future experiments (HAWC and CTA).Figure adopted from [210].

- The small size telescopes have a reflector diameter of ~ 6.5 m with a FoV of 10 degree.
- The distance between telescopes is around the order of 100 m.
- Two arrays will be constructed, a larger one in the southern hemisphere and a smaller one comprising only 23 m and 12 m telescopes in the northern hemisphere.

The parameters described above such as the numbers of telescopes, the diameters of reflectors and the angle of FoVs are not yet fixed. The primary purpose of the CTA project is the observation of VHE gamma-ray sources in the energy range between 100 GeV and 10 TeV with a sensitivity $5 - 10$ times higher than that of current IACTs. The accessible energy range will also be extended down to $10 - 20$ GeV and up to 100 TeV.

For pulsar observations, a sensitivity below 100 GeV is essential. Below 100 GeV, the sensitivity is mainly determined by the large size telescopes, whose reflector area will be ~ 1.7 times larger than that of MAGIC. If the SUM trigger system is used in CTA, and if a coincidence between multiple telescopes is not required for a trigger, then the energy threshold of the CTA may be roughly estimated to be ~ 15 GeV by scaling with the reflector diameter. Since there will be 3 - 5 telescopes, the effective area would increase correspondingly. The coincidence requirement might increase the threshold energy, but the reduction of the effective area may not be as much as in the case of the MAGIC-stereo system. The gain in sensitivity below 100 GeV should be intensely studied before all the designs are fixed and the construction of telescopes starts.

Bibliography

[1] Abbasi, R. U., et al., ”Measurement of the Flux of Ultrahigh Energy Cosmic Rays from Monocular Observations by the High Resolution Fly’s Eye Experiment”, Physical Review Letters, 92 p151101, 2004

[2] Abdo, A. A., et al., “Measurement of the Cosmic Ray $e^+ + e^-$ Spectrum from 20 GeV to 1 TeV with the Fermi Large Area Telescope”, Physical Review Letters, 102, p181101, 2009

[3] Abdo, A. A., et al., “Fermi Large Area Telescope Measurements of the Diffuse Gamma-Ray Emission at Intermediate Galactic Latitudes”, Physical Review Letters, 103, p251101, 2009

[4] Abdo, A. A., et al., “Fermi Large Area Telescope Observations of the Crab Pulsar and Nebula”, ApJ, 708, p1254, 2009

[5] Abdo, A. A. for the Fermi LAT collaboration, ”The First Fermi Large Area Telescope Catalog of Gamma-ray Pulsars”, arXiv:astro-ph/0910.1608, 2009

[6] Abdo, A. A., et al., ”The Vela Pulsar: Results from the First Year of Fermi LAT Observations”, ApJ, 713, p154, 2010

[7] Acero, F., et al., ”Detection of Gamma Rays from a Starburst Galaxy”, Science, 326, p1080, 2009

[8] Aharonian, F., et al., ”Phase-resolved TeV gamma-ray characteristics of the Crab and Geminga pulsars”, A&A, 346, p913, 1999

[9] Aharonian, F., et al., ”The Crab Nebula and Pulsar between 500 GeV and 80 TeV: Observations with the HEGRA Stereoscopic Air Cerenkov Telescopes”, ApJ, 614, p897, 2004

[10] Aharonian, F. A., “Very High Energy Cosmic Gamma Radiation”, World Sicentifc Publishing, 2004

[11] Aharonian, F., et al., “Observations of the Crab nebula with HESS”, A&A, 457, p899, 2006

[12] Aharonian, F., et al., ”3.9 day orbital modulation in the TeV γ-ray flux and spectrum from the X-ray binary LS 5039”, A&A, 460, p743, 2006

[13] Aharonian, F., et al., ”Primary particle acceleration above 100 TeV in the shell-type supernova remnant RX J1713.7-3946 with deep HESS observations”, A&A, 464, p235, 2007

[14] Aharonian, F., et al., ”New constraints on the mid-IR EBL from the HESS discovery of VHE γ-rays from 1ES 0229+200”, A&A, 475, pL9, 2007

[15] Albats, P., Frye, G. M. and Zych, A. D., ”Detection of 10-100 MeV γ-Rays from the Crab Nebula Pulsar NP 0532”, Nature, 240, p221, 1972

[16] Albert, J., et al., ”Variable Very-High-Energy Gamma-Ray Emission from the Microquasar LS I +61 303”, Science, 312, p1771, 2006

[17] Albert, J., et al., ”Observation of Gamma Rays from the Galactic Center with the MAGIC Telescope”, ApJ Letters, 638, pL101, 2006

[18] Albert, J., et al., ”Variable Very High Energy γ-Ray Emission from Markarian 501”, ApJ, 669, p862, 2007

[19] Albert, J., et al., ”FADC signal reconstruction for the MAGIC telescope”, Nuclear Instruments and Methods in Physics Research A, 594, p407, 2008

[20] Albert, J., et al., “VHE gamma-Ray Observation of the Crab Nebula and its Pulsar with the MAGIC Telescope”, ApJ, 674, p1037, 2008

[21] Aleksić, J., et al., ”MAGIC Gamma-ray Telescope Observation of the Perseus Cluster of Galaxies: Implications for Cosmic Rays, Dark Matter, and NGC 1275”, ApJ, 710, p634, 2010

[22] Aliu, E., et al., ”Observation of Pulsed γ-Rays Above 25 GeV from the Crab Pulsar with MAGIC”, Science, 322, p1221, 2008

[23] Aliu E., et al., “Improving the performance of the single-dish Cherenkov telescope MAGIC through the use of signal timing”, Astropart. Phys., 30, p293, 2009

[24] Amelino-Camelia, G., Ellis, J., Mavromatos, N. E., and Nanopoulos, D. V., ”Distance Measurement and Wave Dispersion in a Liouville-String Approach to Quantum Gravity”, International Journal of Modern Physics A, 12, p607, 1997,

[25] Amenomori, M., et al., “Multi-TeV Gamma-Ray Observation from the Crab Nebula Using the Tibet-III Air Shower Array Finely Tuned by the Cosmic Ray Moon’s Shadow”, ApJ, 692, p61, 2009

[26] Amsler, C., et al., Particle Data Group, ”Review of Particle Physics”, Physics Letters B, 667, p1, 2008

[27] Anchordoqui, L. A., Goldberg, H., Hooper, D., Marfatia, D. and Taylor, T. R., ”Neutralino dark matter annihilation to monoenergetic gamma rays as a signal of low mass superstrings”, Physics Letters B, 683, p321, 2010

[28] Arons, J. and Scharlemann, E. T., “Pair Formation Above Pulsar Polar Caps: Structure of The Low Altitude Acceleration Zone”, ApJ, 231, p854, 1979

[29] Arons, J., “Some Problems of Pulsar Physics”, Space Sci. Rev., 24, p437, 1979

[30] Arons, J., “Pair Creation Above Pulsar Polar Caps: Geometrical Structure And Energetics of Slot Gaps”, ApJ, 266, p215, 1983

[31] Atwood, W.B., et al., “The Large Area Telescope on the Fermi Gamma-ray Space Telescope Mission”, ApJ, 697, p1071, 2009

[32] Auger, P., Ehrenfest, P., Maze, R., Daudin, J. and Fréon, R. A., ”Extensive Cosmic-Ray Showers”,Reviews of Modern Physics, 11, p288, 1939

[33] Baring, M. G., ”Identifying the Mysterious EGRET Sources: Signatures of Polar Cap Pulsar Models”, arXiv:astro-ph/0106161, 2001

[34] Baring, M. G., ”High-energy emission from pulsars: the polar cap scenario”, Advances in Space Research, 33, p552, 2004,

[35] Baym, G. C., Pethick, D. and Sutherland, P., “The ground state of matter at high densities: Equation of state and stellar models”, ApJ, 170, p299, 1971

[36] Bean, S.J. and Tsokos, C.P., “ Developments in Nonparametric Density Estimation”, Internatinal Statistical Review, 48, p267, 1980

[37] Becker, W. and Aschenbach, B., “ROSAT HRI Observations of the Crab Pulsar, An Improved Temperature Upper Limit for PSR 0531+21”, The Lives of the Neutron Stars, p47, 1995

[38] Bednarek, W., ”γ-ray production in young open clusters: Berk 87, Cyg OB2 and Westerlund 2”, MNRAS, 382, p367, 2007

[39] Bednarek, W. and Sitarek, J., ”High-energy γ-rays from globular clusters”, MNRAS, 377, p920, 2007

[40] Berezinsky, V., Bottino, A. and Mignola, G., ”High energy gamma-radiation from the galactic center due to neutralino annihilation”, Physics Letters B, 325, p136, 1994

[41] Bernlohr, K., ”Impact of atmospheric parameters on the atmospheric Cherenkov technique*”, Astroparticle Physics, 12, p255, 2000

[42] Bertero, M., “Linear inverse and ill-posed problems”, Advance in Electronics and Electron Physics, 75, p1, 1989

[43] Biller, S. D., et al., ”Limits to Quantum Gravity Effects on Energy Dependence of the Speed of Light from Observations of TeV Flares in Active Galaxies”, Physical Review Letters, 83, p2108, 1999

[44] Biermann, P. L., ”TOPICAL REVIEW: The origin of the highest energy cosmic rays”, Journal of Physics G: Nuclear Physics, 23, p1, 1997

[45] Birk, G. T., Crusius-Wtzel, A. R. and Lesch, H., ”Hard Radio Spectra from Reconnection Regions in Galactic Nuclei”, ApJ, 559, p96, 2001

[46] Bock, R. K., et al., “Methods for multidimensional event classification: a case study using images from a Cherenkov gamma-ray telescope”, Nuclear Instruments and Methods in Physics Research A, 516, p511, 2001

[47] Bradt, H., Rappaport, S. and Mayer, W., ”X-Ray and Optical Observations of the Pulsar NP 0532 in the Crab Nebula”, Nature, 222, p728, 1969

[48] Breiman, L., “Random Forests”, Machine Learning, 45, p5, 2001

[49] Camenzind, M., “Compact Objects in Astrophysics”, Springer, 2007

[50] Carruthers, P. and Duong-van, M., ”New scaling law based on the hydrodynamical model of particle production”, Physics Letters B, 41, p597, 1972

[51] Chaves, R. C. G., et al., ”HESS J1848-018: Discovery Of VHE γ-ray Emission From The Direction Of W 43”, American Institute of Physics Conference Series, 1085, p372, 2008

[52] Cheng, K. S., Ho, C. and Ruderman, M., “Energetic Radiation From Rapidly Spinning Pulsars. I. Outer Magnetosphere Gaps”, ApJ, 300, p500, 1986

[53] Cheng, K.S., Ruderman, M. and Zhang, L., “A Three-dimensional Outer Magnetospheric Gap Model for Gamma-Ray Pulsars: Geometry, Pair Production, Emission Morphologies, and Phase-resolved Spectra”, ApJ, 537, p964, 2000

[54] Chiu, H.-Y. and Salpeter, E. E., ”Surface X-Ray Emission from Neutron Stars”, Physical Review Letters, 12, p413, 1964

[55] Cocke, W. J., Disney, M. J. and Taylor, D. J., ”Discovery of Optical Signals from Pulsar NP 0532”, Nature, 221, p525, 1969

[56] Comella, J. M., Craft, H. D., Lovelace, R. V. E., and Sutton, J. M., “Crab Nebula Pulsar NP 0532”, Nature, 221, p453, 1969

[57] Commichau, S., “Observation of Very High Energy Gamma-Rays from the Galactic Center with the MAGIC Telescope, considering Geomagnetic Field Effects on the Imaging Technique”, PhD Thesis, ETH Zürich, March 2007

[58] Cronin, J. W., Gaisser, T. K. and Swordy, S. P., ”Cosmic rays at the energy frontier”, Scientific American, 276, p32, 1997

[59] Cusumano, G., et al., ”Swift observations of GRB 050904: the most distant cosmic explosion ever observed”, A&A, 462, p73, 2007

[60] D’Ambrosio, C. and Leutz, H., ”Photoelectron backscattering from silicon anodes of hybrid photodetector tubes”, IEEE Transactions on Nuclear Science, 47, p1685, 2000

[61] Daugherty, J. K. and Harding, A. K., ”Gamma-Ray Pulsars: Emission from Extended Polar CAP Cascades”, ApJ, 458, p278, 1996

[62] Daum, A., et al., ”First results on the performance of the HEGRA IACT array”, Astroparticle Physics, 8, p1, 1997

[63] Davison, A. C. and Hinkley, D., “Bootstrap Methods and their Application” Cambridge Series in Statistical and Probabilistic Mathematics, 2006

[64] de Gouveia dal Pino, E. M. and Lazarian, A., ”Production of the large scale superluminal ejections of the microquasar GRS 1915+105 by violent magnetic reconnection”, A&A, 441, p845, 2005

[65] de Jager, O. C., ”Pulsar observations above 1 GeV with future ground-based gamma-ray telescopes”, Bulletin of the Astronomical Society of India, 30, p85, 2002

[66] Dole, H., et al., ”The cosmic infrared background resolved by Spitzer. Contributions of mid-infrared galaxies to the far-infrared background”, A&A, 451, p417, 2006

[67] Domingo-Santamaria, E., et al., ”The DISP analysis method for point-like or extended gamma source searches/studies with the MAGIC Telescope”, Proceedings of 29th International Cosmic Ray Conference, 5, p363, 2005

[68] Drury, L. O., ”Time-dependent diffusive acceleration of test particles at shocks”, MNRAS, 251, p340, 1991

[69] Dyks, J. and Rudak, B., ”Signatures of pulsar polar-cap emission at the high-energy spectral cut-off”, Advances in Space Research, 33, p581, 2004

[70] Efron, B., “Bootstrap Methods: Another Look at the Jackknife”, The Annals of Statistics, 7 p1, 1979

[71] Ellis, J., Mavromatos, N. E., Nanopoulos, D. V. and Sakharov, A. S., ”Cosmology: Synchrotron radiation and quantum gravity”, Nature, 428, p386, 2004

[72] Erber, T., ”High-Energy Electromagnetic Conversion Processes in Intense Magnetic Fields”, Reviews of Modern Physics, 38, p626, 1966

[73] Fan, Y. and Piran, T., ”Gamma-ray burst efficiency and possible physical processes shaping the early afterglow”, MNRAS, 369, p197, 2006

[74] Ferenc, D., Hrupeca, D and Lorenz, E., “Solution to the ion feedback problem in hybrid photon detectors and photomultiplier tubes”, Nuclear instruments and Methods in Physics Research A, 427, p518, 1999

[75] Fermi, E., ”On the Origin of the Cosmic Radiation”, Physical Review, 75, p1169, 1949

[76] Fermi, E.,”Galactic Magnetic Fields and the Origin of Cosmic Radiation.”, ApJ, 119, p1, 1954

[77] Fierro, J. M., Michelson, P. F., Nolan, P. L. and Thompson, D. J., ”Phase-resolved Studies of the High-Energy Gamma-Ray Emission from the Crab, Geminga, and VELA Pulsars”, ApJ, 494, p734, 1998

[78] Flowers, E. G., Sutherland, P. G. and Bond, J. R., ”Neutrino pair bremsstrahlung by nucleons in neutron-star matter”, Physical Review D,12, p315, 1975

[79] Freese, K., ”Review of Observational Evidence for Dark Matter in the Universe and in upcoming searches for Dark Stars”, EAS Publications Series, 36, p113, 2009

[80] Fryer, M. J., “A refiew of Some Non-parametric Methods of Density Estimation”, Journal of Mathematics and its Applications, 20, p335, 1977

[81] Furry, W. H., ”A Symmetry Theorem in the Positron Theory”, Physical Review, 51, p125, 1937

[82] Gaisser, T. K., “Cosmic rays and particle physics”, Cambridge University Press, 1990

[83] Garcia-Munoz, M., et al., ”Cosmic-ray propagation in the Galaxy and in the heliosphere - The path-length distribution at low energy”, ApJS, 64, p269,1987

[84] Ginzburg, V. L. and Zhelezniakov, V. V., ”On the pulsar emission mechanisms”, Annual review of astronomy and astrophysics, 13, p511, 1975

[85] Globus, N., Allard, D. and Parizot, E., ”Propagation of high-energy cosmic rays in extragalactic turbulent magnetic fields: resulting energy spectrum and composition”, A&A, 479, p97, 2008

[86] Gogberashvili, M., Sakharov, A. S. and Sarkisyan, E. K. G., ”Probing brane-world scenarios with vacuum refraction of light using gamma-ray bursts”, Physics Letters B, 644, p179, 2007

[87] Goldreich, P. and Julian, W. H., “Pulsar Electrodynamics”, ApJ, 157, p869, 1969

[88] Grupen, C., Bohrer, A., and Smolik. L., “Particle Detectors”, Cambridge Monographs on Particle Physics, Nuclear Physics and Cosmology, 1996

[89] Gunn, J. E. and Ostriker, J. P., “Acceleration of high-energy cosmic rays by pulsars”, Physical Review Letters, 22, p728, 1969

[90] Harding, A. K., Baring, M. G. and Gonthier, P. L., ”Photon-splitting Cascades in Gamma-Ray Pulsars and the Spectrum of PSR 1509-58”, ApJ, 476, p246, 1997

[91] Harding, A. K., “Gamma Rays From Rotation-Powered Pulsars”, arXiv:astro-ph/0208421, 2002

[92] Harding, A. and Muslimov, A., ”Pulsar Slot Gaps and Unidentified Egret Sources”, Astrophysics and Space Science, 297, p63, 2005

[93] Harding, A. K., Stern, J. V., Dyks, J. and Frackowiak, M., “High-Altitude Emission from Pulsar Slot Gaps: The Crab Pulsar”, ApJ, 680, p1378, 2008

[94] Hayashida, M., “ Observation of Very-High-Energy Gamma-Rays from Blazars with the MAGIC Telescope” PhD Thesis, LMU München, March 2008

[95] Hearn, A. G., “The Absorption of Ozone in the Ultra-violet and Visible Region of the Spectrum”, Proc. Phys. Soc., 78, p932, 1961

[96] Heitler, W., “The Quantum Theory of Radiation”, Clarendon Press, 1954

[97] Hengstebeck, T., “Measurement of the energy spectrum of the BL Lac object PG1553+113 with the MAGIC telescope in 2005 and 2006”, PhD thesis, Humbolt-Universitat zu Berlin.

[98] Hess, V., “Observations of penetrating radiation during seven free balloon flights”, Physikalische Zeitschrift, 13, p1084, 1912

[99] Hewish, A., Bell, S. J., Pilkington, J. D. H., Scott, P. F. and Collins, R. A., “Observation of a Rapidly Pulsating Radio Source”, Nature, 217, p709, 1968

[100] Hillas, A. M., ”Cerenkov light images of EAS produced by primary gamma”, Proceedings of 19th International Cosmic Ray Conference, 3, p445, 1985

[101] Hillas, A. M., ”Cosmic Rays: Recent Progress and some Current Questions”, arXiv:astro-ph/0607109, 2006

[102] Hirotani, K. and Shibata, S., ”Electrodynamic Structure of an Outer Gap Accelerator: Location of the Gap and the Gamma-Ray Emission from the Crab Pulsar”, ApJ, 558, p216, 2001

[103] Hirotani, K., Harding, A. K. and Shibata, S., ”Electrodynamics of an Outer Gap Accelerator: Formation of a Soft Power-Law Spectrum between 100 MeV and 3 GeV”, ApJ, 591, p334, 2003

[104] Hirotani, K., “Outer-Gap Versus Slot-Gap models for Pulsar High-energy Emissions: The Case of the Crab Pulsar”, ApJ, 688, pL25, 2008

[105] Horns, D. and Aharonian, F. A., ”The Crab Nebula: Linking MeV Synchrotron and 50 TeV Inverse Compton Photons”, ESA Special Publication, 552, p439, 2004

[106] Jackson, J. D., ”Classical electrodynamics”, Wiley, 1975

[107] Jauch, J. M. and Rohrlich, F., ”The theory of photons and electrons. The relativistic quantum field theory of charged particles with spin one-half”, Springer, 1976

[108] Joshi, B., et al.,”Magnetic Reconnection During the Two-phase Evolution of a Solar Eruptive Flare”, ApJ, 706, p1438, 2009

[109] Karpov, S., et al., ”Short time scale pulse stability of the Crab pulsar in the optical band”, Astrophysics and Space Science, 308, p595, 2007

[110] Kazbegi, A. Z., Machabeli, G. Z. and Melikidze, G. I., ”On the circular polarization in pulsar emission”, MNRAS, 253, p377, 1991

[111] Kennel, C. F. and Coroniti, F. V., “Confinement of the Crab Pulsar’s Wind by its Supernova Remnant”, ApJ, 283, p694, 1984

[112] Kim, Y. G., Nihei, T., Roszkowski, L. and Ruiz de Austri, R., ”Upper and Lower Limits on Neutralino WIMP Mass and Spin Independent Scattering Cross Section, and Impact of New (g-2)$_\mu$ Measurement”, Journal of High Energy Physics, 12, p34, 2002,

[113] Klepikov N.P., Zh. Eksperim. i Theo. Fiz. 26, p19, 1954

[114] Kuiper, L., et al., “The Crab Pulsar in the 0.75-30MeV range as seen by CGRO COMTEL”, A&A, 378, p918, 2001

[115] Kuiper, L., et al., ”Absolute timing with IBIS, SPI and JEM-X aboard INTEGRAL. Crab main-pulse arrival times in radio, X-rays and high-energy gamma -rays”, A&A, 411, pL31, 2003

[116] Langair, M. S., “High Energy Astrophysics”, Cambrigde University Press, 1981

[117] Langmuir, I, “The Effect of Space Charge And Residual Gases on Thermionic Currents in High Vacuum”, Phys. Rev., 2, p450, 1913

[118] Lessard, R. W., et al., ”Search for Pulsed TEV Gamma-Ray Emission from the Crab Pulsar”, ApJ, 531, p942, 2000

[119] Li, T.-P. and Ma, Y.-Q., ”Analysis methods for results in gamma-ray astronomy”, ApJ, 272, p317, 1983

[120] Lucarelli, F., et al., “The Central Pixel of the MAGIC telescope for optical observations”, Nuclear Instruments and Methods in Physics Research A, 589, p415, 2008

[121] Lyne, A. G., Pritchard, R. S. and Graham-Smith, F., ”Twenty-Three Years of Crab Pulsar Rotational History”, MNRAS, 265, p1003, 1993

[122] Lyutikov, M.,”Role of reconnection in AGN jets”, New Astronomy Review, 47, p513, 2003

[123] Manchester, R. N. and Taylor, J. H., “Pulsars”, Freeman, 1977

[124] Manchester, R. N., Hobbs, G. B., Teoh, A. and Hobbs, M., “The Australia Telescope National Facility Pulsar Catalogue”, Astronomical Journal, 129, p1993, 2005

[125] Marchenko, V. V., Hnatyk, B. I. and Pekur, D. V., ”Particle Acceleration in Hypernova Explosion”, Proceedings of the 16th Young Scientists’ Conference on Astronomy and Space Physics, p62, 2009

[126] Massaro, E., et al., ”The pulse shape and the spectrum of PSR B0531+21 (Crab pulsar) in the low-energy gamma rays observed with FIGARO II”, A&A, 338, p184, 1998

[127] Massaro, E., Cusumano, G., Litterio, M., and Mineo, T., “Fine phase resolved spectroscopy of the X-ray emission of the Crab pulsar (PSR B0531+21) observed with BeppoSAX”, A&A, 361, p695, 2000

[128] Mattingly, D., “Modern Tests of Lorentz Invariance”, Living Review in Relativity, 8, p5, 2005

[129] Mazin, D. and Raue, M., ”New limits on the density of the extragalactic background light in the optical to the far infrared from the spectra of all known TeV blazars”, A&A, 471, p439, 2007

[130] Mazin, D, “A study of very high energy gamma-ray emission from AGNs and constraints on the extragalactic background light”, PhD Thesis, Technische Universität München 2007

[131] Meegan, C., et al., “The Fermi Gamma-ray Burst Monitor”, ApJ, 702, p791, 2009

[132] Mineo, T., et al., ”A BeppoSAX observation of the Crab Pulsar (PSR B0531+21)”, A&A, 327, pL21, 1997

[133] Mirabel, I. F., ”Very energetic gamma-rays from microquasars and binary pulsars”, Science, 312, p1759, 2006

[134] Mitra, D., Gil, J. and Melikidze, G. I., ”Unraveling the Nature of Coherent Pulsar Radio Emission”, ApJ Letters, 696, pL141, 2009

[135] Mirzoyan, R. and Lorenz, E., “Measurement of the night sky light background at La Palma”, MPI-PhE/94-35., 1994

[136] Moffett, D. A. and Hankins, T. H., ”Multifrequency Radio Observations of the Crab Pulsar”, ApJ, 468, p779, 1996

[137] Molkov, S., Jourdain, E. and Roques, J. P., ”Absolute Timing of the Crab Pulsar with the INTEGRAL/SPI Telescope”, ApJ, 708, p403, 2010

[138] Musquere, A., ”Search for VHE pulsed emission from the Crab pulsar with the CELESTE experiment”, Proceedings of 26th International Cosmic Ray Conference, 3, p527, 1999

[139] Negele, J. W., and Vautherin, D, “Density-matrix expansion for an effective nuclear Hamiltonian II”, Phys. Rev. C, 11, p1031, 1975

[140] Nel, H. I. and de Jager, O. C., ”Gamma-Ray Pulsars: Polar CAP or Outer Gap Emission?”, Astrophysics and Space Science, 230, p299, 1995

[141] Ng, C.-Y. and Romani, R. W., ”Fitting Pulsar Wind Tori. II. Error Analysis and Applications”, ApJ, 673, p411, 2008

[142] Nolan, P. L., et al., ”Observations of the Crab pulsar and nebula by the EGRET telescope on the Compton Gamma-Ray Observatory”, ApJ, 409, p697, 1993

[143] Nomoto, K., et al., ”Hypernovae: Their Properties and Gamma-Ray Burst Connection”, Progress of Theoretical Physics Supplement, 155, p299, 2004

[144] Ochelkov, V. V. and Usov, V. V., ”Curvature radiation of relativistic particles in the magnetosphere of pulsars: Theory”, NASA STI/Recon Technical Report N, 80, p30239, 1979

[145] Oosterbroek, T., et al., ”Simultaneous absolute timing of the Crab pulsar at radio and optical wavelengths”, A&A, 488, p271, 2008

[146] Oser, S., et al., ”High-Energy Gamma-Ray Observations of the Crab Nebula and Pulsar with the Solar Tower Atmospheric Cerenkov Effect Experiment”, ApJ, 547, p949, 2001

[147] Paneque, D., Gebauer, H. J., Lorenz, E. and Mirzoyan, R., “A method to enhance the sensitivity of photomultipliers for Air Cherenkov Telescopes by applying a lacquer that scatters light”, Nuclear Instruments and Methods in Physics Research A, 518, p619, 2004

[148] Pelletier, G., Lemoine, M. and Marcowith, A., ”On Fermi acceleration and magnetohydrodynamic instabilities at ultra-relativistic magnetized shock waves”, MNRAS, 393, p587, 2009

[149] Petrova, S. A., ”The effect of synchrotron absorption on the observed radio luminosities of pulsars”, MNRAS, 336, p774, 2002

[150] Piran, T., ”Gamma-Ray Bursts as Probes for Quantum Gravity”, Lecture Notes in Physics, Berlin Springer Verlag, 669, p351, 2005

[151] Rankine, W. J. M., “On the Thermodynamic Theory of Waves of Finite Longitudinal Distrubance”, Philosophical Transactions, 160, p277, 1870

[152] Rees, M. J., and Gunn, J. E., “The origin of the magnetic field and relativistic particles in the Crab Nebula”, MNRAS 167, p1, 1974

[153] Riegel, B., et al., “A tracking monitor for the MAGIC Telescope”, Proceedings of 29th International Cosmic Ray Conference, 5, p219, 2005

[154] Rissi, M, “Detection of Pulsed Very High Energy Gamma-Rays from the Crab Pulsar with the MAGIC telescope using an Analog Sum Trigger”, PhD Thesis, ETH Zürich, 2009

[155] Romani, R. W., ”Gamma-Ray Pulsars: Radiation Processes in the Outer Magnetosphere”, ApJ, 470, p469, 1996

[156] Rots, A. H., Jahoda, K. and Lyne, A. G., ”Absolute Timing of the Crab Pulsar with the Rossi X-Ray Timing Explorer”, ApJ Letters, 605, pL129, 2004

[157] Ruderman, M. A. and Sutherland, P. G., “Theory of Pulsars: Polar Gaps, Sparks, and Coherent Microwave Radiation”, ApJ, 196, p51, 1975

[158] Saito, T.Y., et al., “Very high QE HPDs with a GaAsP photocathode for the MAGIC telescope project”, Nuclear Instruments and Methods in Physics Research A, 610 p258, 2009

[159] Saito, T.Y. and Sitarek, J., “ Improvement of the θ^2 analysis by using the Random Forest method in the DISP estimation”, MAGIC internal notes, TDAS09-01, 2009

[160] Sarkar, S.,”Possible Astrophysical Probes of Quantum Gravity”, Modern Physics Letters A, 17, p1025, 2002

[161] Scharlemann, E. T., Arons, J, and Fawley, W. M., “Potential Drops Above Pulsar Polar Caps: Ultrarelativistic Particle Acceleration Along The Curved Magnetic Field”, ApJ, 222, p297, 1978

[162] Schmelling, M., et al., “The method of reduced cross-entropy. A general approach to unfold probability distributions.”, Nuclear instruments and Methods in Physics Research A, 340, p400, 1994

[163] Schmelling, M., “Numerische Methoden der Datenanalyse”, MPI-K Heidelberg, 1998

[164] Schmidt, F., “CORSIKA Shower Images”, http://www.ast.lees.ac.uk/ fs/showerimages.html

[165] Shapiro, I. I., “Fourth Test of General Relativity”, Physical Review Letters, 13, p789, 1964

[166] Shapiro, S. L and Teukolsky, S. A., “Black Holes White Dwarfs, and Neutron Stars”, Wiley-VCH, 1983

[167] Shayduk, M., et al., “New Image Cleaning Method for the MAGIC Telescope”, MAGIC internal notes, TDAS05-09, 2005

[168] Shockley, W. and Pierce, J. R., “A theory of noise for electron multipliers”, Proc. Inst. Radio Eng., 26, p321, 1938.

[169] Słowikowska, A., Kanbach, G., Kramer, M. and Stefanescu, A., ”Optical polarization of the Crab pulsar: precision measurements and comparison to the radio emission”, MNRAS, 397, p103, 2009

[170] Spergel, D. N., et al., ”Three-Year Wilkinson Microwave Anisotropy Probe (WMAP) Observations: Implications for Cosmology”, ApJS, Cosmology: Cosmic Microwave Background, Cosmology: Observations, 170, p377, 2007

[171] Staelin, D. H. and Reifenstein, III, E. C., ”Pulsating Radio Sources near the Crab Nebula”, Science, 162, p1481, 1968

[172] Swordy, S. P., et al.,”Relative abundances of secondary and primary cosmic rays at high energies”, ApJ, 349, p625, 1990

[173] Takami, H., Yoshiguchi, H. and Sato, K., ”Propagation of Ultra-High-Energy Cosmic Rays above 10^{19} eV in a Structured Extragalactic Magnetic Field and Galactic Magnetic Field”, ApJ, 639, p803, 2006

[174] Takata, J. and Chang, H.-K., ”Pulse Profiles, Spectra, and Polarization Characteristics of Nonthermal Emissions from the Crab-like Pulsars”, ApJ, 670, p677, 2007

[175] Takata, J., Chang, H. K. and Shibata, S., “Particle acceleration and non-thermal emission in the pulsar outer magnetospheric gap”, MNRAS, 386, p748, 2008

[176] Takeda, M., et al., ”Extension of the Cosmic-Ray Energy Spectrum beyond the Predicted Greisen-Zatsepin-Kuz’min Cutoff”, Physical Review Letters, 81, p1163, 1998

[177] Tang, A. P. S., Takata, J., Jia, J. J. and Cheng, K. S., “A Revisit of the Phase-resolved X-Ray and Gamma-Ray Spectra of the Crab Pulsar”, ApJ, 676, p562, 2008

[178] Tapia, R.A. and Thompson, J.R., “Nonparametric Density Estimation”, John Hoplins University Press, 1978

[179] Thompson, D. J., “Gamma Ray Pulsars”, arXiv:astro-ph/0312272, 2003

[180] Thompson, D. J., ”High Energy Emission from Active Pulsars”, Advances in Space Research, 25, p659, 2000

[181] Tikhonov, A. N. and Arsenin, V. J., “Methods of Solution of Ill-posed Problems”, Nauka, 1979

[182] Toll, J.S., “The Dispersion Relation for Light and its Application to Problems Involving Electron Pairs.”, Ph.D. thesis, Princeton University, 1952

[183] Toor, A. and Seward, F. D., ”Observation of X-rays from the Crab Pulsar”,ApJ 216,p560, 1077

[184] Trimble, V., ”The Distance to the Crab Nebula and NP 0532”, Pub. Astron. Soc. Parcific, 85, p579, 1973

[185] Tsai, W.-Y. and Erber, T., ”Photon pair creation in intense magnetic fields”, Physical Review D, 10, p492, 1974

[186] Turlach, B. A., “Bandwidth Selection in Kernel Density Estimation: A Review”, Techinical Report 9317, C.O.R.E. and Institut de Statistique Universite Catholique de Lauvain, 1993

[187] Uchiyama, Y., Takahashi, T., Aharonian, F. A. and Mattox, J. R., “ASCA View of the Supernova Remnant γ Cygni (G78.2+2.1): Bremsstrahlung X-Ray Spectrum from Loss-flattened Electron Distribution”, ApJ, 571, p866, 2002

[188] Völk, H. J., Aharonian, F. A. and Breitschwerdt, D., ”The Nonthermal Energy Content and Gamma-Ray Emission of Starburst Galaxies and Clusters of Galaxies”, Space Science Reviews, 75, p279, 1996

[189] Wagner, R., “Measurement of VHE gamma-ray emission from four blazars using the MAGIC telescope and a comparative blazar study” Ph.D. Thesis, Technische Universität München, 2006

[190] Wagner, R., “VHE gamma-ray Sky Map and Source Catalog”, http://www.mppmu.mpg.de/ rwagner/sources/ , 2009

[191] Watters, K. P., Romani, R. W., Weltevrede, P. and Johnston, S., ”An Atlas for Interpreting γ-Ray Pulsar Light Curves”, ApJ, 695, p1289, 2009

[192] Webb, G. M., Drury, L. O. and Biermann, P., ”Diffusive shock acceleration of energetic electrons subject to synchrotron losses”, A&A, 137, p185, 1984

[193] Weekes, T. C., et al., ”Observation of TeV gamma rays from the Crab nebula using the atmospheric Cerenkov imaging technique”, ApJ, 342, p379, 1989

[194] Wills, R. D., et al., ”High-energy gamma-ray light curve of PSR0531+21”, Nature, 296, p723, 1982

[195] Wilson, D. B. and Rees, M. J., “Induced Compton scattering in pulsar winds”, MNRAS 185, p297, 1978

[196] Wittek, W., “Image parameters”, MAGIC internal notes, TDAS 02-03, 2002

[197] Xiao, C. J., et al., ”In situ evidence for the structure of the magnetic null in a 3D reconnection event in the Earth’s magnetotail”, Nature Physics, 2, p478, 2006

[198] Zatsepin, G. T. and Kuzmin, V. A., “Upper limit on the spectrum of cosmic rays”, JETP Letters, 4, p78, 1966

[199] Zatsepin, G. T. and Kuzmin, V. A., “End to the cosmic-ray spectrum?”, Physical Review Letters, 16, p748, 1966

[200] Zhang, L. and Cheng, K. S., ”High-Energy Radiation from Rapidly Spinning Pulsars with Thick Outer Gaps”, ApJ, 487, p370, 1997

[201] MAGIC Collaboration, ”Very-High-Energy gamma rays from a Distant Quasar: How Transparent Is the Universe?”, Science, 320, p1752, 2008

[202] VERITAS Collaboration, ”A connection between star formation activity and cosmic rays in the starburst galaxy M82”, Nature, 462, p770, 2009

[203] “The ATNF Pulsar Catalogue”, http://www.atnf.csiro.au/research/pulsar/psrcat/

[204] “BeppoSAX ASI Science Data Center”, http://www.asdc.asi.it/bepposax, Observation Codes 20795007 and 207950071

[205] “Chandra :: Photo Album :: CL 0542-4100 & CL 0848.6+4453”, http://chandra.harvard.edu/photo/2007/agns/

[206] “Chandra :: Photo Album :: Crab Nubula”, http://chandra.harvard.edu/photo/1999/0052/

[207] “CGRO Archive”, ftp://cossc.gsfc.nasa.gov/compton/data/comptel/

[208] “The Cherenkov Telescope Array project”, http://www.mpi-hd.mpg.de/hfm/CTA/

[209] “Fermi Science Support Center: Fermi Data”, http://fermi.gsfc.nasa.gov/ssc/data/

[210] “HAWC, The High Altitude Water Cherenkov Experiment”, http://hawc.umd.edu/science.php

[211] “*HEASARC* Online Service”, http://heasarc.gsfc.nasa.gov/cgi-bin/W3Browse/w3browse.pl, observation identifier RH400639N00

[212] “HubbleSite - NewsCenter - Happy Sweet Sixteen, Hubble Telescope!”, http://hubblesite.org/newscenter/archive/releases/2006/14/

[213] “JODRELL BANK CRAB PULSAR MONTHLY EPHEMERIS”, http://www.jb.man.ac.uk/ pulsar/crab.html

[214] “MAGIC - Album: pictures”, http://wwwmagic.mppmu.mpg.de/gallery/pictures/

[215] “Magnetar images and drawings – NASA Science”, http://science.nasa.gov/newhome/headlines/ast05mar99_1a.htm

[216] “National Radio Astronomy Observatory Image Galally”, http://images.nrao.edu/393

[217] “Stopping-Power and Range Tables for Electrons, Protons, and Helium Ions”, http://www.nist.gov/physlab/data/star/index.cfm

[218] “Tempo”, http://www.atnf.csiro.au/research/pulsar/tempo/

[219] “XCOM: Photon Cross Sections Database”, http://www.nist.gov/physlab/data/xcom/index.cfm

[220] Private communication with Jürgen Hose

Acknowledgement

First of all, I would like to thank Prof. Dr. Masahiro Teshima for providing me with the opportunity to join the MAGIC collaboration and to do research in the Max-Planck-Institut für Physik. I also appreciate Prof. Dr. Christian Kiesling for being my academic advisor at the Ludwig-Maximimlian-Universität München.

I am also deeply grateful to Dr. Thomas Schweizer, Dr. Nepomuk Otte, Dr. Michael Rissi and Dr. Maxim Shayduk for their greatest achievement of lowering the energy threshold of the MAGIC telescope by developing and installing the SUM trigger. Without their tremendous efforts and ability, this PhD work would not have been realized.

I am very happy to have been supervised by Prof. Dr. Masahiro Teshima, Dr. Thomas Schweizer, Dr. Maxim Shayduk, Dr. Razmick Mirzoyan and Dr. Eckart Lorenz. Discussions with them were always constructive, educative and very inspiring. Whenever I got stuck in my research, Masahiro gave me accurate advice, which immediately brought things forward. Thomas's deep knowledge, wide experiences, and agile mind helped me to accomplish this work. Maxim, with whom I spent most of my PhD time in the same office, always took great care of my work. I learned many details of the IACT technique and photosensors from Razmick. His expiation was always so quantitative that I could have a clear understanding of the IACT technique and photosensors. Eckart guided my work to the right direction by giving me advice from a long-term perspective, which he can do better than anyone because of his long experience of assisting students. In addition, Eckart's help was essential for finalizing this thesis.

I would also like to thank all my friends in the Max-Planck-Institut für Physik, Daniela Borla Tridon, Emiliano Carmona, Pierre Colin, Antonios Dettlaff, Toni Engelhardt, Christian Fruck, Florian Göbel, Dennis Häfner, Jürgen Hose, Tobias Jogler, Hanna Kellermann, Julian Krause, Matthias Kurz, Hiroko Miyamoto, Koji Saito, Maxim Shayduk, Julian Sitarek, Burkhard Steinke, Hajime Takami, Robert Wagner and many others. I enjoyed with them having many parties, playing many different sports, chatting during lunch and break time and having many physics discussion. Among them, I had the best time with Julian Sitarek and Maxim Shayduk. It was great fun to talk with them because they are not only intelligent but also very cheerful. I am also very grateful to other collaborators in different institutes. Drinking with them after the collaboration meeting in many different cities was the best pleasure during my PhD time.

I thank my parents, my brother and my sister who supported me from my home country. Their letters and their e-mails encouraged me very much. Moreover, nothing could have made me happier than Japanese foods they regularly sent me. Last but not least, I thank and will thank for all my life my wife, Emi, who came over to Munich to live together with me. I could overcome many difficulties in doing my PhD work just because she was always with me.